SCUOLA DI DOTTORATO

UNIVERSITÀ DEGLI STUDI DI MILANO-BICOCCA

Department of Earth and Environmental Sciences

PhD program Chemical, Geological and Environmental Sciences Cycle XXXVIII
Curriculum in Chemical Sciences

Multiscale Molecular Modelling Studies of Enzymes for the Degradation of Non-Biodegradable and Biodegradable Substrates

Orlando Carla

Registration number: 896500

Tutor: Prof. Greco Claudio

Supervisor: Prof. Bertini Luca

Co-Supervisor: Prof. Marino Tiziana

Co-Supervisor: Dr. Arrigoni Federica

Coordinator: Prof. Malusà Marco

ACADEMIC YEAR 2024/2025

Contents

Acknowledgements

This PhD project was funded by the PRIN2020 – SEAfood WAste Valorization by oxidative metalloEnzymes (SEA-WAVE) program. In particular, I would like to thank Prof. Luca De Gioia, (University of Milano-Bicocca) for his support and for providing the scientific framework that made this research possible.

I would like to express my deepest gratitude to all those who supported me throughout this intense PhD journey. In particular, I would like to thank the Molecular Modelling Laboratory at the University of Milano-Bicocca and all its members, who have been both essential and welcoming throughout this experience.

A special thanks goes to my Supervisor, Prof. Luca Bertini (University of Milano-Bicocca), my Co-Supervisors, Prof. Tiziana Marino (University of Calabria) and Dr. Federica Arrigoni (University of Milano-Bicocca), and my Tutor, Prof. Claudio Greco (University of Milano-Bicocca), for their continuous support, scientific guidance, and trust. Their advice, professionalism, and academic integrity are among the most valuable lessons I will carry with me as I move forward in my career.

I am also grateful to Prof. Mario Prejanò and Dr. Giada Ciardullo, from the University of Calabria, for being key scientific references during the development of my research and for always welcoming my questions with kindness and generosity, especially during the most challenging moments of this journey.

Finally, I would like to sincerely thank Prof. Iñaki Tuñón and Prof. Juan Aragó for introducing me to new methodologies and approaches at the Universitat de València and the ICMol Institute, and for the warm hospitality and stimulating research environment they provided.

Amino Acid Abbreviations

Complete Name	Abbreviation	
Amino Acid	**3-letter chemical code**	**1-letter biological code**
Alanine	Ala	A
Arginine	Arg	R
Asparagine	Asn	N
Aspartic acid	Asp	D
Cysteine	Cys	C
Glutamic acid	Glu	E
Glutamine	Gln	Q
Glycine	Gly	G
Histidine	His	H
Isoleucine	Ile	I
Leucine	Leu	L
Lysine	Lys	K
Methionine	Met	M
Phenylalanine	Phe	F
Proline	Pro	P
Serine	Ser	S
Threonine	Thr	T
Tryptophan	Trp	W
Tyrosine	Tyr	Y
Valine	Val	V

List of Abbreviations and Acronyms

AA - Auxiliary Activities

AMBER - Assisted Model Building and Energy Refinement

BsL - *Bacillus subtilis Laccase*

CAZy – Carbohydrate Active enZYmes

CHARMM - Chemistry at HARvard Macromolecular Mechanics

CGr - Conjugate Gradient

CYM - Deprotonated cysteine (thiolate ion)

CYP - Cytochrome P450

DFT - Density Functional Theory

EC - Enzyme Commission

EG - Ethylene glycol

EPR - Enhanced Permeability and Retention

FAD - Flavin Adenine Dinucleotide

$FADH_2$ - Flavin Adenine Dinucleotide, dihydro form

FF - Force Field

FES - Free Energy Surface

FFT - Fast Fourier Transform

FMN – Flavin Mononucleotide

FMNH - Flavin Mononucleotide semiquinone (radical) form

GGA - Generalized Gradient Approximation

GHG - Greenhouse Gases

GLIDE - Grid-based Ligand Docking with Energetics

GROMOS - GROningen MOlecular Simulation

HAA – Hydrogen Atom Abstraction

HDPE – High-density Polyethylene

HK - Hohenberg and Kohn

ID - unique identifier

ILS - Iterated Local Search algorithm

KS - Kohn-Sham

LDA - Local Density Approximation

LDPE – Low-density Polyethylene

LGA - Lamarckian Genetic Algorithm

LJ - Lennard-Jones

LMCO – Laccase Multi-Copper Oxidase

LPMO - Lytic Polysaccharide Monooxygenase

M1 – First Mutation

M2 – Second Mutation

M12 – First and Second Mutations

M1f – First Mutation free form

M2f – Second Mutation free form

M12f – First and Second Mutations free form

MC – Monte Carlo

MD - Molecular Dynamics

MFEP - Minimum Free-Energy Path

MHET - Mono(2-hydroxyethyl) terephthalate

MM - Molecular Mechanics

NPT - Constant Pressure and Temperature Ensemble

NAD - Nicotinamide Adenine Dinucleotide

NADH - Nicotinamide Adenine Dinucleotide (Reduced Form)

NADP+ - Nicotinamide Adenine Dinucleotide Phosphate

NADPH - Nicotinamide Adenine Dinucleotide Phosphate (Reduced Form)

NVE - Constant Energy Ensemble

NVT - Constant Temperature Ensemble

PAHs - Polycyclic Aromatic Hydrocarbons

PAL – Palmitic Acid

PAMETs - Peptidic Artificial METalloenzymes

PDB - Protein Data Bank

PBC - Periodic Boundary Conditions

PCA - Principal Component Analysis

PCET – Proton-coupled electron transfer

PME - Particle Mesh Ewald

PMF - Potential of Mean Force

PE – Polyethylene

PET -Polyethylene terephthalate

POME - Palm Oil Mill Effluent

PP - polypropylene

PS - polystyrene

QM - Quantum Mechanics

QM/MM - Quantum Mechanics/Molecular Mechanics

RCSB - Research Collaboratory for Structural Bioinformatics

RDF - Radial Distribution Function

RMSD - Root Mean Square Deviation

RMSF - Root Mean Square Fluctuation

SD - Steepest Descent

TIP3P - Transferable Intermolecular Potential with 3 Points

TPA - Terephthalic acid

TvL - *Trametes versicolor* Laccase

UFF - Universal Force Field

WT – Wild Type

xTB - extended Tight Binding

Abstract

In recent decades, the growing awareness of the environmental impact of human activities has stimulated the search for sustainable strategies for waste treatment and pollution mitigation. Among the most promising solutions are bioremediation and biovalorization, which exploit the catalytic potential of enzymes to convert organic waste into high-value products while reducing environmental impact.

This doctoral thesis lies within the field of computational bioinorganic chemistry and aims to elucidate the molecular mechanisms underlying the enzymatic degradation and transformation of recalcitrant substrates such as plastics, hydrocarbons, and biomass.

To achieve this goal, a multiscale computational approach was developed, integrating molecular docking, classical molecular dynamics, and density functional theory to investigate enzyme–substrate interactions, catalytic mechanisms, and structure–function relationships. This combination made it possible to analyze the entire catalytic process, from substrate recognition to electronic transformations at the active site, providing theoretical tools for the rational design of efficient biocatalysts.

The research is divided into two main sections. The first part focuses on degradative enzymes active on non-biodegradable polymers: simulations on FAST-PETase and laccases provided new insights into depolymerization and oxidation mechanisms, highlighting structural factors governing enzyme–substrate complex stability. The second part concerns metalloenzymes involved in the valorization of renewable biomass, such as cytochrome P450SPα and Lytic polysaccharide monooxygenase SmAA10, emphasizing the role of structural flexibility in modulating catalytic activity.

Overall, this thesis demonstrates that the integration of multiscale computational methodologies represents an effective tool for understanding and optimizing enzymatic catalysis, contributing to the development of sustainable technologies aligned with the principles of the circular economy.

Riassunto

Negli ultimi decenni, la crescente consapevolezza dell'impatto ambientale delle attività antropiche ha stimolato la ricerca di strategie sostenibili per il trattamento dei rifiuti e la mitigazione dell'inquinamento. Tra le soluzioni più promettenti figurano il biorisanamento e la biovalorizzazione, che sfruttano il potenziale catalitico degli enzimi per convertire i rifiuti organici in prodotti ad alto valore aggiunto, riducendo al contempo l'impatto ambientale.

La presente tesi si colloca nell'ambito della bioinorganica computazionale, con l'obiettivo di chiarire i meccanismi molecolari alla base della degradazione e trasformazione enzimatica di substrati recalcitranti quali plastiche, idrocarburi e biomasse.

A tal fine è stato sviluppato un approccio computazionale multiscala, che integra molecular docking, dinamica molecolare classica e teoria del funzionale della densità per investigare le interazioni enzima–substrato, i meccanismi catalitici e le relazioni struttura–funzione. Tale combinazione ha permesso di analizzare l'intero processo catalitico, dal riconoscimento del substrato fino alle trasformazioni elettroniche nel sito attivo, fornendo strumenti teorici per la progettazione razionale di biocatalizzatori efficienti.

La ricerca è articolata in due sezioni principali. La prima parte riguarda enzimi degradativi attivi su polimeri non biodegradabili: le simulazioni su FAST-PETase e laccasi hanno fornito nuove informazioni sui meccanismi di depolimerizzazione e ossidazione, evidenziando i fattori strutturali che regolano la stabilità del complesso enzima–substrato. La seconda parte è dedicata a metalloenzimi coinvolti nella valorizzazione di biomasse rinnovabili, quali citocromo P450SPα e Lytic polysaccharide monooxygenase SmAA10, evidenziando il ruolo della flessibilità strutturale nella modulazione dell'attività catalitica.

Nel complesso, la tesi dimostra come l'integrazione di metodologie computazionali multiscala rappresenti un efficace strumento per comprendere e ottimizzare la catalisi enzimatica, contribuendo allo sviluppo di tecnologie sostenibili in linea con i principi dell'economia circolare.

Chapter 1
Introduction

In recent decades, the growing awareness of the environmental impact of anthropogenic activities has prompted the scientific community to develop sustainable waste treatment and pollution mitigation strategies. In this context, bioremediation and biovalorization of biomass have emerged as two promising approaches for recovering and converting organic waste materials into high-value-added products, while simultaneously reducing environmental impact [1,2].

Both processes rely on natural or engineered enzymes capable of catalyzing selective degradation reactions, often on recalcitrant substrates such as plastics, polycyclic aromatic hydrocarbons (PAHs), or non-lignocellulosic biomass [3–7].

Within this framework, the present thesis is situated in the field of computational bioinorganic chemistry, providing detailed molecular-level insights that are often difficult to obtain through experimental methods. The focus is on studying metalloenzymes involved in the degradation of complex organic compounds and the valorization of biologically derived materials [8,9].

By employing advanced computational tools, it has been possible to explore the behaviour and properties of these enzymatic systems in depth. Molecular Dynamics (MD) simulations, based on the principles of classical Molecular Mechanics, have allowed for the analysis of the structural flexibility of biomolecular complexes, overcoming the limitations of static crystallographic structures [10]. Molecular docking has been employed to predict the interaction modes between ligands and enzymatic targets, providing useful models to rationalize molecular recognition [11]. Finally, Density Functional Theory (DFT) [12] has enabled the investigation of catalytic mechanisms and electronic properties of active sites, offering a robust theoretical foundation for optimizing catalytic performance and designing more effective mutants or biomimetic systems.

By leveraging these multiscale computational approaches, my research has focused particularly on:

— The structural and functional analysis of degradative enzymes and their possible mutants involved in the breakdown of synthetic polymers (such as PET or PE).

— The study of novel enzymatic targets of environmental and biotechnological interest, with special emphasis on laccases, through the analysis of their dynamic behavior and degradation mechanisms of unconventional hydrocarbon substrates.
— The computational analysis of metalloenzyme mutants aimed at improving the conversion of fatty acids and aromatic compounds into high-value intermediates, using molecular modeling, docking, and dynamic simulations to identify structural modifications capable of enhancing catalytic activity.

Understanding the molecular details underlying these processes is essential not only to improve the efficiency of current waste treatment systems but also to support a circular economy based on renewable resources and low-impact technologies. This thesis, therefore, aims to contribute (through an integrated theoretical approach) to the development of innovative catalytic solutions to address the most pressing environmental challenges of our time.

1.1 Environmental wastes

The growing global production of waste is one of the major environmental issues associated with urbanization, industrialization, and modern agricultural practices. These activities release vast amounts of toxic pollutants into the environment, threatening air, water, and soil ecosystems, and causing diseases that are harmful to all living organisms [13]. According to Directive 2008/98/EC of the European Parliament (Italian Legislative Decree No. 152/2006 and subsequent amendments), environmental waste is defined as:

"Any substance or object which the holder discards or intends or is required to discard."

Waste can be classified based on various criteria, including origin, hazardousness, and physical state, or distinguished by the associated risks, such as industrial, agricultural, WEEE (Waste Electrical and Electronic Equipment), radioactive, and marine waste [14]. However, a fundamental distinction among different types of waste lies in their biodegradability [15]. While some materials can be readily broken down through biological processes, others (more complex and resistant) can persist in the environment for extended periods, posing a significant threat to ecosystems.

1.1.1 Non-biodegradable wastes

Industrial waste, including plastics, heavy metals, solvents, and halogenated compounds, represents one of the most problematic categories of environmental pollutants due to their low degradability and high persistence in environmental compartments. Among the most hazardous substances are numerous synthetic

compounds such as heavy metals, artificial dyes, plastics, pesticides, and PAHs [16–18]. These pollutants, primarily originating from industrial, agricultural, and domestic activities, pose significant challenges in terms of waste management and treatment, as they require specialized technologies to prevent severe impacts on the environment and human health.

For instance, plastics, which are largely derived from fossil resources, are extremely resistant to biodegradation, tend to accumulate in ecosystems, and release toxic substances that threaten wildlife, particularly aquatic organisms. Similarly, PAHs are compounds known for their toxicity and carcinogenicity and can exert harmful effects even at low concentrations when exposure is prolonged over time [18].

Although certain wastes are generally considered non-biodegradable, under specific conditions and through the action of particular organisms (either naturally occurring or genetically modified), partial degradation or transformation can occur.

1.1.1.1 Plastics

The consumption of plastics and related products has increased exponentially in recent decades, owing to their versatility and wide range of applications. Currently, global plastic waste production exceeds 260 million tons per year, a figure projected to double by 2030. Of this amount, approximately 52 million tons are incinerated for energy recovery, while around 100 million tons end up in landfills, which are often located in economically disadvantaged areas [19]. In such contexts, local communities are exposed to the long-term toxic effects, contributing to the worsening of global environmental and social issues [20]. The high production and intensive use of non-biodegradable materials have given rise to a genuine environmental emergency. This category primarily includes synthetic plastic polymers such as polyethylene terephthalate (PET), high- and low-density polyethylene (HDPE and LDPE), polystyrene (PS), polypropylene (PP), polyvinyl chloride (PVC), and other synthetic materials, as shown in Figure 1.1.

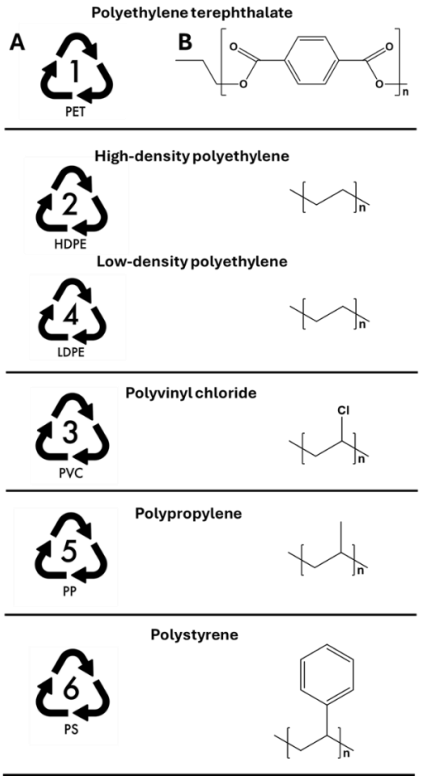

Figure 1.1: A. The international recycling symbols for plastics, B. The monomer sequences of commercial plastic polymers.

Once released into the environment, these materials fragment over time, generating microplastics and nanoplastics [21]. In addition to contributing to greenhouse gas emissions throughout their life cycle, these particles have been associated with harmful effects on human health, including contact dermatitis, as well as bioaccumulation phenomena documented in several scientific studies [22,23]. Currently, plastic waste is managed primarily through conventional practices such as incineration and landfilling, especially in cases where recycling is technically or economically unfeasible. However, these solutions present significant environmental drawbacks: incineration produces harmful emissions, while landfills contaminate soil and groundwater [24]. To address these challenges, several alternative solutions are currently under development and experimentation. These aim not only to mitigate the environmental impact of plastic waste but also to promote energy recovery through more sustainable approaches.

Polyethylene Terephthalate

Since its discovery in 1941, PET has become widely used, particularly in the packaging industry, progressively contributing to a serious environmental pollution issue, which has only been systematically addressed in recent years [25].

PET is an aliphatic polyester composed of bis(2-hydroxyethyl) terephthalate monomers. It is a thermoplastic material with high resistance to biodegradation, and for this reason, it is extensively employed worldwide in the production of bottles, textile fibers, films, and containers. Although several systems exist for the post-consumer recovery of PET bottles, the global recycling rate remains below 50% [26]. As a result, large quantities of PET waste are released into the environment, causing significant ecological consequences. To effectively address this issue, it is essential to promote more sustainable management strategies, including eco-friendly depolymerization processes capable of breaking down the polymer into its original monomers, thus facilitating its reuse [26].

Among the most promising solutions is enzymatic degradation, made possible by the discovery of the bacterium Ideonella sakaiensis 201-F6, which is capable of metabolizing PET. Studies on this microorganism have revealed a catalytic mechanism involving two key enzymes: PETase, which depolymerizes PET into MHET (mono(2-hydroxyethyl) terephthalate), and MHETase, which further hydrolyzes MHET into its constituent monomers (terephthalic acid (TPA) and ethylene glycol) compounds that can be readily assimilated into biological cycles [27]. This biotechnology opens new perspectives for the sustainable management of plastic waste, offering a viable alternative to conventional methods, which are often energy-intensive and polluting.

Polyethylene

Another highly relevant plastic material is polyethylene (PE), which, together with other polyolefins such as polypropylene (PP) and polystyrene (PS), accounts for over 60% of global plastic production [28]. Polyethylene, composed of repeating –CH_2– units, has the simplest chemical structure among all synthetic polymers. Its widespread use is attributed to a combination of factors: low production cost, high chemical resistance, good processability, flexibility, and, in some variants, even transparency in thin films [29]. However, from an environmental standpoint, the accumulation of PE-based waste is an increasing concern due to the material's persistence in the environment. The degradation of PE can occur through two main mechanisms:

- Abiotic, involving physicochemical processes induced by environmental factors such as temperature, UV radiation, and oxygen.
- Biotic, i.e., degradation carried out by microorganisms capable of altering and metabolizing the polymer, thereby modifying its chemical and structural properties [30].

In nature, these two mechanisms act synergistically, but under standard environmental conditions, PE biodegradation is extremely slow, as highlighted by

numerous studies [31]. Over time, microorganisms have partially adapted to the presence of synthetic polymers, developing the ability to attack and degrade highly recalcitrant materials [32]. This degradative potential is enabled by specialized microbial enzymes, which are receiving growing attention in research as biotechnological tools for the sustainable management of plastic waste. Among the most studied enzymatic classes for PE biodegradation are peroxidases, lipases, esterases, and laccases. In particular, laccases have shown promise in the oxidation of complex, degradation-resistant substrates, due to their high redox activity [33]. The targeted production and catalytic use of innovative enzymes now represents an emerging strategy, potentially complementary to traditional recycling methods, for the depolymerization and valorization of PE-based plastics [32].

1.1.1.2 PAHs

Polycyclic aromatic hydrocarbons constitute a class of persistent organic pollutants commonly found in terrestrial and aquatic ecosystems. They are primarily generated from the incomplete combustion of organic materials such as petroleum, coal, wood, and natural gas [34]. Due to their toxic, genotoxic, mutagenic, and carcinogenic properties, PAHs are considered among the most hazardous environmental contaminants [18].

From a structural perspective, PAHs are compounds composed of at least two fused aromatic rings, which confer high chemical stability and resistance to degradation [35,36]. Their physicochemical properties, including hydrophobicity and volatility, promote their environmental dispersion, making them ubiquitous in the atmosphere, soil, and aquatic systems [37]. Based on molecular weight and the number of aromatic rings, PAHs are classified as:

- Low molecular weight PAHs (up to three rings), which are more volatile and less persistent, but also more readily biodegradable.
- High molecular weight PAHs (four or more rings), which are less volatile but more persistent and carcinogenic [38].

Due to their toxicity and widespread occurrence, the United States Environmental Protection Agency (US EPA) has included 16 priority PAHs in the list of pollutants to be monitored shown in Table 1.1.

Among the most hazardous are benzo[a]anthracene, benzo[a]pyrene, and dibenzo[ah]anthracene, which are known for their high carcinogenic potential [39,40].

Name	Structure
Benzo[a]pyrene	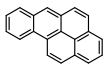
Acenaphthene	
Acenaphthylene	
Anthracene	
Benz[a]anthracene	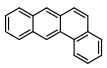
Benzo[b]fluoranthene	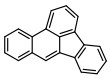
Benzo[k]fluoranthene	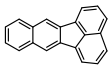
Benzo[g,h,i]perylene	
Chrysene	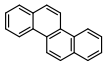
Dibenz[a,h]anthracene	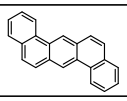
Fluoranthene	
Fluorene	
Indeno[1,2,3-c,d]pyrene	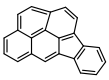
Naphthalene	
Phenanthrene	
Pyrene	

Table 1.1: List and chemical structure of the 16 priority PAHs in the list of pollutants to be monitored

In recent decades, biological technologies for the removal of PAHs, particularly bioremediation, have emerged as some of the most promising solutions for environmental detoxification [41]. This approach relies on the use of microorganisms (including bacteria, fungi, yeasts, and algae) capable of

transforming or mineralizing PAHs into less toxic compounds or into harmless end products such as carbon dioxide and water [42].
Microbial biodegradation is mediated by specific enzymes that catalyze the cleavage of aromatic rings. Various microbial species have been identified for their efficiency in degrading PAHs, including:

- Bacteria: Pseudomonas, Corynebacterium, Acinetobacter.
- Fungi: Trametes versicolor, known for its laccases and other oxidative enzymes involved in the degradation of complex aromatic compounds.

These microorganisms, due to their ability to adapt to harsh environmental conditions and their metabolic versatility, represent a key resource for the sustainable treatment of PAH-contaminated soils and water bodies [43].

1.1.2 Biodegradable wastes

Biomass is a biodegradable and renewable organic waste derived from plant and animal materials. Globally, it is recognized as one of the main sources of organic carbon and represents an ideal alternative to petroleum for producing zero-emission fuels [44]. Currently, it contributes approximately 14% of the world's energy supply and is one of the predominant forms of renewable energy, owing to its ability to be converted into a wide range of useful fuels in liquid, gaseous, or solid form [45].
Biomass encompasses a variety of materials, including agricultural and forestry residues, biogenic components of industrial and municipal solid waste (MSW), algal biomass, and energy crops specifically cultivated for fuel production [46]. Biodegradable waste derived from biomass can be classified into two main categories:

- Lignocellulosic biomass, rich in lignocellulose, is the most extensively studied and successfully utilized substrate for producing renewable biofuels. The primary components of lignocellulosic biomass include cellulose, hemicellulose (polysaccharides), lignin, resins, and minerals [47].
- Non-lignocellulosic biomass, such as algal biomass, has shown significant potential for biofuel production through processes like pyrolysis. This category also includes other organic compounds such as simple sugars, lipids, and proteins [48].

1.1.2.1 Fatty acids

Among the non-lignocellulosic wastes derived from marine biomass, long-chain fatty acids (FAs) present in various sources of biodegradable biomass stand out as key substrates for biochemical valorization processes. These organic compounds

are composed of a linear hydrocarbon chain, typically ranging from 12 to 22 carbon atoms, and a terminal carboxyl group (-COOH), as shown in Table 1.2. Their general chemical structure is represented by the formula R–COOH, where R stands for the hydrophobic part of the molecule.

Fatty acids are classified as saturated when they lack double bonds in the alkyl chain, or unsaturated when they contain one or more double bonds [49]. The nature and length of the hydrocarbon chain significantly influence the physicochemical, biological, and application-related properties of these compounds, making them fundamental to numerous biochemical processes and a wide range of industrial applications, including the production of biofuels, surfactants, and biodegradable polymers [50,51].

n°C atoms	Common name	IUPAC	Structure
12:0	Lauric Acid	Dodecanoic Acid	CH_3-$(CH_2)_{10}$-COOH
14:0	Myristic Acid	Tetradecanoic Acid	CH_3-$(CH_2)_{12}$-COOH
16:0	Palmitic Acid	Hexadecanoic Acid	CH_3-$(CH_2)_{14}$-COOH
18:0	Stearic Acid	Octadecanoic Acid	CH_3-$(CH_2)_{16}$-COOH
20:0	Arachidic Acid	Eicosanoic Acid	CH_3-$(CH_2)_{18}$-COOH
22:0	Lignoceric Acid	Tetracosanoic Acid	CH_3-$(CH_2)_{20}$-COOH

Table 1.2: List of long-chain Saturated Fatty Acids, n° C Atoms" refers to the number of carbon atoms and double bonds, which are all zero here (i.e., saturated fatty acids). The structures follow the general formula for saturated fatty acids.

In particular, fatty acids in marine waste can be valorized through enzymatic transformations catalyzed by bacterial cytochrome P-450 enzymes (CYPs) [52,53]. These heme-containing enzymes utilize molecular oxygen (O_2) or hydrogen peroxide (H_2O_2) to convert fatty acids into alcohols, alkanes, and alkenes, which serve as crucial intermediates in the production of second-generation biofuels,i.e., fuels derived from non-food biomass sources.

1.1.2.2 Chitin

Chitin represents a significant example of non-lignocellulosic biodegradable waste and is, after cellulose, the second most abundant polysaccharide on Earth. In nature, it is degraded by microorganisms that employ specific enzymes, including chitinases, chitosanases, chitin deacetylases, and, more recently, lytic polysaccharide monooxygenases (LPMOs) [54–56].

However, due to its low solubility and high resistance to degradation, chitin-containing waste is often disposed of in landfills [57]. Chitin is a structural polysaccharide composed of 2-acetamido-2-deoxy-β-D-glucopyranose residues linked by β-(1→4) glycosidic bonds, and it can occur in three distinct crystalline forms: α, β, and γ [58]. In the α-form, polymer chains are arranged in an antiparallel fashion; in the β-form, they are parallel; and in the γ-form, every third layer is oriented oppositely to the previous two (Figure 1.2).

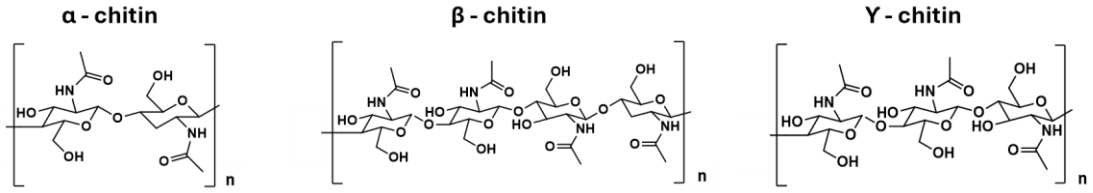

Figure 1.2: Chemical structure of repetitive units of α, β, and Y-chitin, respectively.

Despite its high structural rigidity and resistance to degradation, the activity of chitinases and the commercial value of chitin derivatives enable the industrial recovery of this material, thereby helping to reduce its accumulation in waste. Among the main applications is using chitin as a substrate for biogas and bioethanol production, given its role as a renewable and sustainable energy source [59]. However, the efficiency and sustainability of chitin valorization processes are limited by the need for pretreatment steps. To make crustacean-derived waste suitable for enzymatic degradation, proteins and minerals must be removed, operations that, at the industrial level, typically require using harsh chemicals or high temperatures [60]. In this context, the application of degradative enzymes represents an eco-friendly alternative, capable of producing chitin derivatives with greater homogeneity compared to chemical or mechanical methods [59].

1.2 Degradative microbial enzymes

The biodegradation of complex organic compounds and recalcitrant pollutants relies on the action of microbial degradative enzymes, proteins specialized to catalyze the breakdown of complex molecules into simpler, less toxic metabolites that are more easily assimilated or eliminated from the environment. These enzymes are produced by bacteria, fungi, yeasts, plants, and in some cases, animals [61].

Some enzymes are not only capable of specifically recognizing target substrates, thanks to the three-dimensional complementarity between the active site and the molecule, but may also act on non-native substrates, albeit with lower efficiency or specificity. Such enzymes are referred to as promiscuous enzymes [62]. An example

is represented by certain microbial peroxidases, which exhibit broad substrate specificity and degrade a wide range of persistent xenobiotics [63].

Each biocatalyst operates through distinct mechanisms (oxidative, hydrolytic, cleavage-based), often supported by cofactors such as NAD(P)H, metal ions, or hydrogen peroxide (H_2O_2) [64].

Many emerging xenobiotics, such as synthetic textile dyes and PAHs, contain condensed aromatic rings that are difficult to degrade using conventional physico-chemical methods. The use of specific enzymes, therefore, represents a crucial alternative in biogeochemical cycles, actively contributing to the decomposition of organic matter and the detoxification of xenobiotic compounds [65].

The environmental application of degradative enzymes has significantly increased over the past two decades. Today, one of their most relevant uses is as degradative biocatalysts in bioremediation processes.

Use of degradative enzymes offers numerous advantages in environmental biotechnology, particularly in terms of catalytic efficiency and sustainability. Enzymes are capable of converting both organic and inorganic pollutants into less toxic or inert products [61], acting as catalysts for reactions that would otherwise proceed slowly or inefficiently through conventional chemical catalysis.

1.2.1 Enzyme Classification

The classification of an enzyme is carried out through the assignment of an Enzyme Commission (E.C.) number, by the guidelines established by the International Union of Biochemistry [66]. This system allows for cataloguing all known enzymes into one of six major classes, based on the type of reaction catalyzed (see Table 1.3).

Number	Class	Reaction Catalyzed
1	Oxidoreductases	Transfer of electrons and protons
2	Transferases	Group transfer reactions
3	Hydrolases	Bond cleavage via hydrolysis
4	Lyases	Cleavage of bonds, forming double bonds
5	Isomerases	Transfer of groups within a molecule to form isomers
6	Ligases	bond formation of two molecules

Table 1.3. The International Classification of Enzymes, by the nomenclature established by the International Enzyme Commission. Each class groups together enzymes with specific functions in fundamental biochemical processes.

1.2.2 Enzymatic Classes Involved

The main degradative enzymatic classes correspond to oxidoreductases, hydrolases, and lyases. Among oxidoreductases (EC 1) are laccases, peroxidases, and cytochrome P450-type monooxygenases: these enzymes utilize redox cofactors to insert oxygen into aromatic or aliphatic substrates and to cleave C–C or C–H bonds [67].

Hydrolases (EC 3) include lipases, esterases, nitrilases, and phosphatases, enzymes that break ester, amide, or phosphoric bonds by adding water [68]. These hydrolytic biocatalysts are essential in degrading pesticides, herbicides (e.g., organophosphorus compounds), and polymers, making initially hydrophobic substrates more soluble. Finally, lyases (EC 4) [69] catalyze elimination reactions or the cleavage of functional groups without the use of H_2O, forming double bonds or rings, such as in decarboxylations and dehydrations, which are key steps in the metabolic pathways of complex aromatic compounds. One of the many advantages of these enzymes is their ability to act under mild environmental conditions, reducing the need for physico-chemical interventions and enabling a more sustainable approach [70]. Due to their efficiency and the possibility of large-scale production through biotechnological techniques, these enzymes represent a key resource for sustainable bioremediation strategies and the design of eco-friendly waste treatment technologies.

Numerous studies highlight how oxidoreductive and hydrolytic enzymes are involved in the degradation of various environmental contaminants such as phenolic compounds, PAHs, pesticides, and plastics [71–73].

Among the most representative enzymes produced by natural or engineered microorganisms involved in bioremediation processes and the degradation of different classes of pollutants are cytochrome P450, laccases, hydrolases, dehalogenases, dehydrogenases, proteases, and lipases [74].

1.2.3 Role in Environmental Bioremediation

The application of microbial degradative enzymes is crucial in the bioremediation of contaminated sites, enabling the targeted transformation of persistent substances resistant to conventional treatments [75]. For example, ligninolytic peroxidases and fungal laccases are employed in the decolorization of industrial effluents and the removal of PAHs from soil and water, facilitating the breakdown of aromatic rings into less toxic catabolites [8,43] Similarly, bacterial cytochrome P450 monooxygenases oxidize persistent dioxins and chlorinated solvents, paving the way for complete mineralization [76,77]. Specialized hydrolases such as

phosphotriesterases effectively degrade organophosphorus herbicides and nerve agents (e.g., parathion, VX), neutralizing their toxicity [78]. Overall, biocatalytic systems represent a sustainable approach to remediation: they operate under mild conditions and produce degradation products with low toxicity [61], offering degradation efficiencies comparable to chemical techniques but with reduced environmental impact and higher economic efficiency.

Beyond degradation, enzymes can also be used in other fields such as biosensors to detect the presence and concentration of pollutants or their metabolites, and bioindicators to monitor the ecological status of environmental matrices (soil, water) before and after remediation interventions. However, this work will focus on the ability of these enzymes to degrade specific environmental contaminants [27,43,72]. In conclusion, degradative enzymes represent strategic tools for environmental engineering, both as direct agents in contaminant detoxification and as indicators of remediation processes.

This thesis aims to deepen understanding of the nature, functions, and applications of degradative enzymes, highlighting their role in environmental decontamination and the potential offered by their engineering for the future of environmental biotechnology.

1.3 Hydrolitic enzymes

Hydrolytic enzymes constitute a subclass of hydrolases, belonging to group 3 (E.C. 3) in the enzyme classification system [79]. They catalyze hydrolysis reactions by activating a water molecule, which cleaves bonds within complex macromolecules. Hydrolases can further be classified based on the type of bond they hydrolyze [80].

This subclass includes esterases, lipases, proteases, and glycosidases, which are secreted by native or engineered microorganisms and catalyze the fragmentation of hydrophobic and complex substrates into more soluble and biologically accessible intermediates, thus facilitating subsequent microbial metabolism [81,82]. Within the context of bioremediation, the application of biological systems for the detoxification of environmental contaminants, hydrolytic enzymes such as esterases, lipases, and proteases demonstrate broad potential. They play a central role due to their ability to degrade recalcitrant anthropogenic compounds under mild environmental conditions, including PAHs, organophosphorus pesticides, and synthetic polymers [83,84]. These enzymes also possess extensive biotechnological applications in the industrial sector, further supported by the potential for structural engineering [27].

1.3.1 Esterases

Esterases (EC 3.1.1.x) [85], as previously mentioned, belong to the subclass of hydrolases. They catalyze the cleavage of ester bonds in the presence of water, producing an alcohol and a carboxylic acid. These enzymes are produced by various microbial species, including bacteria, fungi, and actinobacteria [86], and play a crucial role in the degradation of environmental contaminants containing ester groups, such as plasticizers (phthalates), organophosphorus pesticides, synthetic polyesters (e.g.,PET), and numerous surfactant compounds [27,87,88] Environmental esterases exhibit remarkable tolerance to varying pH levels, organic solvents, and heavy metals. Therefore, thanks to their ability to operate under mild environmental conditions and their potential for structural engineering, these enzymes represent promising tools for sustainable and low-impact bioremediation strategies [70].

1.3.1.1 Cutinases

Within the cutinase family, an interesting example is the PETase from Ideonella sakaiensis, which contains the catalytic triad S-H-D and the "lipase box" G-X1-S-X2-G, like other cutinases. Despite these similarities, PETase exhibits significantly higher catalytic efficiency compared to other cutinases. This superiority is attributed to structural modifications that increase the flexibility of the active site, particularly due to the residue Trp156 (W156), whose mobility is favored by the substitution of a histidine with a serine at position 187. This flexibility ("W156 wobbling") allows the active site to adapt to bulky substrates such as PET [89]. For these reasons, PETase represents an ideal candidate for the degradation of plastic materials due to its ability to operate at ambient temperatures. However, the enzyme is highly unstable at moderate to high temperatures, rapidly losing its catalytic activity [90].

To overcome this limitation, PETase, a mesophilic enzyme by nature, has been the subject of protein engineering efforts aimed at improving its thermostability and catalytic activity through single or multiple mutations introduced into its enzymatic structure [27].

1.3.1.2 Engineered PETases

The best-known and developed PETase variants to date are ThermoPETase [91] and DuraPETase [92], which have shown improvements in enzyme stability and activity, as reported in Table 1.4. However, under certain conditions, they still exhibit lower hydrolytic activity compared to the wild-type protein at ambient temperatures. To

overcome these limitations, several efficient variants of PETase and cutinase-like enzymes have been developed in recent years.

Enzymes	Mutations	Optimal T (°C)	Efficency	Thermostability (°C)	Application
PETase	wild-type	30 - 35	Low	37	Limitated
Thermo-PETase	S121E, D186H, R280A	40	Good	46	Limitated
Dura-PETase	T159H, R280A	37-45	High	77	Moderate
FAST-PETase	S121E, R224Q, N233K, D186H, R280A	45 - 50	Very high	30 - 60	Excellent

Table 1.4: Comparative characteristics of different PETase enzyme variants, including specific mutations, optimal activity temperatures, efficiency, thermal stability, and application potential.

In the case of PETase mutants, Son et al. proposed, based on structural information of the wild-type PETase, a rational protein engineering strategy aimed at improving its thermostability and PET degradation activity. Specifically, they developed a variant named ThermoPETase, characterized by three mutations (S121E, D186H, R280A) compared to the wild-type form, which showed an increase in thermal stability of approximately 9 °C and a 14-fold improvement in PET degradation activity at 40 °C [91]. Among the most promising variants is FAST-PETase (Functional, Active, Stable, and Tuned PETase), an engineered version of the natural PETase from *Ideonella sakaiensis*, designed to overcome the limitations of the wild-type enzyme in terms of thermal stability, catalytic efficiency, and adaptability to different types of PET [71].

This variant results from a rational protein engineering approach based on machine learning techniques, particularly using a three-dimensional convolutional neural network (CNN). This approach enabled the identification of stabilizing mutations for PETase, leading to the development of a variant with significantly enhanced hydrolytic activity. Specifically, FAST-PETase contains five mutations relative to the wild-type PETase: N233K, R224Q, S121E, and an aspartic acid mutation predicted algorithmically, in addition to D186H and R280A derived from the original structure. This configuration confers the enzyme a broader operating range (30–60 °C), with an optimal temperature around 50 °C, and superior catalytic activity compared to both the wild-type PETase and other engineered variants (Table 3). Experimental studies have also demonstrated that FAST-PETase can completely degrade a thermally pretreated plastic water bottle at 50 °C, highlighting its significant potential for industrial PET recycling applications [93].

1.3.2 Esterases in Bioremediation

In the context of environmental bioremediation, esterases play a key role due to their ability to catalyze the hydrolysis of ester bonds in various environmental contaminants [94]. Thanks to their distinctive biocatalytic properties, such as high specificity, the ability to function under mild environmental conditions, and structural adaptability, esterases currently hold a prominent position in the industrial enzyme market, finding applications in diverse sectors including wastewater treatment, polymer degradation, and pesticide detoxification [83,95].

A notable example is cutinase, an esterase secreted by the bacterium *Fusarium solani* f. *pisi*, which has demonstrated effectiveness in degrading ester-derived plasticizers such as diethyl phthalate (DEP), significantly reducing their toxicity and promoting biodegradation [96].

Similarly, bacterial strains producing PETase and esterase-like enzymes have shown promising results in the degradation of PET-based microplastics, a polymer still widely used in the production of plastic materials and among the main sources of pollution in marine and terrestrial environments [28]. As previously mentioned, recent studies have shown that engineering these enzymes has improved their thermal stability, affinity for crystalline substrates, and resistance to harsh environmental conditions, thus broadening their applicability for industrial purposes and in situ bioremediation operations [71].

These advances are further reinforced by emerging technologies such as functional metagenomics, heterologous expression, and enzyme immobilization techniques, which allow the recovery and prolonged use of highly efficient esterases [86]. Looking ahead, the integration of protein engineering approaches guided by artificial intelligence, molecular simulations, and molecular docking will enable more precise prediction of functional mutations, optimizing substrate specificity, enzymatic robustness in contaminated environments, and degradation kinetics [27]. These multidisciplinary strategies represent a turning point for the targeted application of esterases in environmental bioremediation, contributing to the development of enzymatic technologies characterized by high efficiency, selectivity, and environmental sustainability.

1.4 Oxidoreductase enzymes

Oxidoreductive enzymes, belonging to group 1 (E.C. 1) of the enzyme classification, constitute a highly heterogeneous group of enzymes capable of acting on a wide range of substrates, catalyzing redox reactions that involve the transfer of electrons from a substrate to an acceptor, often oxygen (O_2), resulting in oxidation and

reduction processes. For this reason, they require complex soluble cofactors involved in their catalytic mechanism [97]. These enzymes include several categories, subdivided based on their mechanism, including:

- **Oxidases**: utilize O_2 as the final electron acceptor, which is reduced to H_2O or H_2O_2, without participating in substrate transformation. An example is laccases, given their industrial relevance and applications [98].
- **Dehydrogenases**: do not use O_2 as an electron acceptor; instead, they transfer two electrons in the form of two hydrogen atoms, generally to cofactors such as NAD^+/NADH, $NADP^+$/NADPH, FAD/$FADH_2$, or FMN/$FMNH_2$. Due to their high specificity and catalytic activity, they find wide application in organic chemistry [99].
- **Peroxidases**: use peroxides, e.g., H_2O_2, as electron acceptors. Many peroxidases are heme proteins containing a heme group essential for catalytic activity. Classical peroxidases do not include cytochromes P450 (CYP450), which belong to the monooxygenase group, although CYP450s can exhibit peroxidase activity under non-physiological conditions [100].
- **Oxygenases**: catalyze oxidation by transferring O_2. They are divided into monooxygenases, which transfer a single atom of O_2 to the substrate, such as the emblematic CYP450, highly versatile heme proteins playing a key role in the biotransformation of xenobiotic compounds and numerous industrial biocatalysis application, and dioxygenases, which incorporate both atoms of O_2 into the substrate, typically involved in compound degradation [101].

Many oxidoreductases, including CYP450 enzymes, display catalytic promiscuity, meaning they can catalyze different reactions or act on different substrates. This feature, combined with their efficiency and selectivity, makes them suitable for numerous biotechnological and environmental applications, such as pollutant degradation and the synthesis of high-value compounds [74].

In recent years, interest in enzymatic catalysis, particularly in heterogeneous systems employing immobilized enzymes, has grown significantly due to the functional and operational advantages offered by such systems, including increased stability, reusability, and process control. Rational design of immobilized derivatives (RDID) is an advanced scientific approach that integrates bioinformatics tools, molecular modeling, and structural analysis to guide the design of optimized biocatalysts. In this context, design is not merely an engineering aspect but a key element of scientific innovation, enabling the overcoming of traditional empirical limitations, reducing development times and costs, and fostering the industrial application of biocatalysts.

1.4.1 Metalloenzymes

Metalloenzymes constitute a broad class of enzymes that utilize metal cations as essential cofactors in their active sites. These metal ions directly participate in catalysis by facilitating a wide range of chemical reactions, including hydrolytic processes, electron transfer, and redox reactions. The metal can function by stabilizing reactive intermediates, activating functional groups, or serving as an electron donor or acceptor, making these metalloenzymes indispensable in numerous biochemical pathways [102].

1.4.2 Oxidative metalloenzymes

In nature, there are oxidative enzymes that are not metalloenzymes; however, most redox enzymes contain metal ions or metallorganic cofactors (e.g., heme groups) that are essential for electron transfer [103]. These enzymes, primarily belonging to the oxidase and peroxidase classes (E.C. 1), catalyze redox reactions in which the central metal ion, such as iron (Fe), copper (Cu), manganese (Mn), cobalt (Co), or zinc (Zn) [104], is involved in electron transfer and O_2 activation. The catalytic function of these metalloenzymes depends on the ability of these metal ions to act as coordination sites for the substrate, facilitating the cleavage of covalent bonds and the oxidation of complex organic compounds.

1.4.3 Multicopper Oxidoreductases

The main example of an oxidative metalloenzyme is laccase (EC 1.10.3.2, oxygen oxidoreductase or multicopper oxidase), which catalyzes the one-electron oxidation of a wide range of substrates, coupled with the reduction of molecular oxygen to water [105]. Laccases are widely distributed among bacteria, fungi, plants, insects, and marine species. The active site of laccases is characterized by the presence of four Cu ions, distributed across three distinct types of copper centers: T1 Cu, T2 Cu, and T3 Cu, as shown in Figure 1.3. Substrate oxidation occurs at the T1 Cu center, which determines the enzyme's redox potential. In particular, the physicochemical properties of the axial amino acid residue at the T1 Cu site have been shown to modulate the redox potential. Electrons are transferred via the histidine-cysteine-histidine (HCH) pathway from the substrate to the T3 and T2 Cu centers, where molecular oxygen is reduced to water [43].

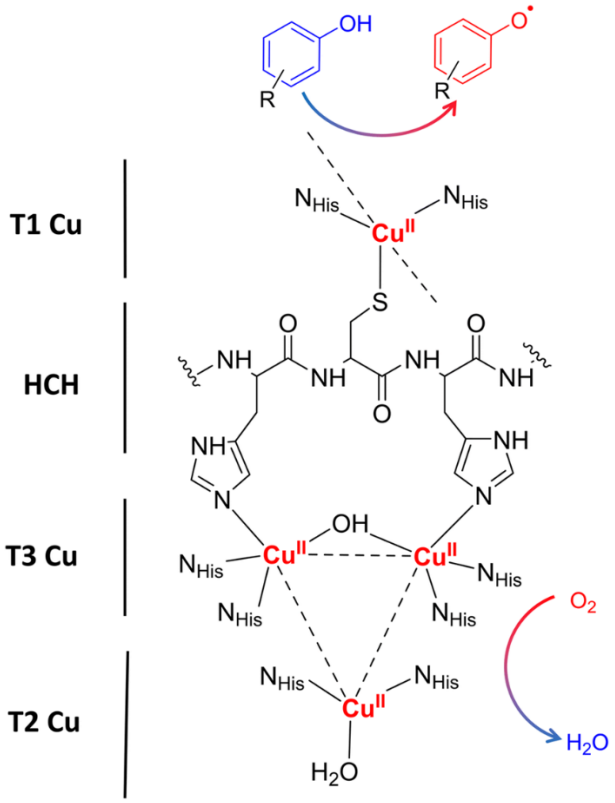

Figure 1.3: schematic representation of the laccase's mechanism

The biological functions of laccases vary depending on their source and are, for instance, highly relevant in lignin metabolism. One of the main challenges in lignocellulosic biomass valorization is the recalcitrance of lignin, and laccases are capable of catalyzing its degradation, leading to the formation of phenolic monomers that can subsequently be used, for example, in the production of biofuels [106]. Laccases are versatile enzymes, known for their catalytic promiscuity and their ability to oxidize a broad spectrum of substrates. Typical laccase substrates include phenolic compounds and lignin derivatives, but these enzymes are also active on a variety of non-phenolic substrates, such as amines, alcohols, dyes, carbohydrates, metal-containing compounds, and certain polymers.

The substrate range of laccases can be significantly expanded through the use of redox mediators, small molecules that act as electron shuttles, enabling laccases to oxidize substrates that are otherwise resistant to direct enzymatic oxidation [8]. While the oxidation mechanism of laccases on phenolic substrates has been extensively studied, the mechanisms involved in the oxidation of non-phenolic substrates remain largely unclear. Among non-phenolic compounds, considerable experimental attention has recently been given to the degradation of PAHs, which are persistent organic pollutants commonly found in terrestrial ecosystems and

derived from the incomplete combustion of organic materials such as oil, coal, and natural gas. Enzymatic biodegradation processes involving laccases hold promise for the remediation of these hazardous molecular systems [43].

Furthermore, recent studies have demonstrated that some laccases are capable of catalyzing the oxidation of plastic polymers such as PE, a material widely used in packaging and containers and known for its resistance to natural degradation [73].

1.4.4 Multicopper Oxidoreductases in Bioremediation

In recent years, there has been a growing interest in the use of laccases in bioremediation, particularly in the degradation of PAHs and plastic polymers, due to their ability to degrade and transform these complex materials into less harmful environmental by-products.

Laccases have shown great potential in the biodegradation of PAHs, which are toxic and persistent environmental pollutants. These enzymes, found in fungi such as Trametes versicolor, Pleurotus ostreatus, and Coriolopsis gallica [107], as well as in bacteria, catalyze the oxidation of PAHs into more metabolically accessible forms [108]. While fungal laccases have been extensively studied for PAH degradation, bacterial laccases are gaining attention due to advantages such as higher thermostability and broader pH tolerance, making them particularly suitable for various contaminated environments [109,110]. Thus, laccases are promising candidates for the bioremediation of soils, water, and air polluted by PAHs, offering an eco-friendly and efficient approach to reducing environmental contamination.

Laccases involved in PE oxidation have been identified in fungi, bacteria, and, more recently, in crustaceans, and the oxidative degradation products are consistently reported as organic acids and polymer fragments bearing hydroxyl and carbonyl groups [111]. This suggests that these laccases may share a common mechanism for PE oxidation.

A crucial aspect of laccase-based bioremediation lies in the role of redox mediators small molecules that facilitate electron transfer and enhance the oxidative capacity of the enzyme [112]. In some laccases, mediators are essential for initiating PE oxidation, whereas in other cases, they merely enhance the reaction or have no effect at all. The application of laccases for PE degradation represents a significant step toward sustainable biotechnological solutions capable of addressing the growing issue of plastic accumulation in ecosystems. A deeper understanding of enzyme–polymer binding modes and the influence of redox potential is crucial to fully exploit laccase catalytic capabilities and improve bioremediation outcomes [113].

1.4.5 Monoxygenases

Monooxygenases are enzymes classified under EC 1.13 and EC 1.14, known for their ability to catalyze the insertion of a single atom of molecular oxygen (O_2) into an organic substrate, while the second oxygen atom is reduced to water. This reaction, which is fundamental to numerous biochemical processes, requires the activation of molecular oxygen, which can only occur through electron transfer. Monooxygenases can be divided into two main categories: internal monooxygenases, which derive electrons directly from the substrate, and external monooxygenases, which rely on external electron donors such as NAD(P)H [114].

Among the most extensively studied are the cytochrome P450 enzymes, which are heme-dependent and found across virtually all domains of life. These enzymes are involved in essential functions such as drug metabolism, hormone biosynthesis, and the detoxification of harmful substances [115]. Due to their role in biotransformation and the selective synthesis of complex molecules, cytochrome P450 monooxygenases are of great scientific and industrial interest.

1.4.5.1 CYP450

One of the most represented classes of oxidative metalloenzymes among monooxygenases is the cytochrome P450 family (CYP450), which catalyzes the incorporation of a single oxygen atom from O_2 into the substrate, while the other atom is reduced to water [115]. Among these, CYP450s are among the most extensively studied examples of heme-dependent monooxygenases. Ubiquitous across all domains of life, they utilize a heme cofactor containing iron at the active site to catalyze the oxidation of a wide variety of substrates, including xenobiotic compounds and endogenous molecules. Their role is fundamental in processes such as detoxification, steroid biosynthesis, and the degradation of environmental pollutants. In CYP enzymes, molecular oxygen is activated through binding to the reduced heme iron (Fe^{2+}), forming a reactive intermediate capable of oxidizing C–H bonds, even in chemically inert substrates [116]. In particular, a subclass of CYP450 enzymes belonging to the CYP152 family represents a distinctive group of microbial monooxygenases capable of catalyzing the oxidative decarboxylation of medium- to long-chain fatty acids via a peroxygenase mechanism. These enzymes oxidize substrates using H_2O_2 as a direct oxidant, generating a highly reactive oxidizing intermediate, Compound I (Fe (IV)=O), which abstracts the β-hydrogen (Cβ–H) and promotes the subsequent release of CO_2, yielding terminal α-alkenes, as shown in Figure 1.4. In CYP152 enzymes, this alternative pathway, known as the peroxide shunt, bypasses the need for reductive cofactors such as NAD(P)H and provides the reactive oxidizing species directly [117,118].

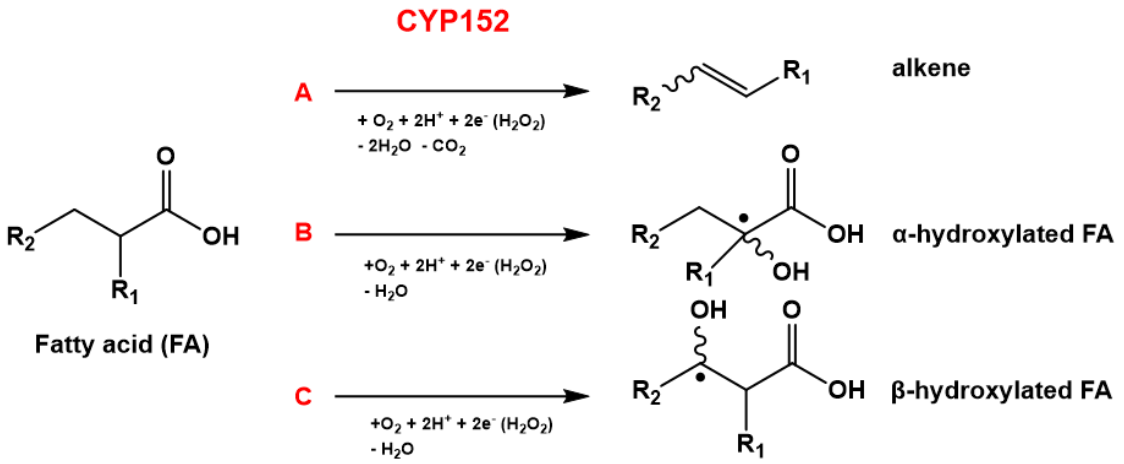

Figure 1.4. Reaction mechanisms mediated by CYP152 family enzymes on a generic fatty acid: A. Decarboxylation forming a terminal alkene (typical activity of OleTJ). B. Hydroxylation at the α position, resulting in an α-hydroxylated fatty acid. C. Hydroxylation at the β, generally not mediated by CYP152 enzymes.

A representative example of this class is OleTJE, a CYP152 enzyme isolated from Jeotgalicoccus sp., known as the first identified α-alkene synthase. OleTJE efficiently catalyzes the decarboxylation of C12–C20 fatty acids even in the absence of redox partners, relying solely on H_2O_2 as the oxidant. In the presence of cofactors such as O_2, it can also act as a monooxygenase, displaying catalytic promiscuity through the concurrent formation of hydroxylated fatty acids (α- or β-hydroxyacids) [119]. Structurally, OleTJE exhibits notable homology with other hydroxylating CYP152 enzymes, such as P450SPα and P450BSβ, suggesting that specific mutations in the catalytic site may modulate selectivity between hydroxylation and decarboxylation.

In summary, CYP152 enzymes represent promising enzymatic platforms for the valorization of lipid-based biomass, offering direct access to bio-based olefins from fatty acids, with significant implications for the sustainable production of fuels and chemical intermediates. [120].

1.4.5.2 Lytic Polysaccharide Monoxygenases

Another example is represented by Lytic Polysaccharide Monoxygenases (LPMOs), a recently discovered class of oxidative enzymes [121]. They catalyze oxidative hydroxylation reactions that promote the cleavage of polysaccharide chains and are found across all domains of life, including bacteria, viruses, yeasts, and fungi. The sequence diversity of LPMO families continues to expand, with eight distinct Auxiliary Activity (AA) families currently identified in the CAZy database. These enzymes are classified based on sequence similarity: the AA9 family acts primarily

on cellulose and hemicellulose, while the AA10 and AA15 families are active on chitin and cellulose [122]. (see Table 5).

AA families	Substrate
AA9	Cellulose and Hemicellulose
AA10	Cellulose and Chitin
AA11	Chitin
AA13	Starch
AA14	Hemicellulose
AA15	Cellulose
AA17	Pectin

Table 1.5. "Auxiliary Activities'' (AA) families in the CAZy database, the LPMOs are classified according to their sequence similarity. Each AA family preferentially processes specific polysaccharides.

Unlike traditional hydrolases, LPMOs act not only on individual polysaccharide chains but also on crystalline polysaccharides, initiating depolymerization synergistically with hydrolases such as cellulases and chitinases [123]. These enzymes contain a mononuclear copper center coordinated through a structure known as the "histidine brace," which serves as the active site for catalysis [124]. Their catalytic cycle involves the reduction of Cu (II) to Cu(I), increasing substrate affinity. Catalysis requires O_2 as a co-substrate; however, recent studies suggest that the true preferred co-substrate is often H_2O_2 rather than molecular oxygen, thereby broadening the application scope of LPMOs in industrial bioconversion and bioremediation processes where controlled use of peroxides enhances catalytic efficiency [125]. These examples demonstrate the high catalytic and functional versatility of monooxygenases, which find crucial applications in environmental, biotechnological, and industrial fields. Their ability to act on hydrophobic and poorly reactive substrates makes them enzymes of great interest for advanced bioremediation strategies and biomass valorization, fundamental for the sustainable production of biofuels.

1.4.6 Monoxygenases in Biomass Valorization

Oxidative metalloenzymes play a fundamental role in the valorization of biomass and organic waste through the decomposition of recalcitrant compounds such as lignin, chitin, and other high-energy biomolecules. In particular, the use of these enzymes in the transformation of chitinous or cellulosic biomass is crucial for optimizing fermentation processes, as they facilitate the release of fermentable sugars from complex substrates, thereby enhancing the efficiency of second-generation biofuel production [126,127].

The CYP152 family represents an extremely versatile class of metalloenzymes whose catalytic potential is especially relevant in the valorization of lipid biomass, particularly long-chain fatty acids (≥ C12), which are converted into high-value products such as ω-hydroxy acids and terminal alkenes [128]. These compounds serve as strategic precursors in the synthesis of biolubricants, bioplastics, surfactants, and advanced biofuels.

Through site-directed mutagenesis, the ω-hydroxylase activity of CYP152 enzymes can be significantly increased by targeting residues proximal to the heme group or along the substrate access channel. Concurrently, the production of linear alkenes can be promoted via fatty acid decarboxylation, enabled by functional mutations in specific CYP isoenzymes such as OleT-type P450s [129], which efficiently catalyze oxidative decarboxylation. These modifications influence the formation of the oxoferryl radical, directing reactivity toward the decarboxylation pathway rather than the conventional hydroxylation pathway.

The combination of rational engineering directed evolution, and optimization of redox conditions allows the development of tailor-made biocatalysts for industrial applications, making CYP152 enzymes promising candidates for use in integrated lipid biorefineries. In this regard, advanced computational studies, including QM/MM simulations [130], have identified strategic mutations in key active site regions that modulate catalytic selectivity and steer reactivity towards ω-hydroxylation or decarboxylation, optimizing the production of fatty alcohols or terminal alkenes. The integration of in silico prediction and evolutionary engineering represents a consolidated strategy for designing more efficient and selective biocatalysts in lipid biomass valorization processes [131].

Similarly, LPMOs represent key enzymes in the valorization of recalcitrant polysaccharide biomass such as chitin, due to their ability to catalyze oxidative reactions that promote the depolymerization of crystalline substrates. LPMOs from the AA10 family [132,133], in particular, exhibit high affinity for chitin, catalyzing its oxidative cleavage into bioactive chitooligosaccharides with promising applications in biomedical, nutraceutical, and agro-industrial sectors. The activity of these enzymes depends on the presence of the “histidine brace,” a structural feature responsible for the reactivity of the copper catalytic center and selectivity towards specific glycosidic bonds. Structural and computational studies are elucidating the molecular determinants of enzyme-substrate interaction, providing a basis for protein engineering efforts aimed at enhancing the catalytic performance of AA10 LPMOs in industrial contexts of chitin valorization [134].

In conclusion, monooxygenases represent central components for the sustainable valorization of biomass and bioremediation, thanks to their ability to catalyze

selective oxidative reactions on complex substrates under mild environmental conditions, with potential applications in organic waste management and the detoxification of environmental contaminants [135,136].

1.5 Outline of Thesis

This thesis is structured into five chapters: the first two provide the necessary background and theoretical framework, while the remaining chapters present and discuss the research outcomes.

Chapter 1 introduces the environmental context in which this study is situated, providing an overview of the main classes of environmental pollutants and discussing the relevance of enzymatic systems in addressing pollution and waste transformation. This chapter also presents the biological targets studied in the thesis, offering the necessary biochemical background.

Chapter 2 presents the theoretical foundations of the computational techniques employed, including molecular docking, classical molecular dynamics, and quantum mechanical calculations based on density functional theory (DFT). These methods constitute the multiscale computational approach that was applied throughout the thesis to investigate and model enzymatic catalysis at different spatial and temporal resolutions.

Chapter 3 outlines the main results obtained, summarizing the five scientific works conducted during the PhD. The chapter is divided into two thematic sections, organized according to the nature of the substrates involved: (i) synthetic, non-biodegradable polymers, and (ii) biodegradable biomass. The goal of this chapter is to provide a concise overview of the research questions addressed, the methodologies adopted, and the principal findings of each work.

ENZYME	EC NUMBER	REACTION TYPE	COFACTORS	MAIN SUBSTRATE	APPLICATIONS
Cutinase (PETase and engineered)	3.1.1.101	Ester hydrolysis	None	PET	Plastic degradation for **bioremediation**
Multicopper oxidoreductase (Laccase)	1.10.3.2	Oxidation polymer oxidation	Cu^{2+}	Phenolic and non-phenolic substrates (PAHs, recalcitrant polymers)	**Bioremediation** of aromatic contaminants and polymers
CYP450 (SPα, OleTJE and engineered)	1.14.x.x	Monooxygenase	Heme, $2e^-$	Fatty acids, aromatic compounds	Biotransformation and **biomass valorization**
LPMO (SmAA10)	1.14.99.53	Polysaccharide oxidation	Cu^{2+}	Chitin, cellulose	Polysaccharide degradation and **biomass valorization**

Table 1.6: Summary of the enzymatic systems discussed in this thesis. The table provides a unified overview of the main characteristics of the enzymes considered, including EC classification, cofactors, substrates, and potential applications, serving as a reference point for the subsequent chapters.

Chapters 4, 5, and 6 form **Section I** of the thesis, which focuses on the computational investigation of enzymes involved in the degradation of non-biodegradable synthetic polymers.

Chapter 4 presents the first work of the thesis, a molecular dynamics investigation of FAST-PETase, a recently engineered enzyme with high PET-depolymerizing efficiency. The simulations at different temperatures provided atomistic insights into substrate recognition and revealed a structural pre-organization of the active site that favors PET binding and activation.

Chapter 5 reports the second work, a DFT investigation of the fungal laccase *Trametes versicolor*, aimed at elucidating the oxidation mechanism of non-phenolic substrates, particularly PAHs. The study provides fundamental insights into the enzymatic degradation of persistent aromatic pollutants.

Chapter 6 focuses on the third work, examining laccases capable of oxidizing PE and comparing their redox properties and interactions with LDPE. Computational modeling identified key structural determinants governing enzyme–polymer binding, offering valuable guidance for the rational design of biocatalysts for plastic degradation.

Chapters 7 and 8 form **Section II** of the thesis, which focuses on the computational investigation of metalloenzymes relevant to the valorization of biodegradable waste.

Chapter 7 presents the fourth work, dedicated to the rational design of cytochrome P450SPα mutants for enhanced lipid waste conversion. Molecular dynamics simulations of three CYP152SPα variants, in both apo and substrate-bound forms, revealed the mutations that improve catalytic efficiency and structural stability, supporting the development of biohybrid systems for sustainable biocatalysis.

Chapter 8 describes the fifth work, focused on a bacterial LPMO involved in chitin degradation. Molecular dynamics simulations of the SmAA10–β-chitin complex highlighted key interactions and conformational stability, providing atomistic insights useful for the rational engineering of metalloenzymes for biomass valorization.

Overall, this thesis demonstrates how computational approaches can complement and, in some cases, replace labor-intensive experimental work, providing structural and dynamic insights that inform the rational design of enzymes. By integrating these methods across all studies, the work contributes to sustainable chemistry and highlights the potential of computational modeling to drive biotechnological innovation for environmental applications.

References

1. Ghosh, D.; Ghorai, P.; Sarkar, S.; Maiti, K.S.; Hansda, S.R.; Das, P. Microbial Assemblage for Solid Waste Bioremediation and Valorization with an Essence of Bioengineering. Environmental Science and Pollution Research 2023, 30, 16797–16816, doi:10.1007/s11356-022-24849-x.
2. Rogers, J.N.; Stokes, B.; Dunn, J.; Cai, H.; Wu, M.; Haq, Z.; Baumes, H. An Assessment of the Potential Products and Economic and Environmental Impacts Resulting from a Billion Ton Bioeconomy. Biofuels, Bioproducts and Biorefining 2017, 11, 110–128, doi:10.1002/bbb.1728.
3. Shakerian, F.; Zhao, J.; Li, S.-P. Recent Development in the Application of Immobilized Oxidative Enzymes for Bioremediation of Hazardous Micropollutants – A Review. Chemosphere 2020, 239, 124716, doi:10.1016/j.chemosphere.2019.124716.
4. Abu-Thabit, N.Y.; Pérez-Rivero, C.; Uwaezuoke, O.J.; Ngwuluka, N.C. From Waste to Wealth: Upcycling of Plastic and Lignocellulosic Wastes to <scp>PHAs</Scp>. Journal of Chemical Technology & Biotechnology 2022, 97, 3217–3240, doi:10.1002/jctb.6966.
5. Manisha; Yadav, S.K. Technological Advances and Applications of Hydrolytic Enzymes for Valorization of Lignocellulosic Biomass. Bioresour Technol 2017, 245, 1727–1739, doi:10.1016/j.biortech.2017.05.066.
6. Lopes, C.; Antelo, L.T.; Franco-Uría, A.; Alonso, A.A.; Pérez-Martín, R. Chitin Production from Crustacean Biomass: Sustainability Assessment of Chemical and Enzymatic Processes. J Clean Prod 2018, 172, 4140–4151, doi:10.1016/j.jclepro.2017.01.082.
7. Zhao, H.; Su, H.; Sun, J.; Dong, H.; Mao, X. Bioconversion of α-Chitin by a Lytic Polysaccharide Monooxygenase Os LPMO10A Coupled with Chitinases and the Synergistic Mechanism Analysis. J Agric Food Chem 2024, 72, 7256–7265, doi:10.1021/acs.jafc.3c08688.
8. Rovaletti, A.; De Gioia, L.; Fantucci, P.; Greco, C.; Vertemara, J.; Zampella, G.; Arrigoni, F.; Bertini, L. Recent Theoretical Insights into the Oxidative Degradation of Biopolymers and Plastics by Metalloenzymes. Int J Mol Sci 2023, 24, 6368, doi:10.3390/ijms24076368.
9. E Torres; M Ayala 6.24 Biocatalysis by Metalloenzymes; 2023.
10. Badar, M.S.; Shamsi, S.; Ahmed, J.; Alam, Md.A. Molecular Dynamics Simulations: Concept, Methods, and Applications. In; 2022; pp. 131–151.
11. Di Nola, A.; Roccatano, D.; Berendsen, H.J.C. Molecular Dynamics Simulation of the Docking of Substrates to Proteins. Proteins: Structure, Function, and Bioinformatics 1994, 19, 174–182, doi:10.1002/prot.340190303.
12. Fonseca Guerra, C.; Snijders, J.G.; te Velde, G.; Baerends, E.J. Towards an Order- N DFT Method. Theoretical Chemistry Accounts: Theory, Computation, and Modeling (Theoretica Chimica Acta) 1998, 99, 391–403, doi:10.1007/s002140050353.

13. Moghimi Dehkordi, M.; Pournuroz Nodeh, Z.; Soleimani Dehkordi, K.; salmanvandi, H.; Rasouli Khorjestan, R.; Ghaffarzadeh, M. Soil, Air, and Water Pollution from Mining and Industrial Activities: Sources of Pollution, Environmental Impacts, and Prevention and Control Methods. Results in Engineering 2024, 23, 102729, doi:10.1016/j.rineng.2024.102729.

14. Hajam, Y.A.; Kumar, R.; Kumar, A. Environmental Waste Management Strategies and Vermi Transformation for Sustainable Development. Environmental Challenges 2023, 13, 100747, doi:10.1016/j.envc.2023.100747.

15. Ghai, H.; Sakhuja, D.; Yadav, S.; Solanki, P.; Putatunda, C.; Bhatia, R.K.; Bhatt, A.K.; Varjani, S.; Yang, Y.-H.; Bhatia, S.K.; et al. An Overview on Co-Pyrolysis of Biodegradable and Non-Biodegradable Wastes. Energies (Basel) 2022, 15, 4168, doi:10.3390/en15114168.

16. Dwivedi, P.; Mishra, P.K.; Mondal, M.K.; Srivastava, N. Non-Biodegradable Polymeric Waste Pyrolysis for Energy Recovery. Heliyon 2019, 5, e02198, doi:10.1016/j.heliyon.2019.e02198.

17. Luo, Y.; Guo, W.; Ngo, H.H.; Nghiem, L.D.; Hai, F.I.; Zhang, J.; Liang, S.; Wang, X.C. A Review on the Occurrence of Micropollutants in the Aquatic Environment and Their Fate and Removal during Wastewater Treatment. Science of The Total Environment 2014, 473–474, 619–641, doi:10.1016/j.scitotenv.2013.12.065.

18. Farmer, P.B.; Singh, R.; Kaur, B.; Sram, R.J.; Binkova, B.; Kalina, I.; Popov, T.A.; Garte, S.; Taioli, E.; Gabelova, A.; et al. Molecular Epidemiology Studies of Carcinogenic Environmental Pollutants. Mutation Research/Reviews in Mutation Research 2003, 544, 397–402, doi:10.1016/j.mrrev.2003.09.002.

19. Morten Ryberg; Alexis Laurent; Michael Zwicky Hauschild Mapping of Global Plastic Value Chain and Plastic Losses to the Environment: With a Particular Focus on Marine Environment; United Nations Environment Programme., 2018;

20. Ragusa, A.; Matta, M.; Cristiano, L.; Matassa, R.; Battaglione, E.; Svelato, A.; De Luca, C.; D'Avino, S.; Gulotta, A.; Rongioletti, M.C.A.; et al. Deeply in Plasticenta: Presence of Microplastics in the Intracellular Compartment of Human Placentas. Int J Environ Res Public Health 2022, 19, 11593, doi:10.3390/ijerph191811593.

21. Akdogan, Z.; Guven, B. Microplastics in the Environment: A Critical Review of Current Understanding and Identification of Future Research Needs. Environmental Pollution 2019, 254, 113011, doi:10.1016/j.envpol.2019.113011.

22. Yee, M.S.-L.; Hii, L.-W.; Looi, C.K.; Lim, W.-M.; Wong, S.-F.; Kok, Y.-Y.; Tan, B.-K.; Wong, C.-Y.; Leong, C.-O. Impact of Microplastics and Nanoplastics on Human Health. Nanomaterials 2021, 11, 496, doi:10.3390/nano11020496.

23. Ramachandraiah, K.; Ameer, K.; Jiang, G.; Hong, G.-P. Micro- and Nanoplastic Contamination in Livestock Production: Entry Pathways, Potential Effects and Analytical Challenges. Science of The Total Environment 2022, 844, 157234, doi:10.1016/j.scitotenv.2022.157234.

24. Li, C.-T.; Zhuang, H.-K.; Hsieh, L.-T.; Lee, W.-J.; Tsao, M.-C. PAH Emission from the Incineration of Three Plastic Wastes. Environ Int 2001, 27, 61–67, doi:10.1016/S0160-4120(01)00056-3.

25. Law, K.L.; Starr, N.; Siegler, T.R.; Jambeck, J.R.; Mallos, N.J.; Leonard, G.H. The United States' Contribution of Plastic Waste to Land and Ocean. Sci Adv 2020, 6, doi:10.1126/sciadv.abd0288.

26. Kawai, F.; Kawabata, T.; Oda, M. Current Knowledge on Enzymatic PET Degradation and Its Possible Application to Waste Stream Management and Other Fields. Appl Microbiol Biotechnol 2019, 103, 4253–4268, doi:10.1007/s00253-019-09717-y.

27. Orlando, C.; Prejanò, M.; Russo, N.; Marino, T. On the Role of Temperature in the Depolymerization of PET by FAST-PETase: An Atomistic Point of View on Possible Active Site Pre-Organization and Substrate-Destabilization Effects. ChemBioChem 2023, 24, doi:10.1002/cbic.202300412.

28. Wang, C.; Liu, Y.; Chen, W.; Zhu, B.; Qu, S.; Xu, M. Critical Review of Global Plastics Stock and Flow Data. J Ind Ecol 2021, 25, 1300–1317, doi:10.1111/jiec.13125.

29. Ronca, S. Polyethylene. In Brydson's Plastics Materials; Elsevier, 2017; pp. 247–278.

30. Hakkarainen, M.; Albertsson, A.-C. Environmental Degradation of Polyethylene. In; 2004; pp. 177–200.

31. Koutny, M.; Lemaire, J.; Delort, A.-M. Biodegradation of Polyethylene Films with Prooxidant Additives. Chemosphere 2006, 64, 1243–1252, doi:10.1016/j.chemosphere.2005.12.060.

32. Restrepo-Flórez, J.-M.; Bassi, A.; Thompson, M.R. Microbial Degradation and Deterioration of Polyethylene – A Review. Int Biodeterior Biodegradation 2014, 88, 83–90, doi:10.1016/j.ibiod.2013.12.014.

33. Ghatge, S.; Yang, Y.; Ahn, J.-H.; Hur, H.-G. Biodegradation of Polyethylene: A Brief Review. Appl Biol Chem 2020, 63, 27, doi:10.1186/s13765-020-00511-3.

34. Boström, C.-E.; Gerde, P.; Hanberg, A.; Jernström, B.; Johansson, C.; Kyrklund, T.; Rannug, A.; Törnqvist, M.; Victorin, K.; Westerholm, R. Cancer Risk Assessment, Indicators, and Guidelines for Polycyclic Aromatic Hydrocarbons in the Ambient Air. Environ Health Perspect 2002, 110, 451–488, doi:10.1289/ehp.110-1241197.

35. Zhang, Y.; Tao, S. Global Atmospheric Emission Inventory of Polycyclic Aromatic Hydrocarbons (PAHs) for 2004. Atmos Environ 2009, 43, 812–819, doi:10.1016/j.atmosenv.2008.10.050.

36. Arey, J.; Atkinson, R. Photochemical Reactions of PAHs in the Atmosphere. In PAHs: An Ecotoxicological Perspective; Wiley, 2003; pp. 47–63.

37. Di Toro, D.M.; McGrath, J.A.; Hansen, D.J. Technical Basis for Narcotic Chemicals and Polycyclic Aromatic Hydrocarbon Criteria. I. Water and Tissue. Environ Toxicol Chem 2000, 19, 1951–1970, doi:10.1002/etc.5620190803.

38. Kanaly, R.A.; Harayama, S. Biodegradation of High-Molecular-Weight Polycyclic Aromatic Hydrocarbons by Bacteria. J Bacteriol 2000, 182, 2059–2067, doi:10.1128/JB.182.8.2059-2067.2000.

39. Zelinkova, Z.; Wenzl, T. The Occurrence of 16 EPA PAHs in Food – A Review. Polycycl Aromat Compd 2015, 35, 248–284, doi:10.1080/10406638.2014.918550.

40. Armstrong, B.; Hutchinson, E.; Unwin, J.; Fletcher, T. Lung Cancer Risk after Exposure to Polycyclic Aromatic Hydrocarbons: A Review and Meta-Analysis. Environ Health Perspect 2004, 112, 970–978, doi:10.1289/ehp.6895.

41. Dhanya, M.S.; Kalia, A. Bioremediation: An Eco-Friendly Cleanup Strategy for Polyaromatic Hydrocarbons from Petroleum Industry Waste. In Bioremediation of Industrial Waste for Environmental Safety; Springer Singapore: Singapore, 2020; pp. 399–436.

42. Juhasz, A.L.; Naidu, R. Bioremediation of High Molecular Weight Polycyclic Aromatic Hydrocarbons: A Review of the Microbial Degradation of Benzo[a]Pyrene. Int Biodeterior Biodegradation 2000, 45, 57–88, doi:10.1016/S0964-8305(00)00052-4.

43. Orlando, C.; Rizzo, I.C.; Arrigoni, F.; Zampolli, J.; Mangiagalli, M.; Di Gennaro, P.; Lotti, M.; De Gioia, L.; Marino, T.; Greco, C.; et al. Mechanism of Non-Phenolic Substrate Oxidation by the Fungal Laccase Type 1 Copper Site from Trametes Versicolor : The Case of Benzo[a]Pyrene and Anthracene. Dalton Transactions 2024, 53, 12152–12161, doi:10.1039/D4DT01377H.

44. Isikgor, F.H.; Becer, C.R. Lignocellulosic Biomass: A Sustainable Platform for the Production of Bio-Based Chemicals and Polymers. Polym Chem 2015, 6, 4497–4559, doi:10.1039/C5PY00263J.

45. Bridgwater, A.V.; Meier, D.; Radlein, D. An Overview of Fast Pyrolysis of Biomass. Org Geochem 1999, 30, 1479–1493, doi:10.1016/S0146-6380(99)00120-5.

46. Vassilev, S. V.; Baxter, D.; Andersen, L.K.; Vassileva, C.G. An Overview of the Chemical Composition of Biomass. Fuel 2010, 89, 913–933, doi:10.1016/j.fuel.2009.10.022.

47. Bhatia, S.K.; Joo, H.-S.; Yang, Y.-H. Biowaste-to-Bioenergy Using Biological Methods – A Mini-Review. Energy Convers Manag 2018, 177, 640–660, doi:10.1016/j.enconman.2018.09.090.

48. Li, D.-C.; Jiang, H. The Thermochemical Conversion of Non-Lignocellulosic Biomass to Form Biochar: A Review on Characterizations and Mechanism Elucidation. Bioresour Technol 2017, 246, 57–68, doi:10.1016/j.biortech.2017.07.029.

49. Ackman, R.G. Marine Biogenic Lipids, Fats and Oils. In Marine biogenic lipids, fats and oils; CRC press, 1989; Vol. II.

50. Janßen, H.; Steinbüchel, A. Fatty Acid Synthesis in Escherichia Coli and Its Applications towards the Production of Fatty Acid Based Biofuels. Biotechnol Biofuels 2014, 7, 7, doi:10.1186/1754-6834-7-7.

51. Langer, O.; Palme, O.; Wray, V.; Tokuda, H.; Lang, S. Production and Modification of Bioactive Biosurfactants. Process Biochemistry 2006, 41, 2138–2145, doi:10.1016/j.procbio.2006.07.036.

52. Liu, Y.; Wang, C.; Yan, J.; Zhang, W.; Guan, W.; Lu, X.; Li, S. Hydrogen Peroxide-Independent Production of α-Alkenes by OleTJE P450 Fatty Acid Decarboxylase. Biotechnol Biofuels 2014, 7, 28, doi:10.1186/1754-6834-7-28.

53. Munro, A.W.; McLean, K.J.; Grant, J.L.; Makris, T.M. Structure and Function of the Cytochrome P450 Peroxygenase Enzymes. Biochem Soc Trans 2018, 46, 183–196, doi:10.1042/BST20170218.

54. Maschmeyer, T.; Luque, R.; Selva, M. Upgrading of Marine (Fish and Crustaceans) Biowaste for High Added-Value Molecules and Bio(Nano)-Materials. Chem Soc Rev 2020, 49, 4527–4563, doi:10.1039/C9CS00653B.

55. Kaczmarek, M.B.; Struszczyk-Swita, K.; Li, X.; Szczęsna-Antczak, M.; Daroch, M. Enzymatic Modifications of Chitin, Chitosan, and Chitooligosaccharides. Front Bioeng Biotechnol 2019, 7, doi:10.3389/fbioe.2019.00243.

56. Hemsworth, G.R.; Johnston, E.M.; Davies, G.J.; Walton, P.H. Lytic Polysaccharide Monooxygenases in Biomass Conversion. Trends Biotechnol 2015, 33, 747–761, doi:10.1016/j.tibtech.2015.09.006.

57. Poria, V.; Rana, A.; Kumari, A.; Grewal, J.; Pranaw, K.; Singh, S. Current Perspectives on Chitinolytic Enzymes and Their Agro-Industrial Applications. Biology (Basel) 2021, 10, 1319, doi:10.3390/biology10121319.

58. Jang, M.; Kong, B.; Jeong, Y.; Lee, C.H.; Nah, J. Physicochemical Characterization of A-chitin, B-chitin, and Γ-chitin Separated from Natural Resources. J Polym Sci A Polym Chem 2004, 42, 3423–3432, doi:10.1002/pola.20176.

59. Ali, G.; Sharma, M.; Salama, E.-S.; Ling, Z.; Li, X. Applications of Chitin and Chitosan as Natural Biopolymer: Potential Sources, Pretreatments, and Degradation Pathways. Biomass Convers Biorefin 2024, 14, 4567–4581, doi:10.1007/s13399-022-02684-x.

60. Deng, J.-J.; Mao, H.-H.; Fang, W.; Li, Z.-Q.; Shi, D.; Li, Z.-W.; Zhou, T.; Luo, X.-C. Enzymatic Conversion and Recovery of Protein, Chitin, and Astaxanthin from Shrimp Shell Waste. J Clean Prod 2020, 271, 122655, doi:10.1016/j.jclepro.2020.122655.

61. Tahri, N.; Bahafid, W.; Sayel, H.; El Ghachtouli, N. Biodegradation: Involved Microorganisms and Genetically Engineered Microorganisms. In Biodegradation - Life of Science; InTech, 2013.

62. Hult, K.; Berglund, P. Enzyme Promiscuity: Mechanism and Applications. Trends Biotechnol 2007, 25, 231–238, doi:10.1016/j.tibtech.2007.03.002.

63. Hollenberg, P.F. Mechanisms of Cytochrome P450 and Peroxidase-catalyzed Xenobiotic Metabolism. The FASEB Journal 1992, 6, 686–694, doi:10.1096/fasebj.6.2.1537457.

64. Hrycay, E.G.; Bandiera, S.M. Monooxygenase, Peroxidase and Peroxygenase Properties and Reaction Mechanisms of Cytochrome P450 Enzymes. In; 2015; pp. 1–61.

65. Miglani, R.; Parveen, N.; Kumar, A.; Ansari, Mohd.A.; Khanna, S.; Rawat, G.; Panda, A.K.; Bisht, S.S.; Upadhyay, J.; Ansari, M.N. Degradation of Xenobiotic Pollutants: An Environmentally Sustainable Approach. Metabolites 2022, 12, 818, doi:10.3390/metabo12090818.

66. Thompson, R.H.S. Classification and Nomenclature of Enzymes. Science (1979) 1962, 137, 405–408, doi:10.1126/science.137.3528.405.

67. Guengerich, F.P.; Yoshimoto, F.K. Formation and Cleavage of C–C Bonds by Enzymatic Oxidation–Reduction Reactions. Chem Rev 2018, 118, 6573–6655, doi:10.1021/acs.chemrev.8b00031.

68. Shukla, E.; D. Bendre, A.; M. Gaikwad, S. Hydrolases: The Most Diverse Class of Enzymes. In; 2022.

69. Linhardt, R.J.; Galliher, P.M.; Cooney, C.L. Polysaccharide Lyases. Appl Biochem Biotechnol 1987, 12, 135–176, doi:10.1007/BF02798420.

70. Yoshida, S.; Hiraga, K.; Taniguchi, I.; Oda, K. Ideonella Sakaiensis, PETase, and MHETase: From Identification of Microbial PET Degradation to Enzyme Characterization. In; 2021; pp. 187–205.

71. Lu, H.; Diaz, D.J.; Czarnecki, N.J.; Zhu, C.; Kim, W.; Shroff, R.; Acosta, D.J.; Alexander, B.R.; Cole, H.O.; Zhang, Y.; et al. Machine Learning-Aided Engineering of Hydrolases for PET Depolymerization. Nature 2022, 604, 662–667, doi:10.1038/s41586-022-04599-z.

72. Wu, Y.; Teng, Y.; Li, Z.; Liao, X.; Luo, Y. Potential Role of Polycyclic Aromatic Hydrocarbons (PAHs) Oxidation by Fungal Laccase in the Remediation of an Aged Contaminated Soil. Soil Biol Biochem 2008, 40, 789–796, doi:10.1016/j.soilbio.2007.10.013.

73. Orlando, C.; Bellei, M.; Zampolli, J.; Mangiagalli, M.; Di Gennaro, P.; Lotti, M.; De Gioia, L.; Marino, T.; Di Rocco, G.; Greco, C.; et al. Comparative Analysis of Polyethylene-Degrading Laccases: Redox Properties and Enzyme-Polyethylene Interaction Mechanism. ChemSusChem 2025, 18, doi:10.1002/cssc.202402253.

74. Bhandari, S.; Poudel, D.K.; Marahatha, R.; Dawadi, S.; Khadayat, K.; Phuyal, S.; Shrestha, S.; Gaire, S.; Basnet, K.; Khadka, U.; et al. Microbial Enzymes Used in Bioremediation. J Chem 2021, 2021, 1–17, doi:10.1155/2021/8849512.

75. Crini, G.; Lichtfouse, E.; Wilson, L.D.; Morin-Crini, N. Conventional and Non-Conventional Adsorbents for Wastewater Treatment. Environ Chem Lett 2019, 17, 195–213, doi:10.1007/s10311-018-0786-8.

76. Sakaki, T.; Yamamoto, K.; Ikushiro, S. Possibility of Application of Cytochrome P450 to Bioremediation of Dioxins. Biotechnol Appl Biochem 2013, 60, 65–70, doi:10.1002/bab.1067.

77. Emanuela Testai; Valentina De Curtis; Simonetta Gemma; Laura Fabrizi; PierGiovanni Gervasi; Luciano Vittozzi The Role of Different Cytochrome P450 Isoforms in in Vitro Chloroform Metabolism. J Biochem Toxicol 1996.

78. Caldwell, S.R.; Raushel, F.M. Detoxification of Organophosphate Pesticides Using an Immobilized Phosphotriesterase from Pseudomonas Diminuta. Biotechnol Bioeng 1991, 37, 103–109, doi:10.1002/bit.260370203.

79. Milligan, B.; Holt, L.A. The Complete Enzymic Hydrolysis of Crosslinked Proteins. In; 1977; pp. 277–284.

80. Nagano, N.; Noguchi, T.; Akiyama, Y. Systematic Comparison of Catalytic Mechanisms of Hydrolysis and Transfer Reactions Classified in the EzCatDB Database. Proteins: Structure, Function, and Bioinformatics 2007, 66, 147–159, doi:10.1002/prot.21193.

81. Henrissat, B.; Davies, G. Structural and Sequence-Based Classification of Glycoside Hydrolases. Curr Opin Struct Biol 1997, 7, 637–644, doi:10.1016/S0959-440X(97)80072-3.

82. Hasan, F.; Shah, A.A.; Hameed, A. Industrial Applications of Microbial Lipases. Enzyme Microb Technol 2006, 39, 235–251, doi:10.1016/j.enzmictec.2005.10.016.

83. Bhatt, P.; Zhou, X.; Huang, Y.; Zhang, W.; Chen, S. Characterization of the Role of Esterases in the Biodegradation of Organophosphate, Carbamate, and Pyrethroid Pesticides. J Hazard Mater 2021, 411, 125026, doi:10.1016/j.jhazmat.2020.125026.

84. Heker, I.; Samak, N.A.; Kong, Y.; Meckenstock, R.U. Anaerobic Degradation of Polycyclic Aromatic Hydrocarbons. Appl Environ Microbiol 2025, 91, doi:10.1128/aem.02268-24.

85. Romano, D.; Bonomi, F.; de Mattos, M.C.; de Sousa Fonseca, T.; de Oliveira, M. da C.F.; Molinari, F. Esterases as Stereoselective Biocatalysts. Biotechnol Adv 2015, 33, 547–565, doi:10.1016/j.biotechadv.2015.01.006.

86. Rafeeq, H.; Hussain, A.; Shabbir, S.; Ali, S.; Bilal, M.; Sher, F.; Iqbal, H.M.N. Esterases as Emerging Biocatalysts: Mechanistic Insights, Genomic and Metagenomic, Immobilization, and Biotechnological Applications. Biotechnol Appl Biochem 2022, 69, 2176–2194, doi:10.1002/bab.2277.

87. Barzkar, N.; Sohail, M.; Tamadoni Jahromi, S.; Gozari, M.; Poormozaffar, S.; Nahavandi, R.; Hafezieh, M. Marine Bacterial Esterases: Emerging Biocatalysts for Industrial Applications. Appl Biochem Biotechnol 2021, 193, 1187–1214, doi:10.1007/s12010-020-03483-8.

88. Bhattacharyya, M.; Basu, S.; Dhar, R.; Dutta, T.K. Phthalate Hydrolase: Distribution, Diversity and Molecular Evolution. Environ Microbiol Rep 2022, 14, 333–346, doi:10.1111/1758-2229.13028.

89. Ding, K.; Levitskaya, Z.; Sana, B.; Pasula, R.R.; Kannan, S.; Adam, A.; Sundaravadanam, V.V.; Verma, C.; Lim, S.; Ghadessy, J.F. Modulation of PETase Active Site Flexibility and Activity on Morphologically Distinct Polyethylene Terephthalate Substrates by Surface Charge Engineering. Biochem Eng J 2024, 209, 109420, doi:10.1016/j.bej.2024.109420.

90. Thomsen, T.B.; Hunt, C.J.; Meyer, A.S. Influence of Substrate Crystallinity and Glass Transition Temperature on Enzymatic Degradation of Polyethylene Terephthalate (PET). N Biotechnol 2022, 69, 28–35, doi:10.1016/j.nbt.2022.02.006.

91. Son, H.F.; Cho, I.J.; Joo, S.; Seo, H.; Sagong, H.-Y.; Choi, S.Y.; Lee, S.Y.; Kim, K.-J. Rational Protein Engineering of Thermo-Stable PETase from Ideonella Sakaiensis for Highly Efficient PET Degradation. ACS Catal 2019, 9, 3519–3526, doi:10.1021/acscatal.9b00568.

92. Cui, Y.; Chen, Y.; Liu, X.; Dong, S.; Tian, Y.; Qiao, Y.; Mitra, R.; Han, J.; Li, C.; Han, X.; et al. Computational Redesign of a PETase for Plastic Biodegradation under Ambient Condition by the GRAPE Strategy. ACS Catal 2021, 11, 1340–1350, doi:10.1021/acscatal.0c05126.

93. Yoshida, S.; Hiraga, K.; Takehana, T.; Taniguchi, I.; Yamaji, H.; Maeda, Y.; Toyohara, K.; Miyamoto, K.; Kimura, Y.; Oda, K. A Bacterium That Degrades and Assimilates Poly(Ethylene Terephthalate). Science (1979) 2016, 351, 1196–1199, doi:10.1126/science.aad6359.

94. Sharma, A.; Sharma, T.; Sharma, T.; Sharma, S.; Kanwar, S.S. Role of Microbial Hydrolases in Bioremediation. In; 2019; pp. 149–164.

95. Zhong, X.-L.; Tian, Y.-Z.; Jia, M.-L.; Liu, Y.-D.; Cheng, D.; Li, G. Characterization and Purification via Nucleic Acid Aptamers of a Novel Esterase from the Metagenome of Paper Mill Wastewater Sediments. Int J Biol Macromol 2020, 153, 441–450, doi:10.1016/j.ijbiomac.2020.02.319.

96. Kim, Y.-H.; Seo, H.-S.; Min, J.; Kim, Y.-C.; Ban, Y.-H.; Han, K.Y.; Park, J.-S.; Bae, K.-D.; Gu, M.B.; Lee, J. Enhanced Degradation and Toxicity Reduction of Dihexyl Phthalate by Fusarium Oxysporum f. Sp. Pisi Cutinase. J Appl Microbiol 2007, 102, 221–228, doi:10.1111/j.1365-2672.2006.03095.x.

97. Gamborg, O.L.; Wetter, L.R.; Neish, A.C. The Oxidation of Some Aromatic α-Hydroxy Acids by Glycollate: O2 Oxidoreductase. Phytochemistry 1962, 1, 159–168, doi:10.1016/S0031-9422(00)82818-6.

98. Upadhyay, P.; Shrivastava, R.; Agrawal, P.K. Bioprospecting and Biotechnological Applications of Fungal Laccase. 3 Biotech 2016, 6, 15, doi:10.1007/s13205-015-0316-3.

99. Sellés Vidal, L.; Kelly, C.L.; Mordaka, P.M.; Heap, J.T. Review of NAD(P)H-Dependent Oxidoreductases: Properties, Engineering and Application. Biochimica et Biophysica Acta (BBA) - Proteins and Proteomics 2018, 1866, 327–347, doi:10.1016/j.bbapap.2017.11.005.

100. Welinder, K.G.; Mauro, J.M.; Nørskov-Lauritsen, L. Structure of Plant and Fungal Peroxidases. Biochem Soc Trans 1992, 20, 337–340, doi:10.1042/bst0200337.

101. Torres Pazmiño, D.E.; Winkler, M.; Glieder, A.; Fraaije, M.W. Monooxygenases as Biocatalysts: Classification, Mechanistic Aspects and Biotechnological Applications. J Biotechnol 2010, 146, 9–24, doi:10.1016/j.jbiotec.2010.01.021.

102. Davis, I.; Geng, J.; Liu, A. Metalloenzymes Involved in Carotenoid Biosynthesis in Plants. In; 2022; pp. 207–222.

103. Siegbahn, P.E.M. Mechanisms of Metalloenzymes Studied by Quantum Chemical Methods. Q Rev Biophys 2003, 36, 91–145, doi:10.1017/S0033583502003827.

104. Valdez, C.E.; Smith, Q.A.; Nechay, M.R.; Alexandrova, A.N. Mysteries of Metals in Metalloenzymes. Acc Chem Res 2014, 47, 3110–3117, doi:10.1021/ar500227u.

105. Jones, S.M.; Solomon, E.I. Electron Transfer and Reaction Mechanism of Laccases. Cellular and Molecular Life Sciences 2015, 72, 869–883, doi:10.1007/s00018-014-1826-6.

106. Kudanga, T.; Le Roes-Hill, M. Laccase Applications in Biofuels Production: Current Status and Future Prospects. Appl Microbiol Biotechnol 2014, 98, 6525–6542, doi:10.1007/s00253-014-5810-8.

107. Kadri, T.; Rouissi, T.; Kaur Brar, S.; Cledon, M.; Sarma, S.; Verma, M. Biodegradation of Polycyclic Aromatic Hydrocarbons (PAHs) by Fungal Enzymes: A Review. Journal of Environmental Sciences 2017, 51, 52–74, doi:10.1016/j.jes.2016.08.023.

108. Premnath, N.; Mohanrasu, K.; Guru Raj Rao, R.; Dinesh, G.H.; Prakash, G.S.; Ananthi, V.; Ponnuchamy, K.; Muthusamy, G.; Arun, A. A Crucial Review on Polycyclic Aromatic Hydrocarbons - Environmental Occurrence and Strategies for Microbial Degradation. Chemosphere 2021, 280, 130608, doi:10.1016/j.chemosphere.2021.130608.

109. Wang, L.; Tan, Y.; Sun, S.; Zhou, L.; Wu, G.; Shao, Y.; Wang, M.; Xin, Z. Improving Degradation of Polycyclic Aromatic Hydrocarbons by Bacillus Atrophaeus Laccase Fused with Vitreoscilla Hemoglobin and a Novel Strong Promoter Replacement. Biology (Basel) 2022, 11, 1129, doi:10.3390/biology11081129.

110. Humel, S.; Führer, B.; Svetitsch, M.; Mayer, P.; Loibner, A.P. Targeting Sorbed PAHs in Historically Contaminated Soil – Can Laccase Mediator Systems or Fenton's Reagent Remove Inaccessible PAHs? J Hazard Mater 2023, 443, 130286, doi:10.1016/j.jhazmat.2022.130286.

111. Shi, L.; Chan, S.; Li, C.; Zhang, S. Identification and Characterization of a Laccase from Litopenaeus Vannamei Involved in Anti-Bacterial Host Defense. Fish Shellfish Immunol 2017, 66, 1–10, doi:10.1016/j.fsi.2017.04.026.

112. Johannes, C.; Majcherczyk, A. Natural Mediators in the Oxidation of Polycyclic Aromatic Hydrocarbons by Laccase Mediator Systems. Appl Environ Microbiol 2000, 66, 524–528, doi:10.1128/AEM.66.2.524-528.2000.

113. Zampolli, J.; Mangiagalli, M.; Vezzini, D.; Lasagni, M.; Ami, D.; Natalello, A.; Arrigoni, F.; Bertini, L.; Lotti, M.; Di Gennaro, P. Oxidative Degradation of Polyethylene by Two Novel Laccase-like Multicopper Oxidases from Rhodococcus Opacus R7. Environ Technol Innov 2023, 32, 103273, doi:10.1016/j.eti.2023.103273.

114. de Gonzalo, G.; Mihovilovic, M.D.; Fraaije, M.W. Recent Developments in the Application of Baeyer–Villiger Monooxygenases as Biocatalysts. ChemBioChem 2010, 11, 2208–2231, doi:10.1002/cbic.201000395.

115. Nelson, D.R.; Koymans, Luc.; Kamataki, T.; Stegeman, J.J.; Feyereisen, R.; Waxman, D.J.; Waterman, M.R.; Gotoh, O.; Coon, M.J.; Estabrook, R.W.; et al. P450 Superfamily: Update on New Sequences, Gene Mapping, Accession Numbers and Nomenclature. . Pharmacogenetics 1996, 6, 1–42.

116. Gilardi, G.; Di Nardo, G. Heme Iron Centers in Cytochrome P450: Structure and Catalytic Activity. Rendiconti Lincei 2017, 28, 159–167, doi:10.1007/s12210-016-0565-z.

117. Ciaramella, A.; Catucci, G.; Di Nardo, G.; Sadeghi, S.J.; Gilardi, G. Peroxide-Driven Catalysis of the Heme Domain of A. Radioresistens Cytochrome P450 116B5 for Sustainable Aromatic Rings Oxidation and Drug Metabolites Production. N Biotechnol 2020, 54, 71–79, doi:10.1016/j.nbt.2019.08.005.

118. Denisov, I.G.; Makris, T.M.; Sligar, S.G.; Schlichting, I. Structure and Chemistry of Cytochrome P450. Chem Rev 2005, 105, 2253–2278, doi:10.1021/cr0307143.

119. Wang, Y.; Chen, S. Reaction Mechanisms of Fe-Dependent Fatty Acid Decarboxylases. ChemCatChem 2024, 16, doi:10.1002/cctc.202301501.

120. Rude, M.A.; Baron, T.S.; Brubaker, S.; Alibhai, M.; Del Cardayre, S.B.; Schirmer, A. Terminal Olefin (1-Alkene) Biosynthesis by a Novel P450 Fatty Acid Decarboxylase from Jeotgalicoccus Species. Appl Environ Microbiol 2011, 77, 1718–1727, doi:10.1128/AEM.02580-10.

121. Vaaje-Kolstad, G.; Westereng, B.; Horn, S.J.; Liu, Z.; Zhai, H.; Sørlie, M.; Eijsink, V.G.H. An Oxidative Enzyme Boosting the Enzymatic Conversion of Recalcitrant Polysaccharides. Science (1979) 2010, 330, 219–222, doi:10.1126/science.1192231.

122. Busk, P.K.; Lange, L. Classification of Fungal and Bacterial Lytic Polysaccharide Monooxygenases. BMC Genomics 2015, 16, 368, doi:10.1186/s12864-015-1601-6.

123. Forsberg, Z.; Sørlie, M.; Petrović, D.; Courtade, G.; Aachmann, F.L.; Vaaje-Kolstad, G.; Bissaro, B.; Røhr, Å.K.; Eijsink, V.G. Polysaccharide Degradation by Lytic Polysaccharide Monooxygenases. Curr Opin Struct Biol 2019, 59, 54–64, doi:10.1016/j.sbi.2019.02.015.

124. Liu, Y.; Harnden, K.A.; Van Stappen, C.; Dikanov, S.A.; Lu, Y. A Designed Copper Histidine-Brace Enzyme for Oxidative Depolymerization of Polysaccharides as a Model of Lytic Polysaccharide Monooxygenase. Proceedings of the National Academy of Sciences 2023, 120, doi:10.1073/pnas.2308286120.

125. Sista Kameshwar, A.K.; Qin, W. Systematic Review of Publicly Available Non-Dikarya Fungal Proteomes for Understanding Their Plant Biomass-Degrading and Bioremediation Potentials. Bioresour Bioprocess 2019, 6, 30, doi:10.1186/s40643-019-0264-6.

126. Fairley, P. Introduction: Next Generation Biofuels. Nature 2011, 474, S2–S5, doi:10.1038/474S02a.

127. Horn, S.J.; Vaaje-Kolstad, G.; Westereng, B.; Eijsink, V. Novel Enzymes for the Degradation of Cellulose. Biotechnol Biofuels 2012, 5, 45, doi:10.1186/1754-6834-5-45.

128. Grant, J.L.; Hsieh, C.H.; Makris, T.M. Decarboxylation of Fatty Acids to Terminal Alkenes by Cytochrome P450 Compound I. J Am Chem Soc 2015, 137, 4940–4943, doi:10.1021/jacs.5b01965.

129. Matthews, S.; Belcher, J.D.; Tee, K.L.; Girvan, H.M.; McLean, K.J.; Rigby, S.E.J.; Levy, C.W.; Leys, D.; Parker, D.A.; Blankley, R.T.; et al. Catalytic Determinants of Alkene Production by the Cytochrome P450 Peroxygenase OleTJE. Journal of Biological Chemistry 2017, 292, 5128–5143, doi:10.1074/jbc.M116.762336.

130. Pickl, M.; Kurakin, S.; Cantú Reinhard, F.G.; Schmid, P.; Pöcheim, A.; Winkler, C.K.; Kroutil, W.; de Visser, S.P.; Faber, K. Mechanistic Studies of Fatty Acid Activation by CYP152 Peroxygenases Reveal Unexpected Desaturase Activity. ACS Catal 2019, 9, 565–577, doi:10.1021/acscatal.8b03733.

131. Okolie, J.A.; Epelle, E.I.; Tabat, M.E.; Orivri, U.; Amenaghawon, A.N.; Okoye, P.U.; Gunes, B. Waste Biomass Valorization for the Production of Biofuels and Value-Added Products: A Comprehensive Review of Thermochemical, Biological and Integrated Processes. Process Safety and Environmental Protection 2022, 159, 323–344, doi:10.1016/j.psep.2021.12.049.

132. Arnold, N.D.; Brück, W.M.; Garbe, D.; Brück, T.B. Enzymatic Modification of Native Chitin and Conversion to Specialty Chemical Products. Mar Drugs 2020, 18, 93, doi:10.3390/md18020093.

133. Filiatrault-Chastel, C.; Navarro, D.; Haon, M.; Grisel, S.; Herpoël-Gimbert, I.; Chevret, D.; Fanuel, M.; Henrissat, B.; Heiss-Blanquet, S.; Margeot, A.; et al. AA16, a New Lytic Polysaccharide Monooxygenase Family Identified in Fungal Secretomes. Biotechnol Biofuels 2019, 12, 55, doi:10.1186/s13068-019-1394-y.

134. Guo, X.; An, Y.; Liu, F.; Lu, F.; Wang, B. Lytic Polysaccharide Monooxygenase – A New Driving Force for Lignocellulosic Biomass Degradation. Bioresour Technol 2022, 362, 127803, doi:10.1016/j.biortech.2022.127803.

135. Deng, D.; Jiang, Z.; Kang, L.; Liao, L.; Zhang, X.; Qiao, Y.; Zhou, Y.; Yang, L.; Wang, B.; Li, A. An Efficient Catalytic Route in Haem Peroxygenases Mediated by O2/Small-Molecule Reductant Pairs for Sustainable Applications. Nat Catal 2025, 8, 20–32, doi:10.1038/s41929-024-01281-7.

136. Cárdenas-Moreno, Y.; González-Bacerio, J.; García Arellano, H.; del Monte-Martínez, A. Oxidoreductase Enzymes: Characteristics, Applications, and Challenges as a Biocatalyst. Biotechnol Appl Biochem 2023, 70, 2108–2135, doi:10.1002/bab.2513.

Chapter 2
Theoretical Background

Computational techniques play a crucial role in studying a wide range of biochemical phenomena, including biomolecular dynamics, molecular recognition, enzymatic reactions, conformational transitions, and the kinetics of biological processes. In particular, numerous mechanisms that regulate life in living organisms are governed by the phenomenon of molecular recognition (MR), that is, by processes in which molecules of different nature (typically substrates) bind, through non-covalent interactions, to specific regions of target macromolecules (binding sites), such as proteins, resulting in stable complexes [1]. A deep understanding of the molecular mechanisms underlying these interactions is fundamental for the rational design of new pharmacological agents as well as for developing biocatalysts capable of selectively acting on substrates of environmental interest [2].

At the same time, from a bioinformatics perspective, attention is focused on developing tools and methodologies for organizing, retrieving, and analyzing large-scale biological data. In this context, computational biochemistry has established itself as a powerful and well-founded approach for the structural and functional analysis of biological systems at the atomic scale. However, the computational modelling of biological macromolecules poses significant challenges due to the intrinsic complexity of the systems involved, such as proteins, enzymes, and metalloenzymes [3].

The two main areas of computational chemistry employed in the study of substrate-protein interactions are Molecular Mechanics (MM) [4] and electronic structure theory [5]. Thermodynamic analysis plays a central role in identifying the most favorable binding between substrate and receptor through geometric optimization (search for the minimum energy configuration) and estimating the energy associated with different molecular conformations.

In cases where the binding process involves significant reorganization of the electronic density, such as in the formation or breaking of chemical bonds, or the

modulation of the redox state of metal centers, a more accurate description of the system's electronic structure becomes necessary, requiring the use of quantum mechanical methods [6].

These methods are based on the laws of quantum mechanics, in particular on the Schrödinger equation:

$$\widehat{H}\Psi(r;R) = E\Psi(r;R) \tag{2.1}$$

where $\widehat{H}$ is the molecular Hamiltonian operator and $\Psi(r;R)$ is the Born–Oppenheimer electronic wave function.

They are mainly divided into two categories:

- Ab initio approaches, based solely on fundamental physical laws and universal constants (such as the mass and charge of particles);
- Semi-empirical approaches introduce parameters derived from experimental data to reduce computational cost.

The choice of method involves a trade-off between accuracy and computational feasibility. For this reason, in recent years, multiscale strategies have emerged that integrate classical (MM) and quantum (QM) approaches, such as hybrid QM/MM models [7] (see Figure 2.1). These are particularly useful for studying complex biological reactions, protein-substrate interactions, electron transfers, and catalytic processes involving the breaking or formation of chemical bonds. Among classical computational methods, molecular dynamics (MD) [8] represents a fundamental tool for analysing the dynamic behaviour of enzymes, allowing the investigation of their interactions with the surrounding environment and substrates. MD simulations, conducted in the presence of explicit solvent, make it possible to explore the conformational landscape of the system and to reach thermodynamic equilibrium.

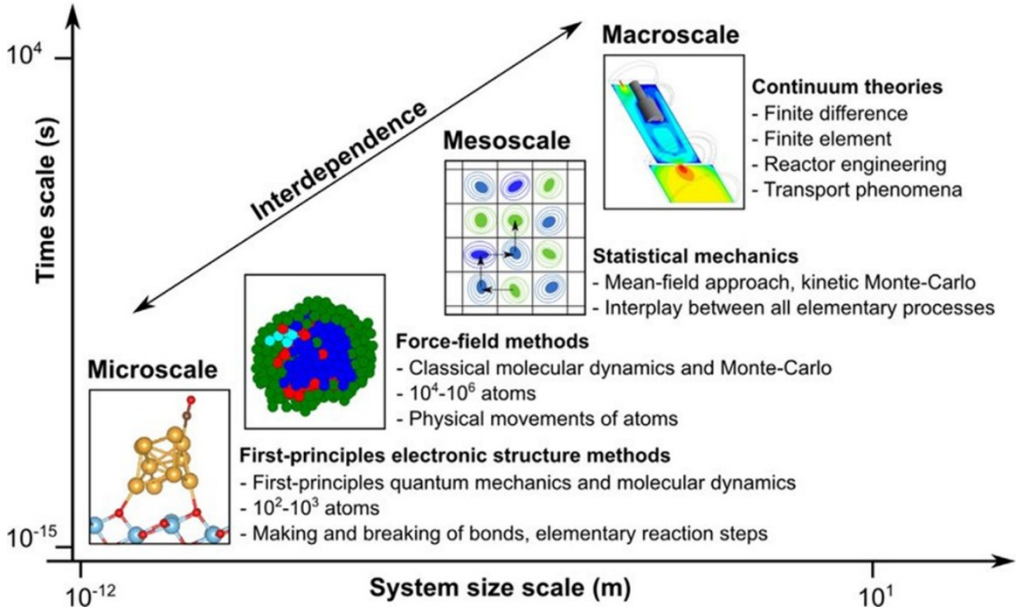

Figure 2.1: Schematic representation of the main multiscale modeling approaches as a function of spatial and temporal scale. The microscale includes ab initio electronic structure methods, based on quantum mechanics, which allow the description of phenomena such as the formation and breaking of chemical bonds. At the mesoscale, methods based on force fields (e.g., classical molecular dynamics and Monte Carlo) and statistical mechanics approaches describe the interaction between elementary processes. Finally, at the macroscale, continuum theories (such as finite element and finite difference methods) are applied to model phenomena on an engineering scale, such as mass and energy transport.

Complementing these simulations, molecular docking [9] is a multi-step computational approach used to predict and evaluate the mode of interaction between two molecules, typically in the absence of experimental structures of the protein-ligand complex. Although more approximate than MD simulations, docking provides a preliminary level of analysis useful for selecting potentially active ligands or exploring enzymatic specificity toward unconventional substrates.

Finally, this chapter will present the main computational methods adopted for studying protein-substrate interactions and catalytic mechanisms: classical molecular dynamics simulations, molecular docking, and quantum mechanics-based methodologies, with particular emphasis on Density Functional Theory (DFT) [10] These tools, used individually or in combination, serve as fundamental resources for interpreting and predicting molecular behaviour in the biochemical field, with applications ranging from enzyme design to environmental bioremediation.

2.1 Classic Computational Methods

In recent years, biomolecular simulations have seen rapid advancement, particularly in the study of interactions between enzymes and large substrates, both of biological and non-biological origin. These techniques have proven essential for identifying binding sites and for detailed analysis of the molecular mechanisms underlying enzymatic catalytic activity. In general, classical computational methods used in computational chemistry and biology are based on classical physics, treating atoms and molecules as point-like entities subject to deterministic forces, without explicitly accounting for the quantum effects associated with electron behaviour.

MM [4] is a static approach that relies on force fields to optimize molecular geometries and calculate the potential energies of the system, without considering temporal evolution. It is widely used for energy minimization operations and preliminary structural studies on large systems. MD builds upon MM principles but applies them over time. It is a widely used computational method that allows for simulating the temporal evolution of a molecular system by calculating atomic trajectories based on Newtonian classical mechanics, under the influence of potentials defined by force fields [11] MD simulations enable exploration of conformational behaviour, structural flexibility, and intermolecular interactions in a realistic environment, often explicitly including solvent. This makes it possible to investigate phenomena across different spatial and temporal scales, enabling the study of large, complex systems. Molecular Docking is a computational method based on molecular mechanics principles. It is used to predict how a potential substrate (or ligand) interacts with a target protein, estimating orientation, position, and binding affinities within the active site [12]. Docking is particularly useful in the absence of crystallographic structures, offering a preliminary analysis of molecular compatibility. Monte Carlo (MC) simulations are a statistical method that explores the conformational space of the system through random sampling [13,14] They are useful for calculating thermodynamic properties and for studying the equilibrium of complex systems, often serving as a complement to dynamic simulations. The main advantage of classical methods lies in their computational efficiency and scalability to large systems, making them particularly suitable for long and large-scale simulations [15]. However, these methods do not explicitly describe the electronic structure and, therefore, are not suitable for simulating phenomena involving the formation or breaking of chemical bonds or charge transfer. In realistic simulations of complex systems, it is essential to explicitly represent the surrounding environment, particularly the solvent, often through the inclusion of

thousands of water molecules. This significantly increases the size of the simulated system, making a fully quantum mechanical treatment computationally prohibitive.

2.1.1 Force Fields (FF)

Within the framework of Molecular Mechanics, the interactions between atoms in a system are described using an empirical potential function known as a force field [16]. This function represents the system's potential energy as the sum of terms that model both covalent interactions (bonded terms) and non-covalent interactions (non-bonded terms).

The total potential energy (E_{TOT}) can be expressed as follows:

$$E_{TOT} = E_{bonded} + E_{non-bonded} \quad (2.2)$$

Where:

$$E_{bonded} = E_{bond} + E_{angle} + E_{dihedral} \quad (2.3)$$

$$E_{non-bonded} = E_{electrostatic} + E_{Van\ der\ Walls} \quad (2.4)$$

The bonded terms include:

— **Stretching**: variation in bond length relative to the equilibrium distance,
— **Bending**: deviation of the bond angle from the equilibrium angle,
— **Torsion**: rotation around bonds, described by periodic potentials.

The non-bonded terms include:

— **Electrostatic interactions**: modeled using Coulomb's law,
— **Van der Waals forces**: typically described by the Lennard-Jones potential [17].

In the Molecular Mechanics model, molecules are represented as assemblies of atoms approximated as rigid spheres connected by elastic "springs," according to the harmonic oscillator approximation.

A simplified expression of a first-generation force field (used, for example, in early models such as AMBER or CHARMM) is as follows:

$$E_{TOT} = \sum_{bonds} \frac{1}{2} K_b (r - r_0)^2 + \sum_{angles} \frac{1}{2} K_\theta (\theta - \theta_0)^2 + \frac{1}{2} \sum_{torsions} \frac{V_n}{2} [1 + \cos(n\varphi - \delta)] + \sum_{i<j} 4\varepsilon_{ij} \left[\left(\frac{\sigma_{ij}}{r_{ij}} \right)^{12} - \left(\frac{\sigma_{ij}}{r_{ij}} \right)^{6} \right] + \sum_{i<j} \frac{q_i q_j}{r_{ij}} \quad (2.5)$$

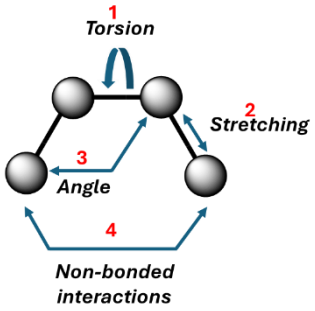

Figure 2.2: (1) Dihedral angles, (2) bond distances, (3) bond angles, and (4) electrostatic and van der Waals interactions contribute to the calculation of the total potential energy. In the equation, the first four terms represent intramolecular (local) contributions related to bond stretching, angle bending, and dihedral or improper torsions. The last two terms describe non-bonded interactions: repulsive and van der Waals forces (modeled using the 12-6 Lennard-Jones potential) and Coulomb interactions between charged particles.

Where:

- K_b: bond force constant
- r, r_0: actual bond length and equilibrium bond length
- K_θ: angle force constant
- θ, θ_0: actual bond angle and equilibrium bond angle
- V_n, n, δ, φ: torsional parameters (amplitude, periodicity, phase)
- $\varepsilon_{ij}, \sigma_{ij}$: Lennard–Jones parameters (well depth and collision diameter)
- q_i, q_j: partial atomic charges
- r_{ij}: interatomic distance between particles i and j

The parameters of a force field can be derived from experimental data, quantum mechanical calculations, or a combination of both. An effective force field must strike a balance between computational simplicity and predictive accuracy. However, these models present certain inherent limitations, including high computational cost, the need for parameterization of non-standard residues, and the use of implicit approximations in the description of molecular interactions. To date, no universal force field exists that can accurately describe every type of molecule. Numerous force fields have been developed, each with varying levels of complexity and optimized for specific classes of molecular systems. Among the most commonly used are:

— AMBER (Assisted Model Building with Energy Refinement), particularly suited for proteins and nucleic acids [18],

— CHARMM (Chemistry at HARvard Macromolecular Mechanics), used for both small molecules and macromolecules [19],
— GROMOS, specifically developed for molecular dynamics simulations of biomolecular systems, not to be confused with the GROMACS software package [20],
— OPLS-AA, optimized for a broad range of organic compounds [21],
— GAFF (General AMBER Force Field), commonly used for parameterizing small ligands [22],
— GLYCAM-06, designed to describe both natural and modified sugars and glycans [23].

It is essential to emphasize that the predictive accuracy of a computational model critically depends on the quality of the force field employed, or the combination of multiple force fields, as well as on the correctness of its parameterization relative to the specific system under investigation.

2.1.2 Molecular Dynamics simulations

MD simulations are widely used to identify potential binding sites on target proteins, taking into account the structural flexibility of protein–substrate complexes [24]. They also allow the estimation of binding free energies and the investigation of catalytic mechanisms at the molecular level. However, these simulations have certain limitations, particularly regarding the accessible timescales and the size of systems that can be studied.

As mentioned earlier, there are different types of MD simulations: all-atom (AA) [25], United Atom (UA) [26], and coarse-grained (CG) [27], each with varying degrees of detail and computational cost. For example, all-atom simulations enable the exploration of dynamics on microsecond to millisecond timescales in complex systems, such as metalloenzymes binding large substrates.

To address diverse biological problems, it is necessary to select the type of simulation best suited to the specific context. The complexity of biological systems and the dynamic nature of targets pose significant challenges for computational modeling. No single simulation approach can capture all these aspects simultaneously.

In the specific context of this work, classical molecular dynamics represents the most appropriate choice. This is because we often work with large substrates, frequently synthetic, making the application of quantum methods difficult. Classical molecular dynamics is a technique that describes the time evolution of a chemical system at the atomic level by solving Newton’s equations of motion.

Within this framework, the temporal behavior of a system composed of *N* interacting particles each of mass m_i is described by the following equations:

$$F_i = -\nabla_{ri} V(r_1, \dots, r_i, \dots, r_N) = m_i \frac{\partial^2 r_i}{\partial t^2} \quad (2.6)$$

where F_i is the force acting particle *i* described by position vector r_i and with the potential energy function (or *force field*), which depends on the positions of all *N* particles in the system. The resulting equations constitute a system of coupled second-order, nonlinear differential equations that must be numerically integrated step-by-step using appropriate integration techniques. To perform an MD simulation, it is necessary to precisely define several initial parameters, including: the initial conditions of the system, namely the positions and velocities of the particles at the initial time; the time step δt used for the numerical integration of the equations of motion; a model of interatomic interactions, a force field; and the boundary conditions [28].

The initial atomic positions in biomolecules can be obtained from experimental data, such as crystallographic structures available in databases (e.g., Protein Data Bank [29]), or, in the absence of experimental data, through predictive methods. In this latter context, the use of AlphaFold [30] is particularly noteworthy: an artificial intelligence-based system developed by DeepMind, capable of predicting with high accuracy the three-dimensional structure of a protein solely from its amino acid sequence.
The initial velocities of particles are commonly assigned randomly, according to a Maxwell-Boltzmann distribution centered on the desired temperature, and subsequently corrected to remove any translational or rotational motion of the entire system (i.e., to eliminate angular momentum and center-of-mass velocity) [28].

MD simulations produce trajectories containing detailed information about the position and velocity of each particle over time. Through statistical mechanics, this information can be correlated with observable macroscopic properties. A central concept in this context is the statistical ensemble, defined as an ideal set of system copies, each in a microscopic state compatible with the same macroscopic conditions (such as temperature, pressure, and number of particles).

Depending on the type of simulation and the conditions to be reproduced, different thermodynamic ensembles can be employed:

— **NVE ensemble (microcanonical):** keeps the number of particles, volume, and total energy of the system constant. In this ensemble, the kinetic energy (and

thus the temperature) can fluctuate. It is useful for studying energy conservation or exploring the potential energy surface, but is less suitable during initial equilibration phases [31].

- **NVT ensemble (canonical):** keeps the number of particles, volume, and temperature constant through the use of thermostats. It is commonly employed to study conformational dynamics, such as protein folding in the gas phase or under controlled conditions [32].
- **NPT ensemble:** maintains the number of particles, pressure, and temperature constant by using both thermostats and barostats. This ensemble is particularly suited for simulations under conditions similar to experimental setups, allowing adjustment of system volume and density [33].

Explicit Solvent and Periodic Boundary Conditions.

A crucial aspect in modelling realistic biological systems is the accurate representation of the solvent environment. The simplest approach involves using an implicit solvent model, where the effects of the solvent (e.g., water) are mediated by a constant dielectric parameter (ε). However, many biomolecular processes, such as the interaction between a ligand and its receptor, strongly depend on the explicit presence and dynamics of water molecules. For this reason, more accurate simulations employ explicit solvent models, in which water molecules (e.g., according to the TIP3P model) [34] and ions (necessary for electrical neutrality) are represented at the atomic level.

In this context, the biomolecular system is immersed in a solvent box with sufficient margins around the target molecule. To simulate an “infinite” system and reduce surface effects, periodic boundary conditions (PBC) [35] are applied. As illustrated in Figure 2.3, the simulation box is replicated in all directions of Cartesian space, generating a periodic system where each particle interacts not only with other particles within its cell but also with images present in adjacent cells.

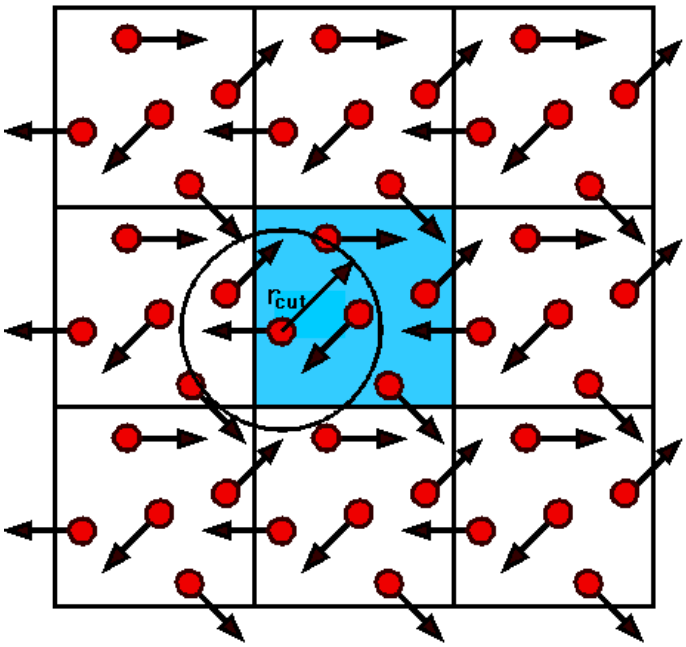

Figure 2.3: Two-dimensional representation of periodic boundary conditions, where a particle leaving the simulation box is automatically reinserted at the equivalent position in the adjacent boxes (*Democritus: Periodic Boundary Condition, University of Bath*).

Thanks to the exponential increase in computational power, MD-based methods for studying ligand-protein binding have become increasingly widespread. These approaches can be broadly divided into two main categories: Methods for calculating binding affinity, which provide thermodynamic information (end-state methods). Methods aimed at understanding the binding mechanism, which describe the association or dissociation pathways of the ligand.

The first category includes the so-called end-state methods, based on the principle that free energy is a state function: it depends only on the initial (unbound) and final (bound) states, not on the pathway taken [36]. These methods are generally applied in post-processing, exploiting data obtained from MD simulations.

Examples of these methods include:

- Linear Interaction Energy (LIE) [37],
- MM-PBSA (Molecular Mechanics Poisson-Boltzmann Surface Area) [38] and MM-GBSA (Molecular Mechanics Generalized Born Surface Area) [39]
- Alchemical methods, such as Thermodynamic Integration (TI) [40] and Free Energy Perturbation (FEP) [41].

The second category, instead, includes Physical Pathway (PP) methods [42]. These allow the direct simulation of the entire process of ligand binding or unbinding,

enabling not only the calculation of thermodynamic properties but also kinetic properties, as well as the analysis of energy barriers and intermediate states along the pathway.

2.2 Molecular Docking

Molecular docking is one of the fundamental techniques in computational chemistry applied to the study of biological systems. Although sometimes described as a “simplified” method, docking fully belongs to classical mechanics–based methodologies, employing an energetic description that integrates key physical terms such as electrostatic interactions, van der Waals forces, hydrogen bonds, and hydrophobic interactions [43]. It is a computational strategy used to predict the interaction between two or more molecules, typically between a protein (receptor) and a small ligand, but also applicable to protein-protein or enzyme-substrate complexes. Such interactions play a crucial role in numerous biological processes, including gene regulation, enzyme inhibition, and the degradation of refractory substrates.

Within molecular modeling, docking enables the prediction of the most probable orientation (pose or binding mode) of the ligand inside the active site of a biological macromolecule, based on enzyme structures available in structural databases (e.g., PDB), and estimates the interaction strength (binding affinity) through appropriate scoring functions.

The docking process is divided into two main phases:

— **Sampling**: exploration of the ligand’s conformational space (and sometimes the receptor’s), using search algorithms to generate a set of possible poses [44],
— **Scoring**: quantitative evaluation of the generated poses, using scoring functions that approximate the free binding energy, selecting the energetically most favorable configurations [45].

A fundamental distinction in docking protocols is between rigid docking and flexible docking (see Figure 2.4).

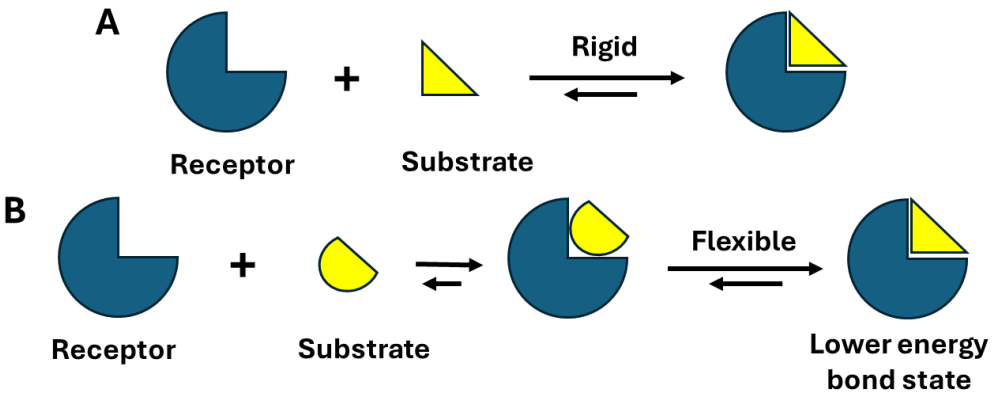

Figure 2.4: Conceptual representation of the main molecular docking strategies A) Rigid docking; B) Flexible docking.

In rigid docking methods, both the receptor and the ligand are treated as static, non-deformable structures, whereas in flexible docking methods, at least the ligand (and in some cases selected residues of the active site) can adopt different conformations during the interaction [46].

Early rigid docking algorithms were based on geometric alignment techniques such as Shape Matching (SM) or Fast Fourier Transform (FFT), in which molecules were considered rigid bodies with six degrees of freedom (three translational and three rotational) [47,48].

Today, thanks to advances in computational approaches, it is possible to model conformational flexibility with greater realism. The main strategies for flexible docking include:

— **Systematic approaches**, where the ligand is divided into fragments that are individually positioned within the active site and subsequently reconstructed through a procedure known as *anchoring and growth* [49],
— **Stochastic approaches**, which use probabilistic methods to explore conformational space in search of the global energy minimum (e.g., Monte Carlo, Simulated Annealing, Particle Swarm Optimization) [50],
— **Deterministic approaches**, based on molecular dynamics simulations, which allow observing the temporal evolution of ligand-receptor interactions [51].

Once the poses are generated, their predictive value relies on scoring functions, which can be classified into several categories:

— **Force field-based (MM)**: employing functions derived from molecular mechanics, explicitly considering van der Waals and electrostatic interaction terms [52],
— **Empirical**: based on statistical parameters derived from complexes with known affinity, calibrated to reflect relevant thermodynamic contributions [53],
— **Knowledge-based**: derived from statistical analyses of large datasets of crystallographic structures, representing a form of learning grounded in experimental evidence [54],
— **Consensus scoring**: combining multiple scoring functions to mitigate the intrinsic limitations of each method and improve overall predictive reliability [55].

The scoring function is employed to estimate the binding affinity between a ligand and its receptor by approximating the free binding energy (ΔG_{bind}). This approximation is expressed by the following equation [56]:

$$Score = w_s C_s + w_h C_h + w_{NB} E_{NB} + w_{Des} E_{Des} + \cdots \qquad (2.7)$$

Where:

- *Score:* estimated binding affinity between the ligand and the receptor, approximating the ΔG_{bind}
- C_s: steric complementarity between ligand and receptor, describing how well their shapes fit together
- C_h: hydrophobic contribution, quantifying favorable interactions between nonpolar regions
- E_{NB}: non-covalent energy, including van der Waals and electrostatic interactions
- E_{Des}: desolvation energy, representing the energetic cost of removing water molecules from the binding site
- w_s, w_h, w_{NB}, w_{Des}: weighting coefficients that adjust the relative importance of each term in the overall score
- ...: optional additional contributions, e.g., hydrogen bonding, torsional penalties, or other interaction terms depending on the scoring function used.

The scoring function integrates multiple physical contributions to provide an estimate of how strongly a ligand binds to its receptor.

2.2.1 AutoDock 4.2

In the context of the present thesis, the AutoDock 4.2 software[57] was employed to perform the molecular docking studies presented herein, particularly those described in Paper I. AutoDock 4.2 is one of the most established and widely used programs for predicting interactions between ligands and biological receptors, thanks to the implementation of a semi-empirical scoring function based on an empirical force field. The AutoDock scoring function integrates a detailed thermodynamic description of the binding process, including intramolecular contributions and an explicit approximation of desolvation. Specifically, the energy model considers the favorable energetics associated with the removal of the solvent environment around apolar atoms (such as carbon), balanced against the unfavorable desolvation of polar or charged atoms, thus reflecting a realistic interplay of solvent-solute interactions during molecular binding. To efficiently explore the conformational space of the ligand and receptor, AutoDock 4.2 employs a Lamarckian Genetic Algorithm (LGA) as its primary sampling method, which combines global search via a genetic algorithm with local optimization to refine binding poses.[58]

AutoDock 4.2 calculates intermolecular interactions through pairwise terms, i.e., considering interactions between atom pairs, and incorporates an empirical evaluation of solvent effects. Unlike classical force fields that model the solvent explicitly, often neglecting entropic contributions, AutoDock 4.2 treats the solvent as a continuous dielectric medium. Within this framework, models such as the Poisson-Boltzmann Surface or the Generalized Born Surface Area (GBSA) [59,60] can be used for a more accurate description of electrostatic screening by the solvent. Another relevant aspect of the approach implemented in AutoDock is the assignment of atomic charges using the Gasteiger-Marsili method [61] which enables a rapid estimation of charge distributions necessary for calculating electrostatic interactions within the ligand-receptor complex.

In summary, AutoDock 4.2 constitutes a versatile and robust tool for studying molecular interactions, providing a balance between physicochemical accuracy and computational efficiency, both essential for in silico screening and predictive analysis in inhibitor design.

2.2.2 AutoDock Vina

For the analyses conducted in Paper II, the AutoDock Vina software [62] was used, which implements a semi-empirical scoring function based on explicit pairwise terms, including van der Waals, electrostatic, hydrophobic interactions, and

hydrogen bonds. This function also incorporates an empirical component that implicitly accounts for solvent effects, contributing to a more realistic representation of the binding process. Electrostatic interactions are calculated using Gasteiger-Marsili atomic charges [61] automatically assigned to ligands and receptors. This allows for an efficient estimation of Coulombic interactions, although simplified compared to more sophisticated methods. To efficiently explore the conformational space of the ligand and receptor, AutoDock Vina employs an Iterated Local Search (ILS) algorithm[63], which iteratively generates random ligand poses and refines them through local optimization to identify favorable binding conformations.

In the same study, AutoDock Vina was also chosen for its higher computational speed and ease of use, features that proved crucial given the considerable size of the substrate analyzed. However, it is important to highlight that, compared to AutoDock 4.2, Vina adopts a more simplified representation of electrostatic interactions, treating them less explicitly. This simplification enables a significant increase in computational efficiency, albeit at the cost of some loss of detail in the description of specific energetic contributions.

2.2.3 Glide

For the study described in PE-laccase investation, the molecular docking software Glide (Grid-based Ligand Docking with Energetics) [64] was employed. Glide offers two main operational modes: Glide SP (Standard Precision) and Glide XP (Extra Precision). These modes differ in the depth of conformational sampling and the complexity of the scoring function used.

- Glide SP utilizes fast and less rigorous algorithms, making it particularly suitable for high-throughput virtual screening of large compound libraries [65].
- Glide XP, on the other hand, employs more sophisticated sampling strategies and a more elaborate scoring function, resulting in higher computational cost. It is preferred for more detailed analyses on smaller ligand sets [66].

In the present work, the Glide SP mode was adopted as it is better suited to efficiently manage the volume of data and system complexity while maintaining a good balance between accuracy and computational time.

Glide relies on the GlideScore scoring function [67], an empirical function optimized from ChemScore [68] and enhanced with numerous additive terms to refine binding affinity estimation. This function thoroughly considers hydrophobic interactions, hydrogen bonds, π–π stacking interactions, steric clash penalties, and desolvation

contributions. Glide models the solvent implicitly as a continuous dielectric medium, without resorting to explicit water simulations. Another distinguishing feature of Glide lies in its method for assigning atomic charges: instead of the simplified Gasteiger-Marsili charges (used in AutoDock 4 and AutoDock Vina), Glide employs charges derived from accurate force fields [61], specifically OPLS (Optimized Potentials for Liquid Simulations) [69]. This enables a more reliable description of the electrostatic interactions between the ligand and the receptor's active site. Due to these characteristics, Glide represents an extremely efficient and accurate tool for in-depth studies of small substrates, as demonstrated in Paper III.

2.3 Quantum Mechanics methods

Quantum mechanical (QM) methods are essential tools in theoretical chemistry for accurately describing electronic structure and molecular properties. Unlike classical approaches, which rely on empirical potentials and simplified models, QM methods are based on the exact or approximate solution of the Schrödinger equation, which represents the fundamental principle for analyzing the stationary properties and time evolution of quantum systems [70]. However, the direct application of this equation to systems with many electrons is impractical due to its computational complexity, which increases rapidly with the number of particles. As a result, exact solutions are only attainable for very simple systems, making the use of approximations and advanced computational strategies necessary for studying more complex molecular systems.

Among the main QM methods are:

Ab initio methods:

Hartree-Fock (HF): Approximates the wavefunction as a single Slater determinant; it neglects dynamic electron correlation [71]. **Post-Hartree-Fock methods** [72], which include:

- *Møller-Plesset perturbation theory* (MP2, MP3, MP4): Corrects the HF energy by including electron correlation via perturbation theory.
- *Configuration Interaction (CI)*: Expands the wavefunction over multiple electronic configurations to better describe correlation.
- *Coupled Cluster (CC)*: A highly accurate method that includes electron correlation through exponential excitation operators.

Density Functional Theory (DFT) [73]: Based on the electron density rather than the wavefunction, employing various functionals (e.g., B3LYP, PBE) that balance accuracy and computational cost.

Semi-empirical methods [74]: Introduce simplifications and empirical parameters to reduce computational cost, such as AM1, PM3, and PM6. These are useful for large molecules, though less accurate than ab initio methods.

Hybrid quantum mechanical/molecular mechanical (QM/MM) methods [75]: Combine a QM-treated region (e.g., the active site of an enzyme) with a surrounding region treated using molecular mechanics (MM), to balance accuracy and computational time for large systems.

Among the various available quantum mechanical approaches, Density Functional Theory (DFT) has emerged as one of the most widely used methods for studying medium-sized chemical and biological systems. DFT provides an effective compromise between accuracy and computational cost, allowing for the analysis of relatively large systems with satisfactory precision. Thanks to this combination, DFT is well suited for modelling chemical reactions, analysing ligand-receptor interactions, and predicting spectroscopic properties.

In the present chapter, the theoretical principles underlying DFT and its application in the contexts relevant to this work will be explored in detail.

2.3.1 Density Functional Theory (DFT)

The intrinsic limitation of quantum chemistry methods is the direct use of the wave function to describe many-electron systems, making the numerical treatment of complex systems computationally prohibitive. In Density Functional Theory (DFT), the electronic structure of an atomic or molecular system is determined using the three-dimensional electron density $\rho(r)$ as the fundamental variable. This represents a major simplification compared to traditional quantum chemistry methods, which are based on the 3N-dimensional (or 4N when spin variables are included) wavefunction, where N is the number of electrons in the system. Density Functional Theory (DFT) has emerged as one of the most established methods [73]. DFT enables the study of many-particle electronic systems by using the electron density ρ(r), a function dependent only on the spatial coordinates (x, y, z), instead of the wave function, which depends on several variables proportional to the number of electrons. This paradigm shift leads to a significant simplification of the quantum mechanical problem. The earliest attempts in this direction date back to the Thomas–Fermi model of 1927, which described the electronic energy of a system by

treating it as a uniformly distributed electron gas. The electron density ρ(r) can be expressed as:

$$\rho(r) = N \int \dots \int |\psi(x_1, x_2, \dots x_N)|^2 dx_1 dx_2 \dots dx_n \quad (2.8)$$

Even in systems containing multiple electrons, the electron density, neglecting spin variables, depends solely on three spatial coordinates, regardless of the number of electrons involved. This characteristic represents one of the main advantages of Density Functional Theory (DFT), as it allows for a simplified treatment of complex electronic systems. The theoretical foundations of modern DFT are based on two theorems formulated by Hohenberg and Kohn in 1964, and on the subsequent formalism developed by Kohn and Sham in 1965.

— First Hohenberg–Kohn theorem: This theorem states that, for an electronic system in its ground state, there exists a one-to-one correspondence between the electron density ρ(r) and the external potential v(r). As a consequence, the density uniquely determines the Hamiltonian, the wave function of the system, and all its observable properties [76].
— Second Hohenberg–Kohn theorem: This theorem establishes the existence of a universal energy functional dependent on the electron density, which reaches its minimum for the ground-state density. Any other trial electron density *ρ(r)* yields an energy greater than or equal to the true ground-state energy.

$$E_0 \leq E[\rho(r)] \quad (2.9)$$

There are two main challenges in Density Functional Theory. The first is that the electron density must correspond to a wavefunction that is a physically possible N-electron state, i.e., a solution of the Schrödinger equation. Since the wavefunction must be antisymmetric due to the Pauli exclusion principle, this gives rise to the well-known problem of N- and V-representability of the electron density. The second is to determine the correct functional form *E[ρ]*. To improve upon the Thomas–Fermi model, Kohn and Sham introduced a reference system of non-interacting electrons with the same density as the real, interacting system. The total kinetic energy can then be written as:

$$T[\rho] = T_s[\rho] + T_c[\rho] \quad (2.10)$$

where $T_s[\rho]$ is the kinetic energy of the non-interacting reference system, and $T_c[\rho]$ is the correction term accounting for electronic correlation. We recall here that exact kinetic energy functional is known only for non-interacting electrons but not for real interacting systems. Because of this, DFT has to use approximations for the

exchange–correlation functional, which needs to account for the gap between the real kinetic energy of interacting electrons and the one calculated for non-interacting electrons. This limitation is one of the main challenges in improving the accuracy of DFT calculations. Using this separation, the universal functional can be expressed as:

$$F[\rho] = T_S[\rho] + J[\rho] + E_{xc}[\rho] \tag{2.11}$$

where $J[\rho]$ is the classical Coulomb (electron–electron repulsion) term, and $E_{xc}[\rho]$ is the exchange-correlation functional, which includes non-classical effects such as the difference between the exact kinetic energy and $T_S[\rho]$, as well as corrections for electron self-interaction:

$$E_{XC}[\rho] = (T[\rho] - T_S[\rho]) + (E_{ee}[\rho] - J[\rho]) \tag{2.12}$$

Considering an external potential v(r) generated by the nuclear charges, and neglecting the nucleus–nucleus interactions, the total energy of the real system becomes:

$$E[\rho] = T_s[\rho] + J[\rho] + E_{xc}[\rho] + \int \rho(r)v(r)dr \tag{2.13}$$

The only term without an explicit expression is $Exc[\rho]$, which represents the main challenge in Density Functional Theory (DFT). By applying the variational principle and the method of Lagrange multipliers, the Kohn-Sham equations are obtained [77]:

$$-\frac{1}{2}\nabla_i^2 + v_s(r)\psi_i^{KS} = \varepsilon_i\psi_i^{KS} \tag{2.14}$$

The effective potential v_S includes the exchange-correlation V_{xc}, which is defined as the functional derivative δ of the exchange-correlation energy:

$$V_{xc} = \frac{\delta E_{xc}[\rho(r)]}{\delta\rho(r)} \tag{2.15}$$

This formalism is mathematically rigorous and computationally efficient; however, the exact form of the exchange correlation functional $E_{xc}[\rho]$ remains unknown. To overcome this limitation, various types of functionals have been developed, broadly categorized into pure and hybrid functionals, the latter incorporating a fraction of Hartree-Fock exchange.

Generally, the functional is expressed as the sum of exchange E_x and correlation contributions E_c :

$$E_{xc}[\rho(r)] = E_x[\rho(r)] + E_c[\rho(r)] \quad (2.16)$$

Among the most widely used approaches are hybrid functionals, which combine exchange and correlation terms from LSDA [78] and GGA [79] with a fraction of Hartree-Fock exchange. Well-known examples include B3LYP [80], M06 [81], and PBE0 [82].

Since many traditional DFT methods exhibit limitations in accurately describing long-range dispersion interactions, specific corrective approaches have been developed to incorporate these effects [83]. In DFT-D, an additional empirical or semi-empirical term E_{disp} is added to the conventional DFT energy to account for van der Waals interactions between atoms or molecules. The total energy is therefore expressed as:

$$E_{DFT-D} = E_{DFT} + E_{disp} \quad (2.17)$$

Here, E_{DFT} is the standard DFT energy (including kinetic, Coulomb, and exchange-correlation contributions), and E_{disp} is the dispersion correction. Several widely used schemes exist for E_{disp}, such as Grimme's D2, D3, D4, and the nonlocal VV10 functional, which differ in how the dispersion interactions are modelled and parametrized.

This correction allows DFT calculations to more accurately predict noncovalent interactions, adsorption energies, and intermolecular forces, making it especially important in studies of molecular complexes, biomolecules, and materials

2.3.2 QM cluster approach

In the investigation of PAH oxidation by laccases, QM cluster approach [84] was adopted to investigate the possible reaction mechanism. Since biological systems are generally too complex to be fully described using quantum mechanical methods, such as wavefunction-based approaches or Density Functional Theory, the QM cluster approach represents an effective strategy to simplify the system while maintaining accuracy in describing local chemical interactions at quantum chemistry level [85,86]. This method, among the first developed for mechanistic studies of enzymes, involves constructing a reduced model derived from the enzyme's three-dimensional structure. An appropriate number of atoms is selected based on computational resources and the chosen theoretical level, including the portion of the enzyme directly involved in the reaction. This portion comprises substrates and reactive atoms, active site residues essential for catalysis, stabilizing residues interacting with the substrate or maintaining the active site

conformation, and residues involved in short- or long-range interactions with the reactive atoms (see Figure 2.5).

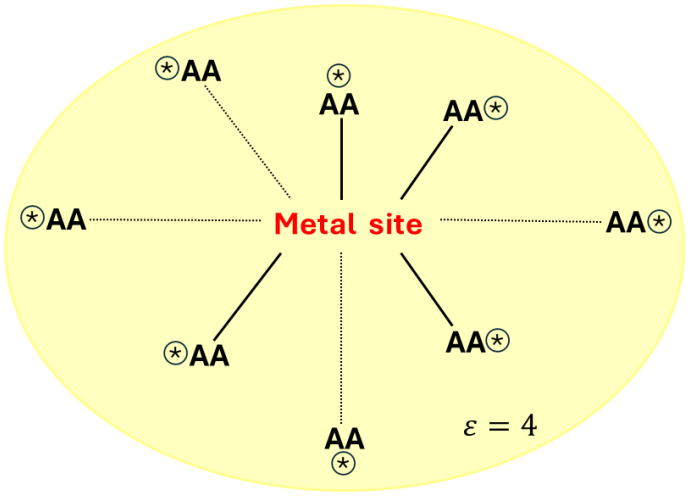

Figure 2.5: General scheme of a QM cluster model for the metalloenzyme active site. In this approach, the enzyme active site is modelled using quantum mechanical (QM) methods. The model includes the key residues involved in the catalytic mechanism, which are truncated to retain only the side chains, while the main backbone is generally omitted. The alpha carbon atoms (Cα, marked with stars) at the truncation points are kept fixed during the geometry optimization to preserve structural integrity. The rest of the enzyme, outside the QM region, is not explicitly modelled but is represented as a homogeneous polarizable continuum characterized by a dielectric constant chosen to simulate the electrostatic influence of the protein environment.

In the specific case of metalloenzymes, the distinction between the first and second coordination spheres of the metal aids in model selection, as the reactivity is strongly influenced by electronic interactions with the metal ion. For such systems, an effective cluster typically includes between 100 and 300 atoms, depending on the complexity and the role of the metal in the reaction. Density Functional Theory (DFT) calculations are performed on this reduced model to obtain an accurate description of the local chemistry. To account for the surrounding protein environment, long-range effects are introduced via a continuum dielectric model, which simulates the electrostatic influence of the enzymatic environment as a homogeneous polarizable medium [87–89]. It is important to note that the influence of the dielectric constant decreases as the cluster size increases. To represent steric effects, some atoms, typically side chain atoms and backbone atoms (alpha carbon and hydrogens), are constrained to their crystallographic positions at the cluster boundaries. The selection of atoms to constrain is crucial to ensure the stability and realism of the model. This approach allows significant computational savings, making high-level quantum mechanical methods feasible.

It is particularly suitable for distinguishing between alternative catalytic mechanisms and for detailed studies of localized reactions, such as those involving metals. However, it also has some limitations: excluding most of the enzymes may lead to the loss of relevant long-range effects; enzyme flexibility and dynamic conformational changes occurring during the reaction are not considered; moreover, results can be sensitive to the selection of included residues. The use of a dielectric model may also represent an oversimplification of the actual protein environment. To overcome some of these limitations, in the second paper, the QM cluster approach was integrated with classical molecular dynamics (MD) simulations to explore conformational changes of the protein and achieve a more comprehensive description of the enzymatic system under study. The main limitations of the QM cluster model lie in its neglect of long-range interactions and its inability to accurately capture the conformational flexibility of large enzymes [90]. In particular, reactions involving charge variations or requiring redox potential calculations cannot be properly addressed within this framework. To overcome these limitations, Warshel and Levitt introduced the hybrid QM/MM approach in 1976 [91].

2.4 Hybrid QM/MM

QM/MM is a hierarchical quantum chemistry method that integrates quantum mechanics (QM) for the reactive region with molecular mechanics (MM) for the remainder of the system. The QM region encompasses the active site, the substrate(s), and the residues directly involved in the reaction. It is treated using quantum mechanics to accurately capture chemical interactions, such as bond formation and cleavage. The MM portion encompasses the remainder of the enzyme and its surrounding environment, modeled using classical molecular mechanics force fields [92]. In the cluster method, solvation of the QM region is usually described by a continuum dielectric model, often with a fixed dielectric constant (e.g., $\varepsilon = 4$). By contrast, in QM/MM approaches, the solvation, and thus the interactions of the QM region with the environment, are explicitly considered at least at the classical level. This represents a clear advantage, since it allows a more realistic description of the system without the need to treat the entire environment quantum mechanically.

On the other hand, QM/MM methods necessarily require the definition of a boundary between the QM and MM regions. This introduces potential drawbacks: artificial effects at the interface, difficulties in treating covalent bonds that cross the boundary, and the need for link atoms or capping schemes, which may affect the accuracy of the simulation if not carefully handled.

This approach allows the investigation of protein chemical processes by combining the computational efficiency of MM techniques with the accuracy of QM calculations. QM/MM methods can be classified into two main types:

— Additive method: Mutual polarization between the QM and MM regions can be accounted for at the MM level, without requiring direct communication between QM and MM calculations. QM and MM energies are computed separately, with an interaction term describing their coupling. In principle, this approach is the most accurate, as the interaction term can be treated at either the MM or QM level, and the polarization of the QM region can be included in the QM calculation [93].

$$E_{tot} = E_{QM}(QM) + E_{MM}(MM) - E_{int}(QM + MM) \quad (2.18)$$

— Subtractive method: Energy corrections are applied to remove overlaps and inconsistencies between the QM and MM regions [93].

$$E_{tot} = E_{QM}(QM) + E_{MM}(QM + MM) - E_{MM}(QM) \quad (2.19)$$

The general formulations of the system's total energy are reported for the two models: additive (2.18) and subtractive (2.19).

The QM/MM approach enables detailed chemical analysis of the active site using QM while maintaining computational efficiency by treating the surrounding environment with MM. This allows the study of enzymatic reactions in realistic biological contexts. The method offers flexibility through various boundary treatments and embedding schemes, and it facilitates comparison of mechanistic predictions with experimental data.

The main limitations include the complexity of system preparation, the necessity of accurately defining QM/MM boundaries, and the risk of artifacts at covalent bonds crossing the interface. Accuracy depends on the choice of QM and MM methods and their parameters, particularly at the QM/MM interface. Although more efficient than full QM simulations, QM/MM remains computationally demanding compared to purely MM approaches, especially for large QM regions or when employing high-level QM methods [94].

2.5 String method

The string method is a computational technique used to determine Minimum Free Energy Pathways (MFEPs) [95] in complex molecular systems, such as chemical reactions and conformational transitions of proteins and enzymes. The reaction pathway is represented as a discrete sequence of configurations, or "images," which are iteratively updated according to the forces acting on the system, while maintaining approximately uniform spacing along the string. This approach allows efficient identification of the most probable pathway between initial and final states, highlighting rare transitions that would be difficult to access through direct simulations. In contrast, Free-Energy Perturbation (FEP) directly computes the free energy difference between two states via statistical sampling, whereas the String Method focuses on the most probable transition pathway rather than solely on the energy difference.

When the string method is combined with QM/MM approaches [96], the string images can be propagated using calculations that integrate quantum mechanics in the active site of the enzyme with molecular mechanics for the surrounding environment. In this context, the choice between an additive or subtractive scheme concerns how the QM and MM energies are combined: in the additive approach, QM and MM energies are computed separately and coupled through an interaction term, whereas in the subtractive approach, corrections are applied to remove overlaps and energetic inconsistencies. Integrating the string method with either QM/MM formulation allows for the tracing of realistic reaction pathways, the identification of transition states and reactive intermediates, and the accurate quantification of energy barriers, accounting both for the detailed chemistry of the active site and the influence of the protein and solvent environment.

This method is employed in the third work of the first section as an approach for studying the degradation mechanism of polyethylene.

2.6 Used Software

The computational protocol adopted for the initial construction of the substrates was consistent across the analyzed systems, with variations only in the choice of specific molecular docking software depending on the nature of the substrate. Below, the main software tools and methodologies employed are outlined.

System and protein preparation were performed using AntechamberTools (tLeap module) [97], which allowed for system neutralization through the addition of Na^+ and Cl^- ions and solvation of the complex within an explicit water box using the TIP3P model.

Force field parameters were also assigned using AntechamberTools: for proteins, the AMBER 99SB force field [98] was used (Papers I, III) and 14SB [99] (Papers II, IV, V); for substrates, the General AMBER Force Field (GAFF) [22] (Papers I, II, III) and GLYCAM06-J [23] (Paper IV) were employed. All DFT calculations were carried out with the TURBOMOLE 7.4 suite [100] (Paper II). Molecular dynamics (MD) simulations were conducted using GROMACS, employing the AMBER force fields (99SB and 14SB) for proteins, as previously mentioned, and the TIP3P model for water. Equilibrated structures were obtained starting from crystallographic data or, when necessary, from predictions generated by the AlphaFold software [30]. Trajectory analysis and data extraction were performed using GROMACS 2020 [101], VMD [102], and CAVER 3.0 [103], the latter specifically for tunnel and channel analysis. Finally, visualization and figure preparation were carried out with VMD, UCSF Chimera (version 1.16) [104], and ChimeraX [105].

References

1. Baron, R.; McCammon, J.A. Molecular Recognition and Ligand Association. Annu Rev Phys Chem 2013, 64, 151–175, doi:10.1146/annurev-physchem-040412-110047.
2. Arnold, F.H. Combinatorial and Computational Challenges for Biocatalyst Design. Nature 2001, 409, 253–257, doi:10.1038/35051731.
3. Siegbahn, P.E.M.; Borowski, T. Modeling Enzymatic Reactions Involving Transition Metals. Acc Chem Res 2006, 39, 729–738, doi:10.1021/ar050123u.
4. Frenkel, D.; Berend Smit. Understanding Molecular Simulation: From Algorithms to Applications. ; Elsevier, 2023;
5. Helgaker, T.; Poul Jorgensen.; Jeppe Olsen Molecular Electronic-Structure Theory..; John Wiley & Sons, 2013;
6. Kosloff, R. Time-Dependent Quantum-Mechanical Methods for Molecular Dynamics. J Phys Chem 1988, 92, 2087–2100, doi:10.1021/j100319a003.
7. Warshel, A. Multiscale Modeling of Biological Functions: From Enzymes to Molecular Machines (Nobel Lecture). Angewandte Chemie International Edition 2014, 53, 10020–10031, doi:10.1002/anie.201403689.
8. Brooks, C.L.; Case, D.A.; Plimpton, S.; Roux, B.; van der Spoel, D.; Tajkhorshid, E. Classical Molecular Dynamics. J Chem Phys 2021, 154, doi:10.1063/5.0045455.
9. Kuntz, I.D.; Blaney, J.M.; Oatley, S.J.; Langridge, R.; Ferrin, T.E. A Geometric Approach to Macromolecule-Ligand Interactions. J Mol Biol 1982, 161, 269–288, doi:10.1016/0022-2836(82)90153-X.
10. Parr, R.G. Density Functional Theory of Atoms and Molecules. In Horizons of Quantum Chemistry; Springer Netherlands: Dordrecht, 1980; pp. 5–15.
11. Cheng, X.; Ivanov, I. Molecular Dynamics. In; 2012; pp. 243–285.
12. Morris, G.M.; Lim-Wilby, M. Molecular Docking. In; 2008; pp. 365–382.
13. Zheng, B. Monte Carlo Simulations of Short-Time Critical Dynamics. Int J Mod Phys B 1998, 12, 1419–1484, doi:10.1142/S021797929800288X.
14. Paquet, E.; Viktor, H.L. Molecular Dynamics, Monte Carlo Simulations, and Langevin Dynamics: A Computational Review. Biomed Res Int 2015, 2015, 1–18, doi:10.1155/2015/183918.
15. Lin, X.; Li, X.; Lin, X. A Review on Applications of Computational Methods in Drug Screening and Design. Molecules 2020, 25, 1375, doi:10.3390/molecules25061375.
16. González, M.A. Force Fields and Molecular Dynamics Simulations. École thématique de la Société Française de la Neutronique 2011, 12, 169–200, doi:10.1051/sfn/201112009.
17. B. Smit Phase Diagrams of Lennard-Jones Fluids. J Chem Phys 1992.

18. Cornell, W.D.; Cieplak, P.; Bayly, C.I.; Gould, I.R.; Merz, K.M.; Ferguson, D.M.; Spellmeyer, D.C.; Fox, T.; Caldwell, J.W.; Kollman, P.A. A Second Generation Force Field for the Simulation of Proteins, Nucleic Acids, and Organic Molecules J . Am . Chem . Soc . 1995 , 117 , 5179–5197. J Am Chem Soc 1996, 118, 2309–2309, doi:10.1021/ja955032e.

19. Brooks, B.R.; Bruccoleri, R.E.; Olafson, B.D.; States, D.J.; Swaminathan, S.; Karplus, M. <scp>CHARMM</Scp> : A Program for Macromolecular Energy, Minimization, and Dynamics Calculations. J Comput Chem 1983, 4, 187–217, doi:10.1002/jcc.540040211.

20. Oostenbrink, C.; Villa, A.; Mark, A.E.; Van Gunsteren, W.F. A Biomolecular Force Field Based on the Free Enthalpy of Hydration and Solvation: The GROMOS Force-field Parameter Sets 53A5 and 53A6. J Comput Chem 2004, 25, 1656–1676, doi:10.1002/jcc.20090.

21. Kaminski, G.A.; Friesner, R.A.; Tirado-Rives, J.; Jorgensen, W.L. Evaluation and Reparametrization of the OPLS-AA Force Field for Proteins via Comparison with Accurate Quantum Chemical Calculations on Peptides. J Phys Chem B 2001, 105, 6474–6487, doi:10.1021/jp003919d.

22. Sprenger, K.G.; Jaeger, V.W.; Pfaendtner, J. The General AMBER Force Field (GAFF) Can Accurately Predict Thermodynamic and Transport Properties of Many Ionic Liquids. J Phys Chem B 2015, 119, 5882–5895, doi:10.1021/acs.jpcb.5b00689.

23. Kirschner, K.N.; Yongye, A.B.; Tschampel, S.M.; González-Outeiriño, J.; Daniels, C.R.; Foley, B.L.; Woods, R.J. GLYCAM06: A Generalizable Biomolecular Force Field. Carbohydrates. J Comput Chem 2008, 29, 622–655, doi:10.1002/jcc.20820.

24. Li, G.; Zheng, F.; Huang, Q.; Wang, J.; Niu, B.; Zhang, Y.; Long, D. Molecular Insight into Pyrolysis Processes via Reactive Force Field Molecular Dynamics: A State-of-the-Art Review. J Anal Appl Pyrolysis 2022, 166, 105620, doi:10.1016/j.jaap.2022.105620.

25. Buch, I.; Harvey, M.J.; Giorgino, T.; Anderson, D.P.; De Fabritiis, G. High-Throughput All-Atom Molecular Dynamics Simulations Using Distributed Computing. J Chem Inf Model 2010, 50, 397–403, doi:10.1021/ci900455r.

26. Kukol, A. Lipid Models for United-Atom Molecular Dynamics Simulations of Proteins. J Chem Theory Comput 2009, 5, 615–626, doi:10.1021/ct8003468.

27. Rudd, R.E.; Broughton, J.Q. Coarse-Grained Molecular Dynamics and the Atomic Limit of Finite Elements. Phys Rev B 1998, 58, R5893–R5896, doi:10.1103/PhysRevB.58.R5893.

28. Silva, R.; Plastino, A.R.; Lima, J.A.S. A Maxwellian Path to the Q-Nonextensive Velocity Distribution Function. Phys Lett A 1998, 249, 401–408, doi:10.1016/S0375-9601(98)00710-5.

29. Crystallography: Protein Data Bank. Nat New Biol 1971, 233, 223–223, doi:10.1038/newbio233223b0.

30. Jumper, J.; Evans, R.; Pritzel, A.; Green, T.; Figurnov, M.; Ronneberger, O.; Tunyasuvunakool, K.; Bates, R.; Žídek, A.; Potapenko, A.; et al. Highly Accurate Protein Structure Prediction with AlphaFold. Nature 2021, 596, 583–589, doi:10.1038/s41586-021-03819-2.

31. Hammonds, K.D.; Heyes, D.M. Shadow Hamiltonian in Classical NVE Molecular Dynamics Simulations: A Path to Long Time Stability. J Chem Phys 2020, 152, doi:10.1063/1.5139708.

32. Nielsen, S.O. Nested Sampling in the Canonical Ensemble: Direct Calculation of the Partition Function from NVT Trajectories. J Chem Phys 2013, 139, doi:10.1063/1.4821761.

33. Marchi, M.; Procacci, P. Coordinates Scaling and Multiple Time Step Algorithms for Simulation of Solvated Proteins in the NPT Ensemble. J Chem Phys 1998, 109, 5194–5202, doi:10.1063/1.477136.

34. Jorgensen, W.L.; Chandrasekhar, J.; Madura, J.D.; Impey, R.W.; Klein, M.L. Comparison of Simple Potential Functions for Simulating Liquid Water. J Chem Phys 1983, 79, 926–935, doi:10.1063/1.445869.

35. White, J.A.; Román, F.L.; González, A.; Velasco, S. Periodic Boundary Conditions and the Correct Molecular-Dynamics Ensemble. Physica A: Statistical Mechanics and its Applications 2008, 387, 6705–6711, doi:10.1016/j.physa.2008.08.008.

36. Limongelli, V. Ligand Binding Free Energy and Kinetics Calculation in 2020. WIREs Computational Molecular Science 2020, 10, doi:10.1002/wcms.1455.

37. Åqvist, J.; Medina, C.; Samuelsson, J.-E. A New Method for Predicting Binding Affinity in Computer-Aided Drug Design. “Protein Engineering, Design and Selection” 1994, 7, 385–391, doi:10.1093/protein/7.3.385.

38. Homeyer, N.; Gohlke, H. Free Energy Calculations by the Molecular Mechanics Poisson−Boltzmann Surface Area Method. Mol Inform 2012, 31, 114–122, doi:10.1002/minf.201100135.

39. Genheden, S.; Ryde, U. The MM/PBSA and MM/GBSA Methods to Estimate Ligand-Binding Affinities. Expert Opin Drug Discov 2015, 10, 449–461, doi:10.1517/17460441.2015.1032936.

40. Kirkwood, J.G. Statistical Mechanics of Fluid Mixtures. J Chem Phys 1935, 3, 300–313, doi:10.1063/1.1749657.

41. Zwanzig, R.W. High-Temperature Equation of State by a Perturbation Method. I. Nonpolar Gases. J Chem Phys 1954, 22, 1420–1426, doi:10.1063/1.1740409.

42. Deng, N.; Cui, D.; Zhang, B.W.; Xia, J.; Cruz, J.; Levy, R. Comparing Alchemical and Physical Pathway Methods for Computing the Absolute Binding Free Energy of Charged Ligands. Physical Chemistry Chemical Physics 2018, 20, 17081–17092, doi:10.1039/C8CP01524D.

43. Meng, X.-Y.; Zhang, H.-X.; Mezei, M.; Cui, M. Molecular Docking: A Powerful Approach for Structure-Based Drug Discovery. Current Computer Aided-Drug Design 2011, 7, 146–157, doi:10.2174/157340911795677602.

44. Coleman, R.G.; Carchia, M.; Sterling, T.; Irwin, J.J.; Shoichet, B.K. Ligand Pose and Orientational Sampling in Molecular Docking. PLoS One 2013, 8, e75992, doi:10.1371/journal.pone.0075992.

45. Bentham Science Publisher, B.S.P. Scoring Functions for Protein-Ligand Docking. Curr Protein Pept Sci 2006, 7, 407–420, doi:10.2174/138920306778559395.

46. Totrov, M.; Abagyan, R. Flexible Ligand Docking to Multiple Receptor Conformations: A Practical Alternative. Curr Opin Struct Biol 2008, 18, 178–184, doi:10.1016/j.sbi.2008.01.004.

47. Shoichet, B.K.; Kuntz, I.D.; Bodian, D.L. Molecular Docking Using Shape Descriptors. J Comput Chem 1992, 13, 380–397, doi:10.1002/jcc.540130311.

48. Katchalski-Katzir, E.; Shariv, I.; Eisenstein, M.; Friesem, A.A.; Aflalo, C.; Vakser, I.A. Molecular Surface Recognition: Determination of Geometric Fit between Proteins and Their Ligands by Correlation Techniques. Proceedings of the National Academy of Sciences 1992, 89, 2195–2199, doi:10.1073/pnas.89.6.2195.

49. DesJarlais, R.L.; Sheridan, R.P.; Dixon, J.S.; Kuntz, I.D.; Venkataraghavan, R. Docking Flexible Ligands to Macromolecular Receptors by Molecular Shape. J Med Chem 1986, 29, 2149–2153, doi:10.1021/jm00161a004.

50. Hart, T.N.; Read, R.J. A Multiple-start Monte Carlo Docking Method. Proteins: Structure, Function, and Bioinformatics 1992, 13, 206–222, doi:10.1002/prot.340130304.

51. Wu, G.; Robertson, D.H.; Brooks, C.L.; Vieth, M. Detailed Analysis of Grid-based Molecular Docking: A Case Study of CDOCKER—A CHARMm-based MD Docking Algorithm. J Comput Chem 2003, 24, 1549–1562, doi:10.1002/jcc.10306.

52. Yin, S.; Biedermannova, L.; Vondrasek, J.; Dokholyan, N. V. MedusaScore: An Accurate Force Field-Based Scoring Function for Virtual Drug Screening. J Chem Inf Model 2008, 48, 1656–1662, doi:10.1021/ci8001167.

53. Dias, R.; Macedo Timmers, L.F.; Caceres, R.; de Azevedo Jr., W. Evaluation of Molecular Docking Using Polynomial Empirical Scoring Functions. Curr Drug Targets 2008, 9, 1062–1070, doi:10.2174/138945008786949450.

54. Gohlke, H.; Hendlich, M.; Klebe, G. Knowledge-Based Scoring Function to Predict Protein-Ligand Interactions. J Mol Biol 2000, 295, 337–356, doi:10.1006/jmbi.1999.3371.

55. Charifson, P.S.; Corkery, J.J.; Murcko, M.A.; Walters, W.P. Consensus Scoring: A Method for Obtaining Improved Hit Rates from Docking Databases of Three-Dimensional Structures into Proteins. J Med Chem 1999, 42, 5100–5109, doi:10.1021/jm990352k.

56. Garrett M. Morris; David S. Goodsell; Robert S. Halliday; Ruth Huey; William E. Hart; Richard K. Belew; Arthur J. Olson Automated Docking Using a Lamarckian Genetic

Algorithm and an Empirical Binding Free Energy Function. J Comput Chem 1998, 19.14, 1639–1662.

57. Rizvi, S.M.D.; Shakil, S.; Haneef, M. A Simple Click by Click Protocol to Perform Docking: AutoDock 4.2 Made Easy for Non-Bioinformaticians. EXCLI J 2013, 12, 831–857.

58. Fu, Y.; Zhao, J.; Chen, Z. Insights into the Molecular Mechanisms of Protein-Ligand Interactions by Molecular Docking and Molecular Dynamics Simulation: A Case of Oligopeptide Binding Protein. Comput Math Methods Med 2018, 2018, 1–12, doi:10.1155/2018/3502514.

59. Still, W.C.; Tempczyk, A.; Hawley, R.C.; Hendrickson, T. Semianalytical Treatment of Solvation for Molecular Mechanics and Dynamics. J Am Chem Soc 1990, 112, 6127–6129, doi:10.1021/ja00172a038.

60. Hawkins, G.D.; Cramer, C.J.; Truhlar, D.G. Pairwise Solute Descreening of Solute Charges from a Dielectric Medium. Chem Phys Lett 1995, 246, 122–129, doi:10.1016/0009-2614(95)01082-K.

61. Gasteiger, J.; Marsili, M. Iterative Partial Equalization of Orbital Electronegativity—a Rapid Access to Atomic Charges. Tetrahedron 1980, 36, 3219–3228, doi:10.1016/0040-4020(80)80168-2.

62. Trott, O.; Olson, A.J. AutoDock Vina: Improving the Speed and Accuracy of Docking with a New Scoring Function, Efficient Optimization, and Multithreading. J Comput Chem 2010, 31, 455–461, doi:10.1002/jcc.21334.

63. Handoko, S.D.; Xuchang Ouyang; Chinh Tran To Su; Chee Keong Kwoh; Yew Soon Ong QuickVina: Accelerating AutoDock Vina Using Gradient-Based Heuristics for Global Optimization. IEEE/ACM Trans Comput Biol Bioinform 2012, 9, 1266–1272, doi:10.1109/TCBB.2012.82.

64. Friesner, R.A.; Banks, J.L.; Murphy, R.B.; Halgren, T.A.; Klicic, J.J.; Mainz, D.T.; Repasky, M.P.; Knoll, E.H.; Shelley, M.; Perry, J.K.; et al. Glide: A New Approach for Rapid, Accurate Docking and Scoring. 1. Method and Assessment of Docking Accuracy. J Med Chem 2004, 47, 1739–1749, doi:10.1021/jm0306430.

65. Friesner, R.A.; Murphy, R.B.; Repasky, M.P.; Frye, L.L.; Greenwood, J.R.; Halgren, T.A.; Sanschagrin, P.C.; Mainz, D.T. Extra Precision Glide: Docking and Scoring Incorporating a Model of Hydrophobic Enclosure for Protein−Ligand Complexes. J Med Chem 2006, 49, 6177–6196, doi:10.1021/jm051256o.

66. Repasky, M.P.; Murphy, R.B.; Banks, J.L.; Greenwood, J.R.; Tubert-Brohman, I.; Bhat, S.; Friesner, R.A. Docking Performance of the Glide Program as Evaluated on the Astex and DUD Datasets: A Complete Set of Glide SP Results and Selected Results for a New Scoring Function Integrating WaterMap and Glide. J Comput Aided Mol Des 2012, 26, 787–799, doi:10.1007/s10822-012-9575-9.

67. Gerçek, M.; Narang, A.; Körber, M.I.; Friedrichs, K.P.; Puthumana, J.J.; Ivannikova, M.; Al-Kazaz, M.; Cremer, P.; Baldridge, A.S.; Meng, Z.; et al. GLIDE Score. JACC Cardiovasc Imaging 2024, 17, 729–742, doi:10.1016/j.jcmg.2024.04.008.

68. Parker, K.C. Scoring Methods in MALDI Peptide Mass Fingerprinting: ChemScore, and the ChemApplex Program. J Am Soc Mass Spectrom 2002, 13, 22–39, doi:10.1016/S1044-0305(01)00320-8.

69. Gupta, S.; Bajaj, A. V. Extra Precision Glide Docking, Free Energy Calculation and Molecular Dynamics Studies of 1,2-Diarylethane Derivatives as Potent Urease Inhibitors. J Mol Model 2018, 24, 261, doi:10.1007/s00894-018-3787-4.

70. Costa, J.M.; Lluch, J.M. The Use of Quantum Mechanics Calculations for the Study of Corrosion Inhibitors. Corros Sci 1984, 24, 929–933, doi:10.1016/0010-938X(84)90113-6.

71. Friesner, R.A. Ab Initio Quantum Chemistry: Methodology and Applications. Proceedings of the National Academy of Sciences 2005, 102, 6648–6653, doi:10.1073/pnas.0408036102.

72. Bartlett, R.J.; John F. Stanton Applications of Post-Hartree—Fock Methods: A Tutorial. Reviews in computational chemistry 1994, 65–169.

73. Sperger, T.; Sanhueza, I.A.; Kalvet, I.; Schoenebeck, F. Computational Studies of Synthetically Relevant Homogeneous Organometallic Catalysis Involving Ni, Pd, Ir, and Rh: An Overview of Commonly Employed DFT Methods and Mechanistic Insights. Chem Rev 2015, 115, 9532–9586, doi:10.1021/acs.chemrev.5b00163.

74. Thiel, W. Semiempirical Quantum–Chemical Methods. WIREs Computational Molecular Science 2014, 4, 145–157, doi:10.1002/wcms.1161.

75. Senn, H.M.; Thiel, W. QM/MM Methods for Biomolecular Systems. Angewandte Chemie International Edition 2009, 48, 1198–1229, doi:10.1002/anie.200802019.

76. Hohenberg, P.; Kohn, W. Inhomogeneous Electron Gas. Physical Review 1964, 136, B864–B871, doi:10.1103/PhysRev.136.B864.

77. Kohn, W.; Sham, L.J. Self-Consistent Equations Including Exchange and Correlation Effects. Physical Review 1965, 140, A1133–A1138, doi:10.1103/PhysRev.140.A1133.

78. Nemeth, J.; Vautherin, D. Study of Finite Nuclei in the Local Density Approximation. Physics Letters B 1970, 32, 561–564, doi:10.1016/0370-2693(70)90543-5.

79. Ziesche, P.; Kurth, S.; Perdew, J.P. Density Functionals from LDA to GGA. Comput Mater Sci 1998, 11, 122–127, doi:10.1016/S0927-0256(97)00206-1.

80. Becke, A.D. Density-Functional Thermochemistry. III. The Role of Exact Exchange. J Chem Phys 1993, 98, 5648–5652, doi:10.1063/1.464913.

81. Zhao, Y.; Truhlar, D.G. The M06 Suite of Density Functionals for Main Group Thermochemistry, Thermochemical Kinetics, Noncovalent Interactions, Excited States, and Transition Elements: Two New Functionals and Systematic Testing of Four M06-

Class Functionals and 12 Other Functionals. Theor Chem Acc 2008, 120, 215–241, doi:10.1007/s00214-007-0310-x.

82. Adamo, C.; Barone, V. Toward Reliable Density Functional Methods without Adjustable Parameters: The PBE0 Model. J Chem Phys 1999, 110, 6158–6170, doi:10.1063/1.478522.

83. Grimme, S.; Antony, J.; Ehrlich, S.; Krieg, H. A Consistent and Accurate Ab Initio Parametrization of Density Functional Dispersion Correction (DFT-D) for the 94 Elements H-Pu. J Chem Phys 2010, 132, doi:10.1063/1.3382344.

84. Ahmadi, S.; Barrios Herrera, L.; Chehelamirani, M.; Hostaš, J.; Jalife, S.; Salahub, D.R. Multiscale Modeling of Enzymes: QM-cluster, QM/MM, and QM/MM/MD: A Tutorial Review. Int J Quantum Chem 2018, 118, doi:10.1002/qua.25558.

85. Liao, R.-Z.; Yu, J.-G.; Himo, F. Quantum Chemical Modeling of Enzymatic Reactions: The Case of Decarboxylation. J Chem Theory Comput 2011, 7, 1494–1501, doi:10.1021/ct200031t.

86. Georgieva, P.; Himo, F. Quantum Chemical Modeling of Enzymatic Reactions: The Case of Histone Lysine Methyltransferase. J Comput Chem 2010, 31, 1707–1714, doi:10.1002/jcc.21458.

87. Siegbahn, P.E.M.; Himo, F. The Quantum Chemical Cluster Approach for Modeling Enzyme Reactions. WIREs Computational Molecular Science 2011, 1, 323–336, doi:10.1002/wcms.13.

88. Siegbahn, P.E.M.; Himo, F. Recent Developments of the Quantum Chemical Cluster Approach for Modeling Enzyme Reactions. JBIC Journal of Biological Inorganic Chemistry 2009, 14, 643–651, doi:10.1007/s00775-009-0511-y.

89. Ramos, M.J.; Fernandes, P.A. Computational Enzymatic Catalysis. Acc Chem Res 2008, 41, 689–698, doi:10.1021/ar7001045.

90. Blomberg, M.R.A.; Borowski, T.; Himo, F.; Liao, R.-Z.; Siegbahn, P.E.M. Quantum Chemical Studies of Mechanisms for Metalloenzymes. Chem Rev 2014, 114, 3601–3658, doi:10.1021/cr400388t.

91. Warshel, A.; Levitt, M. Theoretical Studies of Enzymic Reactions: Dielectric, Electrostatic and Steric Stabilization of the Carbonium Ion in the Reaction of Lysozyme. J Mol Biol 1976, 103, 227–249, doi:10.1016/0022-2836(76)90311-9.

92. Hu, L.; Söderhjelm, P.; Ryde, U. Accurate Reaction Energies in Proteins Obtained by Combining QM/MM and Large QM Calculations. J Chem Theory Comput 2013, 9, 640–649, doi:10.1021/ct3005003.

93. Bulo, R.E.; Ensing, B.; Sikkema, J.; Visscher, L. Toward a Practical Method for Adaptive QM/MM Simulations. J Chem Theory Comput 2009, 5, 2212–2221, doi:10.1021/ct900148e.

94. Cao, L.; Ryde, U. On the Difference Between Additive and Subtractive QM/MM Calculations. Front Chem 2018, 6, doi:10.3389/fchem.2018.00089.

95. Maragliano, L.; Vanden-Eijnden, E. On-the-Fly String Method for Minimum Free Energy Paths Calculation. Chem Phys Lett 2007, 446, 182–190, doi:10.1016/j.cplett.2007.08.017.

96. Tzeliou, C.E.; Mermigki, M.A.; Tzeli, D. Review on the QM/MM Methodologies and Their Application to Metalloproteins. Molecules 2022, 27, 2660, doi:10.3390/molecules27092660.

97. Salomon-Ferrer, R.; Case, D.A.; Walker, R.C. An Overview of the Amber Biomolecular Simulation Package. WIREs Computational Molecular Science 2013, 3, 198–210, doi:10.1002/wcms.1121.

98. Showalter, S.A.; Brüschweiler, R. Validation of Molecular Dynamics Simulations of Biomolecules Using NMR Spin Relaxation as Benchmarks: Application to the AMBER99SB Force Field. J Chem Theory Comput 2007, 3, 961–975, doi:10.1021/ct7000045.

99. Huai, Z.; Shen, Z.; Sun, Z. Binding Thermodynamics and Interaction Patterns of Inhibitor-Major Urinary Protein-I Binding from Extensive Free-Energy Calculations: Benchmarking AMBER Force Fields. J Chem Inf Model 2021, 61, 284–297, doi:10.1021/acs.jcim.0c01217.

100. Balasubramani, S.G.; Chen, G.P.; Coriani, S.; Diedenhofen, M.; Frank, M.S.; Franzke, Y.J.; Furche, F.; Grotjahn, R.; Harding, M.E.; Hättig, C.; et al. TURBOMOLE: Modular Program Suite for Ab Initio Quantum-Chemical and Condensed-Matter Simulations. J Chem Phys 2020, 152, doi:10.1063/5.0004635.

101. Michaud-Agrawal, N.; Denning, E.J.; Woolf, T.B.; Beckstein, O. MDAnalysis: A Toolkit for the Analysis of Molecular Dynamics Simulations. J Comput Chem 2011, 32, 2319–2327, doi:10.1002/jcc.21787.

102. Abraham, M.J.; Murtola, T.; Schulz, R.; Páll, S.; Smith, J.C.; Hess, B.; Lindahl, E. GROMACS: High Performance Molecular Simulations through Multi-Level Parallelism from Laptops to Supercomputers. SoftwareX 2015, 1–2, 19–25, doi:10.1016/j.softx.2015.06.001.

103. Humphrey, W.; Dalke, A.; Schulten, K. VMD: Visual Molecular Dynamics. J Mol Graph 1996, 14, 33–38, doi:10.1016/0263-7855(96)00018-5.

104. Pettersen, E.F.; Goddard, T.D.; Huang, C.C.; Couch, G.S.; Greenblatt, D.M.; Meng, E.C.; Ferrin, T.E. UCSF Chimera—A Visualization System for Exploratory Research and Analysis. J Comput Chem 2004, 25, 1605–1612, doi:10.1002/jcc.20084.

105. Goddard, T.D.; Huang, C.C.; Meng, E.C.; Pettersen, E.F.; Couch, G.S.; Morris, J.H.; Ferrin, T.E. UCSF ChimeraX: Meeting Modern Challenges in Visualization and Analysis. Protein Science 2018, 27, 14–25, doi:10.1002/pro.3235.

Chapter 3
Summary of the Contributions

This chapter presents the summary of the results of the present thesis. The results are organized into two sections, based on the nature of the substrates that the investigated enzymes are capable of degrading.

First Section, which comprises:

- Temperature-Dependent Dynamics of FAST-PETase in PET Depolymerization (I)
- Non-Phenolic Aromatic Substrate Oxidation by the T1 Copper Site of *Trametes versicolor* Laccase (II)
- Laccase-Catalyzed LDPE Oxidation: Interplay of Binding and Redox Effects (III)

It is dedicated to enzymes capable of degrading synthetic, non-biodegradable substrates. In this area, the research aimed to understand, at the molecular and atomic levels, the mechanisms of interaction and catalysis of degradative enzymes (such as FAST-PETase and various laccases) in the degradation of plastic polymers and aromatic compounds (PAHs). The goal was to identify structural, dynamic, and redox factors that influence their catalytic efficiency and to provide a basis for enzyme engineering aimed at developing sustainable biotechnological solutions for bioremediation.

Second Section, which includes (both work in progress):

- Enhanced Fatty Acid Decarboxylation by CYP450SPα Mutants: A Dynamic Comparison with OleTJE (IV)
- Dynamic Insights into LPMO SmAA10 and β-Chitin Interactions (V)

Focuses on the study of metalloenzymes capable of degrading biodegradable substrates (CYP152 and LPMO). Particular attention is given to the molecular mechanisms governing the interactions between these macromolecular substrates and the degradative enzymes. The primary objective is to understand these processes to facilitate the efficient and sustainable valorization of biomass. Each of the enzymatic systems analyzed is involved in the biological degradation of complex and recalcitrant substrates, of both synthetic and natural origin. Clarifying the

molecular mechanisms underlying these processes is therefore crucial, as they drive catalytic activity. In this context, computational methodologies offer a significant advantage, as they enable the atomistic-level exploration of dynamics and interactions within the active site. These insights, often inaccessible through experimental techniques alone, are essential to guide the rational design of more efficient engineered enzymes for applications in both bioremediation and biomass valorization.

For clarity and reference, Table 3.1 summarizes all the works included in this thesis, showing both the titles used throughout this summary and their original published titles.

Paper	Harmonized Title	Original Title
I	Temperature-Dependent Dynamics of FAST-PETase in PET Depolymerization	On the Role of Temperature in the Depolymerization of PET by FAST-PETase: An Atomistic Point of View on Possible Active Site Pre-Organization and Substrate-Destabilization Effects [1]
II	Non-Phenolic Aromatic Substrate Oxidation by the T1 Copper Site of *Trametes versicolor* Laccase	Mechanism of non-phenolic substrate oxidation by the fungal laccase Type 1 copper site from *Trametes versicolor*: the case of benzo[a]pyrene and anthracene [2]
III	Laccase-Catalyzed LDPE Oxidation: Interplay of Binding and Redox Effects	Comparative analysis of Polyethylene-Degrading Laccases: Redox Properties and Enzyme-Polyethylene Interaction Mechanism [3]
IV	Enhanced Fatty Acid Decarboxylation by CYP450SPα Mutants: A Dynamic Comparison with OleTJE	Rational Design of CYP450SPα Mutants for Enhanced Lipid Waste Conversion: Dynamic Comparison with OleTJE *(in progress)*
V	Dynamic Insights into LPMO SmAA10 and β-Chitin Interactions	Molecular Dynamics of the Metallo-enzyme Lytic Polysaccharide Monooxygenase (LPMO) SmAA10 and its interactions with β-chitin *(in progress)*

Table 3.1: Lists the papers published and in preparation presented in this thesis.

3.1 First section – In Silico Investigation of Enzymatic Degradation of Non-Biodegradable Waste

This section focuses on the computational study of two distinct enzymes capable of degrading non-biodegradable waste.

The first is a bacterial hydrolytic enzyme, PETase, isolated from *Ideonella sakaiensis*, which has been extensively studied for its ability to degrade PET [4] PETase acts synergistically with MHETase [5] in the depolymerization of this recalcitrant synthetic polymer (I).

Laccases represent the second enzymatic system [6] Oxidizing metalloenzymes are widely distributed across fungi, bacteria, plants, and animals. These enzymes exhibit broad substrate promiscuity, oxidizing a diverse range of compounds, including aromatic molecules and synthetic polymers. Although the natural substrate of fungal laccases is primarily lignin, numerous studies have demonstrated their effectiveness in degrading PAHs, such as anthracene and benzo[a]pyrene [7] (II). More recent studies have also highlighted the ability of certain bacterial laccases to interact with and oxidize highly recalcitrant aliphatic hydrocarbons, such as LDPE [8] (III).

From a computational perspective, it is therefore essential to explore the molecular mechanisms of action of key bioremediation enzymes, such as those mentioned above, particularly in the context of degrading recalcitrant synthetic polymers. The ultimate goal is to support the development of sustainable biotechnological strategies for managing and recycling plastic waste.

3.1.1 Temperature-Dependent Dynamics of FAST-PETase in PET Depolymerization

PET is a polymer that has been widely used globally since 1941. However, its extensive use has led to serious environmental concerns due to its resistance to degradation and the massive accumulation of plastic waste. Among the few biological systems capable of degrading PET at moderate temperatures, particular attention has been given to PETase, a bacterial enzyme isolated from *Ideonella sakaiensis* [4], which works synergistically with MHETase [5] to efficiently depolymerize this synthetic material.

More recently, machine learning-guided engineering has led to the development of an enhanced enzyme variant, named FAST-PETase (see Figure 3.1) [9] which exhibits improved catalytic activity and a broad operational temperature range (30–60 °C), with peak efficiency around 50 °C. This variant is capable of completely

degrading heat-treated plastic bottles, significantly increasing the industrial application potential of PETase enzymes.

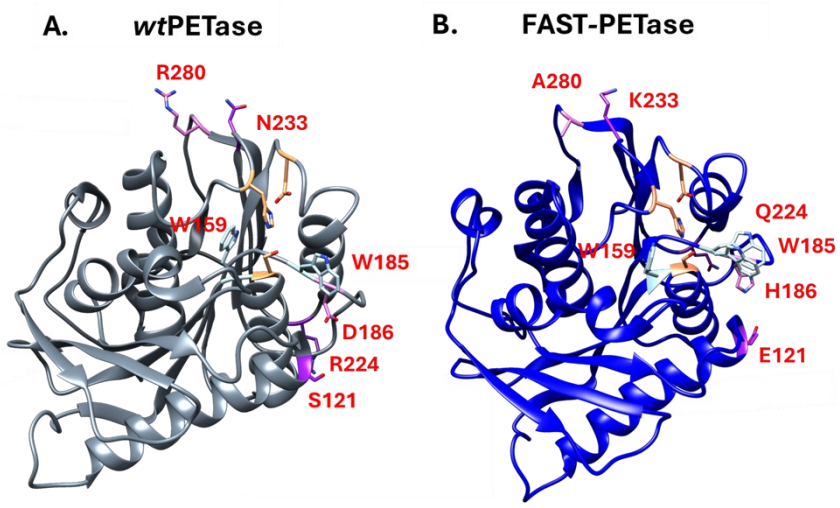

Figure 3.1: Crystallographic structures of A. PETase and B. FAST-PETase. In B, the engineered residues introduced through modifications relative to the wild-type enzyme (PETase) are highlighted in red. These mutations are responsible for the enhanced catalytic activity of FAST-PETase.

In Paper I, to investigate in detail and atomistic terms the interaction mechanism between FAST-PETase and the PET substrate (shown in Figure 3.2), molecular dynamics (MD) simulations were performed on both the apo form of the enzyme and the enzyme–substrate complex with a tetrameric PET model (4PET), at temperatures of 30 °C and 50 °C.

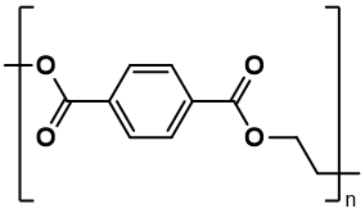

Figure 3.2: Chemical structure of the repeating monomeric unit of PET, formed by the condensation of terephthalic acid and ethylene glycol, resulting in a polymer chain with ester linkages connecting aromatic units (benzene rings) and aliphatic segments.

The objective was to understand how temperature variations influence the conformational dynamics of the enzyme and its interaction with the substrate, considering that 50 °C represents the optimal condition for catalytic activity. Simulations were initiated using the crystallographic structure of FAST-PETase (PDB ID: 7SH6), and the substrate was modeled as a four-unit oligomer (4PET) to

better represent the complexity of the enzyme–substrate interaction. Substrate parameters were derived from quantum mechanical calculations and specific force fields, ensuring an accurate representation of the system. After system preparation (including solvation with water and neutralization with ions), production simulations were performed for 300 nanoseconds for each temperature and enzyme/substrate state. Analysis of the simulations revealed that the conformational response of FAST-PETase is strongly temperature-dependent. Specifically, at 50 °C, the apo form of the enzyme exhibited greater amplitude and frequency of fluctuations in regions near the active site, particularly in the E204–P210 loop and surrounding areas, which appeared less mobile at 30 °C. These fluctuations led to the formation of larger and more numerous surface cavities, potentially enhancing substrate accessibility and binding in the active pocket, and suggesting a structural pre-organization of the catalytic site at 50 °C.

In the FAST-PETase:4PET complex, simulations at 50 °C showed increased structural plasticity of the enzyme, which promoted greater lipophilicity of the active site. This facilitated the stabilization of the PET aromatic rings, which were more effectively anchored by key residues such as W185 and T87 through hydrophobic and π–π stacking interactions, crucial for maintaining the substrate in a catalytically competent configuration. Such stabilization enabled the formation of a particular substrate conformation, referred to as the “W-shaped” conformation (see Figure 3.3), characterized by an extended arrangement of the 4PET oligomer on the binding site surface, in stark contrast to the “wrapped” conformation predominantly observed at 30 °C. The “W-shaped” conformation was not observed in simulations of the wild-type enzyme nor those of the free substrate in solution at various temperatures, suggesting that the structural environment provided by FAST-PETase at 50 °C is essential for its formation. This conformation is further stabilized by a salt bridge between the engineered lysine (K233) and aspartic acid (D204), as well as additional interactions involving R90, which collectively help maintain the substrate in an optimal position for nucleophilic attack.

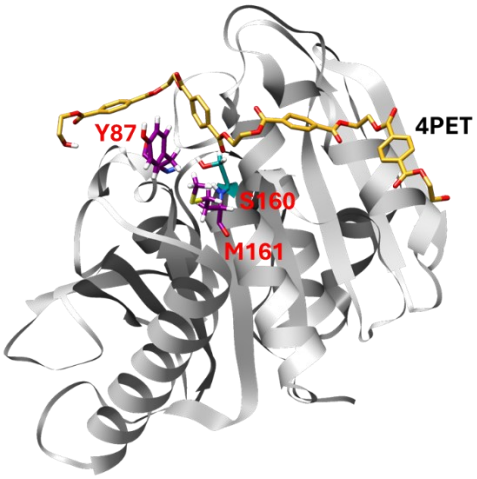

Figure 3.3: "W-shaped" conformation adopted during molecular dynamics (MD) simulation by the PET fragment within the active site of FAST-PETase. This conformation suggests an optimal substrate fit to the catalytic site, promoting enzyme–substrate interaction and facilitating polymer hydrolysis.

The distances between the carbonyl groups of PET and the catalytic residues S160 and M161 were more frequently found within the optimal range for catalysis at 50 °C, indicating an improved alignment of the active site for the enzymatic reaction. To confirm the energetic stability of the conformations, density functional theory (DFT) calculations were performed on both the "wrapped" and "W-shaped" substrate conformations. The results revealed that the "wrapped" conformation corresponds to a high-energy state inaccessible in solution, whereas the "W-shaped" conformation is energetically favored within the enzymatic environment.

Additional MD simulations of the free substrate at different temperatures confirmed that the "W-shaped" conformation does not arise in solution, highlighting the crucial role of the enzyme in promoting high-energy substrate conformations that facilitate its destabilization and, consequently, catalysis. These atomistic-level insights demonstrate that the increased flexibility and pre-organization of the FAST-PETase active site at 50 °C enable the recognition and stabilization of specific, highly reactive PET conformations, directly explaining the experimentally observed enhancement in catalytic efficiency. This structural adaptability not only rationalizes the improved activity of FAST-PETase but also provides a mechanistic foundation for understanding the subsequent reaction steps in PET hydrolysis.

Proposed Catalytic Mechanism: the hydrolysis of polyethylene terephthalate (PET) by PETase, particularly its engineered variant FAST-PETase, follows the classical mechanism of serine hydrolases, based on the catalytic triad S160–H237–D206. The reaction proceeds through two main stages: acylation, which leads to the

formation of a covalent acyl–enzyme intermediate, and deacylation, in which this intermediate is hydrolyzed by a water molecule, resulting in product release and enzyme regeneration [10,11] (see Figure 3.4). The mutations introduced in FAST-PETase enhance substrate binding, stabilize key intermediates, and lower activation barriers compared to the wild-type enzyme.

— Acylation: PET binds to the active site with its ester carbonyl positioned near S160. The oxyanion hole, formed by Y87 and M161, stabilizes the developing negative charge, while π–π stacking with W185 properly orients the aromatic ring of the substrate. H237 abstracts a proton from S160, activating it for nucleophilic attack, while D206 stabilizes the catalytic triad. The nucleophilic attack on the ester carbonyl generates a tetrahedral intermediate that collapses to form the covalent acyl–enzyme intermediate.

— Deacylation: A water molecule enters the active site and is activated by H237, becoming nucleophilic and attacking the acyl carbonyl. The oxyanion hole again stabilizes the formation of a second tetrahedral intermediate. The collapse of this intermediate regenerates the hydroxyl group of S160 and releases mono(2-hydroxyethyl) terephthalate (MHET) Subsequently, the MHETase enzyme catalyzes the final step of hydrolysis, yielding terephthalic acid (TPA) and ethylene glycol (EG). The enzyme is thus fully restored and ready for another catalytic cycle [12].

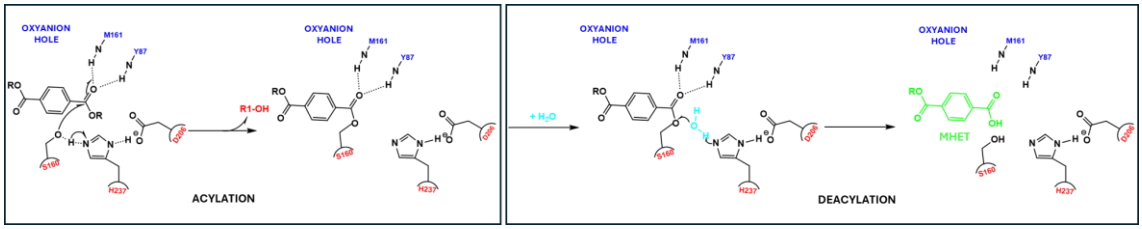

Figure 3.4: Proposed catalytic mechanism of PET hydrolysis by FAST-PETase. The enzyme hydrolyzes polyethylene terephthalate (PET) through a two-step serine hydrolase mechanism involving the catalytic triad S160–H237–D206 and the oxyanion hole formed by Y87 and M161. In the first stage (acylation), S160, activated by H237 and stabilized by D206, attacks the ester carbonyl of PET, stabilized by the oxyanion hole. The collapse of this intermediate results in cleavage of the ester bond and formation of a covalent acyl–enzyme complex. In the second stage (deacylation), a water molecule, activated by H237, attacks the acyl carbon, yielding another tetrahedral intermediate. The subsequent collapse of this intermediate regenerates S160 and releases the hydrolysis products, MHET.

FAST-PETase therefore catalyzes PET hydrolysis through a two-step serine hydrolase mechanism, with the S160–H237–D206 triad orchestrating proton transfers and nucleophilic attacks. The engineered mutations, most notably N233K, along with other substitutions, reshape the hydrogen-bond network and the orientation of residues within the active site, stabilizing transition states and facilitating formation

of the acyl–enzyme intermediate. Although the acylation step remains rate-limiting, the computed activation barrier is reduced to approximately 12.1 kcal mol^{-1}, compared to 16.5 kcal mol^{-1} for the wild-type PETase [11], consistent with the experimentally observed enhancement in catalytic efficiency.

These mechanistic insights, derived from multiscale simulations and supported by structural analyses, provide a robust foundation for the rational design of PETase variants with improved catalytic activity and thermal stability, contributing to the development of sustainable PET depolymerization strategies within a circular economy framework.

3.1.2 Non-Phenolic Aromatic Substrate Oxidation by the T1 Copper Site of *Trametes versicolor* Laccase

In the second study analyzed, the focus was on the oxidation of PAHs [7] by the fungal laccase from *Trametes versicolor* (TvL) [13], with a specific emphasis on the activation of the sp^2 C–H bond, one of the most critical and least understood catalytic steps. While the oxidation mechanism for phenolic substrates is well-documented, the activation of non-phenolic substrates such as PAHs remains poorly characterized. Among these, anthracene (ANT) and benzo[a]pyrene (BaP) (see Figure 3.5) serve as two model molecules of particular interest due to their environmental relevance and differing reactivity: ANT can be oxidized even in the absence of mediators, whereas BaP requires mediators to initiate oxidation, despite having a lower ionization potential and redox potential compared to ANT.

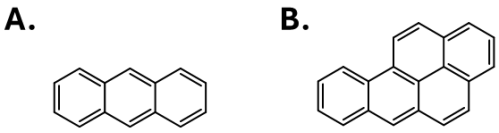

Figure 3.5: Chemical structures of A. anthracene and B. benzo[a]pyrene. Both molecules belong to the class of PAHs, characterized by the presence of multiple fused benzene rings.

The study adopted a multiscale computational approach consisting of two phases: in the first phase, molecular docking simulations were performed to explore the interaction of the two substrates with the catalytic pocket containing the T1 copper site. Results showed that both substrates can bind to the active site with comparable affinity (see Table 3.2), although BaP exhibited a slightly higher affinity. The crystallographic structure used as a reference for Trametes versicolor laccase corresponds to PDB code 1KYA, which has been extensively characterized both functionally and structurally.

Substrate	T1 distance (Å)	π-π	Docking scores (kcal/mol)	Best pose Docking (kcal/mol)
ANT	6.78	H458 - F265	0.81	**-3,61**
BaP	7.20	H458	0.74	**-4,07**

Table 3.2: Types of docking interactions with the crystallographic structure 1KYA of Trametes versicolor laccase (TvL) for A. anthracene and B. benzo[a]pyrene. The table reports the main detected interactions, such as π–π stacking.

In the second phase, DFT calculations were performed on cluster models of increasing complexity to investigate various mechanistic pathways for the initial one-electron oxidation ($1e^-$), a key step in the catalysis. The only thermodynamically accessible pathway identified involved a water molecule acting as a nucleophile toward the oxidized aromatic carbon of the substrate, facilitating the formation of the C–OH species. The role of water was further confirmed by molecular dynamics simulations, which highlighted a persistent presence of water molecules in the catalytic pocket near the T1 copper site. Subsequently, kinetic analysis was refined by extending the DFT model and calculating the full energy profiles for the two-electron oxidation ($2e^-$) of both substrates [2]. The oxidation of ANT and BaP by TvL follows a copper-dependent electron/proton transfer mechanism at the T1 Cu site, involving two sequential one-electron oxidations mediated by water molecules and D206 (Figure 3.6). The process can be summarized as follows:

— First one-electron oxidation: The substrate binds near T1 Cu, with D206 and water molecules forming a hydrogen-bonded network (W1–W5). Electron transfer from the substrate to T1 Cu occurs, while W4 nucleophilically attacks the substrate carbon, assisted by proton shuttling via W3 to D206. This generates a tetrahedral radical intermediate (Int–Cu(I)) with the central carbon adopting sp^3 hybridization and a partially oxidized substrate.

— Second one-electron oxidation: T1 Cu is re-oxidized, and D206 is deprotonated. Electron transfer from the substrate occurs again, coupled with proton transfer via W5 to D206, forming a hydroxy-substituted substrate product. The Cu center returns to its initial oxidation state (Cu(II)), completing the catalytic cycle.

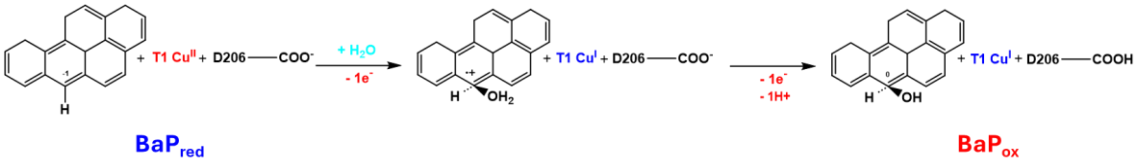

Figure 3.6: Proposed mechanism of ANT and BaP oxidation catalyzed by TvL. The enzyme uses the T1 Cu site and a structured water network to drive one-electron oxidations, leading to substrate radical formation and subsequent hydroxylation.

The results revealed that, in the absence of mediators, both ANT and BaP oxidation exhibit high activation barriers (~30 kcal mol^{-1}), with ANT slightly more favorable, reflecting experimental observations of minimal BaP oxidation without mediators. These findings emphasize the crucial role of water molecules as implicit catalytic cofactors in the T1-mediated oxidation process and provide a mechanistic explanation for the differential reactivity of ANT and BaP. Overall, this analysis lays a theoretical foundation for investigating the role of redox mediators and for guiding future research on enzymatic oxidation of diverse aromatic substrates, including environmental contaminants and plastic-derived compounds.

3.1.3 Laccase-Catalyzed LDPE Oxidation: Interplay of Binding and Redox Effects

In the third study examined, the oxidative activity of three different laccases against LDPE [8] was investigated to understand the structural and redox determinants underlying their catalytic efficiency (Figure 3.7).

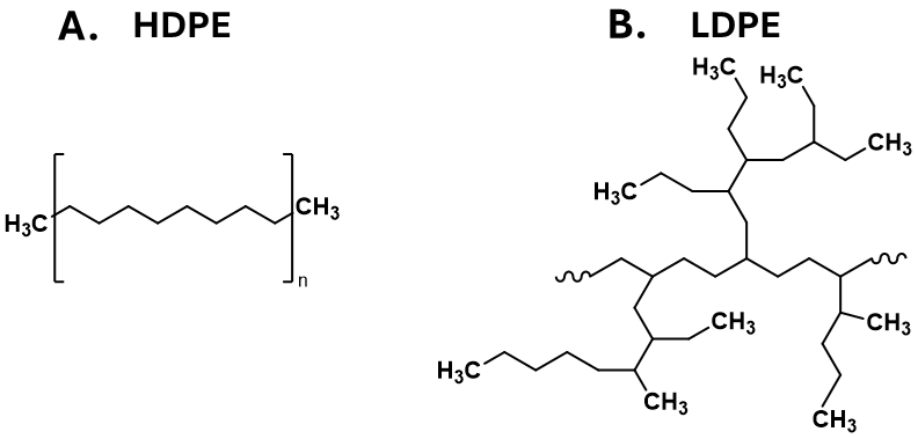

Figure 3.7: Chemical structures of fragments of high-density polyethylene (HDPE) and low-density polyethylene (LDPE). A. HDPE exhibits a linear and ordered structure that promotes the tight packing of polymer chains. In contrast, B. LDPE is characterized by a highly branched and disordered structure, which reduces its density and crystallinity.

The focus was placed on two key aspects: the redox potential of the enzyme and its mode of interaction with the polymeric substrate. Specifically, three enzymatic systems were compared: the high redox potential fungal laccase from *Trametes versicolor* (TvL, PDB ID: 1KYA [13]), The low redox potential bacterial laccase from *Bacillus subtilis* (BsL, PDB ID: 3ZDW [14]) and LMCO2 from *Rhodococcus opacus R7*, recombinantly expressed in *Rhodococcus erythropolis* [15] (see Figure 3.8), which was modeled using AlphaFold2 due to the absence of a crystallographic structure.

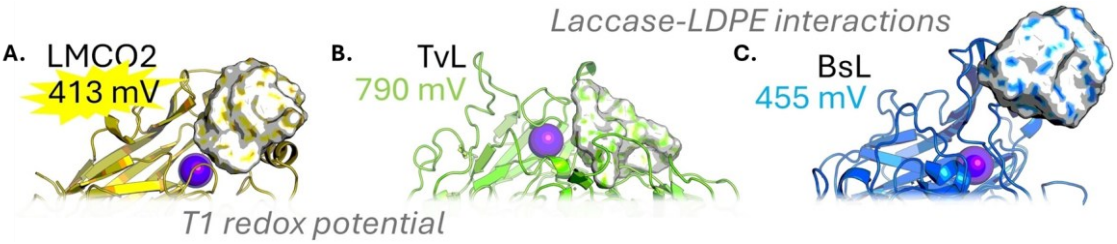

Figure 3.8: Representation of the T1 copper site for A. LMCO2, B. TvL, and C. BsL laccases, with their respective redox potential values. The bacterial laccases (LMCO2 and BsL) exhibit typical redox potentials around 400 mV, whereas the fungal enzyme TvL shows a significantly higher redox potential, consistent with its greater oxidative capacity.

Following the production and purification of LMCO2 [15], computational studies were conducted to evaluate the stability of the enzyme–LDPE complex by simulating interactions between the protein surfaces and an extended polymer model. The results highlighted the crucial role of hydrophobic interactions, particularly near the T1 catalytic site. LMCO2 features a methionine-rich loop (Met-loop) surrounding the T1 copper center, which is likely involved in forming a stable complex with the LDPE substrate. This structural element, absent in the other two laccases, appears to be a distinctive feature that promotes substrate proximity and potentially facilitates electron transfer even under thermodynamically challenging conditions.

Three-dimensional structural models comparing the regions adjacent to the T1 site reveal significant conformational and compositional differences among the laccases: while TvL and BsL exhibit short loops lacking methionine residues at this region, LMCO2 possesses a flexible and hydrophobic segment that may act as an anchoring platform for polymer chains. From a redox perspective, LMCO2 exhibits an oxidation potential of approximately 413 mV, consistent with other bacterial laccases but lower than the fungal TvL enzyme, which has a significantly higher potential. This suggests that for LMCO2, the physical interaction with the substrate plays a more prominent role in catalysis, compensating for its lower oxidative power.

Overall, this study proposes an integrated approach combining heterologous expression, computational modeling, and comparative structural analysis, providing novel insights for the rational design of engineered laccases for environmental applications. Specifically, the identification of the Met-loop as a functional element offers a valuable target for future site-directed mutagenesis campaigns aimed at enhancing enzyme–polymer binding efficiency. These findings strengthen the potential of bacterial laccases as promising biocatalysts for degrading recalcitrant plastics such as LDPE, broadening the prospects of biocatalysis in sustainable plastic waste management. Therefore, it can be concluded that polyethylene oxidation depends not only on the enzyme's redox potential but also significantly on the mode of substrate binding.

Beyond these specific observations, our approach represents a versatile computational strategy applicable to comparative studies of other polymer-oxidizing laccases. Given the experimental challenges in elucidating molecular details of enzyme–polymer interactions, simulations serve as a valuable tool, as previously demonstrated in other enzymatic systems like lytic polysaccharide monooxygenases.

Finally, this work constitutes a pioneering contribution to the use of more realistic LDPE models to investigate enzymatic oxidation processes while maintaining manageable computational costs. The results also underscore how static methods, such as molecular docking alone, are often insufficient and sometimes misleading in identifying key determinants of enzyme–polymer interactions. Employing a model encompassing a significant portion of the protein surrounding the active site enabled the identification of critical binding residues, recognition of acidic residues potentially involved in proton transfer, and verification of water accessibility within the T1 pocket (see Figure 3.9), which may act as a nucleophile in the oxidative mechanism.

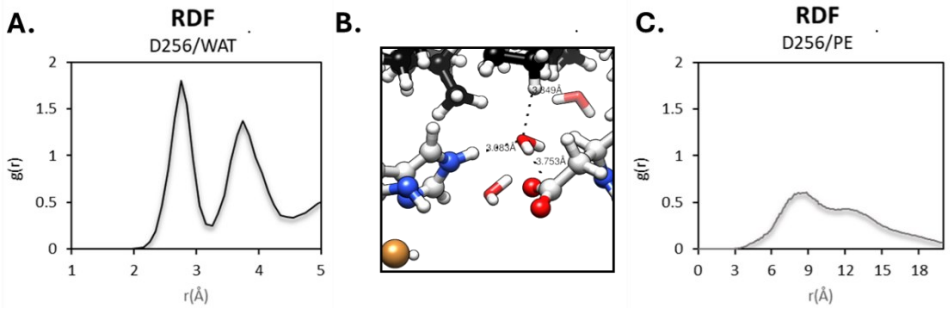

Figure 3.9: A. Radial distribution function (RDF) between residue D256 (proton donor) and water molecules. The peak within the first hydration shell highlights the presence of numerous water molecules close to the residue. B. Graphical representation of the LMCO2 enzyme conformational cluster, showing selected water molecules and their respective

distances from both the proton donor (D256) and the polyethylene fragment. C. RDF between the proton donor and polyethylene, with a peak at approximately 6 Å, supporting the hypothesis that water molecules act as intermediates in proton transfer during the reaction.

Hypothesized Mechanistic Role of Substrate Binding in LDPE Oxidation

The catalytic mechanism of laccases has been comprehensively characterized through a combination of spectroscopic and computational investigations conducted by Solomon and collaborators. Laccases catalyze a four-electron reduction process. Beginning from the fully oxidized resting state, the rate-determining step consists of substrate binding at the T1 copper site followed by its single-electron oxidation. In the case of phenolic substrates, this oxidation occurs via a concerted electron–proton transfer, thereby avoiding the formation of high-energy charged intermediates that would result from separate electron or proton transfers. The subsequent intramolecular electron transfer from the T1 copper to the T2/T3 trinuclear cluster proceeds rapidly through the highly conserved His–Cys–His bridge. Once fully reduced, the enzyme binds molecular oxygen, forming a peroxy intermediate that undergoes O–O bond cleavage and ultimately yields water molecules.

Based on the insights gained from PAH oxidation by TvL [2] and the observed structural features of LMCO2–PE complexes, a tentative mechanism for the oxidation of polyethylene (PE) by laccases can be proposed, integrating the redox and binding effects identified in the previous simulations. The mechanistic scenario considers C–H bond activation as a key step, analogous to the previously discussed PAH case (Figure 3.6), although important differences arise due to the aliphatic nature of PE (Figure 3.10).

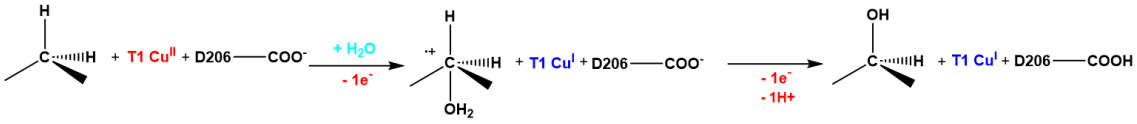

Figure 3.10: Proposed oxidation mechanism of aliphatic substrates by LMCO2, derived from the model established for PAH, involving T1 Cu-mediated electron–proton transfer and substrate radical formation.

— Substrate positioning and water mediation: The polymer is anchored by the Met-loop, maintaining proximity to acidic residues surrounding the T1 copper site (e.g., D213/256 and E504). Radial distribution function (RDF) analysis of water molecules indicates the presence of persistent water in the region between PE and T1 Cu^{2+}, suggesting a potential role of water in mediating proton transfer and substrate oxidation.

— Proton/Electron Transfer (PCET) hypothesis: In analogy with the mechanism proposed for PAHs, the close positioning of PE to T1 Cu^{2+} and acidic residues could facilitate a PCET. Water molecules may act as mediators, bridging the proton transfer from PE to the acidic residues (e.g., D213), while electrons are transferred to the T1 center.

— C–H bond activation and radical formation: The initial oxidative step would generate a radical center on the aliphatic carbon of PE. However, due to the inherent instability of sp^3 carbon radicals, QM/MM calculations using the string method indicated a high energy barrier (~45 kcal mol^{-1}), suggesting that direct C–H activation is kinetically unfavorable.

— Alternative oxidation pathway via pre-oxidized PE: Considering the limitations of direct C–H activation, an alternative scenario involves the oxidation of already partially oxidized PE surfaces containing alcohol (–OH) or ketone functionalities. Such groups can arise from prior exposure to molecular oxygen or mild oxidation processes, which would provide more reactive sites for laccase-mediated electron transfer, thereby lowering the energetic cost of the reaction.

— Implications for catalysis: The proximity of PE to T1 Cu^{2+}, along with interactions with acidic residues and structured water molecules, may enhance residence time and stabilize intermediates, creating conditions favorable for a slow PCET process. In contrast, in systems like *BsL* where PE is less stably bound, the presence of a mediator might be required to facilitate oxidation.

This hypothesis provides a conceptual framework for further mechanistic studies of aliphatic substrate oxidation by laccases. Future work should consider pre-oxidized PE models and extended enzyme models, including the T2 and T3 copper sites to more realistically capture the catalytic environment and potential oxidative pathways.

3.2 Second Section - In Silico Investigation of Metalloenzymes for Biodegradable Waste Valorization

This section focuses on the computational investigation of two distinct enzymes capable of degrading biodegradable waste.

The first enzyme, discussed in the second Section (IV – work in progress), is P450SPα (CYP152B1) [16], a bacterial cytochrome P450 belonging to the CYP152 subfamily. It is known for its ability to selectively hydroxylate fatty acids at the Cα position. A key feature of P450SPα is its independence from external redox partners, functioning as a peroxygenase by directly utilizing H_2O_2 in its catalytic cycle [17]. In the present study, P450SPα has been subjected to targeted engineering to enhance its catalytic activity, using P450OleTJE, a member of the same enzymatic class recognized for its efficiency in converting fatty acids into terminal alkenes, as a functional benchmark.

The second enzymatic system under investigation involves lytic polysaccharide monooxygenases (LPMOs), specifically the bacterial enzyme SmAA10 [18] (V – work in progress). SmAA10 is an oxidative enzyme that catalyzes the oxidative cleavage of β-1,4 linkages in chitin through a copper-containing active site coordinated by the histidine-brace motif. It utilizes O_2 or H_2O_2 as co-substrate [19], along with reducing agents, to degrade crystalline polymeric substrates. In this study, SmAA10 has been analyzed using molecular dynamics simulations to gain insights into enzyme-substrate interactions and key conformational dynamics, thereby providing structural data to support EPR spectroscopy simulations aimed at validating coordination and reactivity mechanisms under physiological conditions.

Ultimately, both of these families of oxidative metalloenzymes, LPMOs and cytochrome P450s (CYPs), emerge as up-and-coming tools for the integrated valorization of fishery industry waste [20]. From a computational perspective, it is essential to explore their mechanisms of action at the atomic level to optimize the conversion of complex biomass into valuable intermediates for advanced biofuel production.

3.2.1 Enhanced Fatty Acid Decarboxylation by CYP450SPα Mutants: A Dynamic Comparison with OleTJE

The CYP152 enzymatic system constitutes a distinctive subclass within the bacterial cytochrome P450 superfamily, characterized by its ability to function as a peroxygenase via the peroxide shunt, directly utilizing H_2O_2 as a co-substrate in the catalytic cycle [16,17] (Figure 3.11). This unique feature renders CYP152 enzymes self-sufficient, as they do not require external redox partners or auxiliary proton

sources for their activity. Among the main reactions catalyzed are the oxidative decarboxylation of fatty acids to produce terminal alkenes and the selective hydroxylation at the α- and β-positions, [21] processes of significant interest for biotechnological applications, such as the valorization of marine biomass and the synthesis of second-generation biofuels.

The cytochrome P450 (CYPα and OleTJE) is a heme-dependent enzyme capable of catalyzing the oxidative decarboxylation of long-chain fatty acids, producing terminal alkenes and CO_2. This reaction occurs without external redox cofactors, using H_2O_2 as the sole oxidant to generate the reactive oxygen species necessary for heme activation directly. The catalytic cycle follows the general peroxygenase mechanism and involves three main stages: heme activation, formation of the reactive oxoferryl species (Compound I), and substrate decarboxylation.

— Heme activation: H_2O_2 binds to the ferric heme center (Fe^{3+}), forming a ferric–hydroperoxo intermediate (Fe^{3+}–OOH). Heterolytic cleavage of the O–O bond generates Compound I, a highly reactive Fe^{4+}=O species coupled to a porphyrin π-cation radical. This step replaces the electron transfer chain typical of monooxygenase P450s.

— Hydrogen abstraction and decarboxylation: Compound I abstracts a hydrogen atom from the β-carbon (Cβ) of the fatty acid, producing a substrate radical and converting the enzyme to Compound II (Fe^{4+}–OH). Instead of hydroxylation, the radical is directed toward decarboxylation, leading to cleavage of the C–C bond at the carboxyl terminus, CO_2 release, and formation of the terminal alkene. The residues Y75 and H85, located near the active site, stabilize the hydrogen-bond network and facilitate proton transfer. His85 acts as a proton donor during O–O bond cleavage, steering the reaction toward decarboxylation rather than hydroxylation.

— Product release and heme regeneration: After decarboxylation, the heme iron returns to its ferric state (Fe^{3+}), ready for a new catalytic cycle. H_2O_2 generates Compound I, which abstracts a hydrogen from the substrate, producing a radical intermediate that undergoes decarboxylation to yield a terminal alkene and CO_2. Y75 and H85 assist in proton transfer and stabilization of reactive intermediates, ensuring selectivity toward decarboxylation.

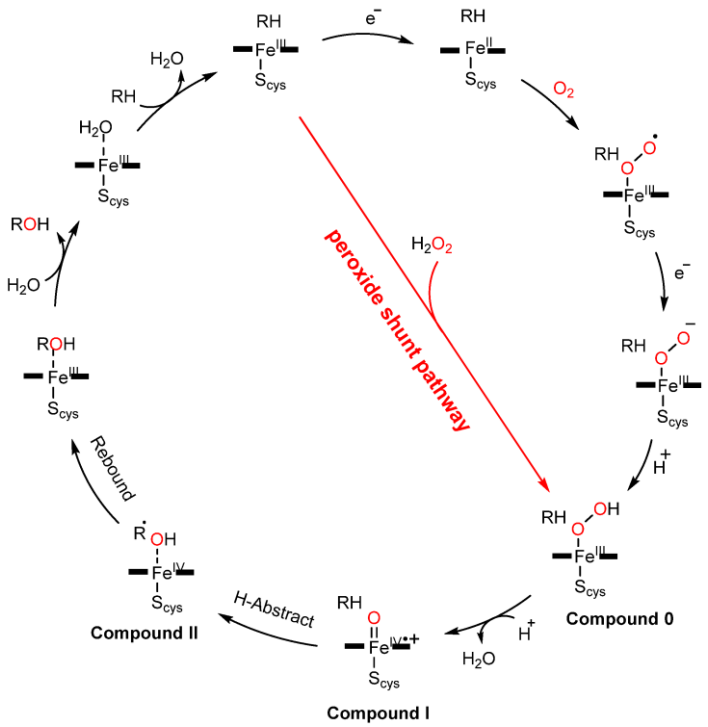

Figure 3.11: Comparison of the Catalytic Mechanisms of Cytochrome P450 (CYP152): A. The Monooxygenase pathway is dependent on molecular oxygen (O_2). B. Peroxygenase pathway via the peroxide shunt (H_2O_2) (Figure 1, Di et al., 2022)

In the present study, attention was focused on the P450SPα enzyme (CYP152B1), known for its high selectivity toward Cα-hydroxylation, to enhance its catalytic efficiency toward decarboxylation by taking inspiration from the more active P450OleTJE (CYP152L1). To this end, three mutant variants were designed (M1: G173F; M2: F288A; M12: double mutant G173F/F288A) based on the wild-type structure, and 200 ns molecular dynamics (MD) simulations were performed in triplicate for both the apo forms and the complexes with palmitic acid (C16:0) as the substrate. Simulations were carried out using GROMACS [22], following a rigorous protocol of energy minimization, heating, and constant pressure equilibration.

Trajectory analysis revealed overall high structural stability, with RMSD values below 3 Å and preservation of the hexagonal configuration of the heme group, where the Fe^{3+} ion is coordinated to residue C361 and a distal water molecule. Superimposition of crystallographic structures and access tunnel analysis using Caver Analyst 3.0 highlighted key differences between the wild-type and mutant forms, particularly in the double mutant M12, where the formation of a new tunnel and a cavity near the porphyrin ring was observed. These features resemble those found in OleTJE and suggest a potential improvement in the access pathway for the substrate and water molecules.

Analysis of enzyme–substrate dynamics revealed that the G173F mutation introduces favorable interactions with the hydrocarbon chain. In contrast, the F288A mutation reduces steric hindrance, enabling the substrate to adopt a closer and more stable position relative to the heme group. As a result, the M12 system exhibited increased substrate binding affinity and a higher frequency of water molecules in the active site region, suggesting improved oxygen availability for catalysis.

These findings thus provide valuable atomistic insights into the molecular determinants governing the catalytic activity of CYP152SPα and constitute a solid foundation for future enzyme engineering strategies aimed at optimizing effective biocatalysts for sustainable industrial processes, such as the valorization of organic waste and the production of second-generation biofuels.

3.2.2 Dynamic Insights into LPMO SmAA10 and β-Chitin Interactions

The growing need to develop sustainable alternatives to fossil fuels has driven the valorization of biomass as a renewable resource for producing biofuels and biobased chemicals. In this context, lignocellulosic and organic waste, particularly fishery by-products rich in chitin, represent promising feedstocks for bioconversion processes. Chitin, a nitrogen-containing polysaccharide with high crystallinity, exhibits significant resistance to both chemical and biological degradation, thus limiting its exploitation.

LPMOs, a class of oxidative copper-dependent metalloenzymes, have emerged as key catalysts in the oxidative cleavage of natural polymers such as chitin, enhancing the efficiency of enzymatic degradation. Among them, the bacterial LPMO SmAA10 (formerly CBP21**)** [18] has been subjected to detailed characterization through classical molecular dynamics (MD) simulations. In this study, 200 ns MD simulations at 302 K were performed on the SmAA10–β–chitin complex, employing a fully atomistic model of the substrate. The computational protocol ensured structural stability and preserved the initial conformational features of the system by applying positional restraints to the chitin monomers.

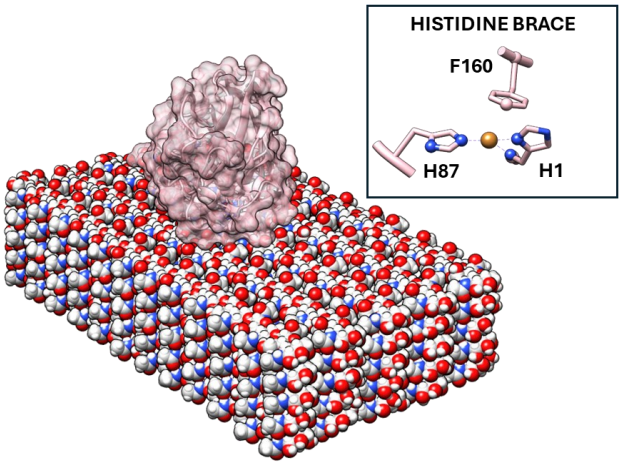

Figure 3.12: Molecular representation of the complex between the LPMO enzyme SmAA10 (in pink, surface representation) and a crystalline model of β-chitin. The top-right inset shows the enzyme's active site, highlighting the copper center (orange) coordinated by the histidine brace motif, which is responsible for the oxidative catalysis.

The analysis of the MD data revealed overall stability of the complex, with RMSD values below 2 Å and limited local fluctuations. The coordination of Cu^{2+} at the active site was maintained throughout the simulation, with a consistent presence of structured water molecules in the immediate hydration shells, a crucial feature for both the catalytic mechanism and electron transfer. Non-covalent interactions between the enzyme and the substrate were characterized by persistent hydrogen bonds and a significant π–π interaction between the tyrosine residue Y27 and a chitin monomer, suggesting a functional role of this residue in stabilizing the complex. Principal component analysis (PCA) revealed dominant collective motions within the complex, including a dynamic "capping" rocking movement that allows the enzyme to conformationally adapt to the polysaccharide surface, thereby enhancing binding affinity and stability. Additional translational and oscillatory movements were associated with the structural plasticity required for specific substrate recognition and catalysis.

The oxidative cleavage of β-chitin by SmAA10 follows a classical copper-dependent monooxygenase mechanism, in which the active site copper ion orchestrates the activation of H_2O_2 or O_2 and subsequent substrate oxidation [19]. The reaction proceeds through three main stages: copper activation, hydrogen atom abstraction from the chitin chain, and oxidative cleavage of the glycosidic bond. Mutations and engineered variants of SmAA10 have been shown to modulate substrate binding and enhance regioselectivity, stabilizing key intermediates during catalysis.

— Copper activation: SmAA10 binds a Cu(I) ion at the histidine brace, coordinated by the N-terminal histidine and a second conserved histidine residue. The Cu(I)

reacts with H_2O_2, the main co-substrate, generating a reactive Cu(II)-oxyl species through peroxide cleavage. Electron transfer from an external reductant (e.g., ascorbate) or a neighboring donor reduces the copper, priming it for substrate oxidation. This step replaces the typical activation of molecular oxygen in other monooxygenases, ensuring selective oxidation of the polysaccharide (Figure 3.13A).

— Hydrogen atom abstraction: The activated copper–oxygen species abstracts a hydrogen atom from the C1 or C4 carbon of the chitin glycosidic unit, generating a radical intermediate on the substrate and forming a Cu(II)-OH species. Specific residues near the binding site, including conserved aromatic residues, stabilize the substrate through stacking interactions with the sugar rings and correctly orient the glycosidic bond for oxidation (Figure 3.13A) [23].

— Oxidative cleavage and product release: The substrate radical undergoes molecular rearrangement at the cleaved glycosidic bond, resulting in the formation of oxidized chitooligosaccharide products (e.g. aldonic acids at C1). The copper ion returns to its initial oxidation state, and the enzyme is ready for another catalytic cycle. Enzyme–substrate interactions, including hydrogen bonding and stacking contacts, ensure regioselectivity and cleavage efficiency. (Figure 3.13B)

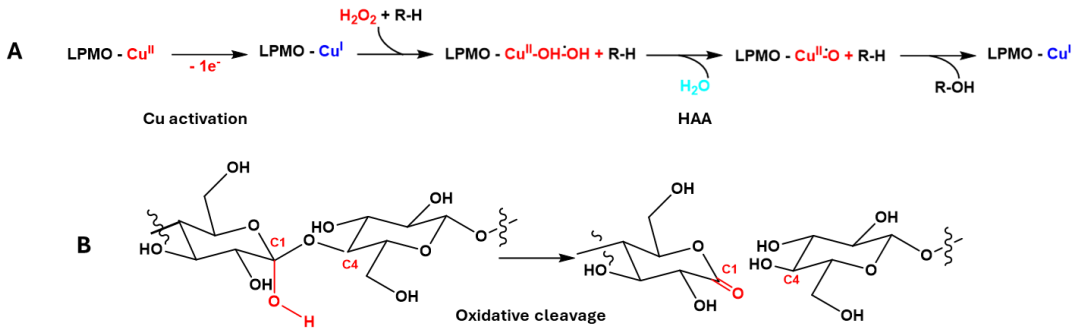

Figure 3.13: A) Proposed catalytic mechanism for β-chitin cleavage by the LPMO SmAA10. The enzyme employs a copper ion (Cu) coordinated in the active site via the histidine brace to activate hydrogen peroxide (H_2O_2), generating a highly reactive copper–oxygen species. This species performs hydrogen atom abstraction (HAA) from the substrate, initiating the formation of a radical at the glycosidic bond. The resulting radical leads to oxidative cleavage of the polysaccharide chain and the formation of oxidized chitooligosaccharides. Aromatic residues and hydrogen-bonding interactions stabilize the substrate and influence the regioselectivity of the reaction. B) Schematic representation of the glycosidic bond cleavage between the C1 and C4 positions of the monomeric unit.

These results support a dynamic and adaptive model of LPMO–chitin interaction, in which conformational flexibility and precise copper-mediated catalysis play key roles in modulating substrate accessibility, regioselectivity, and catalytic efficiency.

The structural and mechanistic insights provide a solid foundation for rational enzyme engineering strategies aimed at optimizing SmAA10 and other LPMOs for sustainable chitin valorization, biofuel production, and biotechnological applications in polysaccharide bioconversion.

References

1. Orlando, C.; Prejanò, M.; Russo, N.; Marino, T. On the Role of Temperature in the Depolymerization of PET by FAST-PETase: An Atomistic Point of View on Possible Active Site Pre-Organization and Substrate-Destabilization Effects. ChemBioChem 2023, 24, doi:10.1002/cbic.202300412.
2. Orlando, C.; Rizzo, I.C.; Arrigoni, F.; Zampolli, J.; Mangiagalli, M.; Di Gennaro, P.; Lotti, M.; De Gioia, L.; Marino, T.; Greco, C.; et al. Mechanism of Non-Phenolic Substrate Oxidation by the Fungal Laccase Type 1 Copper Site from Trametes Versicolor : The Case of Benzo[a]Pyrene and Anthracene. Dalton Transactions 2024, 53, 12152–12161, doi:10.1039/D4DT01377H.
3. Orlando, C.; Bellei, M.; Zampolli, J.; Mangiagalli, M.; Di Gennaro, P.; Lotti, M.; De Gioia, L.; Marino, T.; Di Rocco, G.; Greco, C.; et al. Comparative Analysis of Polyethylene-Degrading Laccases: Redox Properties and Enzyme-Polyethylene Interaction Mechanism. ChemSusChem 2025, 18, doi:10.1002/cssc.202402253.
4. Kawai, F.; Kawabata, T.; Oda, M. Current Knowledge on Enzymatic PET Degradation and Its Possible Application to Waste Stream Management and Other Fields. Appl Microbiol Biotechnol 2019, 103, 4253–4268, doi:10.1007/s00253-019-09717-y.
5. Yoshida, S.; Hiraga, K.; Taniguchi, I.; Oda, K. Ideonella Sakaiensis, PETase, and MHETase: From Identification of Microbial PET Degradation to Enzyme Characterization. In; 2021; pp. 187–205.
6. Mayer, A. Laccase: New Functions for an Old Enzyme. Phytochemistry 2002, 60, 551–565, doi:10.1016/S0031-9422(02)00171-1.
7. Majcherczyk, A.; Johannes, C.; Hüttermann, A. Oxidation of Polycyclic Aromatic Hydrocarbons (PAH) by Laccase of Trametes Versicolor. Enzyme Microb Technol 1998, 22, 335–341, doi:10.1016/S0141-0229(97)00199-3.
8. Gong, Z.; Jin, L.; Yu, X.; Wang, B.; Hu, S.; Ruan, H.; Sung, Y.-J.; Lee, H.-G.; Jin, F. Biodegradation of Low Density Polyethylene by the Fungus Cladosporium Sp. Recovered from a Landfill Site. Journal of Fungi 2023, 9, 605, doi:10.3390/jof9060605.
9. Lu, H.; Diaz, D.J.; Czarnecki, N.J.; Zhu, C.; Kim, W.; Shroff, R.; Acosta, D.J.; Alexander, B.R.; Cole, H.O.; Zhang, Y.; et al. Machine Learning-Aided Engineering of Hydrolases for PET Depolymerization. Nature 2022, 604, 662–667, doi:10.1038/s41586-022-04599-z.
10. Han, X.; Liu, W.; Huang, J.-W.; Ma, J.; Zheng, Y.; Ko, T.-P.; Xu, L.; Cheng, Y.-S.; Chen, C.-C.; Guo, R.-T. Structural Insight into Catalytic Mechanism of PET Hydrolase. Nat Commun 2017, 8, 2106, doi:10.1038/s41467-017-02255-z.
11. García-Meseguer, R.; Ortí, E.; Tuñón, I.; Ruiz-Pernía, J.J.; Aragó, J. Insights into the Enhancement of the Poly(Ethylene Terephthalate) Degradation by FAST-PETase from Computational Modeling. J Am Chem Soc 2023, 145, 19243–19255, doi:10.1021/jacs.3c04427.

12. Jerves, C.; Neves, R.P.P.; Ramos, M.J.; da Silva, S.; Fernandes, P.A. Reaction Mechanism of the PET Degrading Enzyme PETase Studied with DFT/MM Molecular Dynamics Simulations. ACS Catal 2021, 11, 11626–11638, doi:10.1021/acscatal.1c03700.

13. Bertrand, T.; Jolivalt, C.; Briozzo, P.; Caminade, E.; Joly, N.; Madzak, C.; Mougin, C. Crystal Structure of a Four-Copper Laccase Complexed with an Arylamine: Insights into Substrate Recognition and Correlation with Kinetics ,. Biochemistry 2002, 41, 7325–7333, doi:10.1021/bi0201318.

14. Enguita, F.J.; Marçal, D.; Martins, L.O.; Grenha, R.; Henriques, A.O.; Lindley, P.F.; Carrondo, M.A. Substrate and Dioxygen Binding to the Endospore Coat Laccase from Bacillus Subtilis. Journal of Biological Chemistry 2004, 279, 23472–23476, doi:10.1074/jbc.M314000200.

15. Zampolli, J.; Mangiagalli, M.; Vezzini, D.; Lasagni, M.; Ami, D.; Natalello, A.; Arrigoni, F.; Bertini, L.; Lotti, M.; Di Gennaro, P. Oxidative Degradation of Polyethylene by Two Novel Laccase-like Multicopper Oxidases from Rhodococcus Opacus R7. Environ Technol Innov 2023, 32, 103273, doi:10.1016/j.eti.2023.103273.

16. Fujishiro, T.; Shoji, O.; Nagano, S.; Sugimoto, H.; Shiro, Y.; Watanabe, Y. Crystal Structure of H2O2-Dependent Cytochrome P450SPα with Its Bound Fatty Acid Substrate. Journal of Biological Chemistry 2011, 286, 29941–29950, doi:10.1074/jbc.M111.245225.

17. Matsunaga, I.; Sumimoto, T.; Ueda, A.; Kusunose, E.; Ichihara, K. Fatty Acid-specific, Regiospecific, and Stereospecific Hydroxylation by Cytochrome P450 (CYP152B1) from Sphingomonas Paucimobilis : Substrate Structure Required for A-hydroxylation. Lipids 2000, 35, 365–371, doi:10.1007/s11745-000-533-y.

18. Munzone, A.; Pujol, M.; Tamhankar, A.; Joseph, C.; Mazurenko, I.; Réglier, M.; Jannuzzi, S.A. V.; Royant, A.; Sicoli, G.; DeBeer, S.; et al. Integrated Experimental and Theoretical Investigation of Copper Active Site Properties of a Lytic Polysaccharide Monooxygenase from Serratia Marcescens. Inorg Chem 2024, 63, 11063–11078, doi:10.1021/acs.inorgchem.4c00602.

19. Bissaro, B.; Streit, B.; Isaksen, I.; Eijsink, V.G.H.; Beckham, G.T.; DuBois, J.L.; Røhr, Å.K. Molecular Mechanism of the Chitinolytic Peroxygenase Reaction. Proceedings of the National Academy of Sciences 2020, 117, 1504–1513, doi:10.1073/pnas.1904889117.

20. Fairley, P. Introduction: Next Generation Biofuels. Nature 2011, 474, S2–S5, doi:10.1038/474S02a.

21. Matsunaga, I.; Yamada, A.; Lee, D.-S.; Obayashi, E.; Fujiwara, N.; Kobayashi, K.; Ogura, H.; Shiro, Y. Enzymatic Reaction of Hydrogen Peroxide-Dependent Peroxygenase Cytochrome P450s: Kinetic Deuterium Isotope Effects and Analyses by Resonance Raman Spectroscopy. Biochemistry 2002, 41, 1886–1892, doi:10.1021/bi011883p.

22. Van Der Spoel, D.; Lindahl, E.; Hess, B.; Groenhof, G.; Mark, A.E.; Berendsen, H.J.C. GROMACS: Fast, Flexible, and Free. J Comput Chem 2005, 26, 1701–1718, doi:10.1002/jcc.20291.

23. Bissaro, B.; Isaksen, I.; Vaaje-Kolstad, G.; Eijsink, V.G.H.; Røhr, Å.K. How a Lytic Polysaccharide Monooxygenase Binds Crystalline Chitin. Biochemistry 2018, 57, 1893–1906, doi:10.1021/acs.biochem.8b00138.

SECTION 1

Enzymatic Degradation of Non-Biodegradable Waste: Computational Studies

The first section of the previous chapter provided a summarized overview of the results obtained from three studies, corresponding to Papers I, II, and III. This chapter presents the full content of these works, which focus on the computational investigation of two distinct enzymatic systems involved in the degradation of non-biodegradable waste: the bacterial hydrolytic enzyme PETase (Paper I), isolated from *Ideonella sakaiensis*, and laccases (Papers II and III), oxidative metalloenzymes found in fungi, bacteria, and other organisms. The analyses are based on classical (MD) simulations to study substrate interactions and structural dynamics, while the oxidative mechanisms of s (PAHs) are explored through de (DFT) calculations using a cluster approach. These studies aim to contribute to the development of sustainable biotechnological strategies for the management and recycling of synthetic waste.

Chapter 4

Temperature Effects on PET Depolymerization by FAST-PETase: Insights into Active Site Pre-Organization and Substrate Destabilization

This chapter focuses on FAST-PETase, a recently engineered enzyme with remarkable PET-depolymerizing capabilities, and details a molecular dynamics study designed to uncover the molecular basis of its substrate recognition and activation.

FAST-PETase is an enzyme recently developed through machine learning approaches, capable of depolymerizing (PET), a synthetic resin widely used in both plastics and textile fibers. This ability makes the enzyme a particularly promising strategy for recycling PET-based materials, contributing to the reduction of plastic waste and its environmental impact.

In this study, a molecular model of PET was employed to represent the substrate, and all-atom classical molecular dynamics (MD) simulations were performed on both the apo enzyme and the substrate-bound complex at two temperatures, 30 and 50°C, to provide detailed atomistic insights into the substrate-binding step of the catalytic cycle. Comparative analysis of the data highlighted the interactions between FAST-PETase and 4PET at 50°C, corresponding to the enzyme's optimal working conditions. The simulations also revealed a pre-organization of the enzyme's active and binding sites, suggesting that FAST-PETase is structurally predisposed for PET recognition. Moreover, simulations of the FAST-PETase:4PET complex showed the formation of substrate conformations inaccessible to solvent, induced by the enzyme; these conformations were not observed in simulations of the free substrate in solution at 30, 50, or 150°C.

These findings support the hypothesis that, at 50°C, FAST-PETase is already pre-organized for PET binding and that interactions within the binding site can promote a more reactive substrate conformation, thereby enhancing the enzyme's catalytic efficiency. The study provides important atomistic insights into the mechanism of

PET recognition and activation by FAST-PETase, paving the way for future strategies aimed at enzyme optimization for plastic recycling.

In this work, biological code amino acid abbreviations (D, E, F) are used throughout the text for clarity, while chemical code abbreviations (Asp, Glu, Phe) are used in figures and tables. Both notations refer to the same residues.

4.1 Introduction

As one of the most commonly produced synthetic polymers, poly(ethylene terephthalate) (PET) has contributed significantly to global plastic consumption and environmental accumulation. While its versatility and durability have driven industrial and consumer applications, its widespread use has also generated persistent environmental pollution, which has only recently begun to be addressed systematically. Global plastic waste currently exceeds 260 million tons annually, a figure that is expected to double by 2030 [1,2]. Alarmingly, approximately 52 million tons of this waste are incinerated each year for energy recovery, whereas about 100 million tons are disposed of in landfills, predominantly in low-income regions. These communities often bear the disproportionate burden of the toxic legacy of plastic pollution, creating severe global environmental and societal challenges [3].

Once accumulated in the environment, plastics are gradually transformed into micro- and nanoplastics, particles that have multiple harmful consequences. Besides contributing significantly to greenhouse gas emissions, which exacerbate climate change [4], micro- and nanoplastics have been associated with adverse effects on human health. Acute impacts include contact dermatitis, while chronic exposure has been linked to the accumulation of microplastics in the human body [5], with potential consequences such as diabetes, obesity, infertility, and even carcinogenic effects [5,6]. PET, like many other plastic products, represents one of the most produced thermoplastic polymers for packaging [7], emphasizing the urgent need for environmentally sound approaches to depolymerize it into its constituent monomers [8,9].

Among the most promising solutions is enzymatic degradation [10–13], inspired by the mesophilic bacterium *Ideonella sakaiensis* 201-F6, recently isolated and demonstrated to efficiently degrade PET [14,15]. Extensive studies have elucidated the synergistic mechanism of two key enzymes: PET hydrolase (PETase) and mono(2-hydroxyethyl)-terephthalate hydrolase (MHETase) [16,17]. PETase initiates the depolymerization process by converting PET into MHET (mono(2-hydroxyethyl) terephthalate), which is subsequently hydrolyzed by MHETase into readily metabolizable monomers, namely terephthalic acid (TPA) and ethylene glycol (Scheme 1) [18]. Structurally, both enzymes share an α/β hydrolase fold that is

crucial for catalytic activity [19]. PETase, recognized as the most efficient protein for PET depolymerization, utilizes a catalytic triad (S160-H237-D206) to carry out its function [20], and its mesophilic origin allows it to operate under mild temperature conditions, providing an advantage for environmentally friendly recycling [21].

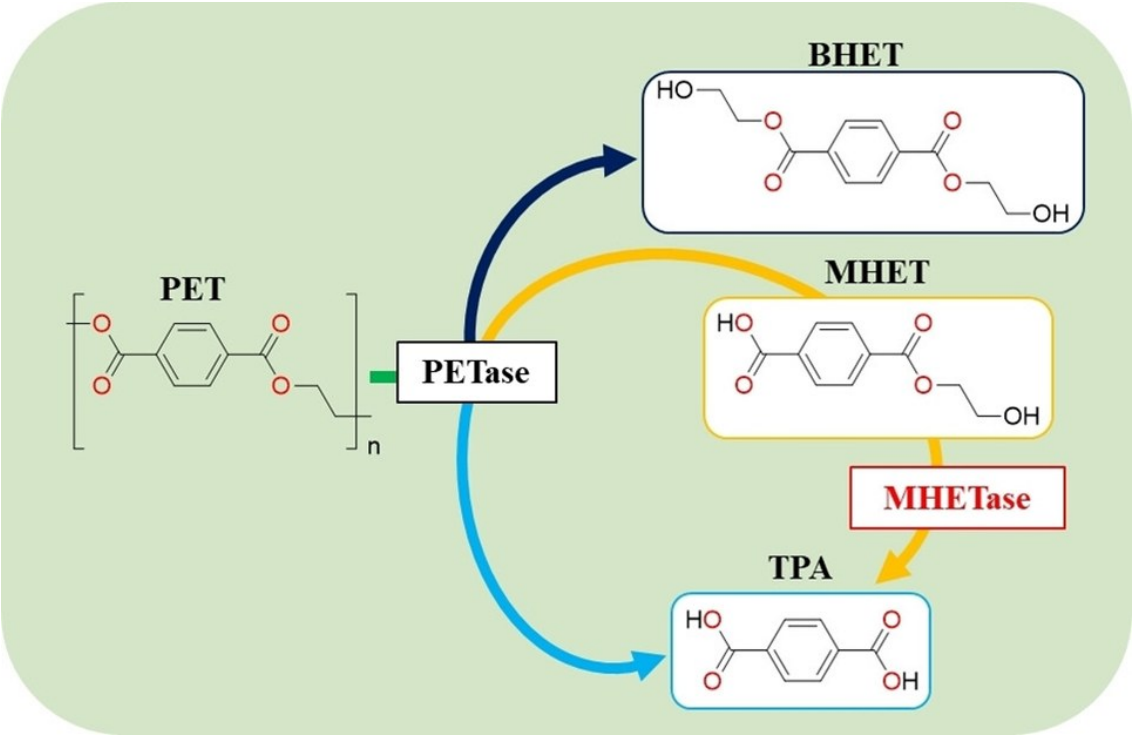

Scheme 4.1: The products of PET degradation catalyzed by PETase.

Other PET-degrading enzymes, derived from cutinases, esterases, and lipases, have been investigated [21–23], but they are typically thermophilic, requiring high temperatures (~70°C) for optimal activity. An example of such enzymes is represented by LCC, derived from the cutinase class, which is also considered a promising candidate for PET hydrolysis. It is indeed structurally very similar to PETase and has an identical catalytic triad (S165- H242-D210) [22,24]. However, these enzymes, as mentioned earlier, work at unsuitable temperatures, making them out-of range for both the in-situ degradation conditions process and for the cost. In fact, one of the goals for the PET degradation is to set working ambient temperatures (<30°C), which would lead to a considerable reduction in costs, thus making the recycling process scalable [14].

Given this, PETase seems to be the ideal candidate to degrade the plastic material but it is highly unstable at these temperatures and can easily lose its activity. For this reason, this mesophilic enzyme has been engineered to improve its stability, including single or multiple mutations to the enzyme scaffold [15,18,24–26]. The most notable obtained PETase variants are ThermoPETase [24] and DuraPETase [25], which, although an improvement of both stability and enzyme activity has been

obtained, in some states still show lower hydrolytic activity than the wild-type (wtPETase) protein at ambient temperatures (Figure 4.1) [24,25]. A recent study, using machine learning techniques based on 3D convolutional neural network (CNN), identified stable mutations for the PETase enzyme [27] and allowed for focusing on one of these variants that has improved hydrolytic activity, which was named FAST-PETase (FAST-: functional, active, stable, and tolerant; Figure 4.1).

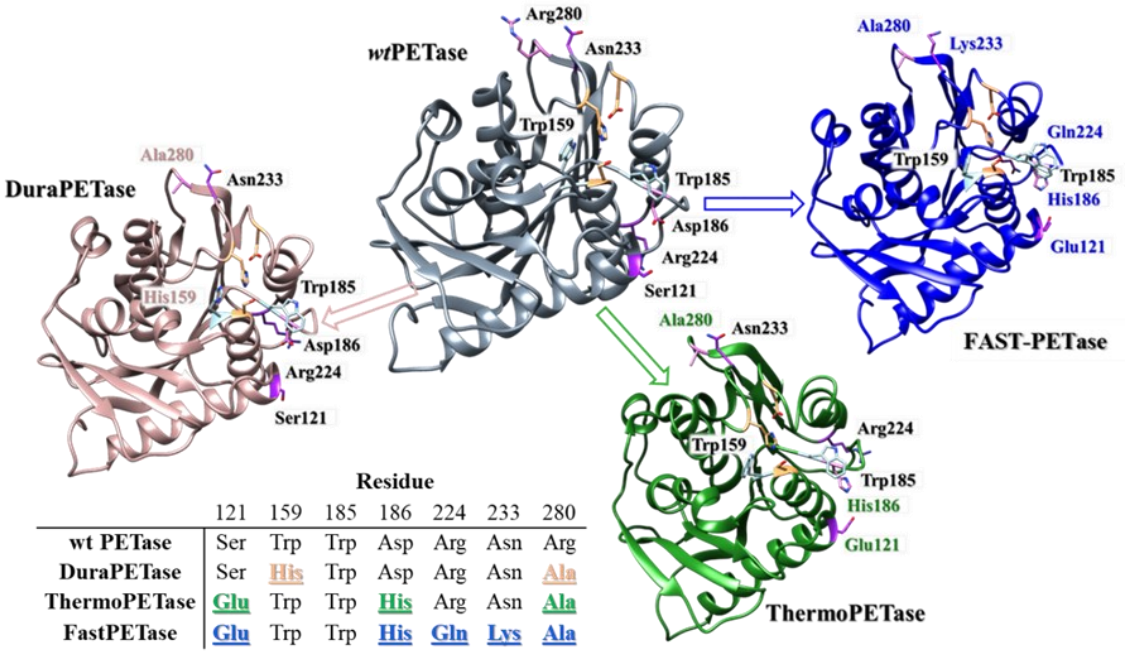

Residue

	121	159	185	186	224	233	280
wt PETase	Ser	Trp	Trp	Asp	Arg	Asn	Arg
DuraPETase	Ser	His	Trp	Asp	Arg	Asn	Ala
ThermoPETase	Glu	Trp	Trp	His	Arg	Asn	Ala
FastPETase	Glu	Trp	Trp	His	Gln	Lys	Ala

Figure 4.1: The PET hydrolase enzymes. Mutations are indicated in pink, green and blue for DuraPETase, ThermoPETase and FAST-PETase, respectively.

This enzyme, engineered on the ThermoPETase scaffold [24] incorporates five mutations compared to the wild-type (N233K, R224Q, S121E-D predicted, D186H, R280A scaffold-based; refer to the legend on page 6 for definition), and demonstrates a broader operational temperature range (30–60°C) with an optimal temperature of ~50°C. Importantly, FAST-PETase exhibits superior catalytic activity compared to wild-type and previously engineered enzymes, and can fully degrade a thermally pre-treated PET water bottle at 50°C [27].

Although FAST-PETase represents a major advancement, atomistic details of its mechanism, particularly during the initial substrate-binding steps, remain poorly understood. The concentration of numerous experimental and theoretical studies on wtPETase-induced plastic degradation in a short time span reflects the scientific community's keen interest in this crucial issue [28–31]. Previous studies on wild-type PETase have highlighted the role of structural plasticity in accommodating PET in the active site before catalysis, with productive binding strongly influenced by the

flexibility of the β1-β2 connecting loop [32]. Moreover, insights into PET trans–gauche orientation selection by the enzyme have been obtained [31], yet a complete understanding at the atomistic level is still lacking.

In this framework, we carried out a computational investigation using molecular docking and classical molecular dynamics (MD) simulations on FAST-PETase, both in its apo form and in complex with a tetramer PET substrate. Our study focuses on the enzyme's structural and dynamic properties at the lower end of its operational temperature range (30°C) and at the optimal working temperature (50°C), with femtosecond time resolution and atomistic detail. MD simulations were employed to probe the effects of temperature on enzyme-substrate and substrate-substrate interactions during the binding step, which likely underlie FAST-PETase's enhanced catalytic activity. Molecular modeling thus offers unique insights not always accessible through experimental techniques alone, providing valuable information for the industrial application and scalability of this promising biocatalyst.

4.2 Computational details

Molecular dynamics. The initial coordinates of the FAST-PETase were obtained from the X-ray structure PDB ID: 7SH6 [27]. In all the simulations, the ff99SB force field was selected to describe the protein. The studied polymer substrate was modeled considering four monomers (4PET; Scheme 2), as already found in other in silico investigations [15,29]. The substrate parameters were obtained from HF/6-31G* optimizations using the Gaussian16 D.01 package [33]. To extrapolate the parameters and unbound charges, the General Amber Force Field (GAFF) and Restrained Electrostatic Potential methods were adopted, respectively [34,35]. MDs simulations of both apo- and substrate bound forms of the protein were conducted at the 30°C (303 K) and 50°C (323 K). The FAST-PETase was placed in a 62×61×58 $Å^3$ cubic box containing water molecules as a buffer and counterions, to set the total charge to zero for each considered case. Starting from the 3D models, the systems were initially minimized and relaxed by applying harmonic positional constraints on all atoms (50 kcal $mol^{-1}Å^{-2}$) using 5000 steepest descent (SD) steps, followed by 5000 conjugate gradient (CG) steps. In the second minimization step, the entire system was unconstrained and then progressively heated to 30 and 50°C for 20 ns, using the Langevin thermostat in the NVT ensemble. To produce MDs, 300 ns trajectory were collected, keeping the systems at 1 bar pressure in the NPT ensemble and selecting the Berendsen barostat with a time constant τp=2.0 ps. In all the simulations, the SHAKE algorithm, and Particle Mesh Ewald (PME) summation method were adopted, with an integration step of 2 fs and a cutoff radius of 10.0 Å, and the water molecules were treated with the TIP3P scheme.

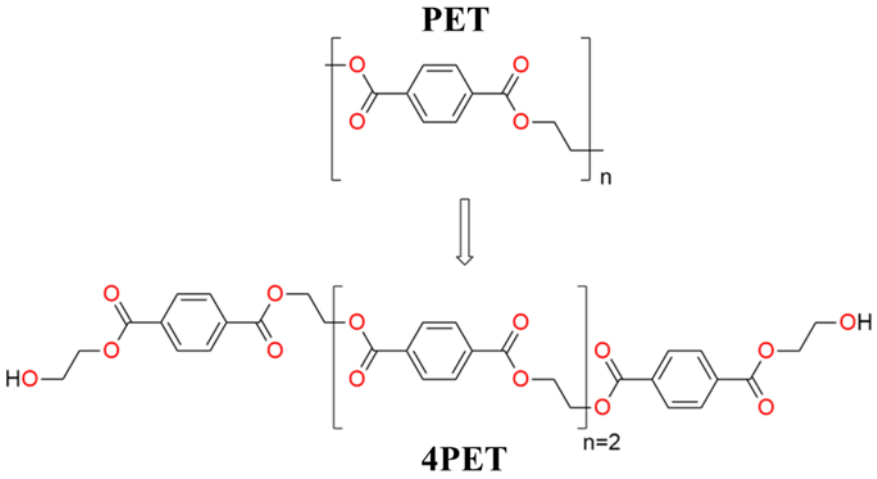

Scheme 4.2: The 4PET model adopted in this investigation.

The above-described protocol was successfully adopted in previous investigations[36–39]. The intrinsic conformational behavior of the 4PET in solution (34×30×38 $Å^3$ TIP3P water box) was further investigated, via three different MDs at 30°C (303 K), 50°C (323 K) and 150 °C (425 K). The final production, in each condition, was carried out for 150 ns. In summary, 1.2 μs for apo FAST-PETase, and its complexed form, and 0.45 μs of MDs for 4PET systems were performed. An additional 1.2 μs of MD simulations (3x100 ns replicas for the four systems) were preliminary carried out on the investigated systems, to detect any relevant conformational change.

For comparison purposes with the conformational behavior of FAST-PETase, MD simulations on wtPETase (PDB ID: 5XJH) [15] were also performed at 30°C and 50°C (3×100 ns replicas for both apo and 4PET-bound systems), to obtain 1.2 μs of MD simulations. In total, 3.65 μs MD simulations were carried out for the present investigations. All the simulations were performed adopting the Gromacs package [40].

To capture the representative conformation for each system, geometric clustering based on root mean square deviation (RMSD) was performed to identify similar structures sampled during the MD simulation, using the cpptraj module as implemented in AMBER16, choosing a cut-off of 0.7 Å. The binding free energies between the FAST-PETase and the 4PET substrate at different temperatures were calculated by solving the linearized Poisson– Boltzmann equation using the molecular mechanics-generalized Born surface area (MM-GBSA) method, implemented in the Amber16 code [41]. The igb flag value of 5, associated with a

salt concentration of 0.1 M, was used. For the calculations, 200 frames of each MD trajectory over the last 100 ns were analyzed.

Molecular docking. To investigate possible binding modes and substrate interactions in the vicinity of the catalytic triad of the FAST-PETase protein (S160, H237, D206), molecular docking simulations were performed using AutoDock version 4.2 [42]. Each representative structure was prepared by assigning atom types and adding Gasteiger charges to the FAST-PETase protein and 4PET substrate. The docking area was established using AutoGrid. A size of 46×46×46 $Å^3$ was chosen and the grid was centered on the C_α of S160. The Lamarckian genetic algorithm (LGA) was used for the conformational search of the ligand. The docking calculations were performed on the X-ray structure of the protein, with a population size of 150, random initial position and conformation, local search rate of 0.6 and 2,500,000 energy evaluations. The final docked poses were grouped using an RMSD tolerance of 2 Å.

4.3 MD simulations of FAST-PETase apoform revealed preorganization of the active site

As largely reported, molecular docking and molecular dynamics simulations can play an important role also for corroborating conclusions validated by means of experimental assays [17,43,44]. In the present study, we performed 300 ns of MD simulation on apoform FAST-PETase at 30 and 50°C, starting from the crystallographic structure of the enzyme. During the simulation, an equilibrated trend of RMSD has been observed for both temperatures. The analysis of representative geometries arising from the hierarchical clustering procedure indicated that conformational homogeneity was kept by the system with respect to the X-ray structure in both cases (Figure 4.2).

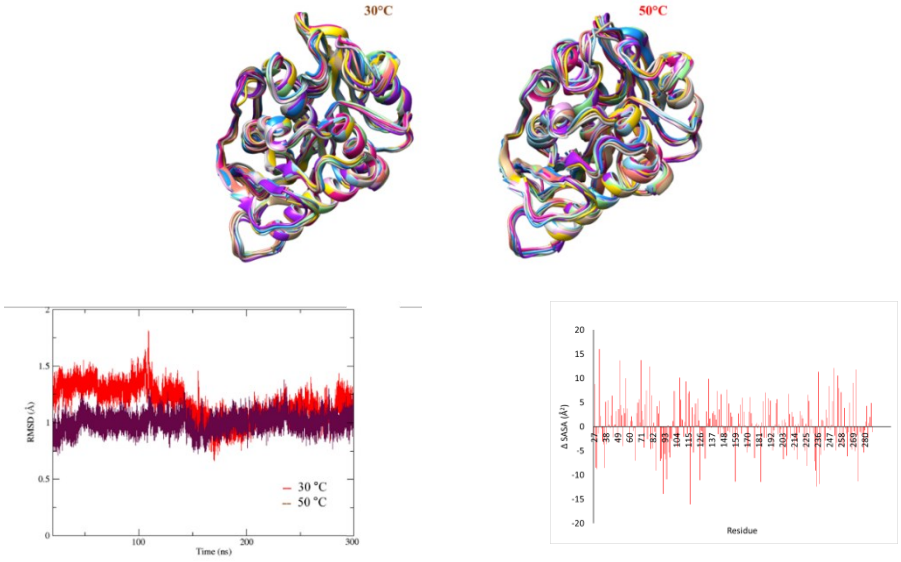

Figure 4.2: On the top, superposition of geometries obtained from the hierarchical clustering and root mean square deviation values calculated for backbone atoms, on the bottom-left, of apo-form FAST-PETase trajectory, carried out at 30 °C and 50 °C. On the bottom-right the variation of per-residue SASA (Δ SASA= $SASA_{FAST\text{-}PETase\ 30\ °C}$ -$SASA_{FAST\text{-}PETase\ 50\ °C}$).

However, some differences, in terms of conformational behavior, were observed for FAST-PETase at the selected temperatures. In particular, the analysis of RMSD calculated for backbone atoms of the protein highlighted a slight shifted trend in the case of 50°C with respect to 30°C, with values oscillating in proximity of 1.2 and 1 Å (Figure 4.2), respectively. The RMSD trend calculated for the wtPETase enzyme revealed instead values centered to about 2 Å, at 30 and 50°C, which can be linked to the higher stability of the mutated enzyme [27]. The obtained RMSD trend for the wtPETase is further in agreement with the recently published results on the R103G/S131A mutated enzyme, observed in 500 ns of MD simulation [32]. Despite the visual inspection of MDs trajectories did not highlight any relevant variation of FAST-PETase secondary structures, the analysis of root mean square fluctuation plot (RMSF; Figure 4.3A) revealed some differences. The protein at 30°C showed a major fluctuation in proximity of loop E204- P210, caused by a major re-orientation of D206 and, consequently of the loop itself. This solvent-exposed residue of the catalytic triad (S160-H237-D206) tended to re-orient its carboxylate group during the simulation, due to hydrogen bond interactions with water molecules, and some variations of the distances involving the catalytic residues. Such conformational re-organization was indeed observed in the principal component analysis (PCA) of FASTPETase at 30°C (Figure 4.3B), which highlighted how the loop E204-P210 is the main shifting region of FAST-PETase. It is interesting to point out that from the comparison between the two considered temperatures, several higher peaks were observed for the MDs of apoform protein at 50°C. In first instance, slightly higher

values were registered for the amino acids of the catalytic triad, due to water-bridged hydrogen bonds with surrounding W159 and W185 amino acids. More interestingly, the regions involved in major fluctuations correspond to the antiparallel β-sheet of V52-T56 and V106- D112 and loops in the segment A65-G79. In addition, the PCA calculated at 50°C revealed movements of Q237-M262 and K233-N246 α-helices, with latter peptide sequence corresponding to one of the regions where machine-learning suggested mutation occurred [27]. Such fluctuations generated a network of vicinal grooves in the protein cleft, where the substrate is supposed to bind, and the reaction takes place. The presence of these grooves, extended on the solvent-exposed side of the protein (see shaded areas in Figure 4.3C), made the FAST-PETase richer of sites to accommodate 4PET substrate and expanded the enzyme surface available for protein-substrate interactions (Figure 4.3).

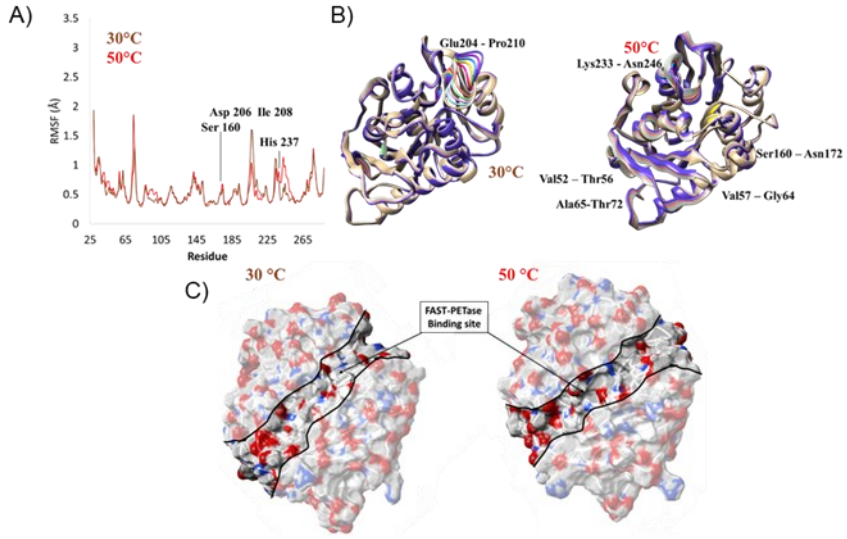

Figure 4.3: A) RMSF plot and B) PCA visualization obtained for apoform FAST-PETase molecular dynamics simulation at 30 and 50 °C. C) Surfaces of representative clustered geometries obtained for apoform FAST-PETase from molecular dynamics simulations at 30 and 50 °C. Red and blue areas are localized in the presence of O and N atoms, respectively, while gray and white indicate C and H, respectively.

A number of these pockets were thus filled by a higher number of water molecules due to the higher kinetic energy generated by the different temperatures, as further confirmed by the calculation of solvent-accessible surface area (SASA) at 30 and 50°C, reported in Figure 4.2.

A consequence of this movement might be represented by the more frequent interactions with the solvent-exposed amino acids that led to the spreader fluctuations of many of the above-mentioned regions of the protein, keeping the loop E204-P210 in similar orientation for the entire dynamics at 50°C.

The observed behavior led us to hypothesize that the higher temperature might favor the pre-organization of the active site, which at 50°C is tailored to bind and react with the substrate. This fact was further confirmed by analyzing MD trajectories of 4PET binding systems, as will be shown in the next paragraph.

4.4 FAST-PETase promotes solvent-inaccessible conformation of 4PET that can be relevant for the catalysis

In the following section, the comparative analysis of FASTPETase: 4PET binary complex at 30 and 50°C is presented. As mentioned in the Methods section, the starting protein-substrate complex was chosen from the docking pose having the best binding energy of -3.4 kcal mol^{-1} and was later subjected to MDs at 30 and 50°C. This protocol represents an alternative to that already applied in similar systems, where, to obtain multiple orientations of the substrate in the active site of both wild-type and double mutant PETases, multiple PET orientations were predicted by induced fit docking (IFD) [26,29].

Very interestingly, the FAST-PETase:4PET binary complex showed a different structural behavior as a function of the selected temperature. In accordance with the results obtained for the apoform, RMSD analysis of the protein-substrate complex evidenced a shift to higher values in the case of 50°C (~1.5 vs. ~1.0 Å for 30°C; Figure 4.4). RMSF plots indicated that the E204-P210 loop and V211-P217 portion of the adjacent helix significantly fluctuated at 50°C during the simulation (Figure 4.5).

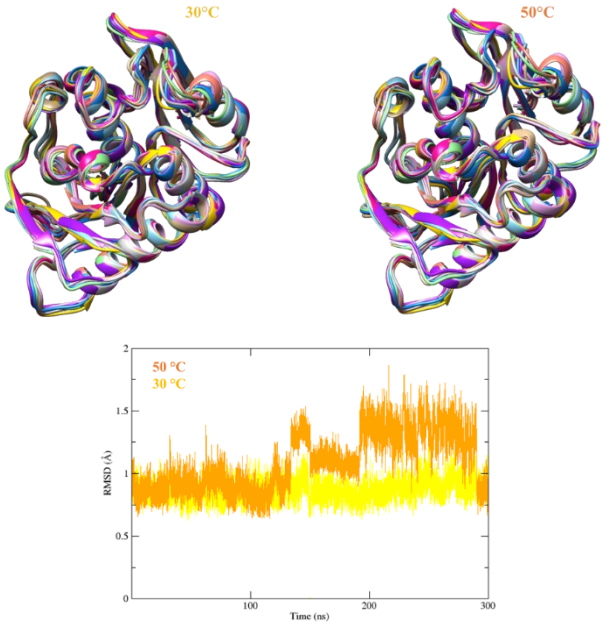

Figure 4.4: On the top, superposition of geometries obtained from the hierarchical clustering and root mean square deviation values calculated for backbone atoms, on the bottom, of FAST-PETase-4PET trajectory, carried out at 30 °C and 50 °C.

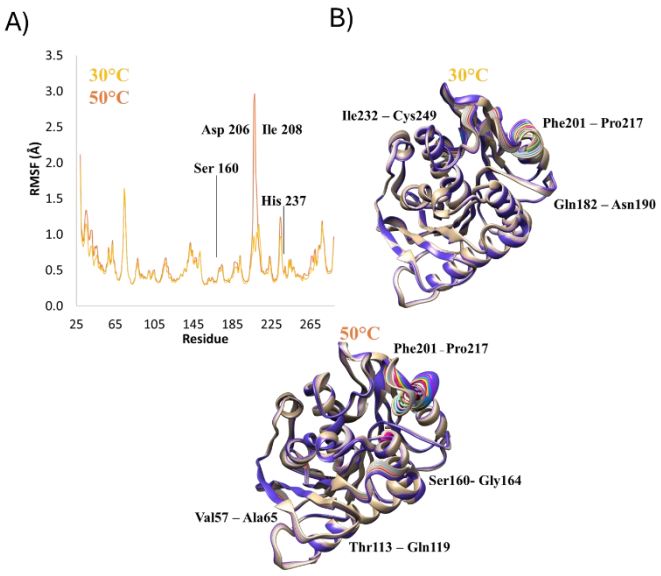

Figure 4.5: A) RMSF plot and B) PCA (top and bottom) visualization obtained for FAST-PETase:4PET molecular dynamics simulation at 30 and 50 °C.

The movement of the above-mentioned loop resembles an open–closed conformation with respect to the opposite P85- R90 loop; this gives birth to the active-site cleft, which is strictly correlated to the ability of the enzyme to accommodate the substrate and which characterizes FAST-PETase protein. Such a cleft's width was approximately 9 Å for both considered temperatures (Figure 4.6A

and B) and 0.5 Å larger than in the case of wtPETase [15] and of other cutinases that were previously compared to the wild-type enzyme [26]. This larger cavity allowed conformational rearrangement of the 4PET substrate within the protein binding site. Indeed, during the simulations, several conformations were observed for the substrate. At 30°C, the aromatic groups of 4PET tended to establish intramolecular π–π interactions in a range of 4–6 Å, characterizing a wrapped form of the substrate as observed in the radial distribution functions (RDF) calculated for centroids of the 4PET aromatic rings (Figure 4.6C). The analysis of simulation at 50°C showed, instead, a different conformational arrangement of the substrate, which passed from a wrapped form to an unwrapped one (W-shape) after 100 ns of MDs. Such behavior was further confirmed from the occurrence of longer head-to-tail distance of the substrate, which was measured considering the terminal -CH_2OH groups of the 1st and 4th monomer of the model substrate (Figure 4.6D). Indeed, using a cut-off head-to-tail distance of 15 Å, the wrapped-like conformations have been observed for 78% of the FAST-PETase:4PET simulation at 30°C, while W-shaped like ones for a total of 28%. At 50°C, the wrapped-like and the Wshaped-like conformations were differently populated, as evidenced by the estimated frequencies of 45 and 55%, respectively. The W-shaped of 4PET conformation here-presented for FAST-PETase resembled the conformations observed in previously published experimental-computational works, devoted to study of wtPETase or some of its mutations with PET models [26,28,29]. It is interesting to note that the occurrence of such conformation can be obtained only by considering an adequate number of model monomers (>2) [26,28,29]. DFT optimizations (B3LYP-D3/6-31G(d,p) for all atoms, SMD implicit solvent model, ε = 78) of 4PET conformations revealed a marked tendency of the molecule to adopt a wrapped form in solution. [45–49]

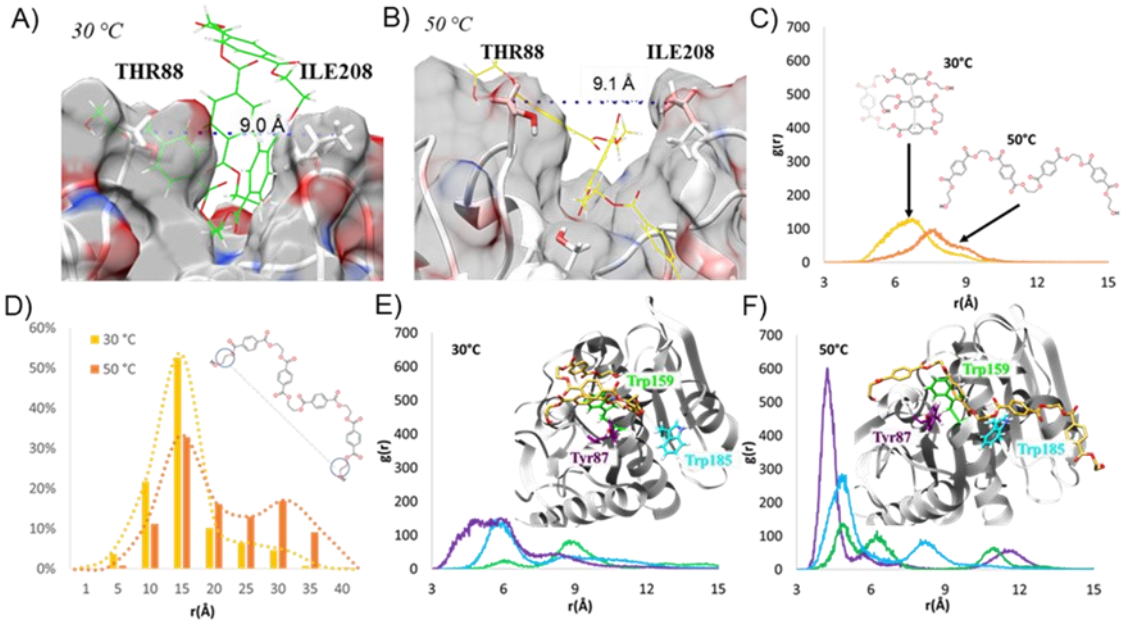

Figure 4.6: Focus on the enzymatic cleft in the presence of 4PET substrate, obtained from the representative clustered geometry of FAST-PETase-4PET simulations at A) 30 and B) 50 °C. C) RDF calculated for the center of masses of aromatic ring–ring pairs of 4PET. D) frequency of head-to-tail distance and E), F) RDFs calculated for centers of masses of aromatic ring–ring pairs of 4PET and Y87, W159 and W185 obtained for enzyme–substrate complexes at the two selected temperatures.

To evaluate the energy of W-shaped form at DFT level of theory, it was therefore necessary to keep fixed the dihedrals of the substrate ester groups. The comparison of relative energies revealed that, in such a state, the 4PET lies at 10.2 kcal mol^{-1} higher than the optimized wrapped one (Figure 4.7).

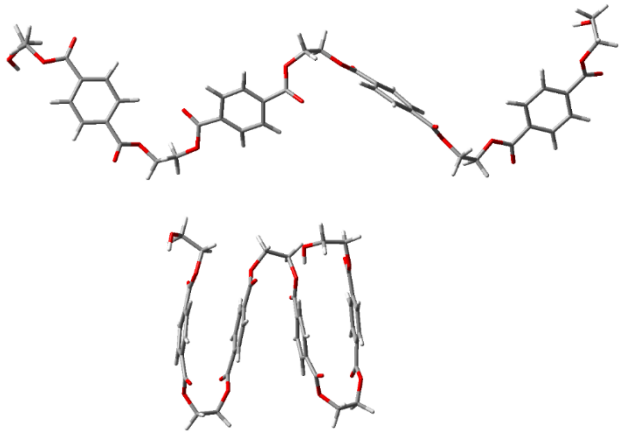

Figure 4.7: Structures of W-shaped (constrained) and the wrapped conformations. The latter has been obtained from unconstrained DFT optimization of the former.

This suggests that the enzyme can promote the occurrence of the substrate's conformation that is otherwise inaccessible, which may have an impact on the hydrolysis of the polymer, as will be highlighted in the next sections of this paragraph. In addition, all the MD simulations performed on the wtPETase:4PET system did not show such a W-shaped conformation also, either performing replicas or extending the molecular dynamics to longer simulation time, that is, 300 ns.

When lying in the more open W-shaped form, 4PET enters into contact with different solvent-exposed residues that comprise the binding site of FAST-PETase (Figure 4.6E and F). Among these, are of particular interest those implicated in the formation of stacking interactions (face to face or point-to-face) that allow the good engagement by the protein counterpart. The most frequent interaction with the Y87 has been identified from the calculation of RDFs obtained for the 4PET aromatic rings and theY87 phenol moiety, at 50°C. The peak resulting at around 4 Å can be reasonable linked to the presence of a frequent π–π stacking occurring between 4PET substrate and the amino acid.

In analogy with the Y87, less frequent π–π interactions with the W159 and W185 were identified from RDF calculations, with highest peaks obtained in proximity of 5 Å. W159, in addition, represents a key residue in proximity of the active site owing to X1 of the consensus sequence G-X1-S- X2-G [15]. Interestingly, the RDFs at 30°C highlighted a remarkably different behavior of π-π interactions occurring between the 4PET and FAST-PETase enzyme. Indeed, for all the three considered pairs, five times lower or 1 Å distance-shifted peaks resulted. These results are a direct consequence of the different conformations observed at the selected temperatures, being the W-shaped conformation at 50°C more spread on the protein surface than the wrapped form at 30°C. In addition, the resulting occurrence of π-π interactions with the aromatic amino acids, led to hypothesize that Y87, W159 and W185 support the detection from the solution, and the binding, of 4PET, before the catalytic reaction and that, furthermore, the "antenna function" can be favored by the temperature, as analogously discussed in recent review [28]. MMPBSA calculations further revealed a better binding affinity of the enzyme in the W-shaped 4PET ($\Delta\Delta E$= 15 kcal mol^{-1}; Figure 4.8) in comparison with that in spiral-shaped one, a trend that can be further related to the occurrence of a more frequent protein-substrate interactions.

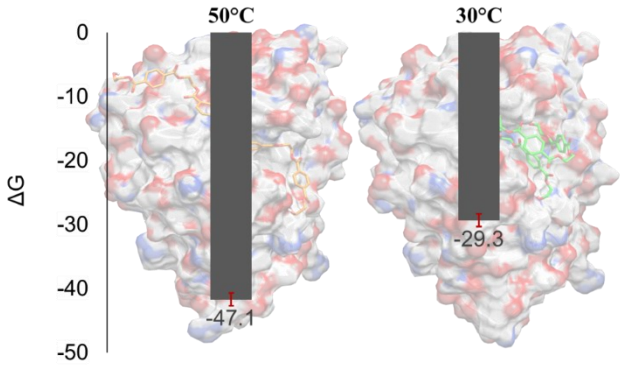

Figure 4.8: Binding affinities calculated for 4PET substrate via MM-GBSA method, at 30 °C and 50 °C.8

For the active site, the catalytic triad behavior was monitored in terms of relevant distances between amino acids, like S160-H237 and H237-D206 (Figure 4.9). It is possible to note that no remarkable differences emerged at 30 and 50°C. However, in the case of the MD simulation at 50°C, the distance of OH moiety of S160 from Nδ of H237 presented a larger span of values than the corresponding one at 30°C.

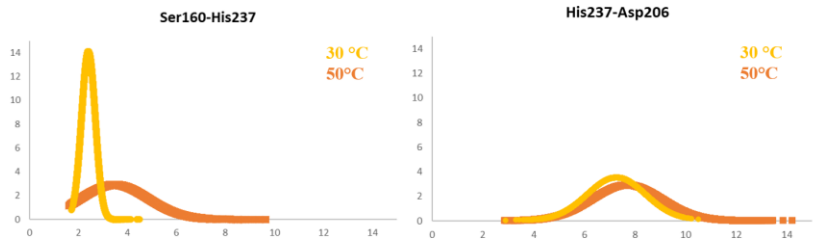

Figure 4.9: Gaussian distributions of OH_{S160}-$N\delta_{H237}$ and $N\varepsilon H_{H237}$-$OG1_{D206}$ values, obtained from FAST-PETase-4PET simulations at 30 °C and 50 °C.

The obtained distances are anyway coherent with a suitable orientation of the amino acid residues for the occurrence the catalysis since, as recently suggested, the activation of S160 borne by the H237 can be mediated by water molecules bridging the residues [9,30]. From the RDF analysis performed at both temperatures and obtained as a function of the distance between the water oxygen and the side chain of S160, it was possible to detect the different hydration shells starting from 2.5 Å that are characteristic of extensive network of H-bonds with the closer water molecules.

This behavior favors a different orientation of the aromatic amino acid, not observed at 30°C, and increases the frequency of π–π stacking with 4PET, thus highlighting a possible correlation to the more pronounced plasticity of the enzyme at 50°C (Figure 4.5B) evidenced at experimental level [27]. Upon the occurrence of this interaction, the substrate and its eight carbonyl groups that can undergo to the catalytic

mechanism in detail, resulted averagely at closer distance from the -OH group of S160 and from the -NH- group of M161 backbone. According to the proposed catalytic reaction, the former residue is the nucleophilic agent, while the latter is deputed to generate the oxyanion hole for stabilizing the transition states and intermediates, together with the cooperative action of -NH- group of Y87 [27,28]. Therefore, the OH_{S160}-C=O_{4PET} and NH_{M161}-O=C_{4PET} were measured during the simulations at 30 and 50°C, taking into account each target carbonyl group of 4PET (Figures 4.10 and 4.11).

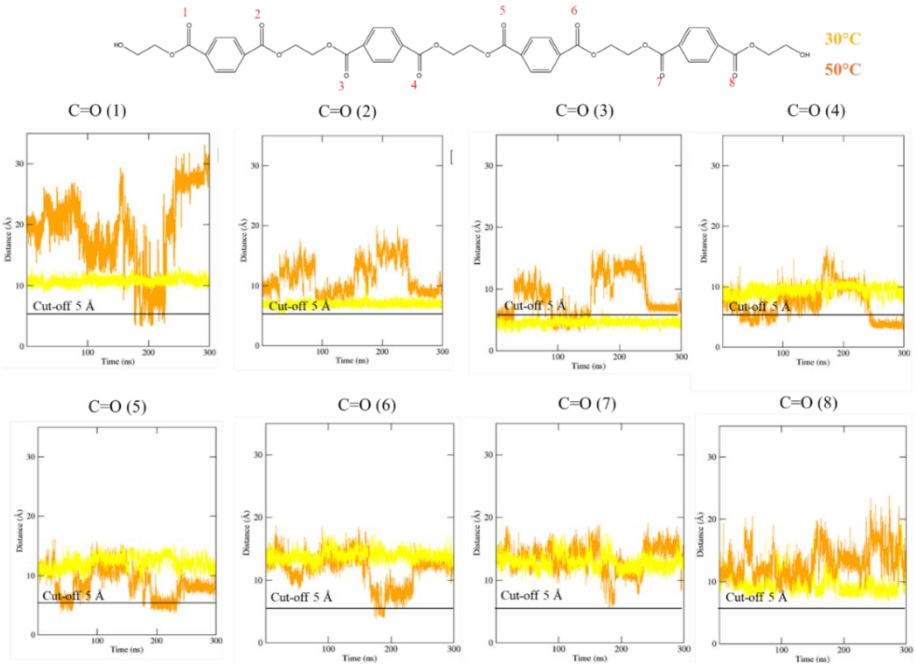

Figure 4.10: OH_{S160}-C=O_{4PET} distances obtained from FAST-PETase-4PET simulations at 30 °C and 50 °C.

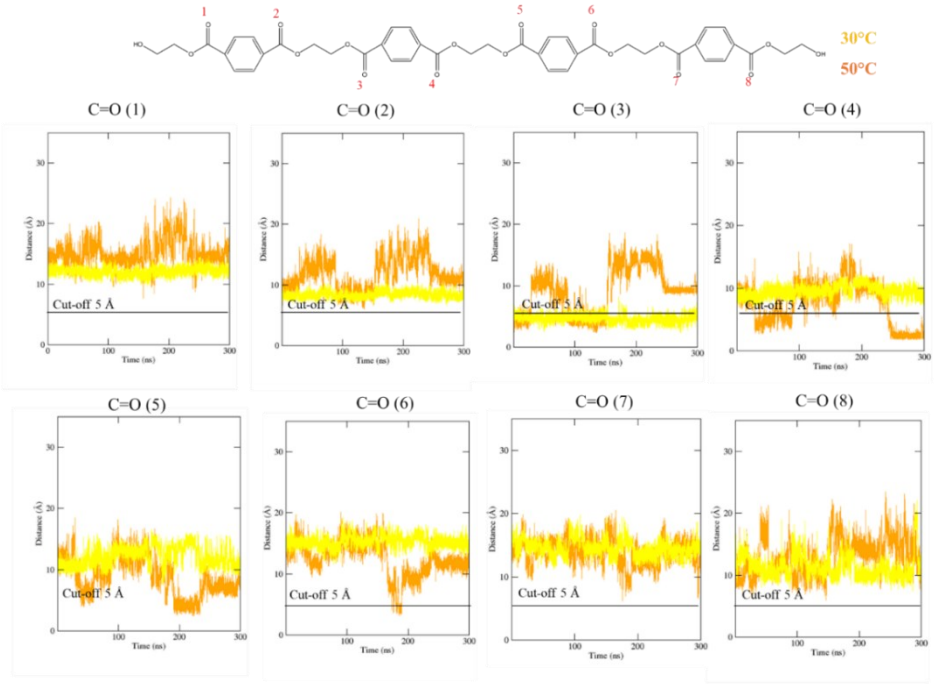

Figure 4.11: NH_{M161}-O=C_{4PET} distances obtained from FAST-PETase-4PET simulations at 30 °C and 50 °C.

A cut-off of 5 Å for both selected distances was later adopted to identify possible catalytically productive conformations of 4PET. Overall, it turned out that, at 50°C, the relative abundances of good orientations of the substrate are observed for both OH_{S160}-C=O_{4PET} and NH_{M161}-O=C_{4PET} distances for many moieties that are involved in the catalytic mechanism. More interestingly, at this temperature, the productive distances were observed for both core- and terminal monomers, examining the OH_{S160}-C=O_{4PET} distances (Figures 4.10 and 4.11), as consequence of the more extended W-shape form. Such more frequent proximity of 4PET carbonyl groups to the catalytic residues suggested that FAST-PETase enzyme, in these working conditions, can increase the chances to catch the substrate productively for the catalysis from the early step of the catalytic mechanism, where efficient stabilization of transient intermediates is required. In absence of further indications about the preference for core- or terminal-monomers of FAST-PETase, such results can be nicely considered representative of, and can thus linked with, the enhanced catalytic activity of FAST-PETase, which was experimentally observed and measured in terms of yielded TPA and MHET monomers [27]. Furthermore, the W-shaped substrate resulted in hydrogen-bond interaction with the solvent exposed guanidine group of the R90, as evidenced by the RDF obtained for the center of mass of amino acid side chain and the terminal ester group of 4PET (intense peak at 2.8 Å at 50°C, Figure 4.12A). On the contrary, the highest value at 30°C was found in proximity of 10 Å (Figure 4.12A). A salt bridge occurring between K233 and E204 was observed at

50°C as shown in Figure 4.12B. The charged side chains of the amino acids were faced at 3 Å for the 30% of molecular dynamics at 50°C, while the highest percentage of 30% was obtained in proximity of 8 Å at 30°C.

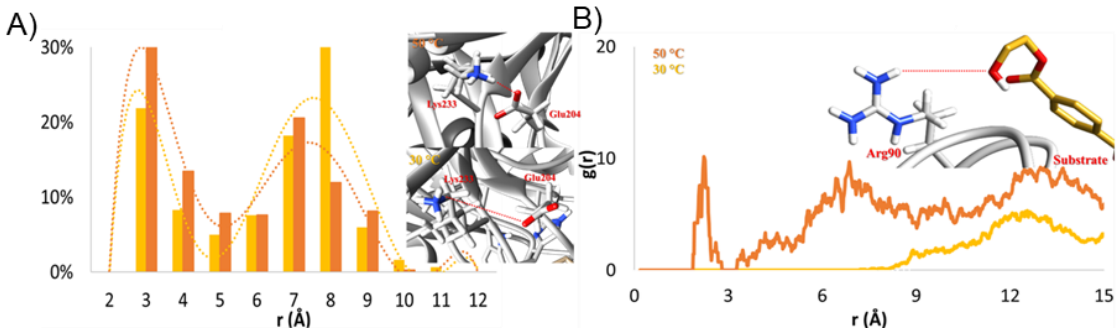

Figure 4.12: A) Frequency of distances measured for the salt-bridge between K233 and E204 residues and B) and RDF calculated for the center of mass of the guanidium side chain of R90 and terminal OH group of 4PET obtained for FAST-PETase-4PET complex at 30 (yellow) and 50 °C (orange).

The keeping of this interaction favored the W-shaped form at higher temperature, thus highlighting the effectiveness of machine-learning-based K233N mutation coupled to the selection of 50°C as working temperature. Indeed, during the MD simulations on the wtPETase. W-shaped conformation of 4PET was not observed in solution. In accordance with the above-discussed results, it was pointed out that an increasing temperature can favor FAST-PETase:4PET interactions, promoting accessibility to high-energy conformations of the substrate. To further verify this hypothesis, three different molecular dynamics simulations of 150 ns were performed on the 4PET in solution, at increasing values of temperature (30, 50 and 150°C). PET has a glass transition temperature above 70°C and for this reason it has been suggested as a more favorable reaction condition for enzymatic PET hydrolysis [50–53]. However, the choice of the temperatures higher than 50°C allowed to evaluate the thermic stress on the conformation in absence of protein surroundings to the selected substrate model.

Over the selected timeframe and under the temperature conditions, 4PET never showed a conformation resembling Wshaped form, as can be evinced by FESs calculated for PCA1 and PCA2 in Figure 4.13.

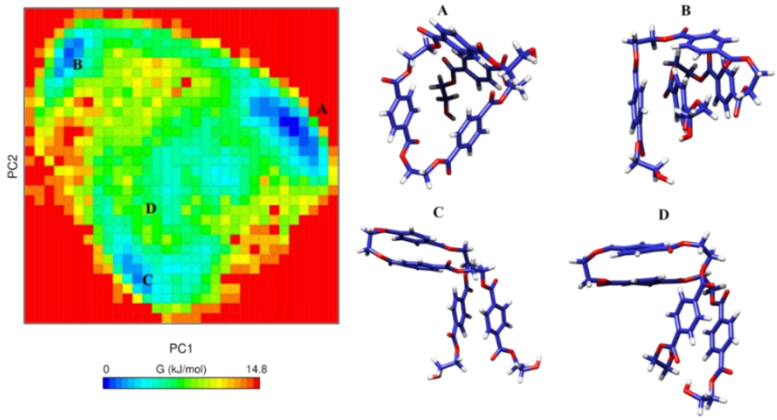

Figure 4.13: Free energy surfaces related to PCA1 and PCA2 of 4PET substrate, obtained from solvated 4PET simulations at 30 °C.

At 30 and 50°C there were three main free-energy wells/basins in the global free energy minimum region, indicating mainly three stable wrapped states characterized by π–π staking interactions (A, B, and C; Figures 4.13 and 4.14) over a range of ~4 kcal mol^{-1}.

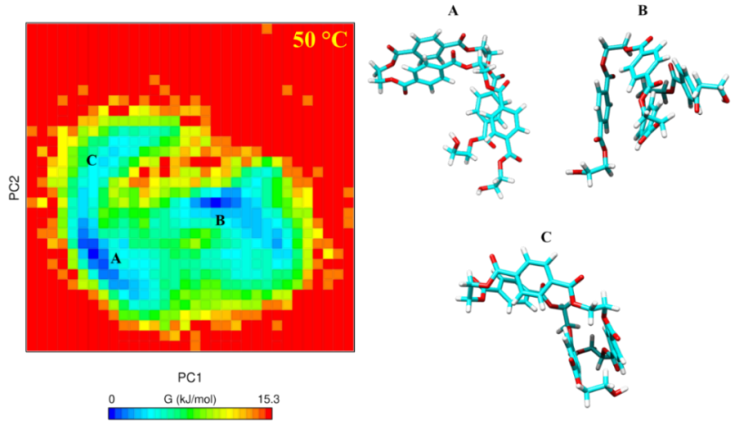

Figure 4.14: Free energy surfaces related to PCA1 and PCA2 of 4PET substrate, obtained from solvated 4PET simulations at 50 °C.

The mutual local structural organization within the 4PET was analyzed in terms of RDFs for each temperature, considering all four rings and their related distributions (Figure 4.15).

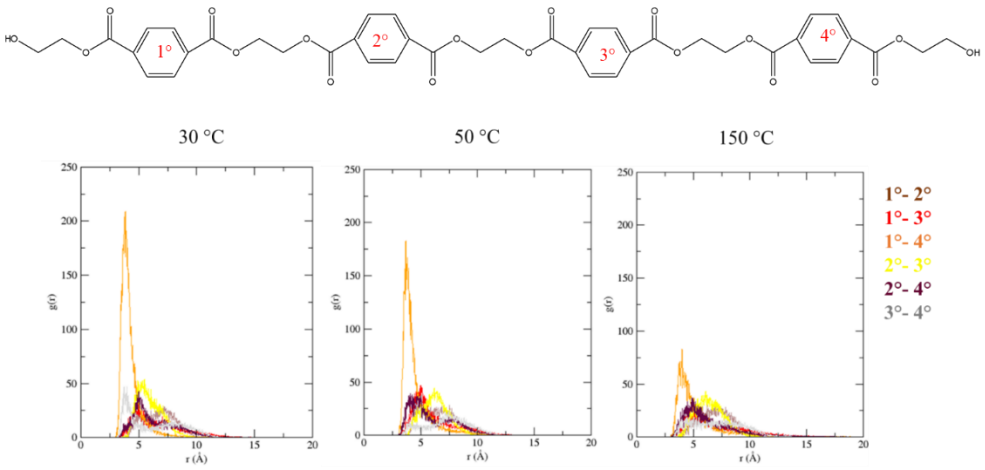

Figure 4.15: Radial distribution functions of ring-ring pairs, calculated for 4PET substrate, obtained from solvated 4PET simulations at 30 °C, 50 °C and 150 °C.

It was interesting to note that, at an increasing temperature, a decreasing height of the peaks of about 4 Å can be observed, thus emphasizing that the temperature can favor a conformational distribution shifted towards the extended conformation. However, the analysis of FES at 150°C did not still present any W-shaped form of the substrate (Figure 4.16), in analogy to those conformations observed for wtPETase and for FAST-PETase at 30°C also.

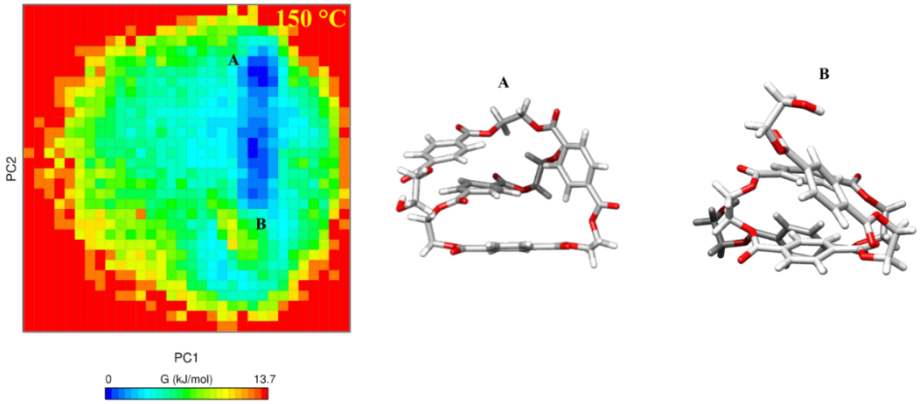

Figure 4.16: Free energy surfaces related to PCA1 and PCA2 of 4PET substrate, obtained from solvated 4PET simulations at 150 °C.

According to the simulations, the results underlined that 4PET in solution tends to assume a wrapped conformation, to favor substrate-substrate hydrophobic interactions, in agreement with the available structural information of the PET polymer [54–56]. Due to its chemical composition, PET indeed tends to establish intramolecular π-π interactions that are the main source of the polymer mechanical properties [54–56].

Despite the use of a representative model, it is worth nothing that the here-described simulations reasonably reproduced, at atomistic level, the

conformational behavior that might be representative of what occurs in PET-based material. Thus, the insights obtained from these simulations can represent indirect evidence of the role played by FAST-PETase enzyme, which, with its engineered protein architecture, owns a binding site that promote the access to more reactive conformations, which would not spontaneously occur for the polymer itself. This aspect is further in accordance with previous in silico works on other mutants of wtPETase [28].

4.5 Replicas of apoform- and 4PET FAST-PETase simulations at 30 °C and 50 °C.

The reproducibility of the conformational behavior observed for FAST-PETase, in both apo and 4PET-bounded forms, was considered and preliminarily investigated. In detail, 3x100 ns replicas of molecular dynamics were performed from input geometry obtained from the heating step of the simulation carried out to temperatures of 30 °C and 50 °C, following the same computational procedure discussed in the main text (see Computational methodologies section).

In total, at this stage, 1.2 μs of molecular dynamics were obtained. Main attention was focused on those structural parameters that were considered in the initial phase of the investigation, such as RMSD, RMSF, and analysis of the population *via a* hierarchical clustering procedure. At the equilibrium, the analysis of RMSD has highlighted a reproducible trend for all the systems, as evidenced by an overall variation of values in the range of 0.5 Å (see Figure 4.17).

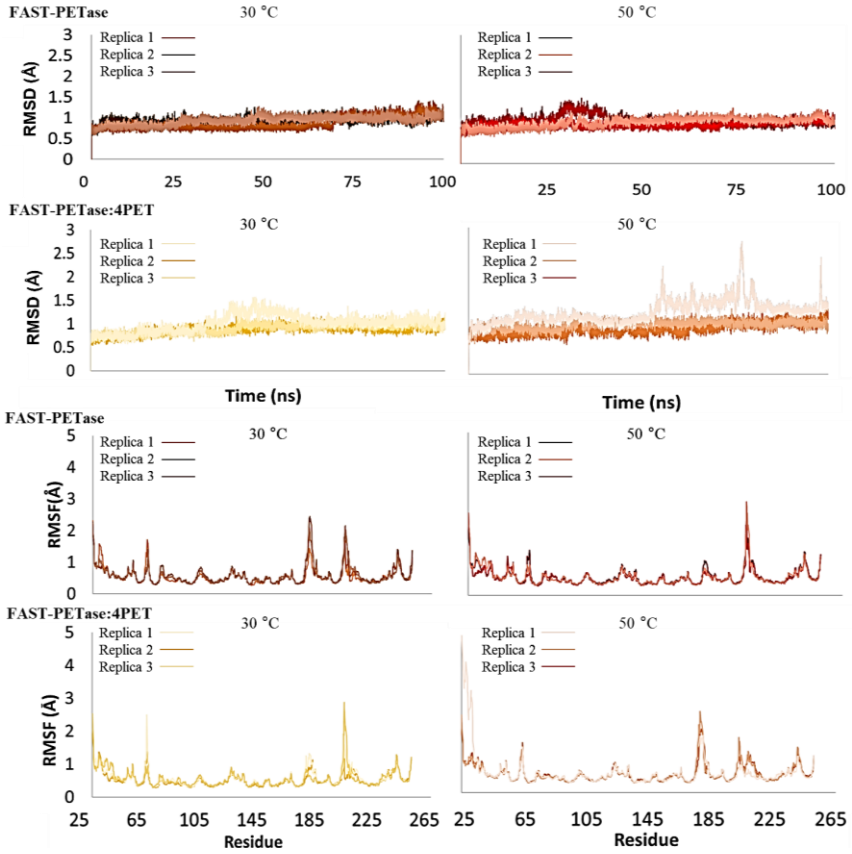

Figure 4.17: RMSD and RMSF analysis of the replicas carried out for the investigated FAST-PETase systems.

Some more evident shifts of RMSD occurred in the case of replica 1 of FAST-PETase:4PET complex at 50 °C, up to 2.5 Å. The main reason for such behavior can be assigned to the fluctuations of 25-35 terminal residues, which during the simulations shifted more with respect to their initial position. However, the above-described movements did not affect the general secondary structures organization of the investigated systems. This is confirmed by the observation of superimposable RMSD and RMSF trends.

4.6 Conclusions

In this study, molecular dynamics simulations were employed to gain in-depth atomistic insights into the interactions between FAST-PETase and a tetrameric PET substrate (4PET). FAST-PETase, an engineered variant of PETase from *Ideonella sakaiensis*, was designed through machine learning approaches to enhance both stability and hydrolytic efficiency. This enzyme demonstrates a significantly improved ability to depolymerize PET, making it a promising candidate for environmentally sustainable plastic waste management and biocatalytic recycling strategies.

Our analyses revealed that the conformational behavior of FAST-PETase is strongly dependent on temperature. At 50°C, the apoenzyme exhibits increased flexibility and pronounced fluctuations, particularly near the active-site cleft, where substrate binding occurs. These structural fluctuations create solvent-exposed grooves and cavities on the enzyme surface that appear to facilitate the initial docking and accommodation of 4PET. Such pre-organization of the active site is likely a key factor contributing to the enzyme's enhanced catalytic efficiency at its optimal working temperature. Conversely, at lower temperatures, such as 30°C, the enzyme is less flexible, leading to a more restricted active site and less favorable substrate alignment.

Simulations of the FAST-PETase:4PET complex further highlighted how temperature influences productive enzyme–substrate interactions. At 50°C, the increased plasticity of the active site enhances its lipophilic character, stabilizing the aromatic moieties of 4PET and promoting their orientation into catalytically favorable configurations. Residues such as W185 and Y87 play a central role in anchoring the terephthalic rings through hydrophobic and π-stacking interactions, ensuring that the substrate is correctly positioned for catalysis. These interactions also favor the formation of a W-shaped conformation of 4PET, characterized by an extended arrangement of the substrate over the enzyme surface. This W-shaped conformation, not observed in simulations with wild-type PETase or at 30°C, positions the substrate in closer proximity to the nucleophilic S160 and the oxyanion hole formed by M161, thereby enhancing the likelihood of productive catalysis.

The W-shaped conformation is further stabilized by a network of electrostatic interactions, including a salt bridge between K233 and D204, reinforced by R90. Density Functional Theory calculations indicate that this conformation corresponds to a higher-energy, otherwise inaccessible state in solution (~12 kcal mol^{-1} above the wrapped conformation), confirming that FAST-PETase at 50°C actively promotes substrate destabilization. This destabilization likely reduces the energy barrier for bond cleavage, thus contributing to the improved hydrolytic activity observed

experimentally. MD simulations of 4PET in solution at various temperatures (30, 50, 150°C) confirmed that the W-shaped conformation does not occur spontaneously, highlighting the enzyme's unique role in guiding the substrate into reactive conformations.

Overall, these in silico findings are consistent with experimental data, demonstrating that the structural pre-organization of FAST-PETase, combined with the conformational plasticity of key mutated residues, contributes to an increased production of monomers at elevated temperatures. The results provide a detailed mechanistic explanation for the enhanced catalytic performance of FAST-PETase, linking the dynamic behavior of the enzyme to substrate orientation, stabilization of transition states, and formation of high-energy conformations conducive to catalysis.

Beyond the mechanistic insights, our study underscores the potential of FAST-PETase for industrial applications. By stabilizing reactive conformations of PET at moderate temperatures (30–50°C), the enzyme allows for energy-efficient, scalable processes that could reduce reliance on high-temperature chemical recycling methods. These atomistic insights may inform future enzyme engineering efforts aimed at further improving activity, specificity, and thermostability, ultimately contributing to sustainable plastic recycling and mitigating the environmental impact of PET accumulation.

In summary, this work provides a comprehensive atomistic view of FAST-PETase–substrate interactions, emphasizing the interplay between enzyme flexibility, substrate conformation, and catalysis. By integrating structural, dynamic, and energetic analyses, our findings offer a robust foundation for ongoing theoretical and experimental research aimed at optimizing PET degradation under mild, environmentally friendly conditions, advancing both the science of biocatalysis and practical strategies for a circular, sustainable economy.

References

1. Helms, B.A. Polydiketoenamines for a Circular Plastics Economy. Acc Chem Res 2022, 55, 2753–2765, doi:10.1021/acs.accounts.2c00308.
2. Geyer, R.; Jambeck, J.R.; Law, K.L. Production, Use, and Fate of All Plastics Ever Made. Sci Adv 2017, 3, doi:10.1126/sciadv.1700782.
3. Ryberg, M.; Laurent, A.; Hauschild, M.Z. Mapping of Global Plastic Value Chain and Plastic Losses to the Environment: With a Particular Focus on Marine Environment.; 2018;
4. De Jesus, R.; Alkendi, R. A Minireview on the Bioremediative Potential of Microbial Enzymes as Solution to Emerging Microplastic Pollution. Front Microbiol 2023, 13, doi:10.3389/fmicb.2022.1066133.
5. Ragusa, A.; Matta, M.; Cristiano, L.; Matassa, R.; Battaglione, E.; Svelato, A.; De Luca, C.; D'Avino, S.; Gulotta, A.; Rongioletti, M.C.A.; et al. Deeply in Plasticenta: Presence of Microplastics in the Intracellular Compartment of Human Placentas. Int J Environ Res Public Health 2022, 19, 11593, doi:10.3390/ijerph191811593.
6. Sarkar, S.; Diab, H.; Thompson, J. Microplastic Pollution: Chemical Characterization and Impact on Wildlife. Int J Environ Res Public Health 2023, 20, 1745, doi:10.3390/ijerph20031745.
7. The New Plastics Economy: Rethinking the Future of Plastics. World Economic Forum 2016, 36.
8. Coates, G.W.; Getzler, Y.D.Y.L. Chemical Recycling to Monomer for an Ideal, Circular Polymer Economy. Nat Rev Mater 2020, 5, 501–516, doi:10.1038/s41578-020-0190-4.
9. Boneta, S.; Arafet, K.; Moliner, V. QM/MM Study of the Enzymatic Biodegradation Mechanism of Polyethylene Terephthalate. J Chem Inf Model 2021, 61, 3041–3051, doi:10.1021/acs.jcim.1c00394.
10. Kawai, F.; Kawabata, T.; Oda, M. Current State and Perspectives Related to the Polyethylene Terephthalate Hydrolases Available for Biorecycling. ACS Sustain Chem Eng 2020, 8, 8894–8908, doi:10.1021/acssuschemeng.0c01638.
11. Papadopoulou, A.; Hecht, K.; Buller, R. Enzymatic PET Degradation. Chimia (Aarau) 2019, 73, 743, doi:10.2533/chimia.2019.743.
12. Kawai, F.; Kawabata, T.; Oda, M. Current Knowledge on Enzymatic PET Degradation and Its Possible Application to Waste Stream Management and Other Fields. Appl Microbiol Biotechnol 2019, 103, 4253–4268, doi:10.1007/s00253-019-09717-y.
13. Müller, R.; Schrader, H.; Profe, J.; Dresler, K.; Deckwer, W. Enzymatic Degradation of Poly(Ethylene Terephthalate): Rapid Hydrolyse Using a Hydrolase from T. Fusca. Macromol Rapid Commun 2005, 26, 1400–1405, doi:10.1002/marc.200500410.
14. Yoshida, S.; Hiraga, K.; Takehana, T.; Taniguchi, I.; Yamaji, H.; Maeda, Y.; Toyohara, K.; Miyamoto, K.; Kimura, Y.; Oda, K. A Bacterium That Degrades and Assimilates

Poly(Ethylene Terephthalate). Science (1979) 2016, 351, 1196–1199, doi:10.1126/science.aad6359.

15. Joo, S.; Cho, I.J.; Seo, H.; Son, H.F.; Sagong, H.-Y.; Shin, T.J.; Choi, S.Y.; Lee, S.Y.; Kim, K.-J. Structural Insight into Molecular Mechanism of Poly(Ethylene Terephthalate) Degradation. Nat Commun 2018, 9, 382, doi:10.1038/s41467-018-02881-1.

16. Liu, C.; Shi, C.; Zhu, S.; Wei, R.; Yin, C.-C. Structural and Functional Characterization of Polyethylene Terephthalate Hydrolase from Ideonella Sakaiensis. Biochem Biophys Res Commun 2019, 508, 289–294, doi:10.1016/j.bbrc.2018.11.148.

17. Knott, B.C.; Erickson, E.; Allen, M.D.; Gado, J.E.; Graham, R.; Kearns, F.L.; Pardo, I.; Topuzlu, E.; Anderson, J.J.; Austin, H.P.; et al. Characterization and Engineering of a Two-Enzyme System for Plastics Depolymerization. Proceedings of the National Academy of Sciences 2020, 117, 25476–25485, doi:10.1073/pnas.2006753117.

18. Han, X.; Liu, W.; Huang, J.-W.; Ma, J.; Zheng, Y.; Ko, T.-P.; Xu, L.; Cheng, Y.-S.; Chen, C.-C.; Guo, R.-T. Structural Insight into Catalytic Mechanism of PET Hydrolase. Nat Commun 2017, 8, 2106, doi:10.1038/s41467-017-02255-z.

19. Feng, S.; Yue, Y.; Zheng, M.; Li, Y.; Zhang, Q.; Wang, W. Is PETase- and Is MHETase-Catalyzed Cascade Degradation Mechanism toward Polyethylene Terephthalate. ACS Sustain Chem Eng 2021, 9, 9823–9832, doi:10.1021/acssuschemeng.1c02420.

20. Fecker, T.; Galaz-Davison, P.; Engelberger, F.; Narui, Y.; Sotomayor, M.; Parra, L.P.; Ramírez-Sarmiento, C.A. Active Site Flexibility as a Hallmark for Efficient PET Degradation by I. Sakaiensis PETase. Biophys J 2018, 114, 1302–1312, doi:10.1016/j.bpj.2018.02.005.

21. Chen, C.-C.; Dai, L.; Ma, L.; Guo, R.-T. Enzymatic Degradation of Plant Biomass and Synthetic Polymers. Nat Rev Chem 2020, 4, 114–126, doi:10.1038/s41570-020-0163-6.

22. Taniguchi, I.; Yoshida, S.; Hiraga, K.; Miyamoto, K.; Kimura, Y.; Oda, K. Biodegradation of PET: Current Status and Application Aspects. ACS Catal 2019, 9, 4089–4105, doi:10.1021/acscatal.8b05171.

23. Tournier, V.; Topham, C.M.; Gilles, A.; David, B.; Folgoas, C.; Moya-Leclair, E.; Kamionka, E.; Desrousseaux, M.-L.; Texier, H.; Gavalda, S.; et al. An Engineered PET Depolymerase to Break down and Recycle Plastic Bottles. Nature 2020, 580, 216–219, doi:10.1038/s41586-020-2149-4.

24. Son, H.F.; Cho, I.J.; Joo, S.; Seo, H.; Sagong, H.-Y.; Choi, S.Y.; Lee, S.Y.; Kim, K.-J. Rational Protein Engineering of Thermo-Stable PETase from Ideonella Sakaiensis for Highly Efficient PET Degradation. ACS Catal 2019, 9, 3519–3526, doi:10.1021/acscatal.9b00568.

25. Cui, Y.; Chen, Y.; Liu, X.; Dong, S.; Tian, Y.; Qiao, Y.; Mitra, R.; Han, J.; Li, C.; Han, X.; et al. Computational Redesign of a PETase for Plastic Biodegradation under Ambient Condition by the GRAPE Strategy. ACS Catal 2021, 11, 1340–1350, doi:10.1021/acscatal.0c05126.

26. Austin, H.P.; Allen, M.D.; Donohoe, B.S.; Rorrer, N.A.; Kearns, F.L.; Silveira, R.L.; Pollard, B.C.; Dominick, G.; Duman, R.; El Omari, K.; et al. Characterization and Engineering of a Plastic-Degrading Aromatic Polyesterase. Proceedings of the National Academy of Sciences 2018, 115, doi:10.1073/pnas.1718804115.

27. Lu, H.; Diaz, D.J.; Czarnecki, N.J.; Zhu, C.; Kim, W.; Shroff, R.; Acosta, D.J.; Alexander, B.R.; Cole, H.O.; Zhang, Y.; et al. Machine Learning-Aided Engineering of Hydrolases for PET Depolymerization. Nature 2022, 604, 662–667, doi:10.1038/s41586-022-04599-z.

28. Berselli, A.; Ramos, M.J.; Menziani, M.C. Novel Pet-Degrading Enzymes: Structure-Function from a Computational Perspective. ChemBioChem 2021, 22, 2032–2050, doi:10.1002/cbic.202000841.

29. Guo, B.; Vanga, S.R.; Lopez-Lorenzo, X.; Saenz-Mendez, P.; Ericsson, S.R.; Fang, Y.; Ye, X.; Schriever, K.; Bäckström, E.; Biundo, A.; et al. Conformational Selection in Biocatalytic Plastic Degradation by PETase. ACS Catal 2022, 12, 3397–3409, doi:10.1021/acscatal.1c05548.

30. Jerves, C.; Neves, R.P.P.; Ramos, M.J.; da Silva, S.; Fernandes, P.A. Reaction Mechanism of the PET Degrading Enzyme PETase Studied with DFT/MM Molecular Dynamics Simulations. ACS Catal 2021, 11, 11626–11638, doi:10.1021/acscatal.1c03700.

31. Bell, E.L.; Smithson, R.; Kilbride, S.; Foster, J.; Hardy, F.J.; Ramachandran, S.; Tedstone, A.A.; Haigh, S.J.; Garforth, A.A.; Day, P.J.R.; et al. Directed Evolution of an Efficient and Thermostable PET Depolymerase. Nat Catal 2022, 5, 673–681, doi:10.1038/s41929-022-00821-3.

32. da Costa, C.H.S.; dos Santos, A.M.; Alves, C.N.; Martí, S.; Moliner, V.; Santana, K.; Lameira, J. Assessment of the <scp>PETase</Scp> Conformational Changes Induced by Poly(Ethylene Terephthalate) Binding. Proteins: Structure, Function, and Bioinformatics 2021, 89, 1340–1352, doi:10.1002/prot.26155.

33. M. J. Frisch, G. W. Trucks, H. B. Schlegel, G. E. Scuseria, M.A. Robb, J.R. Cheeseman, G. Scalmani, V. Barone, G.A. Petersson, H. Nakatsuji, X. Li, M. Caricato, A. V. Marenich, J. Bloino, B. G. Janesko, R. Gomperts, B. Mennucci, H. P. Hratchian, J. V. Ortiz, A. F. Izmaylov, J. L. Sonnenberg, D. Williams-Young, F. Ding, F. Lipparini, F. Egidi, J. Goings, B. Peng, A. Petrone, T. Henderson, D. Ranasinghe, V. G. Zakrzewski, J. Gao, N. Rega, G. Zheng, W. Liang, M. Hada, M. Ehara, K. Toyota, R. Fukuda, J. Hasegawa, M. Ishida, T. Nakajima, Y. Honda, O. Kitao, H. Nakai, T. Vreven, K. Throssell, J. A. Montgomery Jr, J. E. Peralta, F. Ogliaro, M. J. Bearpark, J. J. Heyd, E. N. Brothers, K. N. Kudin, V. N. Staroverov, T. A. Keith, R. Kobayashi, J. Normand, K. Raghavachari, A. P. Rendell, J. C. Burant, S. S. Iyengar, J. Tomasi, M. Cossi, J. M. Millam, M. Klene, C. Adamo, R. Cammi, J. W. Ochterski, R. L. Martin, K. Morokuma, O. Farkas, J. B. Foresman, D. J. Fox Gaussian 16, Revision C.01. Gaussian, Inc., Wallingford CT 2016.

34. Wang, J.; Wolf, R.M.; Caldwell, J.W.; Kollman, P.A.; Case, D.A. Development and Testing of a General Amber Force Field. J Comput Chem 2004, 25, 1157–1174, doi:10.1002/jcc.20035.

35. Wang, J.; Cieplak, P.; Kollman, P.A. How Well Does a Restrained Electrostatic Potential (RESP) Model Perform in Calculating Conformational Energies of Organic and Biological Molecules? J Comput Chem 2000.

36. Pérez-González, A.; Prejanò, M.; Russo, N.; Marino, T.; Galano, A. Capsaicin, a Powerful •OH-Inactivating Ligand. Antioxidants 2020, 9, 1247, doi:10.3390/antiox9121247.

37. Prejanò, M.; Medina, F.E.; Ramos, M.J.; Russo, N.; Fernandes, P.A.; Marino, T. How the Destabilization of a Reaction Intermediate Affects Enzymatic Efficiency: The Case of Human Transketolase. ACS Catal 2020, 10, 2872–2881, doi:10.1021/acscatal.9b04690.

38. Prejanò, M.; Romeo, I.; La Serra, M.A.; Russo, N.; Marino, T. Computational Study Reveals the Role of Water Molecules in the Inhibition Mechanism of LAT1 by 1,2,3-Dithiazoles. J Chem Inf Model 2021, 61, 5883–5892, doi:10.1021/acs.jcim.1c01012.

39. Parise, A.; Ciardullo, G.; Prejanò, M.; Lande, A. de la; Marino, T. On the Recognition of Natural Substrate CTP and Endogenous Inhibitor DdhCTP of SARS-CoV-2 RNA-Dependent RNA Polymerase: A Molecular Dynamics Study. J Chem Inf Model 2022, 62, 4916–4927, doi:10.1021/acs.jcim.2c01002.

40. Abraham, M.J.; Murtola, T.; Schulz, R.; Páll, S.; Smith, J.C.; Hess, B.; Lindahl, E. GROMACS: High Performance Molecular Simulations through Multi-Level Parallelism from Laptops to Supercomputers. SoftwareX 2015, 1–2, 19–25, doi:10.1016/j.softx.2015.06.001.

41. Case, D.A.; Aktulga, H.M.; Belfon, K.; Cerutti, D.S.; Cisneros, G.A.; Cruzeiro, V.W.D.; Forouzesh, N.; Giese, T.J.; Götz, A.W.; Gohlke, H.; et al. AmberTools. J Chem Inf Model 2023, 63, 6183–6191, doi:10.1021/acs.jcim.3c01153.

42. Morris, G.M.; Huey, R.; Lindstrom, W.; Sanner, M.F.; Belew, R.K.; Goodsell, D.S.; Olson, A.J. AutoDock4 and AutoDockTools4: Automated Docking with Selective Receptor Flexibility. J Comput Chem 2009, 30, 2785–2791, doi:10.1002/jcc.21256.

43. Pagadala, N.S.; Syed, K.; Tuszynski, J. Software for Molecular Docking: A Review. Biophys Rev 2017, 9, 91–102, doi:10.1007/s12551-016-0247-1.

44. Chahal, V.; Nirwan, S.; Kakkar, R. Combined Approach of Homology Modeling, Molecular Dynamics, and Docking: Computer-Aided Drug Discovery. Physical Sciences Reviews 2019, 4, doi:10.1515/psr-2019-0066.

45. Lazim, R.; Suh, D.; Choi, S. Advances in Molecular Dynamics Simulations and Enhanced Sampling Methods for the Study of Protein Systems. Int J Mol Sci 2020, 21, 6339, doi:10.3390/ijms21176339.

46. Lee, C.; Yang, W.; Parr, R.G. Development of the Colle-Salvetti Correlation-Energy Formula into a Functional of the Electron Density. Phys Rev B 1988, 37, 785–789, doi:10.1103/PhysRevB.37.785.

47. Becke, A.D. Density-Functional Thermochemistry. III. The Role of Exact Exchange. J Chem Phys 1993, 98, 5648–5652, doi:10.1063/1.464913.

48. Grimme, S.; Antony, J.; Ehrlich, S.; Krieg, H. A Consistent and Accurate Ab Initio Parametrization of Density Functional Dispersion Correction (DFT-D) for the 94 Elements H-Pu. J Chem Phys 2010, 132, doi:10.1063/1.3382344.

49. Grimme, S.; Ehrlich, S.; Goerigk, L. Effect of the Damping Function in Dispersion Corrected Density Functional Theory. J Comput Chem 2011, 32, 1456–1465, doi:10.1002/jcc.21759.

50. Marenich, A. V.; Cramer, C.J.; Truhlar, D.G. Universal Solvation Model Based on Solute Electron Density and on a Continuum Model of the Solvent Defined by the Bulk Dielectric Constant and Atomic Surface Tensions. J Phys Chem B 2009, 113, 6378–6396, doi:10.1021/jp810292n.

51. Ronkvist, Å.M.; Xie, W.; Lu, W.; Gross, R.A. Cutinase-Catalyzed Hydrolysis of Poly(Ethylene Terephthalate). Macromolecules 2009, 42, 5128–5138, doi:10.1021/ma9005318.

52. Wei, R.; Zimmermann, W. Biocatalysis as a Green Route for Recycling the Recalcitrant Plastic Polyethylene Terephthalate. Microb Biotechnol 2017, 10, 1302–1307, doi:10.1111/1751-7915.12714.

53. Wei, R.; Song, C.; Gräsing, D.; Schneider, T.; Bielytskyi, P.; Böttcher, D.; Matysik, J.; Bornscheuer, U.T.; Zimmermann, W. Conformational Fitting of a Flexible Oligomeric Substrate Does Not Explain the Enzymatic PET Degradation. Nat Commun 2019, 10, 5581, doi:10.1038/s41467-019-13492-9.

54. Daubeny, R.D.P., B.C.W.C., B.J. The Crystal Structure of Polyethylene Terephthalate. Proc R Soc Lond A Math Phys Sci 1954, 226, 531–542, doi:10.1098/rspa.1954.0273.

55. Fu, Y.; Busing, W.R.; Jin, Y.; Affholter, K.A.; Wunderlich, B. Poly(Ethylene Terephthalate) Fibers. 1. Crystal Structure and Morphology Studies with Full-Pattern x-Ray Diffraction Refinement. Macromolecules 1993, 26, 2187–2193, doi:10.1021/ma00061a007.

56. Yokouchi, M.; Sakakibara, Y.; Chatani, Y.; Tadokoro, H.; Tanaka, T.; Yoda, K. Structures of Two Crystalline Forms of Poly(Butylene Terephthalate) and Reversible Transition between Them by Mechanical Deformation. Macromolecules 1976, 9, 266–273, doi:10.1021/ma60050a018.

Chapter 5

Study of Non-Phenolic Substrate Oxidation at the Type 1 Copper Center of *Trametes versicolor* Laccase: Benzo[a]pyrene and Anthracene

In this chapter, we outline the catalytic properties of laccases and describe a computational investigation aimed at elucidating their reactivity toward polycyclic aromatic hydrocarbons (PAHs).

Laccases (EC 1.10.3.2) are enzymes belonging to the multicopper oxidase family, characterized by their ability to catalyze the oxidation of a wide variety of substrates, including both phenolic and non-phenolic compounds. The detailed molecular mechanism underlying their activity toward phenolic substrates is well-established, supported by extensive experimental and computational studies. However, the reactivity of laccases toward non-phenolic substrates, particularly polycyclic aromatic hydrocarbons (PAHs), remains largely unexplored and represents a significant subject of scientific inquiry. Understanding the oxidation mechanisms of PAHs is crucial not only for elucidating the catalytic capabilities of these enzymes but also for assessing their potential applications in biotechnological and environmental contexts, such as the degradation of persistent organic pollutants.

To investigate the oxidation mechanism of PAHs in greater detail, with a particular focus on the activation of the sp^2 aromatic C–H bond, we performed a density functional theory (DFT) study. The analysis focused on the oxidation of two representative PAHs, anthracene and benzo[a]pyrene, using an extensive computational model of the T1 copper catalytic site of the fungal laccase from *Trametes versicolor*. This approach allowed us to gain in-depth insights into the electronic interactions and key mechanistic steps involved in the catalytic process, providing a more comprehensive understanding of PAH oxidation mediated by laccases.

Also in this work, single-letter amino acid abbreviations (D, E, F) are used throughout the text for clarity, while three-letter abbreviations (Asp, Glu, Phe) are used in figures and tables. Both notations refer to the same residues.

5.1 Introduction

Laccases (EC 1.10.3.2, oxygen oxidoreductases or multicopper oxidases) are versatile enzymes belonging to the class of phenol-oxidases, widely distributed across a broad range of organisms, including bacteria [1], fungi [2–6], plants, insects [7], and marine species [8]. Their broad occurrence in nature reflects their evolutionary importance in mediating oxidative processes essential for cellular metabolism, structural remodeling, and environmental detoxification. These enzymes catalyze the one-electron oxidation of a wide spectrum of substrates while concomitantly reducing molecular oxygen to water, a reaction that is central to their multifunctional catalytic behavior [9].

The laccase active site contains four copper ions arranged into three distinct types of copper centers: Type 1 (T1 Cu), Type 2 (T2 Cu), and a binuclear Type 3 (T3 Cu), which together form a trinuclear cluster (TNC), as illustrated in Figure 5.1.

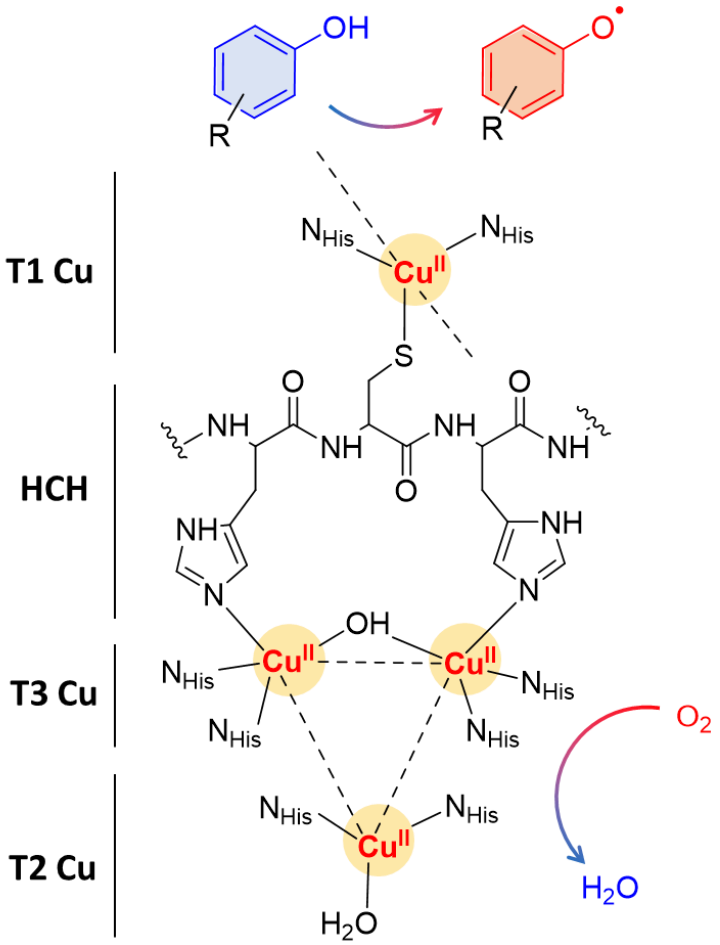

Figure 5.1: Schematic representation of the laccase catalytic site processing a phenolic compound. The Type-1 Copper site (T1 Cu) is located at the surface of the substrate-binding pocket and coordinates one copper atom with two histidine residues and one cysteine residue. Two additional weakly coordinating residues occupy the axial position, typically Phe or Leu for high-potential fungal laccases, and Met for low-potential bacterial laccases. The Type 2 (T2 Cu) and Type 3 (T3 Cu) copper ions form the TNC, coordinated by eight histidine residues and connected to T1 Cu through the highly conserved histidine–cysteine–histidine (HCH) motif. Upon substrate oxidation at the T1 Cu site, electrons are sequentially transferred along the HCH pathway to the TNC, where molecular oxygen is bound and reduced to water.

The T1 Cu site is the locus of substrate oxidation and largely determines the redox potential of the enzyme. Notably, the physicochemical properties of the amino acid in the axial position of T1 Cu play a pivotal role in modulating this redox potential [10], thereby influencing the efficiency of electron transfer from substrate to enzyme. Electrons are subsequently relayed from T1 Cu to T2 and T3 Cu, which are situated approximately 12–13 Å away [11], culminating in the reduction of molecular oxygen to water at the TNC [12].

Laccases exhibit a remarkable diversity of biological functions that are intimately linked to their source organism. In fungi, laccases are key mediators of lignin degradation, facilitating the recycling of organic matter in ecosystems, whereas in plants, they contribute to lignin biosynthesis and defense against pathogens. In bacteria, laccases participate in processes such as spore-coating, pigmentation, and biofilm formation [13]. This broad spectrum of roles reflects their catalytic versatility and substrate promiscuity, which allows them to oxidize an extensive array of compounds. Typical substrates include phenolic and lignin-related molecules, yet laccases can also act on non-phenolic compounds such as amines, alcohols, dyes [14,15], carbohydrates, metal complexes [16], and polymers[17,18].

The catalytic potential of laccases can be further amplified by the use of redox mediators, small molecules that serve as electron shuttles to extend enzymatic oxidation to otherwise recalcitrant substrates [19,20]. While the oxidation mechanisms for phenolic compounds have been extensively characterized and documented [19,21–26], the pathways for non-phenolic substrates remain less well understood. Among these, polycyclic aromatic hydrocarbons (PAHs) have received particular attention due to their environmental persistence, hydrophobicity, and recognized toxicity [27,28]. PAHs are primarily generated from the incomplete combustion of organic matter such as oil, coal, and natural gas, and are pervasive pollutants in terrestrial and aquatic ecosystems. Bioremediation strategies utilizing laccases offer a promising approach for mitigating the ecological impact of these compounds.

Several studies have demonstrated the ability of fungal laccases, including those from *Trametes versicolor* [29,30], *Pleurotus ostreatus* [31], and *Coriolopsis gallica* [32], to oxidize PAHs. Subsequent research has sought to improve oxidation efficiency by modifying the chemical nature of mediators [33–39] or by employing immobilized enzyme systems [33,34,40–42], highlighting the interplay between substrate accessibility and enzymatic performance. Beyond fungi [43–48], bacterial laccases have also been explored for PAH degradation [46,49,50], offering advantages in terms of thermal stability and pH tolerance, which are crucial parameters for environmental applications.

Mechanistically, the rate-limiting step in laccase-catalyzed reactions is typically the initial one-electron oxidation of the substrate [51,52], governed by the difference in standard reduction potentials (E°) between T1 Cu and the substrate [53]. Phenolic substrates achieve this through concerted electron-proton transfer, minimizing the formation of high-energy intermediates. In *T. versicolor* laccase (TvL), this proton transfer is facilitated by the acidic nature of the phenolic proton and by a proximate aspartic acid residue [49]. In contrast, non-phenolic substrates such as PAHs possess aromatic C–H bonds with markedly lower acidity, making proton transfer

less favorable. Despite this, fungal laccases can oxidize PAHs even in the absence of mediators, albeit with lower efficiency, implying alternative mechanisms for facilitating proton and electron transfer. PAH oxidation by laccases involves a sequence of six electron transfers to generate quinone products, as shown in Figure 5.2.

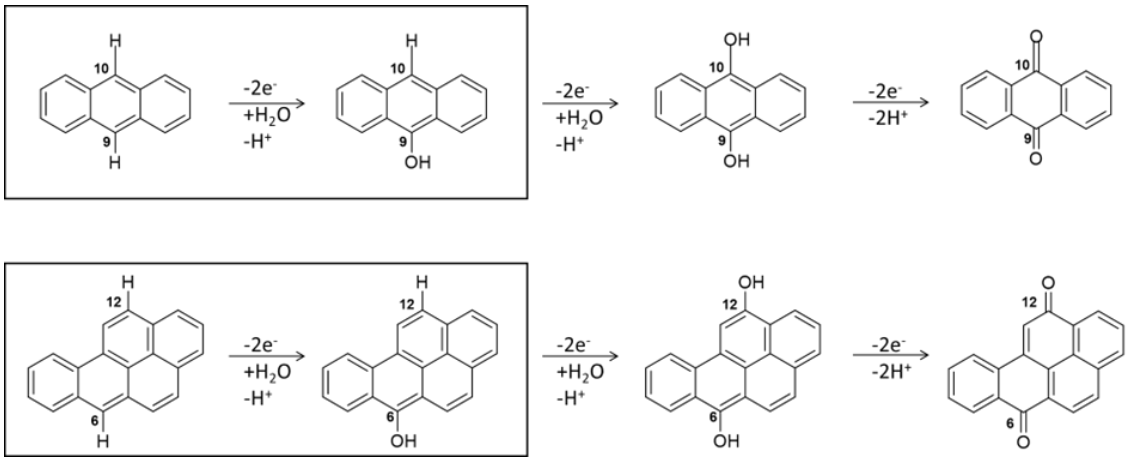

Figure 5.2: The six-electron oxidation of ANT e BaP to quinone species catalyzed by laccases. The IUPAC numbering shown is that relating to the BaP.56 The carbon atoms 6 and 10b in BaP correspond to the carbon 9 and 10 in ANT. The reaction evidenced in the box is the focal point of the present investigation. The whole conversion requires at least two water molecules.

The initial stage of PAH oxidation, involving the direct activation of the aromatic C–H bond, is widely recognized as the rate-limiting step in laccase-catalyzed reactions. This step is particularly challenging due to the high bond dissociation energy and the low acidity of aromatic protons, which make the direct proton transfer intrinsically unfavorable. Once the C–H bond is oxidized, the resulting intermediates carry hydroxyl (C–OH) functionalities. These hydroxylated intermediates exhibit lower redox potentials compared to the parent PAHs, rendering them significantly more reactive and facilitating the subsequent electron transfer steps required to complete the full six-electron oxidation to quinone products. This stepwise increase in reactivity illustrates how the enzyme strategically exploits intermediate formation to overcome thermodynamic barriers inherent to the oxidation of chemically inert substrates.

In this work, we aim to provide a detailed atomic-level understanding of the PAH oxidation mechanism at the T1 Cu site of *Trametes versicolor* laccase (TvL), deliberately excluding the influence of redox mediators to isolate the intrinsic catalytic properties of the enzyme. TvL is classified as a high-redox-potential laccase ($E° \approx 785$ mV), a property largely attributed to the presence of a hydrophobic residue in the axial position of the T1 Cu center, which stabilizes the oxidized copper

state and facilitates electron transfer [53]. By focusing on the critical step of direct aromatic C–H bond activation, we seek to elucidate the mechanistic principles underlying this transformation. Insights gained from this study may also have broader implications, including guiding the design of enzymatic systems for the activation of sp^3 aliphatic C–H bonds, relevant in the enzymatic degradation of synthetic polymers such as polyethylene [18].

Two representative PAHs were selected for computational analysis: anthracene (ANT) and benzo[a]pyrene (BaP). These molecules were chosen for their comparable reduction potentials in acetonitrile (886 mV for ANT and 712 mV for BaP) [33,54,55] and their low aqueous solubility (0.045 mg L^{-1} for ANT and 0.0016 mg L^{-1} for BaP) [44]. Notably, fungal laccases, including TvL, efficiently catalyze the oxidation of ANT, whereas BaP is largely resistant in the absence of mediators [29,30,33,34] despite having a lower ionization potential (7.12 eV vs. 7.55 eV for ANT) and a slightly less positive redox potential [32]. This apparent discrepancy highlights the complex interplay between substrate accessibility, solubility, and enzyme-substrate electronic interactions. Reaction conditions play a critical role in modulating oxidation efficiency. For example, the addition of the surfactant Tween 80 improves BaP solubility and consequently enhances its oxidation yield, underscoring the importance of both chemical and physical factors in laccase-mediated PAH transformations.

Our investigation proceeds in two integrated stages. First, molecular docking simulations are employed to characterize substrate binding orientations and to identify key residues involved in stabilizing the PAH within the active site. This step provides a structural framework and plausible geometries for subsequent mechanistic studies. In the second stage, the oxidation mechanism is probed through Density Functional Theory (DFT) calculations using a cluster approach [56,57], based on the most representative binding poses obtained from docking. This methodology allows for a detailed evaluation of electron and proton transfer events, providing insights into the energetic and structural factors that govern the catalytic efficiency of TvL toward challenging non-phenolic substrates.

5.2 Computational Details

Molecular Docking was performed using Glide, as implemented in Maestro Schrödinger Suite software (Schrödinger Release 2020-3: Maestro, Schrödinger, LLC, New York, NY, 2021). We tested the reliability of the docking protocol by performing a molecular recognition of the known inhibitors, such as 2,2'-azino-bis(3-ethylbenzothiazoline-6-sulfonic acid) (ABTS) and 2,6-dimethoxyphenol (2,6 DMP), into the binding site of TvL (PDB ID: 1KYA [58])More in detail, a flexible ligand

extra precision (XP) docking was carried out, using the OPLS3 force field (see Figure 5.3). To have a more accurate estimation of ligand-binding affinities, Prime Molecular Mechanics Generalized Born and Surface Area (MM/GBSA) calculations were carried out[59]. Molecular Dynamics (MD) simulations assessed the stability of substrate positioning within the pocket.

All DFT calculations have been performed with the TURBOMOLE 7.4 suite [60]. Geometry optimizations were performed using the pure GGA BP86 [61,62] functional. The RI technique [63] was adopted to speed up calculations. Single point energies on BP86-optimized geometries have also been recalculated using the hybrid PBE0 [64] functional. Basis sets of triple-ζ plus polarization split valence quality [65] (def-TZVP) were adopted for all atoms. Solvent effect is accounted for by using the Conductor-like Screening Model (COSMO) approach [66]. Water solvation has been considered by setting the dielectric constant equal to 80. In general, this computational setting provides ground state geometry parameters in good agreement with experimental X-ray values [67]. Charge distribution was evaluated using Natural Bond Orbital (NBO) analysis using the PBE0 functional. Geometry optimizations were carried out with convergence criteria fixed to 10^{-6} Hartree for the energy and 0.001 Hartree·per bohr for the gradient norm vector. D3 Grimme empirical dispersion correction [68] was adopted. This theoretical scheme has already been tested and successfully adopted in previous DFT investigations carried out in our laboratory on various bioinorganic copper systems [69–71].

Molecular Dynamics details: two replicas of 100 ns were performed for the protein in complex with ANT, starting from the best docking pose. By using AmberTools23 [72], the 3D system was placed in a 10 Å cubic box containing a neutralized water buffer with counterions. The system was described by the model from the general Amber force field (GAFF) [73] and ff99SB [74] in combination with the TIP3P water model [75]; proper restraints have been added to maintain proper coordination in T1 Cu. Using the GROMACS 2020 package [76] the system was relaxed by applying harmonic positional constraints on all atoms (50 kcal mol-1 Å 2) using 5000 steps of steepest descent (SD), followed by 5000 steps of conjugate gradient (CG). The system was progressively heated for 10 ns at 300 K using the Langevin thermostat in the NVT ensemble. The system was maintained at constant pressure with the NPT ensemble at 1 bar pressure using the Berendsen barostat with a time constant τp = 2.0 ps. The 100 ns MDs were produced with an integration step of 2 fs and a cutoff radius of 10.0, with the SHAKE algorithm coupling the Particle Mesh Ewald (PME) summation method. The stability of the complex was verified by monitoring the T1 Cu - ANT distance, calculated with respect to the barycenter of the latter. To verify the presence of water molecules in the proximity of T1 Cu, the radial distribution function (RDF) was also calculated.

5.3 Characterization of enzyme–substrate interactions

To reliably unravel the mechanism(s) of PAH oxidation, a preliminary study on PAHs recognition by the enzyme is needed. Thus, molecular docking of BaP and ANT to the *TvL* (1KYA [58]) was carried out, allowing to characterize the nature of the enzyme–substrate interaction and to drive subsequent higher-level calculations. Indeed, for each substrate, the best-energy pose was chosen as the starting point for subsequent DFT calculations. The analysis of enzyme–substrate interactions also allowed the selection of those residues to be included in our DFT model(s) (*vide infra*). Furthermore, the obtained docking poses/scores for ANT and BaP provided indications about similarities and/or differences in both their accommodation mode within the binding pocket and their affinity towards *TvL*. More in detail, the analyses of the five top-ranked poses for both ANT and BaP clearly indicate that they both bind at the same site, in proximity to T1 Cu (see Figure 5.3).

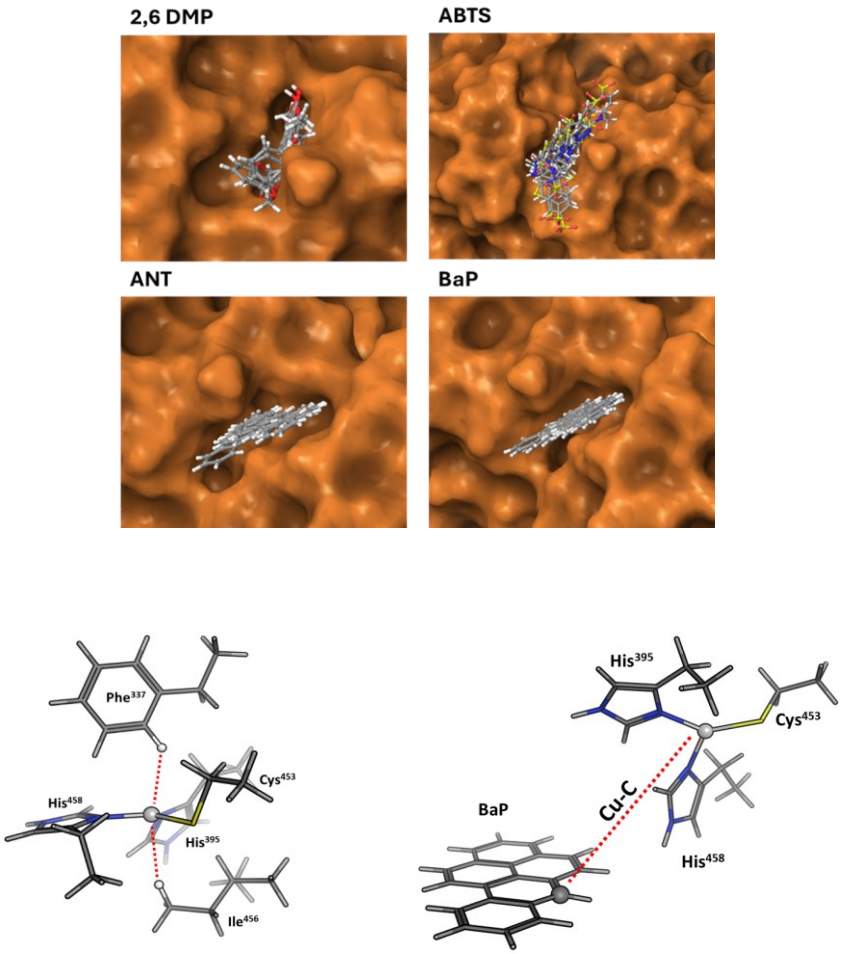

Figure 5.3: The positions of each ligand in the TvL binding pocket.

Almost all the poses for both ligands are superimposed on the first-ranked one (Figure 5.4 top, yellow ligand structures), except for fewer stable dispositions, in which the three-ring common scaffold of ANT and BaP is slightly rotated in the pocket.

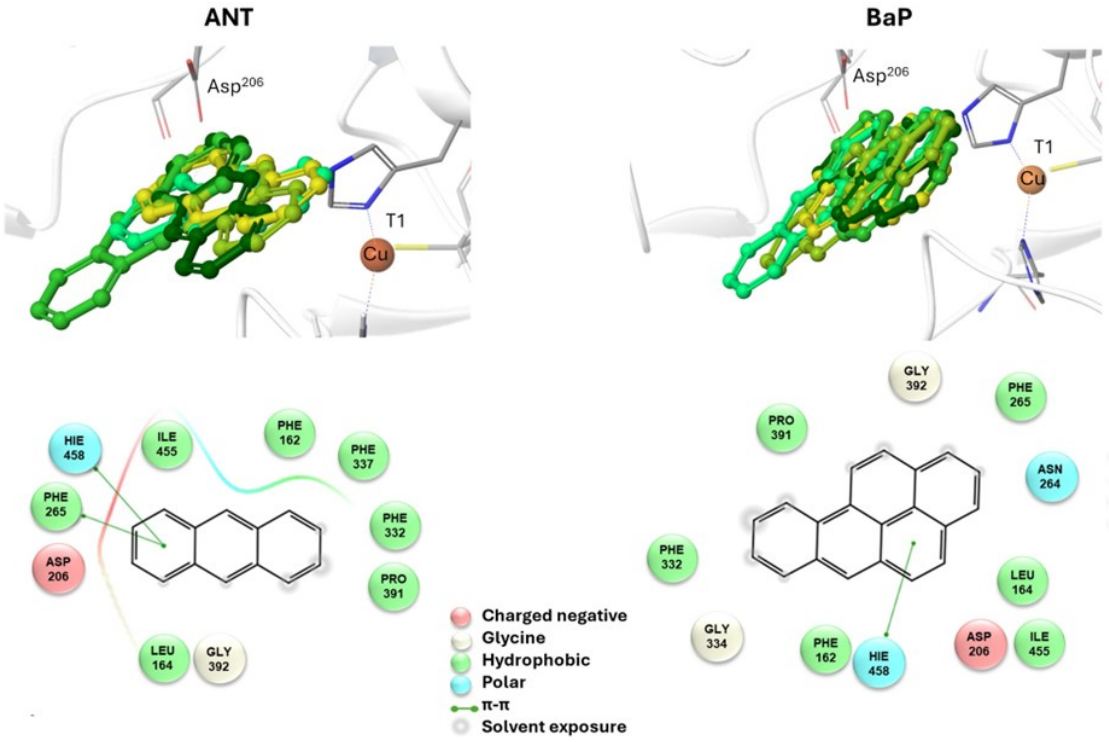

Figure 5.4: Top: a focus on the superimposition of the top-ranked five docking poses of ANT (left) and BaP (right) to TvL (PDB: 1KYA). Bottom: interaction diagrams of the best pose obtained for each substrate to TvL.

Considering the best pose resulting from the docking of each substrate (Figure 5.4), we observed quite similar docking scores (kcal mol^{-1}), equal to −3.61 for ANT and −4.07 for BAP.

The binding is driven by hydrophobic interactions mainly involving the same residues in the two cases (Figure 5.2). Indeed, both ligands form intermolecular interactions with residues H458, D206, I455, L164, F265, G392, P391, F332, and F162; for ANT, an additional interaction with Phe337 was detected, while BaP was also found to interact with G334 and N264. We recall that H458 is also coordinated with T1 Cu while D206 is responsible for proton transfer.

By using the MM/GBSA method, the binding energies of the two substrates slightly diverged, with BaP binding favored by 4.8 kcal mol^{-1} over ANT.

5.4 Exploration of the most likely mechanism with a minimal T1 Cu model

The structures of the experimentally observed quinone species, resulting from ANT and BaP oxidation by laccases, support the mechanistic proposal reported in Figure 5.2 , which involves six consecutive mono-electronic oxidation steps [52]. The C–H bonds involved in oxidation are those at the centrally fused benzene rings, namely C10 and C9 for ANT, and C6 and C12 for BaP (according to IUPAC numbering, Figure 5.4). This mechanism is similar to that reported for the degradation of BaP by P450 peroxidase [77].

The oxidation mechanism consists of three different stages. The first stage involves the two-electron oxidation of the C–H bond, resulting in the formation of phenolic analog intermediates (6-OH BaP and 10-OH ANT). During this stage, the oxidation state of the carbon atom goes from −1 to +1. Subsequently, in the second stage, a successive oxidation occurs, leading to the generation of a di-hydroxy intermediate, which then undergoes further oxidation to quinone species.

Our DFT investigation is focused on the first stage, *i.e.* the two-electron oxidation of the C–H bond to C–OH, since it is the most critical (and thus relevant) of the whole catalytic cycle (Figure 5.4). This stage has been fully characterized following a two-step procedure, in which two T1 Cu models of increasing complexity have been used. In an explorative phase, a minimal model (Figure 5.5) has been scrutinized to provide a thermodynamic picture for the first oxidation, taking BaP as a case study. Indeed, different mechanistic alternatives can underlie this reaction, as also proposed in a previous investigation by Guan *et al* [50].

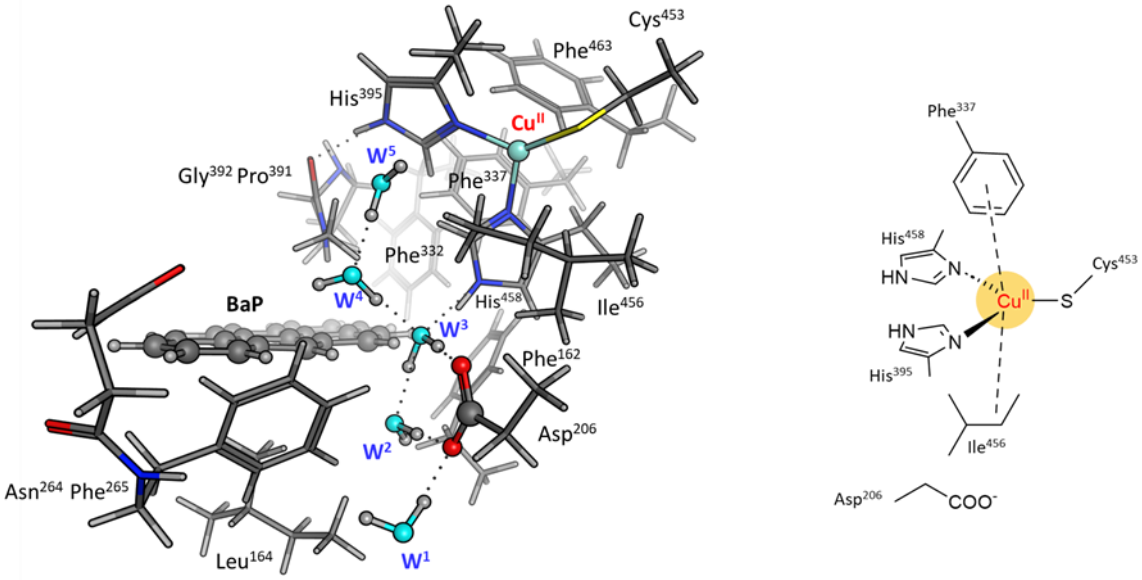

Figure 5.5: Right: structure of the minimal model used for our preliminary calculations, also providing details on the T1 Cu first coordination sphere. Left: structure of the extended cluster model used in this investigation. This model includes 14 residue side chains plus Cu(II), the ligand, and five water molecules (W1–5). The approach of the W4 oxygen atom to the BaP/ANT carbon atom involved in the reaction, defines the reaction coordinate for the first mono-electronic oxidation.

The minimal model only includes the first coordination sphere of T1 Cu, along with the side chain of D206. Three different scenarios for the early oxidation were considered (Figure 5.6):

(A) Oxidation of the ligand at C6 with the formation of a radical cation species;
(B) Hydrogen atom transfer (HAT) process from BaP with the protonation of the D206 side chain;
(C) Oxidation of BaP with the concomitant nucleophilic attack of a water molecule and the protonation of the D206 side chain.

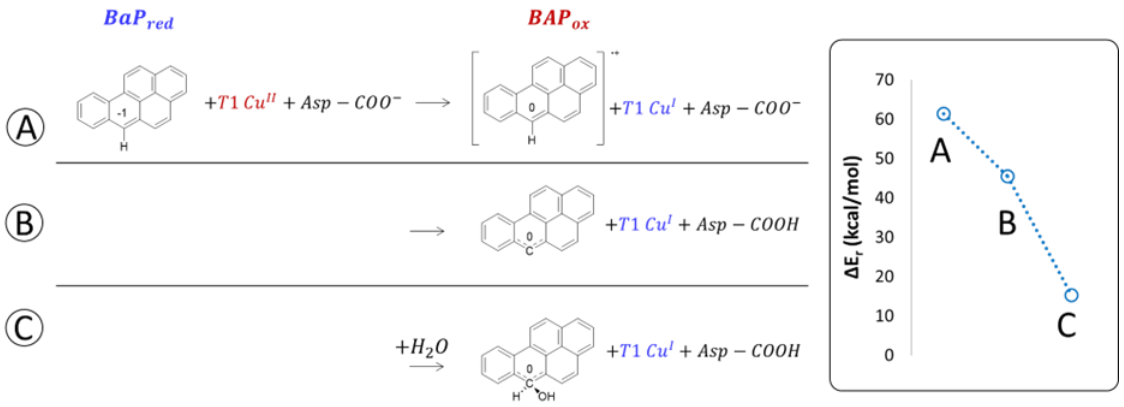

Figure 5.6: DFT energies (in kcal mol−1) for the first oxidation of BaP, computed using the minimal model, are reported in blue. Results are based on three mechanistic hypotheses: (A) monoelectronic oxidation with the formation of a carbocation, (B) HAT process with the formation of a neutral radical species and protonation of D206, (C) nucleophilic attack on the carbocation by a water molecule, and protonation of D206. All shown energy values are obtained from single point calculations at the PBE0-D3/TZVP/COSMO level on BP86-D3/TZVP/COSMO-optimized geometries.

Considering both the first and second hypotheses, we calculated too high reaction energies (>45 kcal mol^{-1}) for these reactive channels to be feasible, so these mechanistic possibilities have been ruled out and excluded from subsequent calculations. According to the third hypothesis, an intriguing intermediate was obtained in which the reactive carbon, undergoing the nucleophilic attack by water, transiently adopts a sp^3 geometry. The estimated reaction energy of 15.6 kcal mol^{-1} suggests that this is the most likely reactive channel for the first oxidation, being thermodynamically feasible.

5.5 Detailed mechanism characterization using an extended model

In a second step, the investigation proceeded by switching to a more comprehensive T1 Cu cluster model (denoted as extended model herein, see figure 5.5), which was used to (i) recalculate and refine the most likely mechanism previously elucidated using the minimal model, (ii) investigate the second oxidation, (iii) complete the calculated energy profiles by also providing kinetic information, (iv) compare the results obtained for BaP with those for ANT to highlight eventual differences in reactivity between the two, and (v) provide a detailed characterization of the structures of all the species involved in the first two-electron oxidation. The extended model was built considering the interaction pattern of the bulkier substrate, *i.e.* BaP, with the enzyme, as obtained from molecular docking. It thus incorporates the eight residues mainly involved in the ligand–TvL interaction and an

additional six residues to ensure the complete coordination of T1 Cu, resulting in a total of 14 residues.

For structural simplification, each residue was restricted to its side chain, originating from the Cα position, unless it exhibited contiguous connectivity (N264–F265 and G392–P391). The total charge of the model is zero. Since water is directly involved in the most likely mechanism, as suggested by preliminary calculations on the minimal model, our extended model also incorporates five water molecules (W1–5) strategically positioned between the D206 side chain and the substrate, forming a "Grotthuss-like" channel to assist proton transfer. Remarkably, the presence and persistence of water molecules in the T1 Cu proximity, in between the metal center and the substrate, was confirmed by MD simulations (see Figure 5.7). W4 is placed in proximity to the reactive C–H bond of both substrates. A visual examination of the model reveals that the C–H bond is in the vicinity of both the Cu T1 (which will undergo reduction by the substrate) and the side chain of D206 (which will accept the proton from the substrate).

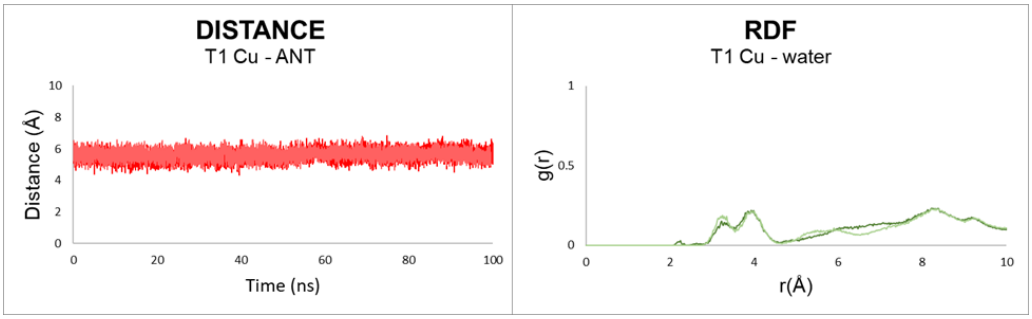

Figure 5.7: Analysis of MD simulations (two replicas) of the enzyme-substrate complex (taking ANT as an example), performed starting from the best docking pose. Left: Distance calculation between ANT and T1 Cu. During both simulations, the substrate maintains essentially the same positioning within the pocket and a distance from T1 Cu similar to the initial conformation. Right: RDF analysis for the T1 Cu and water molecules, calculated for each replica along the entire simulations. This result confirms the presence of water molecules in the first hydration sphere of T1 Cu (2 - 4 Å) in between the metal and the substrate.

By scanning the potential energy surface (PES) along the reaction coordinate for both ligands, we identified the transition state geometry and evaluated the activation barriers associated with both first and second one-electron oxidation (see Figure 5.8).

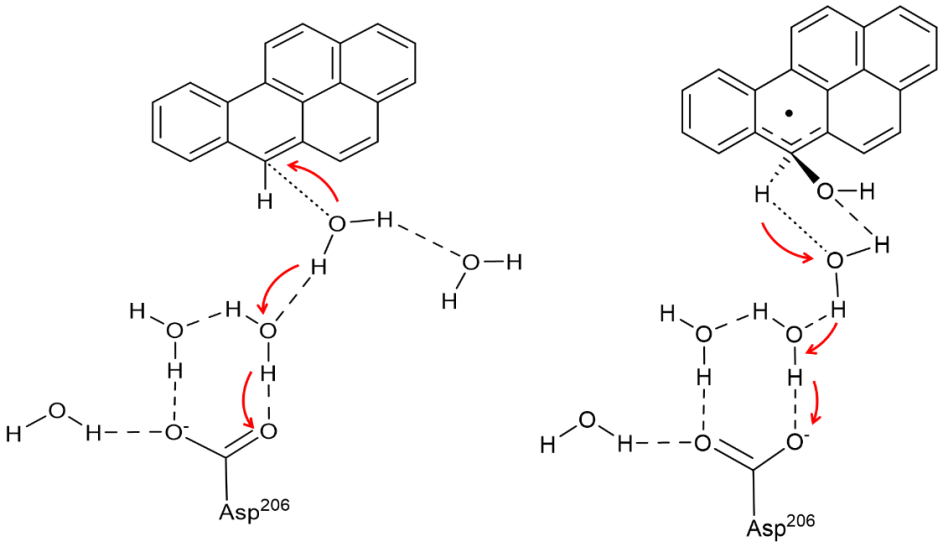

Figure 5.8: Molecular motions along the reaction coordinates for the first (left) and second (right) oxidation steps of BaP. The observed atomic displacements in BaP are equally observed in ANT. The dotted line indicates the interatomic distance explored in the PES scan. The red arrows indicate the atomic displacements observed during the PES scan.

The characterized mechanism is sketched in Figure 5.9. The DFT optimized starting species (R–Cu(ii)) are in S = ½ state and are substantially similar for the two substrates (see Table 5.1) as might be expected based on the small differences between BaP and ANT.

	R-Cu(II) ANT		**R-Cu(II) BaP**		**ANT Intermediate Cu(I)**	**BaP Intermediate Cu(I)**
	BP86	**PBE0**	**BP86**	**PBE0**	**BP86**	**BP86**
Cu-N_H	1.974	1.965	1.972	1.959	1.990	1.992
Cu-N_H	1.975	1.979	1.978	1.976	2.067	2.067
Cu-S_C	2.155	2.142	2.151	2.139	2.192	2.192
Cu-H_F	2.567	2.604	2.630	2.635	2.541	2.539
Cu-H_I	2.708	2.801	2.720	2.824	2.725	2.715
Cu-C	8.210	8.674	8.385	8.614	8.505	8.740

	R-Cu(II)				Int-Cu(I)			
	ANT		**BaP**		**ANT**		**BaP**	
	BP86	**PBE0**	**BP86**	**PBE0**	**BP86**	**PBE0**	**BP86**	**PBE0**
Cu	0.43	0.50	0.43	0.49	0.12	0.00	0.13	0.00
S_C	0.45	0.43	0.45	0.43	0.08	0.00	0.09	0.00
NHi	0.03	0.03	0.04	0.03	0.00	0.00	0.00	0.00
NHi	0.03	0.03	0.03	0.03	0.00	0.00	0.00	0.00
Ligand	0.00	0.00	0.00	0.00	0.80	1.02	0.75	1.01

Table 5.1:NBO spin population (in electrons) for R-Cu(II) large models computed at BP86 and PBE0 level using optimized BP86/TZVP/D3/Cosmo geometries. Large model optimized T1 Cu coordination sphere Cu-ligand bond distances (in Å) for the reactant R-Cu(II) at BP86/TZVP/D3/Cosmo and PBE0/TZVP/D3/Cosmo level of theory; for the Int-Cu(I) at BP86/TZVP/D3/Cosmo. The Cu-H_F and Cu-H_I distances refer to the distances between copper (Cu) and the hydrogen (H) atoms of the side chains of hydrophobic residues, specifically phenylalanine (F) and isoleucine (I), within the first coordination sphere of T1 copper. These distances are calculated based on the shortest distance between one of the hydrogen atoms within the side chain (see figure above).

Indeed, the two substrates are accommodated similarly within the binding pocket, with the ANT molecular plane slightly bent compared to that of BaP by approximately 14 degrees. The T1 Cu site shows the typical trigonally distorted C_{3v} structure, characterized by an unusually short Cu–S_C bond [78,79]. The carbon atom belonging to the carboxylic acid group of the side chain of D206 is distant from T1 Cu 7.7 Å (BaP) and 7.1 Å (ANT).

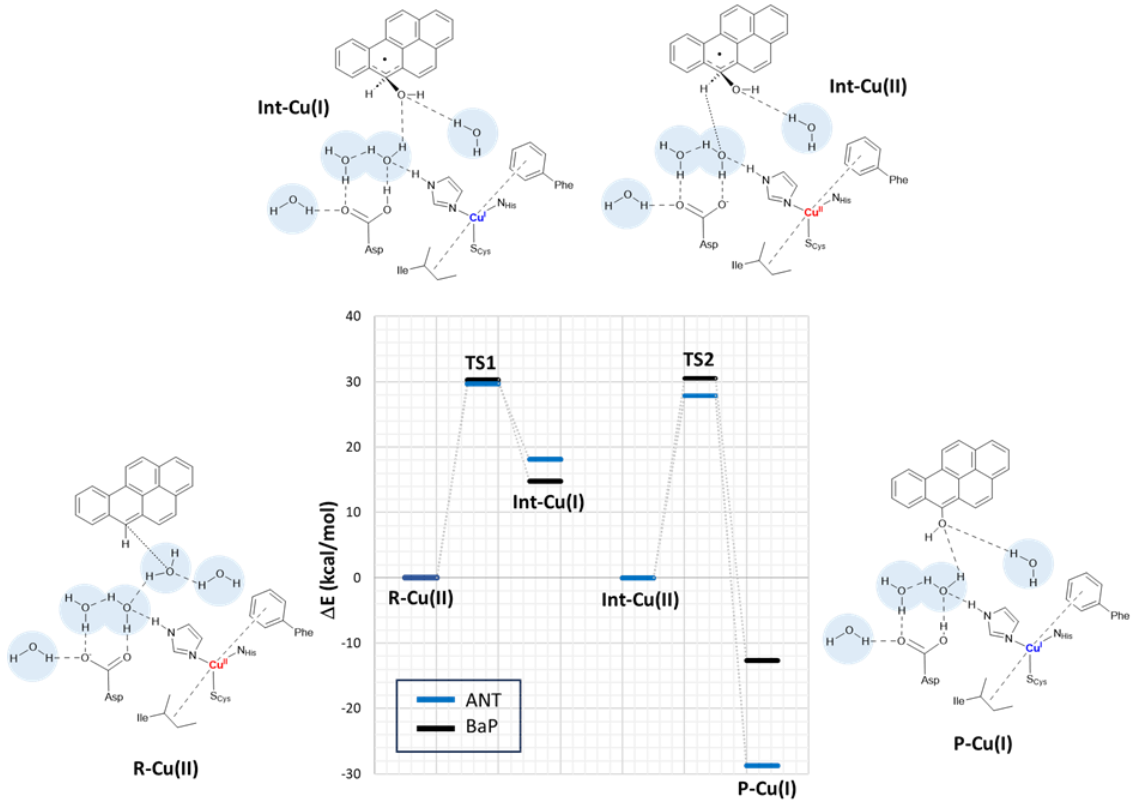

Figure 5.9: Proposed mechanism for the two-electron oxidation of ANT and BAP catalyzed by TvL based on DFT calculations on the extended model. Energy differences (in kcal mol−1) at the PBE0-D3/TZVP/COSMO level are derived from single-point calculations on BP86-D3/TZVP/COSMO optimized structures. The structures of the various forms (reactant R–Cu(II), Cu(I)/Cu(II) intermediate Int–Cu(I) and Int–Cu(II), and product P–Cu(I)) are depicted on the side, considering BaP as example TS1 and TS2 refer to the transition states along the pathway and are associated with the first and second ET from the ligand to T1 Cu. Initially, the ligand is located in the binding pocket near T1 Cu and D206. The latter assists a proton transfer from the substrate, facilitating the ET. The proton transfer is mediated by at least one solvent molecule. The 1e oxidized form of the ligand has a tetrahedral carbon carrying an alcohol function. In the second step, T1 Cu is re-oxidized and D206 deprotonated obtaining a S = 0 broken-symmetry state. Then, in the second electron/proton transfer, T1 Cu is reduced and the D206 side chain protonated again with the formation of a mono-hydroxy product.

Cu and S_C spin densities in the Cu(ii) equilibrium structures are on average 0.50 and 0.43, respectively, in line with previous DFT investigations. The Cu–C distances with the carbon atom formally under oxidation are 8.4 Å (ANT) and 8.5 Å (BaP) (Figure 5.5).

The first oxidation step is a concomitant electron/proton transfer during which we observe the:

(1) electron transfer from the substrate to T1 Cu;

(2) nucleophilic attack of W4 to the substrate mono-oxidized carbon atom. W4 is in a suitable position for nucleophilic attack with a C–O internuclear distance of 3.851 Å and 3.218 Å for ANT and BaP, respectively;
(3) proton transfer from W4 to W3 and then from the latter to the side chain of D206;
(4) approaching W5 in proximity to the substrate, positioning suitably to serve as a bridge in the subsequent oxidation process.

This initial step changes the hybridization of the central carbon atom of the substrate from sp^2 to sp^3, with the formation of a radical intermediate featuring a tetrahedral carbon carrying an alcohol function (Int-Cu(i)). This induces a slight bending of the system, as depicted in Figure 5.10. This structural feature is in line with the Jahn–Teller distortion observed for the benzene radical cation by ab Initio molecular dynamics [80]. T1 Cu is reduced with no spin population on Cu and S_C and with Cu–N_H and Cu–S_C distances similar to those of T1 Cu(II) [81]. The radical is entirely delocalized among the carbon atoms on the substrate, as illustrated in Figure 5.10. In both substrates, particularly with ANT, we observe the localization of a substantial portion of the spin population on the C10 atom positioned opposite to the C6–OH, consistent with the electronic structure of the anthracene radical cation [79,80]. This carbon atom will ultimately be responsible for the formation of the final quinone species in the 6-electron oxidation process (Figure 5.2).

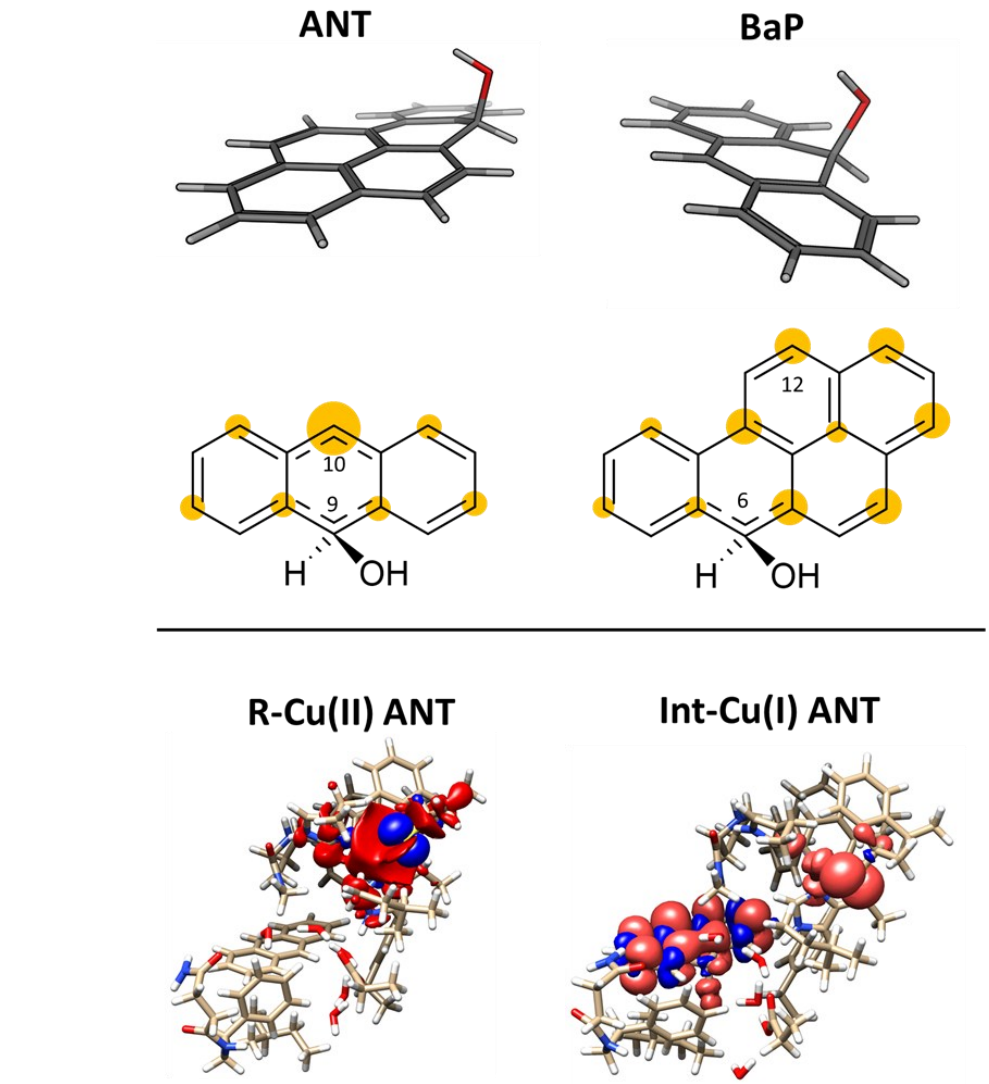

Figure 5.10: On the top: molecular shape and below spin populations of mono-oxidized ligand in the Int–Cu(I) intermediate for ANT and BaP. The highlighted areas in yellow on the carbon atoms are qualitatively proportional to the PBE0 spin population on that nucleus. At the bottom, the total spin density for R–Cu(II) and Int–Cu(I) is shown, computed from the PBE0 level wave function at the minimum geometry.

The structures of the TS1 transition states (Figure 5.11) for both substrates exhibit remarkable similarity, with their electronic structure being defined by a copper spin population, enabling us to attribute the redox state to $Cu^{1.5}$.

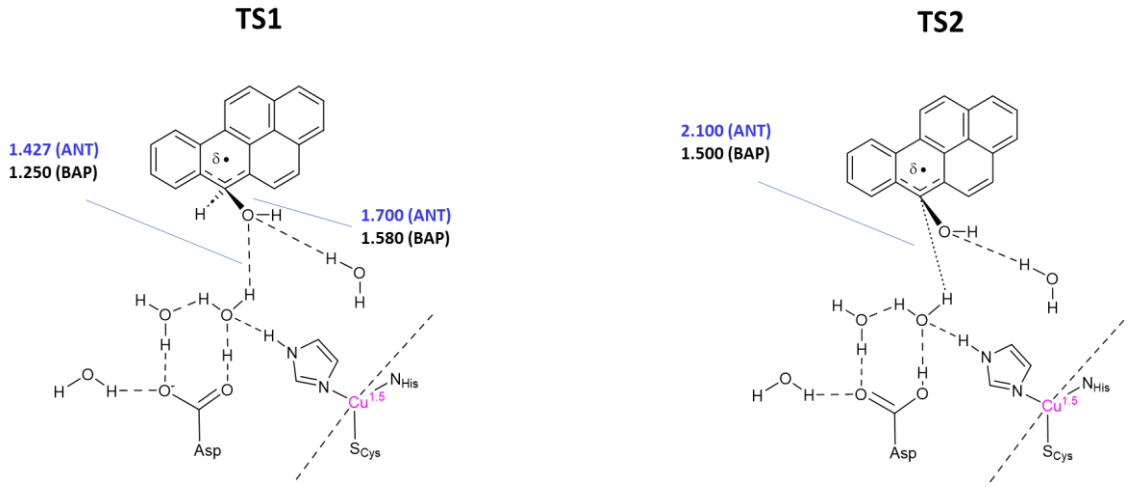

Figure 5.11: Geometries of the first and second transition state (TS1 and TS2) along the reaction coordinates for the first and second oxidation steps. In both cases the NBO spin population computed at PBE0/TZVP/D3 COSMO ε=80 DFT level of the copper ion is compatible with the $Cu^{1.5}$ redox state. In the case of TS1 for BaP, a spin population of 0.6 is observed on the ligand, indicating that Cu is slightly more reduced compared to ANT.

The reaction profiles for ANT and BaP during the first ET exhibits remarkable similarity. The values show minimal deviation between BP86 to PBE0 results (Tables 5.2 and 5.3). On average, the estimated activation energy remains constant at approximately 30 kcal mol^{-1}, indicating a kinetically impeded process. This result suggests that, even invoking the most likely mechanism among those investigated, PAH first oxidation is not effective.

	TS1		**TS2**	
	ANT	**BaP**	**ANT**	**BaP**
Cu-N_H	2.002	1.996	2.001	1.972
Cu-N_H	2.007	2.047	2.017	1.977
Cu-S_C	2.184	2.193	2.186	2.156
Cu-H_F	2.594	2.630	2.532	2.608
Cu-H_I	2.702	2.814	2.612	2.673

Table 5.2: Transition state Cu-X (in Å) optimized bond distances at BP86/TZVP/D3/COSMO level.

Level of theory	BP86 TZVP/D3/Cosmo		PBE0 TZVP/D3/Cosmo	
	ANT	**BaP**	**ANT**	**BaP**
$\Delta E_1^{\#}$	31.1	29.1	29.7	30.3
$\Delta E_{r,1ox}$	26.4	20.1	18.1	14.8
$\Delta E_2^{\#}$	19.3	28.1	27.9	30.5
$\Delta E_{r,2ox}$	-48.8	-31.7	-46.8	-27.5

Table 5.3: Reaction energy barriers (in kcal mol^{-1}) computed at BP86/TZVP/D3/Cosmo level and PBE0/TZVP/D3/Cosmo level from BP86/TZVP/D3/Cosmo level optimized geometries. $\Delta E_1^{\#}$ and $\Delta E_2^{\#}$ are the energy barrier between the R-Cu(II) and Int-Cu(I) ($\Delta E_1^{\#}$) and between Int-Cu(II)/P-Cu(I).

At this stage, the model exhibits one fewer water molecule due to the dissociation of W4 (one proton migrates to the D206 side chain, while the OH– ion is now bound to the substrate). The second substrate oxidation requires the restoring of a Cu(ii) center, with an electron transfer towards the TNC from the reduced T1 Cu(i), and the deprotonation of the D206 side chain. This step was modeled simply by removing one electron from the system and the proton from the D206 side chain and finally re-optimizing the geometry. The resulting structure (Int–Cu(ii)) is a S = 0 broken symmetry solution, in which one unpaired electron is localized on T1 Cu(ii) and the other on the mono-oxidized substrate. The second 1e oxidation of the substrate, shown in Figure 5.9, involves a hydrogen atom abstraction from the C–H bond of the tetrahedral carbon atom of the radical species during which we observe the:

(1) reduction of T1 Cu;
(2) proton transfer from the substrate to the D206 side chain *via* the W5 water molecule;
(3) formation of the hydroxy derivative of the substrate.

Again, we evaluated the activation energy of this step for both substrates by scanning the PES of each system along the reaction coordinate that identifies the overall process. During the second electron transfer process, the activation energy barrier for ANT, albeit slightly, is lowered by 2.1 kcal mol^{-1} compared to that computed for BaP. Furthermore, the reaction energy for ANT is significantly more negative, surpassing that of BaP by as much as 19.3 kcal mol^{-1}.

The overall energy profiles depicted in Figure 5.9 are compatible with a kinetically hindered process, since they entail activation barriers as high as 30 kcal mol^{-1} for both BaP and ANT. In general, extended cluster models such as those adopted here

are inherently more precise in the description of the real system, encompassing first- and second-coordination sphere effects [57]. Nevertheless, large models with a consistent number of constraints may result, in some cases, in artifactual rigidity during geometry optimizations, which could result in slightly overestimated energy barriers. In any case, even accounting for hypothetical overestimation of barriers, our calculations clearly suggest that *direct* PAH oxidation (*i.e.* in the absence of mediators) should be minimal. This agrees with the observation made by Johannes and Majcherczyk [34] that the initial oxidation step (resulting in the formation of a radical species) is endergonic, as the standard reduction potential of the $PAH^{\cdot+}$/PAH pair is more positive than that of T1 Cu, rendering it kinetically unfavorable. Such a process may remain chemically feasible if a subsequent irreversible step removes one of the reaction products, in this case, the reactive intermediate $PAH^{\cdot+}$ radical species.

Our results nicely match the low yields reported in the literature for BaP oxidation by TvL (and by other fungal laccases as well, see Table 5.4), which indicate that the process is reasonably characterized by high activation barriers approaching the threshold beyond which a reaction becomes kinetically unfeasible.

Organism	Experimental condition with no mediator	% ox ANT	% ox BaP	Reference
Trametes versicolor	27 °C, pH=5, Tween80, 24h	85%	<2%	(Collins et al. 1996)
Trametes versicolor	pH 5.0, RT, 72h	18%	19%	(Majcherczyk, Johannes, and Hüttermann 1998)
Marasmius quercophilus	pH 4.5	30%		(Farnet et al. 2009)
Trametes versicolor	pH 4.5, Tween80	73.8 %	5.3 %	(Johannes and Majcherczyk 2000)
Pycnoporus cinnabarinus	pH 5, Tween80	65%		(Cañas et al. 2007)
Trametes versicolor	Immobilized enzyme, pH 4.5, Tween80	17%	19%	(Dodor, Hwang, and Ekunwe 2004)
Rigidoporus lignosus	pH 4.5, 30°C, 72h	9%		(Cambria et al. 2008)
Pleurotus ostreatus D1	pH 4.5	0%		(Natalia N. Pozdnyakova et al. 2006)
yellow laccase from *Pleurotus ostreatus D1*	pH 6, Tween80	95%		(N.N. Pozdnyakova, Rodakiewicz-Nowak, and Turkovskaya 2004)

Table 5.4: Summary of the ANT and BaP oxidation experiment with fungal laccases in the absence of a mediator. % ox refers to the percentage of oxidized quinone product with respect to the control without enzyme

Conversely, on the basis of our energy profiles, we could not rationalize the higher yields observed for ANT oxidation. Consequently, additional remarks are needed, specifically delving into the ANT and BaP oxidation experiments already present in the literature [82]. For instance, as it follows from Table 5.3, the presence of a surfactant (such as Tween 80) can enhance ANT oxidation yields by TvL and other laccases. This is intriguing in light of the recent suggestion by Yang *et al* [83]. that Tween 80 may also act as a mediator, facilitating substrate oxidation. It is thus possible to suppose that in some cases, depending on different combinations of substrate nature and experimental conditions, oxidation is favored not so much by an effective positioning of the substrate in the ligand-binding pocket, but by the presence of the surfactant, which may act as a mediator.

5.6 Conclusions

The present study provides a comprehensive insight into the oxidation of anthracene (ANT) and benzo[a]pyrene (BaP) by the T1 Cu catalytic site of *Trametes versicolor laccase* (TvL), shedding light on the complex molecular mechanisms underlying these reactions. To date, the majority of computational studies on laccases have primarily focused on the reactivity of the T2/T3 trinuclear cluster [7,50,81], while the T1 Cu site, which is responsible for substrate oxidation, has received considerably less attention. Furthermore, previous mechanistic studies often analyzed substrate oxidation without explicitly modeling the interaction between the substrate and the enzyme's binding pocket, leaving a significant gap in our understanding of the enzymatic environment's role. In this context, the present work represents a pioneering investigation, providing for the first time mechanistic insights into the oxidation of aromatic hydrocarbons at the T1 Cu site.

The study integrates multiple computational approaches, combining molecular docking with Density Functional Theory (DFT) calculations on progressively detailed T1 Cu models. In the first stage, molecular docking simulations were employed to explore the binding of ANT and BaP within the T1 Cu pocket. The results revealed that both PAHs can interact effectively with the enzyme's active site, exhibiting comparable affinities, with a slightly higher binding preference observed for BaP relative to ANT.

Subsequently, DFT calculations using a minimal cluster model of T1 Cu enabled the investigation of different mechanistic hypotheses previously proposed for the initial one-electron ($1e^-$) oxidation step, which represents the most critical stage of catalysis. These calculations allowed us to identify the mechanistic pathway most likely to occur under physiological conditions. Our findings indicate that the only thermodynamically feasible route involves a water molecule acting as a nucleophile toward the oxidized carbon of the substrate. This role of water is further

corroborated by Molecular Dynamics (MD) simulations, which consistently show the presence of water molecules in the T1 Cu pocket, positioned between the copper center and the ligand.

To evaluate the kinetic feasibility of this pathway, an extended DFT model was employed, providing complete energy profiles for the two-electron ($2e^-$) oxidation of both ANT and BaP. In the absence of redox mediators, the oxidation of both substrates is characterized by high activation barriers, and no energetic preference emerges for either substrate. These results underscore the inherent difficulty of direct PAH oxidation and highlight the potential importance of mediators in facilitating the process.

These findings point to the necessity for future studies to investigate the specific role of mediators of diverse chemical nature in laccase-catalyzed oxidation, particularly at the molecular level. The mechanistic understanding of mediator oxidation by T1 Cu, followed by electron transfer to various PAHs, remains largely unexplored in the literature. The present computational study establishes a solid foundation for addressing this knowledge gap and provides a framework for more detailed investigations.

Finally, this work delivers novel insights into the C–H bond oxidation mechanism by laccases, offering mechanistic principles that can be generalized to other classes of hydrocarbons. These insights have the potential to inspire future theoretical and experimental studies on the enzymatic oxidation of a wide range of aromatic pollutants, as well as on hydrocarbon-based materials such as plastics, thus broadening the scope and applicability of laccase biocatalysis in environmental and industrial contexts [84].

References

1. Chauhan, P.S.; Goradia, B.; Saxena, A. Bacterial Laccase: Recent Update on Production, Properties and Industrial Applications. 3 Biotech 2017, 7, 323, doi:10.1007/s13205-017-0955-7.
2. Baldrian, P. Fungal Laccases – Occurrence and Properties. FEMS Microbiol Rev 2006, 30, 215–242, doi:10.1111/j.1574-4976.2005.00010.x.
3. Zeng, J.; Lin, X.; Zhang, J.; Li, X.; Wong, M.H. Oxidation of Polycyclic Aromatic Hydrocarbons by the Bacterial Laccase CueO from E. Coli. Appl Microbiol Biotechnol 2011, 89, 1841–1849, doi:10.1007/s00253-010-3009-1.
4. Zeng, J.; Zhu, Q.; Wu, Y.; Lin, X. Oxidation of Polycyclic Aromatic Hydrocarbons Using Bacillus Subtilis CotA with High Laccase Activity and Copper Independence. Chemosphere 2016, 148, 1–7, doi:10.1016/j.chemosphere.2016.01.019.
5. Loi, M.; Glazunova, O.; Fedorova, T.; Logrieco, A.F.; Mulè, G. Fungal Laccases: The Forefront of Enzymes for Sustainability. Journal of Fungi 2021, 7, 1048, doi:10.3390/jof7121048.
6. Aza, P.; Camarero, S. Fungal Laccases: Fundamentals, Engineering and Classification Update. Biomolecules 2023, 13, 1716, doi:10.3390/biom13121716.
7. Singh, D.; Gupta, N. Microbial Laccase: A Robust Enzyme and Its Industrial Applications. Biologia (Bratisl) 2020, 75, 1183–1193, doi:10.2478/s11756-019-00414-9.
8. da Rocha, A.B.; de Aquino Saraiva, R.; de Siqueira, V.M.; Yogui, G.T.; de Souza Bezerra, R.; de Assis, C.R.D.; Sousa, M.S.B.; de Souza Buarque, D. Shrimp Laccase Degrades Polycyclic Aromatic Hydrocarbons from an Oil Spill Disaster in Brazil: A Tool for Marine Environmental Bioremediation. Mar Pollut Bull 2023, 194, 115445, doi:10.1016/j.marpolbul.2023.115445.
9. Jones, S.M.; Solomon, E.I. Electron Transfer and Reaction Mechanism of Laccases. Cellular and Molecular Life Sciences 2015, 72, 869–883, doi:10.1007/s00018-014-1826-6.
10. Zhu, Y.; Zhang, Y.; Zhan, J.; Lin, Y.; Yang, X. Axial Bonds at the T1 Cu Site of Thermus Thermophilus <scp>SG</Scp> 0.5 <scp>JP</Scp> 17-16 Laccase Influence Enzymatic Properties. FEBS Open Bio 2019, 9, 986–995, doi:10.1002/2211-5463.12633.
11. Mot, A.C.; Silaghi-Dumitrescu, R. Laccases: Complex Architectures for One-Electron Oxidations. Biochemistry (Moscow) 2012, 77, 1395–1407, doi:10.1134/S0006297912120085.
12. Solomon, E.I.; Augustine, A.J.; Yoon, J. O2 Reduction to H2O by the Multicopper Oxidases. Dalton Transactions 2008, 3921, doi:10.1039/b800799c.
13. Arregui, L.; Ayala, M.; Gómez-Gil, X.; Gutiérrez-Soto, G.; Hernández-Luna, C.E.; Herrera de los Santos, M.; Levin, L.; Rojo-Domínguez, A.; Romero-Martínez, D.; Saparrat,

M.C.N.; et al. Laccases: Structure, Function, and Potential Application in Water Bioremediation. Microb Cell Fact 2019, 18, 200, doi:10.1186/s12934-019-1248-0.

14. Yang, J.; Yang, X.; Lin, Y.; Ng, T.B.; Lin, J.; Ye, X. Laccase-Catalyzed Decolorization of Malachite Green: Performance Optimization and Degradation Mechanism. PLoS One 2015, 10, e0127714, doi:10.1371/journal.pone.0127714.

15. Jeyabalan, J.; Veluchamy, A.; V, V.P.; Kumar, A.; Chandrasekar, R.; Narayanasamy, S. A Review on the Laccase Assisted Decolourization of Dyes: Recent Trends and Research Progress. J Taiwan Inst Chem Eng 2023, 151, 105081, doi:10.1016/j.jtice.2023.105081.

16. Frasconi, M.; Favero, G.; Boer, H.; Koivula, A.; Mazzei, F. Kinetic and Biochemical Properties of High and Low Redox Potential Laccases from Fungal and Plant Origin. Biochimica et Biophysica Acta (BBA) - Proteins and Proteomics 2010, 1804, 899–908, doi:10.1016/j.bbapap.2009.12.018.

17. Santo, M.; Weitsman, R.; Sivan, A. The Role of the Copper-Binding Enzyme – Laccase – in the Biodegradation of Polyethylene by the Actinomycete Rhodococcus Ruber. Int Biodeterior Biodegradation 2013, 84, 204–210, doi:10.1016/j.ibiod.2012.03.001.

18. Zampolli, J.; Mangiagalli, M.; Vezzini, D.; Lasagni, M.; Ami, D.; Natalello, A.; Arrigoni, F.; Bertini, L.; Lotti, M.; Di Gennaro, P. Oxidative Degradation of Polyethylene by Two Novel Laccase-like Multicopper Oxidases from Rhodococcus Opacus R7. Environ Technol Innov 2023, 32, 103273, doi:10.1016/j.eti.2023.103273.

19. Astolfi, P.; Brandi, P.; Galli, C.; Gentili, P.; Gerini, M.F.; Greci, L.; Lanzalunga, O. New Mediators for the Enzyme Laccase: Mechanistic Features and Selectivity in the Oxidation of Non-Phenolic Substrates. New Journal of Chemistry 2005, 29, 1308, doi:10.1039/b507657a.

20. Majeau, J.-A.; Brar, S.K.; Tyagi, R.D. Laccases for Removal of Recalcitrant and Emerging Pollutants. Bioresour Technol 2010, 101, 2331–2350, doi:10.1016/j.biortech.2009.10.087.

21. Tadesse, M.A.; D'Annibale, A.; Galli, C.; Gentili, P.; Sergi, F. An Assessment of the Relative Contributions of Redox and Steric Issues to Laccase Specificity towards Putative Substrates. Org Biomol Chem 2008, 6, 868, doi:10.1039/b716002j.

22. Galli, C.; Madzak, C.; Vadalà, R.; Jolivalt, C.; Gentili, P. Concerted Electron/Proton Transfer Mechanism in the Oxidation of Phenols by Laccase. ChemBioChem 2013, 14, 2500–2505, doi:10.1002/cbic.201300531.

23. Monza, E.; Lucas, M.F.; Camarero, S.; Alejaldre, L.C.; Martínez, A.T.; Guallar, V. Insights into Laccase Engineering from Molecular Simulations: Toward a Binding-Focused Strategy. J Phys Chem Lett 2015, 6, 1447–1453, doi:10.1021/acs.jpclett.5b00225.

24. Pardo, I.; Santiago, G.; Gentili, P.; Lucas, F.; Monza, E.; Medrano, F.J.; Galli, C.; Martínez, A.T.; Guallar, V.; Camarero, S. Re-Designing the Substrate Binding Pocket of Laccase for Enhanced Oxidation of Sinapic Acid. Catal Sci Technol 2016, 6, 3900–3910, doi:10.1039/C5CY01725D.

25. Lucas, M.F.; Monza, E.; Jørgensen, L.J.; Ernst, H.A.; Piontek, K.; Bjerrum, M.J.; Martinez, Á.T.; Camarero, S.; Guallar, V. Simulating Substrate Recognition and Oxidation in Laccases: From Description to Design. J Chem Theory Comput 2017, 13, 1462–1467, doi:10.1021/acs.jctc.6b01158.

26. Mehra, R.; Kepp, K.P. Contribution of Substrate Reorganization Energies of Electron Transfer to Laccase Activity. Physical Chemistry Chemical Physics 2019, 21, 15805–15814, doi:10.1039/C9CP01012B.

27. Premnath, N.; Mohanrasu, K.; Guru Raj Rao, R.; Dinesh, G.H.; Prakash, G.S.; Ananthi, V.; Ponnuchamy, K.; Muthusamy, G.; Arun, A. A Crucial Review on Polycyclic Aromatic Hydrocarbons - Environmental Occurrence and Strategies for Microbial Degradation. Chemosphere 2021, 280, 130608, doi:10.1016/j.chemosphere.2021.130608.

28. Kadri, T.; Rouissi, T.; Kaur Brar, S.; Cledon, M.; Sarma, S.; Verma, M. Biodegradation of Polycyclic Aromatic Hydrocarbons (PAHs) by Fungal Enzymes: A Review. Journal of Environmental Sciences 2017, 51, 52–74, doi:10.1016/j.jes.2016.08.023.

29. Collins, P.J.; Kotterman, M.; Field, J.A.; Dobson, A. Oxidation of Anthracene and Benzo[a]Pyrene by Laccases from Trametes Versicolor. Appl Environ Microbiol 1996, 62, 4563–4567, doi:10.1128/aem.62.12.4563-4567.1996.

30. Johannes, C.; Majcherczyk, A.; Hüttermann, A. Degradation of Anthracene by Laccase of Trametes Versicolor in the Presence of Different Mediator Compounds. Appl Microbiol Biotechnol 1996, 46, 313–317, doi:10.1007/s002530050823.

31. Bezalel, L.; Hadar, Y.; Cerniglia, C.E. Mineralization of Polycyclic Aromatic Hydrocarbons by the White Rot Fungus Pleurotus Ostreatus. Appl Environ Microbiol 1996, 62, 292–295, doi:10.1128/aem.62.1.292-295.1996.

32. Pickard, M.A.; Roman, R.; Tinoco, R.; Vazquez-Duhalt, R. Polycyclic Aromatic Hydrocarbon Metabolism by White Rot Fungi and Oxidation by Coriolopsis Gallica UAMH 8260 Laccase. Appl Environ Microbiol 1999, 65, 3805–3809, doi:10.1128/AEM.65.9.3805-3809.1999.

33. Majcherczyk, A.; Johannes, C.; Hüttermann, A. Oxidation of Polycyclic Aromatic Hydrocarbons (PAH) by Laccase of Trametes Versicolor. Enzyme Microb Technol 1998, 22, 335–341, doi:10.1016/S0141-0229(97)00199-3.

34. Johannes, C.; Majcherczyk, A. Natural Mediators in the Oxidation of Polycyclic Aromatic Hydrocarbons by Laccase Mediator Systems. Appl Environ Microbiol 2000, 66, 524–528, doi:10.1128/AEM.66.2.524-528.2000.

35. Pozdnyakova, N.N.; Rodakiewicz-Nowak, J.; Turkovskaya, O. V.; Haber, J. Oxidative Degradation of Polyaromatic Hydrocarbons Catalyzed by Blue Laccase from Pleurotus Ostreatus D1 in the Presence of Synthetic Mediators. Enzyme Microb Technol 2006, 39, 1242–1249, doi:10.1016/j.enzmictec.2006.03.009.

36. Cañas, A.I.; Alcalde, M.; Plou, F.; Martínez, M.J.; Martínez, Á.T.; Camarero, S. Transformation of Polycyclic Aromatic Hydrocarbons by Laccase Is Strongly Enhanced

by Phenolic Compounds Present in Soil. Environ Sci Technol 2007, 41, 2964–2971, doi:10.1021/es062328j.

37. Camarero, S.; CaÑas, A.I.; Nousiainen, P.; Record, E.; Lomascolo, A.; MartÍnez, M.J.; MartÍnez, Á.T. P -Hydroxycinnamic Acids as Natural Mediators for Laccase Oxidation of Recalcitrant Compounds. Environ Sci Technol 2008, 42, 6703–6709, doi:10.1021/es8008979.

38. Cambria, M.T.; Minniti, Z.; Librando, V.; Cambria, A. Degradation of Polycyclic Aromatic Hydrocarbons by Rigidoporus Lignosus and Its Laccase in the Presence of Redox Mediators. Appl Biochem Biotechnol 2008, 149, 1–8, doi:10.1007/s12010-007-8100-4.

39. Zeng, J.; Zhu, Q.; Wu, Y.; Shan, J.; Ji, R.; Lin, X. Oxidation of Benzo[a]Pyrene by Laccase in Soil Enhances Bound Residue Formation and Reduces Disturbance to Soil Bacterial Community Composition. Environmental Pollution 2018, 242, 462–469, doi:10.1016/j.envpol.2018.06.075.

40. Dodor, D.E.; Hwang, H.-M.; Ekunwe, S.I.N. Oxidation of Anthracene and Benzo[a]Pyrene by Immobilized Laccase from Trametes Versicolor. Enzyme Microb Technol 2004, 35, 210–217, doi:10.1016/j.enzmictec.2004.04.007.

41. Hu, X.; Wang, P.; Hwang, H. Oxidation of Anthracene by Immobilized Laccase from Trametes Versicolor. Bioresour Technol 2009, 100, 4963–4968, doi:10.1016/j.biortech.2009.03.089.

42. Bautista, L.F.; Morales, G.; Sanz, R. Biodegradation of Polycyclic Aromatic Hydrocarbons (PAHs) by Laccase from Trametes Versicolor Covalently Immobilized on Amino-Functionalized SBA-15. Chemosphere 2015, 136, 273–280, doi:10.1016/j.chemosphere.2015.05.071.

43. Soo-Jin Oxidation of Polycyclic Aromatic Hydrocarbons by Laccase of Coriolus Hirsutus. Biotechnol Lett 2002, 24, 1337–1340.

44. Farnet, A.M.; Gil, G.; Ruaudel, F.; Chevremont, A.C.; Ferre, E. Polycyclic Aromatic Hydrocarbon Transformation with Laccases of a White-Rot Fungus Isolated from a Mediterranean Schlerophyllous Litter. Geoderma 2009, 149, 267–271, doi:10.1016/j.geoderma.2008.12.011.

45. Vipotnik, Z.; Michelin, M.; Tavares, T. Biodegradation of Chrysene and Benzo[a]Pyrene and Removal of Metals from Naturally Contaminated Soil by Isolated Trametes Versicolor Strain and Laccase Produced Thereof. Environ Technol Innov 2022, 28, 102737, doi:10.1016/j.eti.2022.102737.

46. Wang, L.; Tan, Y.; Sun, S.; Zhou, L.; Wu, G.; Shao, Y.; Wang, M.; Xin, Z. Improving Degradation of Polycyclic Aromatic Hydrocarbons by Bacillus Atrophaeus Laccase Fused with Vitreoscilla Hemoglobin and a Novel Strong Promoter Replacement. Biology (Basel) 2022, 11, 1129, doi:10.3390/biology11081129.

47. Humel, S.; Führer, B.; Svetitsch, M.; Mayer, P.; Loibner, A.P. Targeting Sorbed PAHs in Historically Contaminated Soil – Can Laccase Mediator Systems or Fenton's Reagent

Remove Inaccessible PAHs? J Hazard Mater 2023, 443, 130286, doi:10.1016/j.jhazmat.2022.130286.

48. Sorrentino, I.; Carrière, M.; Jamet, H.; Stanzione, I.; Piscitelli, A.; Giardina, P.; Le Goff, A. The Laccase Mediator System at Carbon Nanotubes for Anthracene Oxidation and Femtomolar Electrochemical Biosensing. Analyst 2022, 147, 897–904, doi:10.1039/D1AN02091A.

49. Bueno-Nieto, C.; Cortés-Antiquera, R.; Espina, G.; Atalah, J.; Villanueva, J.; Aliaga, C.; Zuñiga, G.E.; Blamey, J.M. Biochemical and Spectroscopic Characterization of a Recombinant Laccase from Thermoalkaliphilic Bacillus Sp. FNT with Potential for Degradation of Polycyclic Aromatic Hydrocarbons (PAHs). Catalysts 2023, 13, 763, doi:10.3390/catal13040763.

50. Guan, Z.-B.; Luo, Q.; Wang, H.-R.; Chen, Y.; Liao, X.-R. Bacterial Laccases: Promising Biological Green Tools for Industrial Applications. Cellular and Molecular Life Sciences 2018, 75, 3569–3592, doi:10.1007/s00018-018-2883-z.

51. Agustin, M.B.; de Carvalho, D.M.; Lahtinen, M.H.; Hilden, K.; Lundell, T.; Mikkonen, K.S. Laccase as a Tool in Building Advanced Lignin-Based Materials. ChemSusChem 2021, 14, 4615–4635, doi:10.1002/cssc.202101169.

52. Farran, R.; Mekmouche, Y.; Vo, N.T.; Herrero, C.; Quaranta, A.; Sircoglou, M.; Banse, F.; Rousselot-Pailley, P.; Simaan, A.J.; Aukauloo, A.; et al. Tracking Light-Induced Electron Transfer toward O2 in a Hybrid Photoredox-Laccase System. iScience 2021, 24, 102378, doi:10.1016/j.isci.2021.102378.

53. Mate, D.M.; Alcalde, M. Laccase Engineering: From Rational Design to Directed Evolution. Biotechnol Adv 2015, 33, 25–40, doi:10.1016/j.biotechadv.2014.12.007.

54. Lund, H.; Tegnér, C.; Takman, B. Electroorganic Preparations. IV. Oxidation of Aromatic Hydrocarbons. Acta Chem Scand 1957, 11, 1323–1330, doi:10.3891/acta.chem.scand.11-1323.

55. Davis, A.P.; Fry, A.J. Experimental and Computed Absolute Redox Potentials of Polycyclic Aromatic Hydrocarbons Are Highly Linearly Correlated Over a Wide Range of Structures and Potentials. J Phys Chem A 2010, 114, 12299–12304, doi:10.1021/jp106088n.

56. Sheng, X.; Himo, F. The Quantum Chemical Cluster Approach in Biocatalysis. Acc Chem Res 2023, 56, 938–947, doi:10.1021/acs.accounts.2c00795.

57. Himo, F.; de Visser, S.P. Status Report on the Quantum Chemical Cluster Approach for Modeling Enzyme Reactions. Commun Chem 2022, 5, 29, doi:10.1038/s42004-022-00642-2.

58. Bertrand, T.; Jolivalt, C.; Briozzo, P.; Caminade, E.; Joly, N.; Madzak, C.; Mougin, C. Crystal Structure of a Four-Copper Laccase Complexed with an Arylamine: Insights into Substrate Recognition and Correlation with Kinetics ,. Biochemistry 2002, 41, 7325–7333, doi:10.1021/bi0201318.

59. Genheden, S.; Ryde, U. The MM/PBSA and MM/GBSA Methods to Estimate Ligand-Binding Affinities. Expert Opin Drug Discov 2015, 10, 449–461, doi:10.1517/17460441.2015.1032936.

60. Ahlrichs, R.; Bär, M.; Häser, M.; Horn, H.; Kölmel, C. Electronic Structure Calculations on Workstation Computers: The Program System Turbomole. Chem Phys Lett 1989, 162, 165–169, doi:10.1016/0009-2614(89)85118-8.

61. Becke, A.D. Density-Functional Exchange-Energy Approximation with Correct Asymptotic Behavior. Phys Rev A (Coll Park) 1988, 38, 3098–3100, doi:10.1103/PhysRevA.38.3098.

62. Perdew, J.P. Density-Functional Approximation for the Correlation Energy of the Inhomogeneous Electron Gas. Phys Rev B 1986, 33, 8822–8824, doi:10.1103/PhysRevB.33.8822.

63. Eichkorn, K.; Weigend, F.; Treutler, O.; Ahlrichs, R. Auxiliary Basis Sets for Main Row Atoms and Transition Metals and Their Use to Approximate Coulomb Potentials. Theoretical Chemistry Accounts: Theory, Computation, and Modeling (Theoretica Chimica Acta) 1997, 97, 119–124, doi:10.1007/s002140050244.

64. Adamo, C.; Cossi, M.; Barone, V. An Accurate Density Functional Method for the Study of Magnetic Properties: The PBE0 Model. Journal of Molecular Structure: THEOCHEM 1999, 493, 145–157, doi:10.1016/S0166-1280(99)00235-3.

65. Schäfer, A.; Huber, C.; Ahlrichs, R. Fully Optimized Contracted Gaussian Basis Sets of Triple Zeta Valence Quality for Atoms Li to Kr. J Chem Phys 1994, 100, 5829–5835, doi:10.1063/1.467146.

66. Bertini, L.; Bruschi, M.; Romaniello, M.; Zampella, G.; Tiberti, M.; Barbieri, V.; Greco, C.; La Mendola, D.; Bonomo, R.P.; Fantucci, P.; et al. Copper Coordination to the Putative Cell Binding Site of Angiogenin: A DFT Investigation. Theor Chem Acc 2012, 131, 1186, doi:10.1007/s00214-012-1186-y.

67. Klamt, A.; Schüürmann, G. COSMO: A New Approach to Dielectric Screening in Solvents with Explicit Expressions for the Screening Energy and Its Gradient. J. Chem. Soc., Perkin Trans. 2 1993, 799–805, doi:10.1039/P29930000799.

68. Grimme, S. Semiempirical GGA-type Density Functional Constructed with a Long-range Dispersion Correction. J Comput Chem 2006, 27, 1787–1799, doi:10.1002/jcc.20495.

69. Arrigoni, F.; Rizza, F.; Tisi, R.; De Gioia, L.; Zampella, G.; Bertini, L. On the Propagation of the OH Radical Produced by Cu-Amyloid Beta Peptide Model Complexes. Insight from Molecular Modelling. Metallomics 2020, 12, 1765–1780, doi:10.1039/d0mt00113a.

70. Rovetta, A.; Carosella, L.; Arrigoni, F.; Vertemara, J.; De Gioia, L.; Zampella, G.; Bertini, L. Oxidation of Phospholipids by OH Radical Coordinated to Copper Amyloid-β Peptide—A Density Functional Theory Modeling. Inorganics (Basel) 2023, 11, 227, doi:10.3390/inorganics11060227.

71. Pirro, F.; La Gatta, S.; Arrigoni, F.; Famulari, A.; Maglio, O.; Del Vecchio, P.; Chiesa, M.; De Gioia, L.; Bertini, L.; Chino, M.; et al. A De Novo-Designed Type 3 Copper Protein Tunes Catechol Substrate Recognition and Reactivity. Angewandte Chemie 2023, 135, doi:10.1002/ange.202211552.

72. Case, D.A.; Aktulga, H.M.; Belfon, K.; Cerutti, D.S.; Cisneros, G.A.; Cruzeiro, V.W.D.; Forouzesh, N.; Giese, T.J.; Götz, A.W.; Gohlke, H.; et al. AmberTools. J Chem Inf Model 2023, 63, 6183–6191, doi:10.1021/acs.jcim.3c01153.

73. Sprenger, K.G.; Jaeger, V.W.; Pfaendtner, J. The General AMBER Force Field (GAFF) Can Accurately Predict Thermodynamic and Transport Properties of Many Ionic Liquids. J Phys Chem B 2015, 119, 5882–5895, doi:10.1021/acs.jpcb.5b00689.

74. Lindorff-Larsen, K.; Piana, S.; Palmo, K.; Maragakis, P.; Klepeis, J.L.; Dror, R.O.; Shaw, D.E. Improved Side-chain Torsion Potentials for the Amber Ff99SB Protein Force Field. Proteins: Structure, Function, and Bioinformatics 2010, 78, 1950–1958, doi:10.1002/prot.22711.

75. Li, Z.; Song, L.F.; Li, P.; Merz, K.M.Jr. Systematic Parametrization of Divalent Metal Ions for the OPC3, OPC, TIP3P-FB, and TIP4P-FB Water Models. J Chem Theory Comput 2020, 16, 4429–4442, doi:10.1021/acs.jctc.0c00194.

76. Pronk, S.; Páll, S.; Schulz, R.; Larsson, P.; Bjelkmar, P.; Apostolov, R.; Shirts, M.R.; Smith, J.C.; Kasson, P.M.; van der Spoel, D.; et al. GROMACS 4.5: A High-Throughput and Highly Parallel Open Source Molecular Simulation Toolkit. Bioinformatics 2013, 29, 845–854, doi:10.1093/bioinformatics/btt055.

77. Sen, S.; Bhojnagarwala, P.; Francey, L.; Lu, D.; Penning, T.M.; Field, J. P53 Mutagenesis by Benzo[a]Pyrene Derived Radical Cations. Chem Res Toxicol 2012, 25, 2117–2126, doi:10.1021/tx300201p.

78. Singha, A.; Sekretareva, A.; Tao, L.; Lim, H.; Ha, Y.; Braun, A.; Jones, S.M.; Hedman, B.; Hodgson, K.O.; Britt, R.D.; et al. Tuning the Type 1 Reduction Potential of Multicopper Oxidases: Uncoupling the Effects of Electrostatics and H-Bonding to Histidine Ligands. J Am Chem Soc 2023, 145, 13284–13301, doi:10.1021/jacs.3c03241.

79. Randall, D.W.; Gamelin, D.R.; LaCroix, L.B.; Solomon, E.I. Electronic Structure Contributions to Electron Transfer in Blue Cu and CuA. JBIC Journal of Biological Inorganic Chemistry 2000, 5, 16–29, doi:10.1007/s007750050003.

80. Tachikawa, H. Jahn–Teller Effect of the Benzene Radical Cation: A Direct Ab Initio Molecular Dynamics Study. J Phys Chem A 2018, 122, 4121–4129, doi:10.1021/acs.jpca.8b00292.

81. Ryde, U.; Olsson, M.H.M.; Pierloot, K.; Roos, B.O. The Cupric Geometry of Blue Copper Proteins Is Not Strained. J Mol Biol 1996, 261, 586–596, doi:10.1006/jmbi.1996.0484.

82. Pozdnyakova, N.N.; Rodakiewicz-Nowak, J.; Turkovskaya, O.V. Catalytic Properties of Yellow Laccase from Pleurotus Ostreatus D1. J Mol Catal B Enzym 2004, 30, 19–24, doi:10.1016/j.molcatb.2004.03.005.

83. Yang, Z.; Mao, X.; Cui, J.; Wang, Y.; Zhang, Y. Enhancement and Analysis of Anthracene Degradation by Tween 80 in LMS-HOBt. Sci Rep 2021, 11, 13121, doi:10.1038/s41598-021-90609-5.

84. Rovaletti, A.; De Gioia, L.; Fantucci, P.; Greco, C.; Vertemara, J.; Zampella, G.; Arrigoni, F.; Bertini, L. Recent Theoretical Insights into the Oxidative Degradation of Biopolymers and Plastics by Metalloenzymes. Int J Mol Sci 2023, 24, 6368, doi:10.3390/ijms24076368.

Chapter 6

Polyethylene-Degrading Laccases: Comparative Insights into Redox Properties and Enzyme–Polyethylene Interaction

The following section explores the oxidation of low-density polyethylene (LDPE) by different laccases and presents a computational investigation aimed at elucidating the redox properties and enzyme–polymer interactions that govern their catalytic activity. Since the early 2000s, both bacterial and fungal laccases have been identified that are capable of degrading non-phenolic substrates, most notably polycyclic aromatic hydrocarbons (PAHs) and, more recently, polyethylene (PE) and other plastic polymers. In these studies, it has generally been observed that certain microorganisms can grow by utilizing such substrates as sources of carbon and electrons, even though these compounds do not represent their preferred metabolites under natural conditions. While research on PAHs has advanced to the point of clarifying the oxidation mechanism at the atomic level, the situation for PE and other plastic polymers remains less understood. In these cases, not only is the oxidation mechanism unknown, but even the fundamental aspects of substrate binding have yet to be elucidated. The present study is therefore focused on addressing this latter issue.

Laccases able to oxidize LDPE are considered a promising tool for bioremediation. To understand and improve their activity toward PE, it is essential to take into account two main factors: the enzyme's redox potential and the manner and strength of its interaction with the polymer. Notably, the formation of a stable laccase–PE complex may facilitate electron transfer even under thermodynamically unfavorable conditions, without the need for redox mediators. Since, as far as we are concerned, there are no investigations regarding the structure of this complex, in this study, we compared the redox properties and LDPE-binding characteristics of three PE-oxidizing laccases: a high-redox potential fungal laccase from *Trametes versicolor*, a low-redox potential bacterial laccase from *Bacillus subtilis*, and the recently characterized LMCO2 from *Rhodococcus opacus* R7. Our analyses

confirmed that LMCO2 is a low-potential laccase (E° = 413 mV), consistent with other bacterial variants. Using advanced computational modeling, we simulated the interactions of these laccases with an extended LDPE model, highlighting the critical role of hydrophobic residues surrounding the T1 copper site in stabilizing the enzyme–polymer complex. Remarkably, a methionine-rich loop in LMCO2 appears to enhance complex formation with LDPE, potentially facilitating electron transfer despite its low redox potential. These findings emphasize the necessity of comprehensive computational strategies to investigate enzyme–polymer interactions beyond simplified models. By identifying key structural determinants for LDPE binding, this work provides valuable insights for rational enzyme engineering and future mutagenesis efforts aimed at enhancing laccase activity toward polyolefin degradation.

6.1 Introduction

The rapid expansion of global plastic production in recent years has led to widespread environmental accumulation, contributing approximately 3.4% to global greenhouse gas emissions. In 2022, worldwide synthetic plastic production reached 400 million tons, with polyolefins, including polyethylene, polypropylene, and polystyrene, accounting for more than 60% of the total output (Plastics Europe (Ed.), 2023. Plastics – the Facts, 2023 ed., Plastics Europe, Accessed 02 August 2024). The widespread accumulation of these highly recalcitrant polymers in natural environments has led to mounting ecological concerns, including long-term persistence in soils and aquatic systems, physical hazards to wildlife, and chemical leaching that can disrupt ecosystems. Consequently, there is an urgent need to develop sustainable and efficient strategies for mitigating plastic waste.

Microorganisms have evolved to cope with the presence of synthetic polymers, deploying enzymatic machinery capable of attacking and degrading plastics. This microbial degradative potential is driven by enzymes adapted to recalcitrant substrates, which catalyze the cleavage of strong C–C and C–H bonds present in polyolefins. Enzymatic approaches are particularly appealing because they can complement conventional recycling methods by enabling selective depolymerization under milder and environmentally friendly conditions [1–4]. Several enzyme classes have been investigated for polyethylene degradation, including manganese peroxidases, lignin peroxidases, lipases, esterases, and laccases [3–8]. Among these, laccases have garnered special interest due to their oxidative versatility and ability to act on a wide array of nonphenolic and recalcitrant substrates, including lignin and polyolefins.

Laccases (benzenediol: oxygen oxidoreductase, EC 1.10.3.2) are blue multicopper oxidases that catalyze substrate oxidation in conjunction with the four-electron

reduction of molecular oxygen to water. They are widely distributed across bacteria, fungi, plants, and insects, with biological functions that vary depending on their source. Bacterial laccases, in particular, are often favored for bioremediation because of their enhanced stability under harsh environmental conditions, including elevated temperatures and alkaline pH, which are frequently encountered in industrial and environmental contexts [9]. Catalysis relies on four copper atoms: one type I (T1) paramagnetic copper, responsible for the characteristic blue color; one type II (T2) paramagnetic copper; and two type III (T3) diamagnetic, spin-coupled copper atoms. Substrate oxidation occurs at the T1 site, while O_2 reduction is mediated at the T2/T3 cluster [10–12]. Despite highly conserved structures, laccases display a broad spectrum of redox potentials (E° vs. NHE), ranging from +430 to +800 mV. Typically, white-rot fungal laccases exhibit higher potentials than bacterial or plant laccases [13].

Enzymes capable of oxidizing LDPE have been identified in fungi [6,14–22], bacteria [23–34], and, more recently, even in shrimp [35]. The oxidation products generally include organic acids and polymer fragments containing hydroxyl and carbonyl groups, indicating a conserved oxidative mechanism across species [5,6,15,23–25]. Nonetheless, the differences in redox potentials among these laccases suggest that the mode of interaction with LDPE may significantly influence reaction efficiency, particularly in the context of C–H bond activation in nonphenolic substrates [36–38]. Therefore, understanding both the redox properties of laccases and their binding modes to LDPE is crucial for elucidating reaction mechanisms and designing effective enzymatic degradation strategies [4,39].

The role of mediators in PE oxidation is similarly complex. Some laccases strictly require mediators to catalyze polymer oxidation, others exhibit enhanced efficiency in their presence, while certain enzymes operate independently of mediators [24,29]. The variability in mediator dependence further highlights the need to understand enzyme–substrate interactions at a molecular level.

To address these knowledge gaps, we conducted a multiscale computational study, employing molecular docking and molecular dynamics (MD) simulations to characterize the interactions between PE-oxidizing laccases and a realistic LDPE model. Two well-characterized laccases with available 3D structures were initially selected: the high-redox potential fungal laccase from *Trametes versicolor* (TvL, T1 E° = 790 mV) [40], capable of oxidizing LDPE even without mediators (albeit at reduced catalytic efficiency), and the low-redox potential bacterial laccase from *Bacillus subtilis* (BsL, T1 E° = 455 mV) [41], which requires mediators to perform LDPE oxidation (Figure 6.1).

Additionally, we included the bacterial laccase LMCO2 from *Rhodococcus opacus* R7. The story of this bacterial strain is closely tied to a significant environmental event. This Gram-positive, G-C rich bacterium was isolated from the contaminated site of Trecate, Italy, following the 1994 oil spill. The soil at the site was heavily polluted with a mixture of diverse PAHs and phthalates.

This particular R7 strain was identified for its crucial ability to degrade PAHs and alkanes found in the contaminated soil. Its discovery aligns with the general characteristics of the *Rhodococcus genus*, which is widely distributed in nature (soil, fresh, and marine habitats) and known for its remarkable metabolic versatility. Members of the genus, like R7, thrive across a range of temperatures (4–35 ◦C) and possess a multiplicity of catabolic genes, high redundancy, and sophisticated regulatory networks.

Like other *Rhodococcus* species that metabolize diverse compounds such as hydrocarbons, nitroaromatics, and steroids, R. opacus R7 has been specifically noted for degrading a broad spectrum of metabolites including PAH, alkylbenzenes, n-alkanes (C12–C30), naphthenic and carboxylic acids, and even plastic polymers. Its isolation marked an important instance of a naturally occurring microbe possessing the genetic toolkit necessary to bioremediate the complex pollutants left by the Trecate oil spill.

The enzymes LMCO2 and LMCO3 were identified by transcriptomic analysis of *R. opacus* R7 when it was grown on polyethylene as its sole source of carbon and electrons. The enzymes are multi-copper oxidases and have different functional features: LMCO2 is most active at 65 °C and pH 7.0, while LMCO3 is most active at 80 °C under acidic conditions. Both are thermostable and active on both phenolic and non-phenolic compounds.

Crucially, LMCO2 and LMCO3 showed oxidative activity on untreated low-density polyethylene within a short time frame (24–48 h). This degradation was confirmed by advanced spectroscopy and mass spectrometry, which revealed the production of previously undescribed alkyl compounds and oxygenated products like ketones, alcohols, and carboxylic acids.

Focusing on LMCO2's, its PE-oxidizing activity appears independent of mediator presence, raising two possibilities: either LMCO2 exhibits an unusually high redox potential for a bacterial enzyme, or it possesses unique structural features that enhance its affinity for LDPE. One candidate structural determinant is a hydrophobic methionine-rich loop (Met-loop) located near the T1 site [29,42]. Met-rich loops and inserts are recurrent motifs in prokaryotic laccases and multicopper oxidases, including the E. coli Copper Efflux Oxidase (CueO) [43–48]. Although their precise roles remain under investigation, Met-rich motifs have been implicated in

processes such as pigmentation, toxin oxidation, and copper homeostasis [49–52]. Regarding this last point, the CotA gene *in Bacillus subtilis* is known to encode a laccase that plays a vital role during the sporulation phase of the bacterium. Specifically, the CotA laccase is involved in the homeostasis of both copper and H2O2. Also CotA is believed to participate in generating the brown spore pigment, a substance resembling melanin that provides defense against UV radiation.

In CueO, the Met-loop has been shown to facilitate binding to hydrophobic surfaces, such as carbon nanotubes, suggesting a potential analogous role in LDPE binding [4,53].

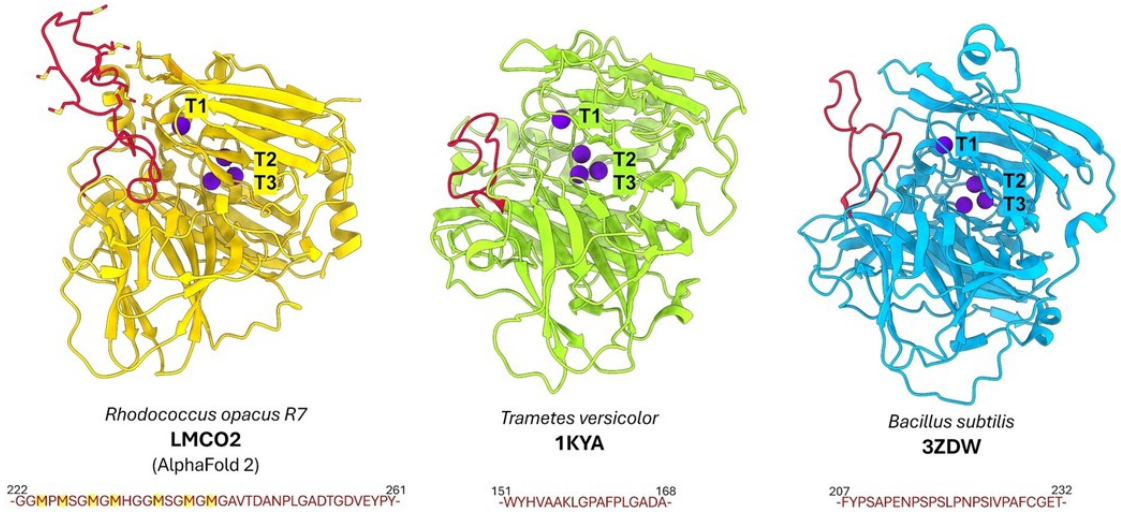

Figure 6.1: 3D structures of the three laccases investigated in the present study: LMCO2 from Rhodococcus opacus R7 (left, AlphaFol2 model), the fungal laccase from Trametes versicolor (middle, TvL, PDB ID: 1KYA) and the bacterial laccase from Bacillus subtilis (right, BsL, PDB ID: 3ZDW). The methionine-rich loop (Met-loop) of LMCO2 is highlighted in red, with Met side chains surrounding the T1 site shown as sticks. In the other two systems, in the same position, two significantly different loops with low structural identity and the total absence of methionines are present and have been highlighted in red too.

Overall, this work represents the first comprehensive computational study combining structural, redox, and binding analyses of laccases interacting with a realistic LDPE model. Integrating these aspects, one can provide mechanistic insights into enzymatic PE oxidation and establish a foundation for the rational design of improved laccases for sustainable bioremediation. Furthermore, the study sets the stage for future experimental and computational investigations into the role of structural motifs, mediator effects, and enzyme–substrate dynamics in polyolefin degradation.

6.2 Materials and Methods: experimental part

In collaboration with Professor Di Gennaro's group from the Department of Biotechnology and Biosciences at the University of Milano-Bicocca, the purification of the recombinant LMCOs was carried out. Recombinant production of LMCO2 was performed using *Rhodococcus erythropolis* AP cells carrying pTipQC2-LMCO2 as described in Zampolli et al. 2023. Briefly, LMCO2 was produced in 1.5 L Luria Bertani broth (5 g L^{-1} yeast extract, 10 g L^{-1} tryptone, and 250 µM $CuSO_4$) supplemented with chloramphenicol. Cells were induced in the exponential phase by the addition of 1 µg mL^{-1} thiostrepton, and proteins were extracted as previously described[29]. Recombinant LMCO2 was purified from the soluble fraction of *R. erythropolis* AP cells using a 5 mL HIS-TRAP high-performance column (Cytiva, Marlborough, US) and an NGC Quest Plus Chromatography System (Bio-Rad) according to the methods previously described [54]. Fifteen fractions were collected and tested for their ability to oxidize 2,6-dimethoxyphenol. Fractions exhibiting the desired activity were pooled, concentrated using Amicon Ultra-15 centrifugal filters (Merck- Millipore, MW cut-off: 30 kDa), and then buffer-exchanged in 150 mM Tris-HCl buffer (pH 7.0) with 50 mM KCl using a PD10 column. The fractions were subsequently stored at 4°C.

In collaboration with Professor Di Rocco's group at the University of Modena and Reggio Emilia, we determined the redox potential by spectroelectrochemistry. All experiments were carried out in a homemade OTTLE (optical transparent thin layer spectroelectrochemical) cell as detailed before [55,56]. The three-electrode configuration included a gold mini-grid working electrode (Buckbee-Mears), a silver chloride micro-reference electrode (AMEL Electrochemistry), which was separated from the working solution by a Vycor set, and a platinum wire as the counter electrode. The reference electrode was calibrated against a saturated calomel (HgCl) electrode before each set of measurements. All potentials are referenced to the SHE (standard hydrogen electrode). Potentials were applied to the OTTLE cell using an Amel model 2053 potentiostat/galvanostat. A circulating water bath kept the temperature constant, while a micro-thermocouple monitored the temperature of the OTTLE cell. UV-vis spectra were recorded using a Varian Cary C50 spectrophotometer. The OTTLE cell was flushed with argon gas to create an oxygen-free environment within. Experiments were carried out using 1 ml samples of 0.7 mg/mL LMCO2 in 150 mM Tris-HCl buffer (pH 7.0) with 50 mM KCl. Potassium hexacyanoferrate(III) (1.6 mM) serves as a mediator. The spectroelectrochemical studies were repeated three times, and the resulting redox potential value is consistent within 4 mV.

6.3 Computational Details

Molecular dynamics simulations. The 3D structures of TvL (PDB ID: 1KYA) and BsL (PDB ID: 3ZDW) were retrieved from the Protein Data Bank, while the LMCO2 structure was predicted using AlphaFold2 [57], with metal content added by superimposing it onto BsL. The LMCO2 model showed high confidence [29], except for the N-terminal tail (omitted) and the flexible Met-loop (residues 222–261). MD simulations were performed using GROMACS 2020[47,58] with the Amber ff14SB force field [59], TIP3P water model [60], and Li and Merz parameters for divalent ions [61], applying restraints to maintain copper coordination. Systems were minimized (harmonic positional constraints: 50 kcal mol-1 A2, 5000 steps steepest descent and conjugate gradient) and equilibrated at 300 K (NVT, 20 ns) and 1 bar (NPT, Berendsen barostat, τp=2 ps). Simulations were run with a 2 fs integration step and the SHAKE algorithm, using 100 ns for TvL and BsL, and 400 ns for LMCO2, to refine the AlphaFold2 model and sample Met-loop flexibility. Representative clusters (cutoff=2.5 A) were identified and used for molecular docking [62,63]. The LDPE ligand (modelled as branched $C_{100}H_{202}$) was prepared by folding a linear chain in 100 ns MD using General Amber Force Field (GAFF), following published approaches [39]. After docking, the lowest-energy laccase-PE complexes underwent 1000 ns MD simulations in triplicate. Since all replicas showed consistent behavior, only one per system is discussed in the main text, with details on the others provided in the SI. Binding free energies were calculated using the linearized Molecular Mechanics Poisson-Boltzmann surface area (MM-PBSA) equation method (AmberTools23,[64]) with an igb flag value of 5 (0.1 M salt concentration): a total of 100 frames per trajectory were analyzed after 200 ns of stable ligand binding.

Molecular docking. AutoDock vina [65] was used to perform molecular docking simulations, to study the possible binding modes and interactions of PE in proximity to the catalytic site (T1). The most representative clustered geometries of each enzyme, deriving from a previous MD round (see previous paragraph) were prepared by assigning atom types and adding Gasteiger charges. The docking area was established using AutoGrid. A size of 50×50×50 A was chosen, and the grid was centered on the Cε atom of H458. Lamarckian Genetic Algorithm (LGA) was used for the conformational search of the substrate, to allow for a (at least partial) sampling of the PE conformational space within the enzyme pocket. Docking simulations of PE were performed, with a population size of 150, random initial position and conformation, local search rate of 0.6, and 2,500,000 energy evaluations. The final docked poses were clustered using an RMSD tolerance of 2 A. The top-ranked pose obtained for each enzyme-PE system was chosen for another extensive round of MD (see previous paragraph).

QM/MM simulations were performed using the sander.MPI module of the Amber20 package [66]. The system was first minimized, and the reactant structure was equilibrated for 50 ps in the NVT ensemble using a Langevin thermostat at 300 K, with an integration timestep of 1 fs. The QM region, comprising the T1 copper site, a five-carbon fragment of PE, D256, and two water molecules, was described using xTB [67]. This method has previously been shown to be essential in the initial stages of the calculation to rapidly identify the lowest-energy pathway. The remaining atoms were treated classically using the ff14SB force field [59]. The product structure was obtained via steered MD, and subsequently equilibrated for an additional 50 ps. The resulting reactant and product structures in the enzyme were then used to determine the Minimum Free-Energy Pathway (MFEP) within the enzymatic environment.

Minimum Free-Energy Path (MFEP) was obtained using an in-house implementation of the string method [68], following a common protocol for all three systems studied. The progress of the reaction was monitored through three collective variables (CVs) directly involved in the proton transfer. The QM region was described using the xTB method. The string consisted of 64 nodes, with the initial and final nodes defined by the CVs obtained from the QM/MM minimization and 50 ps equilibration of the reactants and products. Initial coordinates for the intermediate nodes of the string were generated by linear interpolation of the CV values between the reactant and product structures.

6.4 Redox Potential in Laccases

LMCO2 is a low-potential laccase. To allow for a meaningful and fair comparison of laccase behavior with respect to PE oxidation, it is of primary importance to consider their redox potential. In this regard, it was first experimentally measured the redox properties of freely diffusing laccase LMCO2 using UV– visible spectroelectrochemistry. Figure 6.2 depicts the electronic spectra for LMCO2 collected at different applied potentials in the OTTLE cell at 25°C and pH 7. Monitoring the absorbance at 607 nm at each applied potential revealed the approach to equilibrium between the oxidized and reduced forms of the protein. Data points were gathered in both the reducing and oxidizing directions, and the absorbance of the fully oxidized protein was measured again at the end of the experiment to detect any protein degradation. The Nernst plot (Figure 6.2, insets) shows a linear slope similar to the theoretical value of RT298/F= 0.059 V, consistent with the one-electron $Cu^{2+} \rightarrow Cu^{+}$ reduction [69,70] of the type I copper center present in LMCO2. The E°’ values for the Cu^{2+}/Cu^{+} couple, determined from the corresponding Nernst plot (inset to Figure 6.2), were calculated to be 413±4 mV (vs. SHE) for LMCO2. This result shows that LMCO2 has a “canonical” potential for a

bacterial laccase, as it falls within the typical range of redox potentials measured for this class of enzymes in these organisms, and is thus similar to that of BsL, which, however, requires a redox mediator to oxidize LDPE. (Figure 6.2, right). This finding allows us to rule out the possibility that LMCO2 possesses an unusually high redox potential compared to other bacterial laccases. Therefore, the observed difference in its behavior in PE oxidation, compared to BsL, likely arises from a distinct mode of interaction and binding affinity toward the polymer.

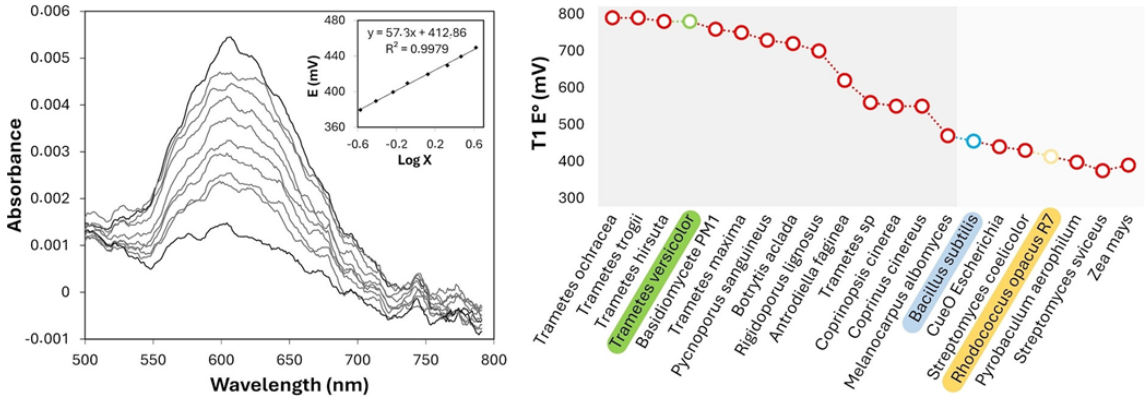

Figure 6.2: Left: electronic spectra of LMCO2 laccase recorded at various potentials in spectroelectrochemical experiments carried out with an OTTLE cell at 25 °C. Conditions: 0.7 mg/mL LMCO2 laccase in 150 mM Tris-HCl buffer (pH 7.0) containing 50 mM KCl and 1.6 mM potassium hexacyanoferrate(III) as mediator. Inset depicts the Nernst plot of redox titration versus SHE, where X represents $[(A_{\lambda ox} - A^{min}{}_{\lambda ox})/(A^{max}{}_{\lambda ox} - A_{\lambda ox})]$ *with absorbance of the oxidized form at* λ_{ox} *= 607 nm. Titration has been performed in triplicates, with one representative titration presented. Right: standard redox potential of the T1 site of laccases (in mV) from various organisms with values decreasing progressively from the highest positive value downward. The values in the dark gray area correspond to high-potential fungal laccases, while those in the light gray area represent bacterial or plant laccases. The three highlighted values refer to the systems considered in this study: 790 mV for Trametes versicolor [40], 455 mV for Bacillus subtilis [41], and 413 ± 4 (vs. SHE) mV for LMCO2 .*

6.5 Nature of the laccase-PE recognition

To gain insights into the binding mechanism of LDPE, we initially carried out molecular docking simulations using an LDPE branched alkane model (C100H202) as the substrate, referred to as 'PE' for simplicity throughout (in Figure 6.3).

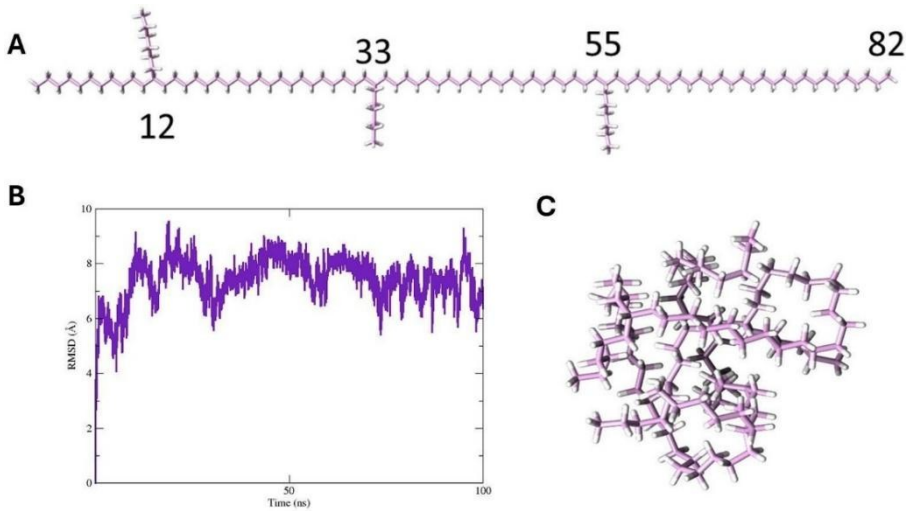

Figure 6.3: A) LDPE branched model $C_{100}H_{202}$ (referred to as PE) is considered in this investigation. In positions 12, 33, 55, C6 branches are inserted. B) Root mean square deviation (RMSD, in Å) over the PE folding trajectory. C) Structure of the most representative cluster of folded PE obtained with 100 ns MD simulation at 302K in explicit water.

This choice of LDPE model was made after systematically folding PE structures of increasing size, ranging from 12 [71,72] to 150 carbon atoms, and subsequently docking them onto the *LMCO2* laccase structure. This range of alkane sizes also makes the calculation computationally feasible and, with a view toward future DFT studies, allows us to test lower molecular weight PE models. These simpler models can still effectively represent the binding pose of a higher molecular weight ligand within the enzyme's binding pocket.

The resulting complexes were then analyzed by evaluating their substrate affinity through MMPBSA calculations. Based on the results summarized in Table 6.1, the chosen model emerged as the most suitable candidate [73], as it ensures a balance between a realistic description of the bulk material and the reduction of computational complexity. More specifically, this model allows for the preservation of the system's intrinsic symmetries while limiting numerical artifacts, thus providing a reliable compromise between structural realism, methodological accuracy, and computational feasibility.

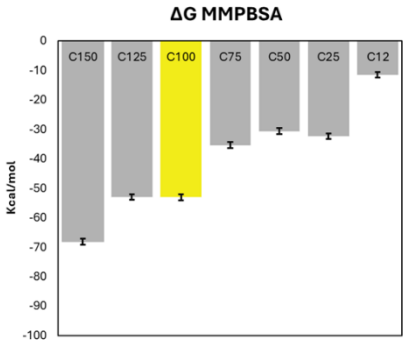

Table 6.1: Binding free energy (ΔG) values obtained by MMPBSA analysis for PE models of increasing size, ranging from C12 to C150. While larger structures (C125 and C150) exhibit the most favorable binding energies, the C100 model (in yellow) provides an optimal balance between affinity and computational feasibility, making it the representative structure chosen for subsequent analyses.

The model dimension is suited to interact with the binding pocket and its outer regions, thus considering a substantial portion of the protein surface surrounding the T1 site. This approach enables us to focus on the laccase-PE affinity and binding modes at the most relevant region, specifically near the T1 site, where PE is expected to be located for the electron transfer process to occur. In other words, our study aims to address whether a specific laccase, in the vicinity of the T1 site, is inclined to bind the PE, and which structural determinants underpin this phenomenon. We proceeded with a comparative analysis of all three selected systems to pinpoint eventual differences/similarities in both binding features and dynamic properties.

Examining the region surrounding T1 in the three enzymes, it is evident that the most significant difference can be attributed to the physicochemical nature and length of a specific loop (highlighted in red in Figure 6.1). In LMCO2, as previously mentioned, this pertains to the Met-loop (whose structure has never been resolved experimentally due to its dynamic nature), which has a notable length of 39 residues and an overall hydrophobicity percentage of 69.2%. Upon analyzing the sequence, it is possible to identify two regions of approximately equal length: a non-polar region comprising 20 residues, consisting of hydrophobic residues and glycine at 87.5 %, where 7 methionines are located, and another region richer in polar residues, including three D and one E. The same region is occupied by a much shorter loop (17 residues) in TvL, predominantly (76.5%) hydrophobic, and by a 25 residues-long loop in BsL, which is less hydrophobic in composition (44%) with polar residues distributed uniformly along the sequence.

Molecular docking was performed using the most representative cluster structures obtained from MD simulations of each enzyme in its free form, with two main objectives: (i) to verify that PE can bind near the T1 Cu site, and (ii) to use the best

docking poses as the starting point for subsequent, extensive MD simulations of each laccase-PE complex. Indeed, the presence of flexible loops near the catalytic site, along with the inherent flexibility of PE, makes the static representation derived from molecular docking insufficient for providing a comprehensive and accurate depiction of the enzyme-substrate interaction. Points (i) and (ii) should allow us, in principle, to highlight whether the differences in the surroundings of T1 in the three enzymes (such as the nature of the above-described loops) may have any effect on the binding modes and energy of the used PE model. We observed that in the best docking pose for each case, PE binds in proximity to T1, rearranging its structure to fit the shape of the catalytic pocket and occupying the pocket either fully or partially (Figure 6.5A). The T1 Cu – PE distance decreases in the order LMCO2 (8.8 Å) > TvL (6.2 Å) > BsL (4.3 Å) but the calculated docking scores are comparable among the three enzymes (Figure 6.5B and Table 6.2 for further details). Indeed, docking scores of -5.0 kcal mol^{-1}, -4.5 kcal mol^{-1}, and -4.2 kcal mol^{-1} were obtained for TvL, LMCO2, and BsL, respectively, with very low variation among the first 9 predicted PE docking poses (Table 6.2). Remarkably, this picture was not confirmed by MD simulations of the three enzyme-PE complexes (Figure 6.5C and D). Energetically, as indicated by free energy estimates obtained via MMPBSA, the complexes show distinct behaviors: LMCO2 and TvL bind PE with similar affinities, while BsL exhibits significantly weaker binding. Routine trajectory analyses, such as Root Mean Square Fluctuation (RMSF) of each residue and Root Mean Square Deviation (RMSD) of backbone atoms (Figure 6.5E and F), reveal that all three enzymes maintain stability upon binding with PE, since a trend of balanced RMSD was observed in all systems.

Additionally, reduced flexibility is observed in certain regions of LMCO2 and TvL upon PE binding, whereas no significant changes in flexibility are detected in BsL, as suggested by RMSF profiles. More specifically, in the case of LMCO2, the Met-loop is the protein region that exhibits the greatest flexibility by adopting closed and open transient conformations (Figure 6.4), a result consistent with previous findings [45,46].

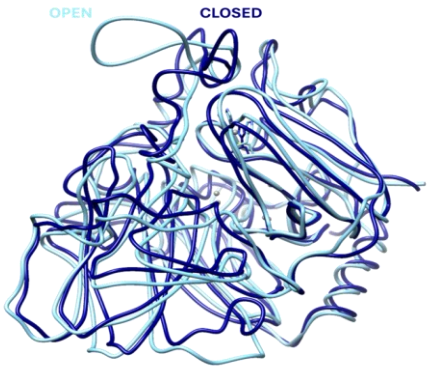

Figure 6.4: Open and closed conformation of the Met-loop observed along MD trajectories for LMCO2.

Indeed, in bacterial laccases, substrate processing can occur with or without a flexible Met-loop. This loop alternates between open and closed states, exposing the T1 copper site for substrate interaction in the open state and limiting access in the closed state [45,46].

LMCO2

POSE	SCORE (kcal/mol)	DISTANCE FROM THE BEST POSE	
		RMSD l.b	RMSD u.b
1	-4.5	0.000	0.000
2	-4.3	1.650	9.700
3	-4.3	1.617	9.598
4	-4.3	1.876	9.756
5	-4.3	1.866	10.305
6	-4.2	2.028	9.836
7	-4.2	1.708	7.996
8	-4.2	1.663	7.638
9	-4.2	2.126	10.257

TvL

POSE	SCORE (kcal/mol)	DISTANCE FROM THE BEST POSE	
		RMSD l.b	RMSD u.b
1	-5.0	0.000	0.000
2	-4.9	1.906	9.059
3	-4.9	2.063	8.801
4	-4.9	1.498	12.202
5	-4.9	2.160	12.691
6	-4.9	2.606	9.070
7	-4.8	1.291	2.654
8	-4.8	2.071	9.890
9	-4.7	2.441	13.263

BsL

POSE	SCORE (kcal/mol)	DISTANCE FROM THE BEST POSE	
		RMSD l.b	RMSD u.b
1	-4.2	0.000	0.000
2	-4.0	2.799	8.717
3	-4.0	3.327	9.992
4	-4.0	3.965	12.005
5	-3.9	4.040	12.568
6	-3.9	2.299	10.462
7	-3.9	3.560	10.608
8	-3.8	4.073	9.519
9	-3.8	4.110	10.875

Table 6.2: Results of molecular docking simulation regarding the LDPE-laccase interaction in the selected three case studies. Docking scores are in kcal mol^{-1}, RMSD values in Å.

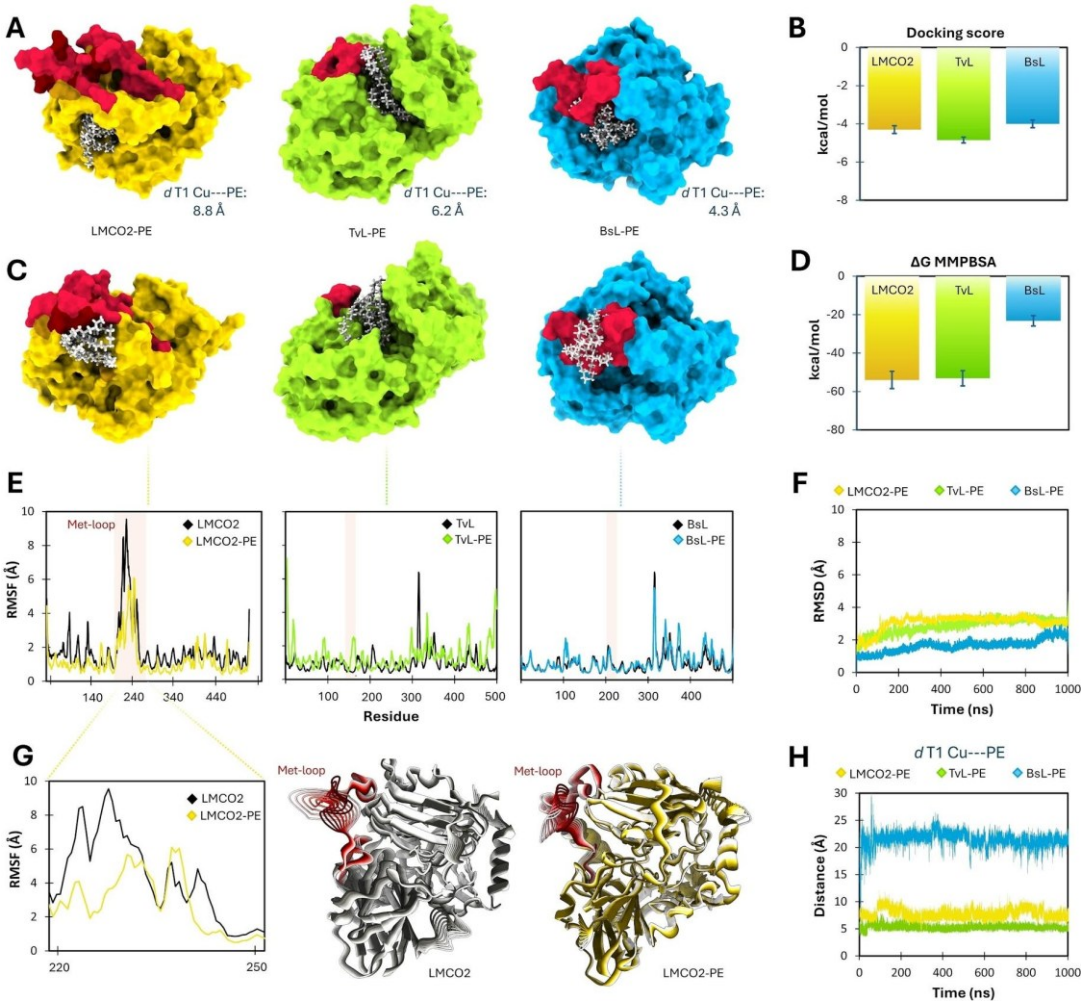

Figure 6.5: A) Best docking pose obtained for each laccase (LMCO2 in yellow, TvL in light green, and BsL in light blue). The distance between T1 Cu and the PE center of mass is also reported (in Å). The Met-loop and those found in the same enzyme region in both TvL and BsL are highlighted in red; B) Docking scores (in kcal mol^{-1}) associated with PE binding to the three laccases; C) Most representative cluster of the PE-laccase complex obtained from MD simulations; D) MMPBSA free energy estimate (in kcal mol^{-1}) for PE binding to each laccase, calculated over MD trajectories; E) RMSF (in Å) calculated from MD trajectories of the three enzymes, before and after complexation with PE. The Met-loop region in LMCO2 (and that of the corresponding loops in TvL and BsL) is highlighted; F) RMSD calculated over the whole MD simulations for the three laccases in complex with PE; G) Focus on the Met-loop region in LMCO2, showing RMSF changes upon PE binding, together with a representation of the eigenvector corresponding to PC1 in both LMCO2 and LMCO2-PE systems; H) Monitoring of the T1 Cu — PE distance (in Å) over MD trajectories for the three laccases.

These conformations have been shown to regulate substrate access to the binding pocket, so we may infer that they can also drive PE access close to T1. Indeed, we found that Metloop fluctuation is significantly reduced in the presence of PE (Figure 6.5G). This variation was further analyzed through principal component analysis (PCA), where the first eigenvector is associated with the movement of the Met-loop

in both the free enzyme and the PE-bound complex (Figure 6.5G). Nevertheless, the extent of the loop displacement is notably diminished in the complex. Regarding TvL, the loop corresponding to the Met-loop in LMCO2 does not exhibit significant structural flexibility, nor does it undergo any changes in mobility upon binding with PE. A mobility variation, however, is observed in the region between residues 300–310, which also corresponds to a loop approaching the T1 site, although this effect is less pronounced. Similarly, Met-loop is way more flexible than that found in BsL in the same region. In this latter case, the 310–320 region is quite dynamic, but, as described later, this is not predicted to have a functional role in PE affinity, and its RMSF profile remains unchanged upon binding. Furthermore, BsL differs from the other two proteins not only in its affinity for PE but also in the average distance at which PE is maintained relative to the T1 site during the simulation.

In both LMCO2 and TvL, PE remains bound near the T1 site (between 5 and 10 Å) over MD simulation. In contrast, in BsL, PE is initially positioned near the T1 site in the docking pose, but it drifts significantly away from the catalytic center during simulations, stabilizing at a distance of about 20 Å from the T1 site (Figure 6.3H).

To rationalize these observations, we conducted a more detailed analysis of the interactions between PE and the three enzymes, considering both those identified from molecular docking and how this interaction pattern changed throughout MD simulations.

The 2D interaction patterns of the best docking poses show that nearly all residues involved form hydrophobic interactions, consistent with the non-polar nature of PE. In LMCO2, the most stable pose positions PE near the T1 site, interacting fully with the pocket but without engaging the Met-loop (Figure 6.5A). In the case of LMCO2, molecular docking identifies as the most stable pose a complex in which PE is positioned near the T1 site, fully interacting with the binding pocket but without engaging the Met-loop (Figure 6.5A, no red-bordered circle appears in the diagram). The interaction is predicted to be primarily mediated by other regions on the protein surface where the T1 Cu^{2+} is exposed (such as residues in the 214–220, 170–173, and 493–508 regions). However, as the system evolves in MD starting from best docking pose, the Met-loop rearranges to interact strongly with PE, keeping it persistently near the active site. Indeed, initially, the Met-loop and PE are at a distance of 8.8 Å, which quickly decreases to an equilibrium distance of around 2 Å after about 200 ns, indicating that a close and stable contact between the Met-loop and the substrate is formed until the end of the simulation (Figure 6.5B). This is mainly evidenced by the absence of water molecules in the Met-loop's first hydration shell, indicating that water does not mediate their interaction and that PE significantly shields the Met-loop from bulk water (Figure 6.5C). Additionally, this is confirmed by evaluating the van der Waals (vdW) contribution (derived from

MMPBSA free energy decomposition) of the residues within 5 Å of the substrate, many of which belong to the Met-loop (Figure 6.5D, red region). These observations help rationalize the previously described loss of Met-loop flexibility upon substrate binding. Notably, M224, M229, and M241, part of the hydrophobic half of the loop, form strong van der Waals interactions with PE. Moreover, the binding is also stabilized by other regions of the protein that are not part of the Met-loop but contribute to the interaction with PE through the exposure of hydrophobic residues, with Y414, W416, and Y501 contributing the most. In other words, PE is stably embraced by the Met-loop, and the PE/Met-loop *couple* is immobilized close to the catalytic site also thanks to the additional assistance of surface-exposed hydrophobic hooks. This result suggests that the Met-loop may enhance binding to PE, aligning with previous studies that indicate its role in increasing affinity for hydrophobic materials [51].

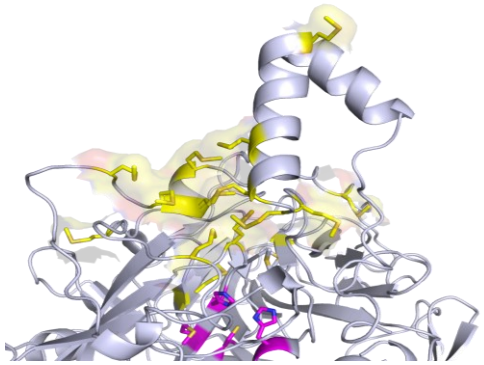

Figure 6.6: Detail of the AlphaFold 2 model predicted for PsLAC. T1 Cu^{2+} coordinating residues are reported in magenta, while the surface-exposed methionine residues in T1 proximity are colored in yellow.

Notably, the cold-adapted bacterial laccase PsLAC, which, like LMCO2, does not require mediators to oxidize LDPE, [24] is also characterized by a T1 site that is particularly rich in methionine residues (Figure 6.6). We may thus infer that this feature could serve as a significant driving force for PE oxidation, and we intend to further investigate this through mutagenesis experiments.

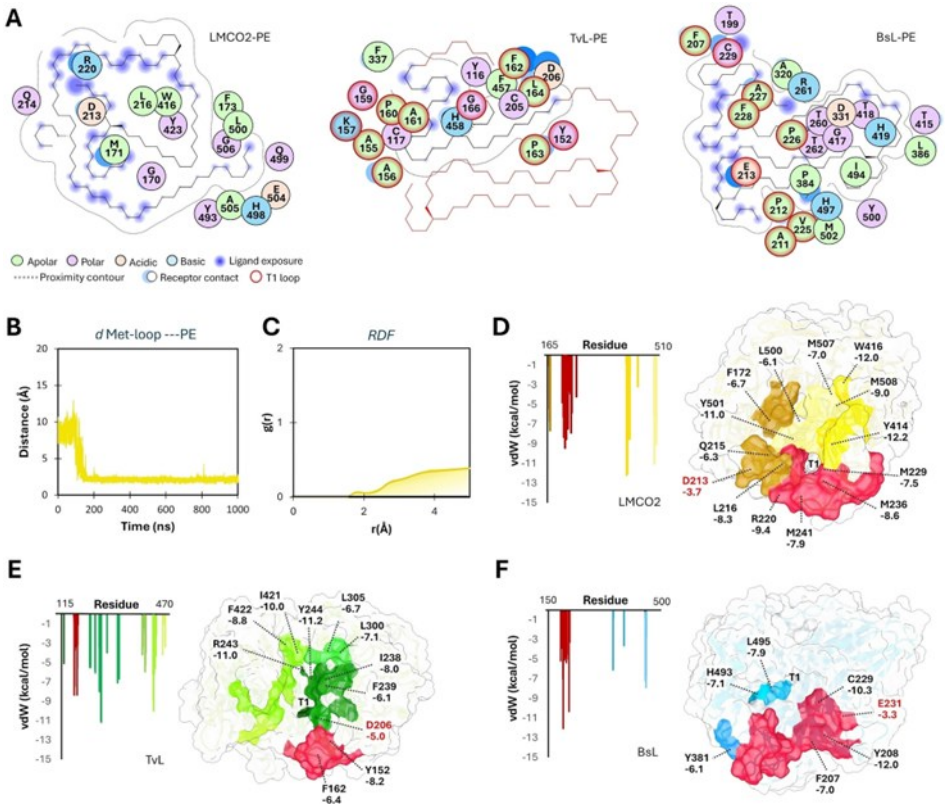

Figure 6.7: A) 2D interaction diagrams obtained from the best docking poses of PE to LMCO2, TvL, and BsL. Red portions of the ligand are not involved in contacts with the protein (i.e. are found outside the catalytic pocket). Red-bordered residues are those belonging to the Met-loop in LMCO2 or in the loop found in the same region in TvL and BsL, for simplicity labeled as "T1 loop" in the interaction legend; B) Monitoring of the Met-loop — PE distance (in Å) over MD trajectory for the LMCO2-PE complex; C) Water RDF considering Met-loop surroundings in LMCO2; D-F) MMPBSA decomposition for PE binding free energy to each laccase (D: LMCO2, E: TvL and F: BsL), focusing on the vdW contribution (if any, kcal mol^{-1}) of residues found in a cutoff of 5 Å with respect to PE. Residues characterized by the larger vdW contributions (more negative than -6 kcal mol^{-1}) have been mapped onto the protein surfaces (Met-loop or loop in the corresponding region highlighted in red), as well as eventual acidic residues involved in vdW contacts (i.e. D213 in LMCO2, D206 in TvL and E231 in BsL). The position of the T1 copper (buried by the protein surface) is also indicated.

In the case of TvL, docking results suggest that PE is only partially enclosed by the binding pocket, with a portion remaining exposed. In this case, and differently to what was observed with LMCO2, in the best docking pose several residues of the loop (corresponding to the LMCO2 Met-loop) are involved in the interaction, primarily hydrophobic in nature (Figure 6.7A). Then, by monitoring TvL-PE interactions along MD, a structural evolution of the complex is observed, leading to the complete insertion and adhesion of PE to the binding pocket. While in LMCO2 the Met-loop plays a key role in anchoring PE and holding it near the T1 site, in TvL, the stability of the complex is instead driven by multiple interactions with

hydrophobic residues that are strategically 'delocalized' on an extended surface surrounding the T1 site (Figure 6.7E).

For BsL, the situation is almost the opposite of what was described in the previous two cases. In fact, the docking results show that PE is located in proximity to Cu T1, establishing several interactions with the loop 207–232, and is fully enclosed within the binding pocket (Figure 6.7A). However, during the simulation, PE moves away from T1 and exits the pocket, while primarily maintaining interactions with the aforementioned loop, with which it strongly interacts (similarly to what is observed with the Met-loop in LMCO2). In this case, however, the loop tends to stabilize PE in a region that is distant from T1 (about 20 Å away), and this same behavior is observed in all the replicas (Figure 6.5H). The number of contacts PE forms with the surface of the protein in BsL, and with them the number of effective hydrophobic interactions, is significantly lower compared to the other two cases (Figure 6.7F), and this explains the less favorable ΔG MMPBSA value calculated during the dynamics. This also suggests that the total or near-total insertion of the substrate into the binding pocket, near T1, is crucial for promoting favorable interactions.

6.6 Potential Mechanistic Roles of PE Binding in Laccase Activity

Substrate oxidation mediated by laccases occurs through two fundamental chemical processes, regardless of the substrate's nature, namely electron transfer (mediated by T1 $Cu^{2+/+}$) and proton transfer steps. Clearly, the oxidation mechanism differs between phenolic and non-phenolic substrates. For non-phenolic substrates, specifically, a source of oxygen atoms is required to obtain any kind of oxidized product in addition to an acidic residue side chain to assist assist proton transfer Recently, it has been proposed that water molecules may serve this purpose, as shown in the case of benzo[a]pyrene oxidation by TvL [38]. In particular, water is expected to intervene between the substrate and the T1 center, possibly near an acidic residue (see below). Given the strong interaction observed between PE and both LMCO2 and TvL, along with significant substrate adhesion in the binding pocket, we explored whether water could access the region between PE and the catalytic center in these cases. We calculated the RDF for water near the T1 center and found that, in all three cases, there is persistent water in the first hydration shell of the active site, specifically between T1 and PE, suggesting that water molecules play a key role in mediating interactions in this region (Figure 6.8A). This finding supports a possible active role of water molecules, following the hypothesis previously proposed in the literature.

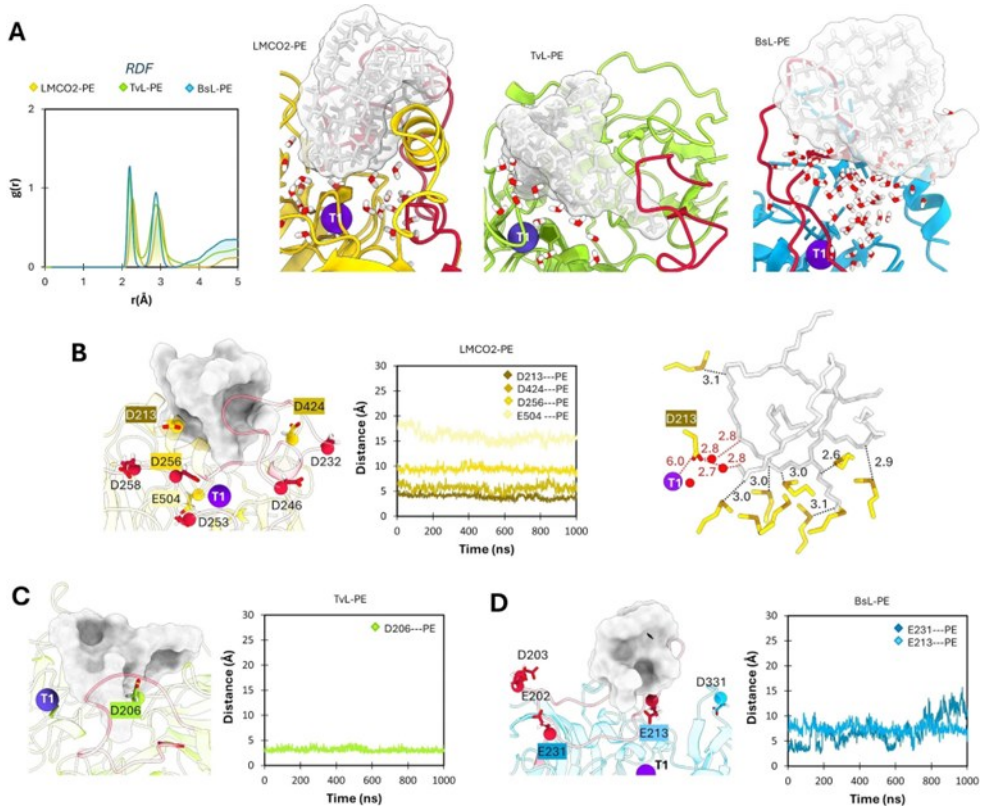

Figure 6.8: A) Water RDF in T1 Cu proximity for the three systems, with a focus on the T1-PE region highlighting the presence of water molecules between them, considering a representative frame taken from the most populated cluster of each enzyme-PE complex. B) Detail on acidic residues in the most representative cluster structure for LMCO2 in complex with PE, together with the monitoring of their distance (in Å) with respect to PE over MD simulation. A more detailed picture is also reported, showing the close PE - Met-loop contact and the short relative distances (in Å) between PE, D213, water molecules, and T1; C-D) Detail on acidic residues in the most representative cluster structure for TvL (C), and BsL (D), and monitoring of their distance (in Å) with respect to PE.

Notably, in BsL - where the PE model positions itself farther from T1 compared to TvL and LMCO2 - a higher number of water molecules is observed in this region. These water molecules may help compensate for the increased T1-PE distance and contribute to maintaining oxidative activity.

As previously mentioned, proton transfer is a crucial step in the oxidation mechanism and it is typically facilitated by the presence of acidic residues near both the T1 center and the substrate, as suggested for D206 in TvL [74]. We therefore investigated the presence of acidic residues capable of interacting with PE or located in proximity to both the substrate and the T1 center.

We observed that in LMCO2 the Met-loop maintains the substrate in proximity to acidic residues (in particular D213/232/246/253/258/424 and E504) surrounding T1, thus potentially enhancing the overall oxidation mechanism by promoting proton

transfer (Figure 6.8B). Interestingly, most of them are part of the polar half of the loop itself. More in detail, from the inspection of a significant frame (taken from the most populated cluster), we observed a particular structural configuration in which: a) the side chain of D213 interacts with a CH_2 group of the PE via two water molecules; b) this CH_2 group is, in turn, only 6 A away from the T1 Cu^{2+} (Figure 6.8B). In this specific scenario, we can hypothesize that a concerted Proton/Electron Transfer (PCET) mechanism may occur, exactly as proposed in the literature [38,74]. These results suggest a model for LMCO2 reactivity towards PE oxidation, where the polymer is initially anchored by the Met-loop, positioning it near several acidic residues.This increases the residence time of the LMCO2- PE complex, creating favorable conditions for a *potential* PCET to occur, which, based on the reduction potentials, is likely to proceed slowly. Further mechanistic details will be required to confirm that this mechanism also applies to PE as a substrate. A similar situation is also observed in the case of TvL: here, D206 is located near the PE (Figure 6.8C) and, in turn, is close to the T1 Cu^{2+}. This acidic residue is the one identified in the TvL laccase as responsible for proton transfer [75].

Acidic residues are also found near the PE when bound to BsL. In fact, similar to LMCO2, the loop corresponding to the Met-loop contains certain residues (E202, D203, E213, E231, and D331, Figure 6.8D) that could facilitate the proton transfer process. Specifically, E213 and E231 are located at a distance oscillating between 5 and 10 A from the PE. This oscillation observed in BsL, which is much more pronounced than in TvL and LMCO2, is because the PE is less stably bound to the protein and is essentially anchored to the loop, which retains its flexibility even after binding (unlike the Met-loop). In this scenario, where PE is positioned further away from the T1 Cu site, the relative distances between the PE, acidic residues, and the catalytic center could make a PCET process less likely compared to the other two case studies. In BsL, where the substrate occupies the binding pocket less persistently, we infer that this allows more space for a mediator to access the binding site and assist in ET. On the other hand, in LMCO2 and TvL, where the substrate occupies the binding pocket more stably and remains close to the T1 site, conditions seem more favorable for a potential PCET mechanism, even in the absence of a mediator. Therefore, we suggest that the mediator in BsL may play a more critical role in PE oxidation, while in LMCO2 and TvL, the substrate's proximity to T1 may facilitate oxidation without the need for a mediator.

6.7 Prospects

We hypothesized studying the same C–H activation mechanism (as described in the previous Section 6.2 [38]) also in laccases with aliphatic substrates (Figure 6.9 hypothesized mechanism).

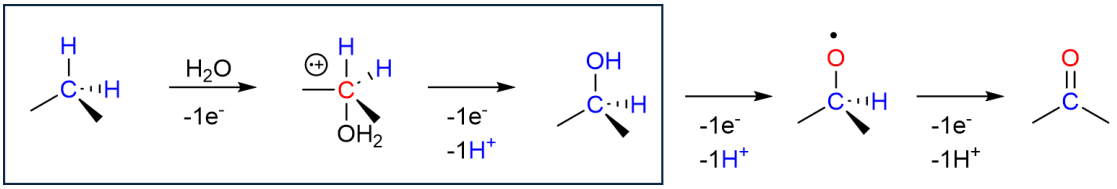

Figure 6.9: Hypothesized mechanism of C–H bond activation in aliphatic substrates: protonation of the aliphatic carbon, formation of a carbocation intermediate, and nucleophilic attack of water leading to the formation of an alcohol.

We proceeded with the determination of the MFEP using the string method combined with QM/MM for the LMCO2 system, with the QM region described using XTB and only T1 Cu2+, including the residues essential for the first mono-electronic oxidative step (the QM region is shown in Figure 6.10).

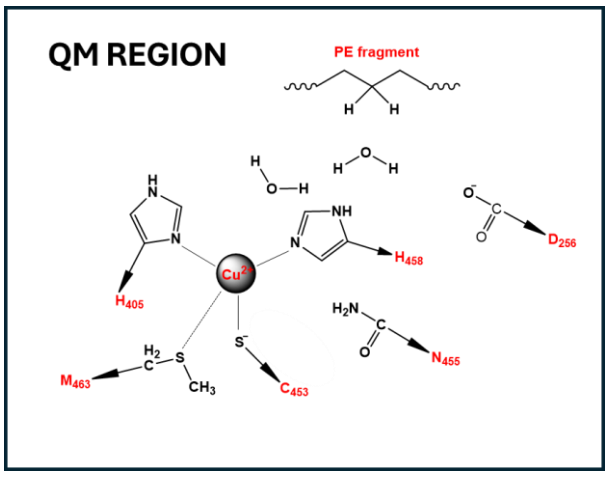

Figure 6.10: Representation of the QM region selected for the QM/MM simulations of the laccase system. The QM region includes the T1 copper site (Cu^{2+}), the relevant residues (H458, H455, H402, D256), and a fragment of PE and two water molecules. Atoms included in the QM region are highlighted, while the remaining enzyme and solvent environment are treated at the MM level.

Unfortunately, the calculated energy barrier for this pathway was around 45 kcal mol^{-1}, which is excessively high and therefore indicates that the mechanism is not kinetically plausible. As a result, this reaction route cannot be considered a reliable hypothesis.

QM/MM calculations using the string method did not prove to be productive, and several possible issues related to the application of this approach were considered. Alternative catalytic mechanisms were hypothesized, but the calculations failed to reach convergence. At present, attention has focused on three possible causes: (i) adopting a QM cluster approach to verify whether the method is more suitable for this system, (ii) the possibility that the problem originates from the initial enzyme model generated by AlphaFold, and (iii) the hypothesis, that the laccase LMCO2 is unable to degrade PE without prior pre-oxidation; consequently, the step we attempted to study may not be reliable. As an additional alternative, testing the mechanism with another laccase, such as that from *Trametes versicolor*, is also being considered.

From a chemical standpoint, the key issue in attempting to translate the mechanism observed for the oxidation of BAP to the case of PE lies like the substrate. Since laccases invariably catalyze one-electron oxidation steps, the corresponding process on PE would generate a radical center on an aliphatic carbon. Such a species is notoriously unstable and likely difficult to stabilize by LMCO2, making this pathway mechanistically unfavorable.

These findings represent an initial step in a mechanistic investigation of PE degradation by LMCO2. A natural extension of this work would involve considering a more complete model that also includes the T2 and T3 sites of the enzyme. However, the present results already suggest an alternative possibility: laccases may not directly catalyze the activation of sp^3 C–H bonds, but rather the oxidation of alcohol functionalities. These groups could arise from the partial oxidative degradation of PE surfaces by molecular oxygen, a process that inevitably occurs to some extent. Indeed, literature reports consistently show that many laccases display significantly higher activity on pre-oxidized PE, i.e. materials containing alcohol (–OH) or ketone groups.

This observation opens a new perspective for future studies: instead of starting from pristine PE models, it may be more realistic to investigate laccase activity using pre-oxidized PE models as substrates.

6.8 Conclusions

In this study, we explored the activity of different laccases through a comparative analysis of their redox potential and their capacity to interact with PE. The enzymes investigated represent a diverse group of natural laccases with proven or potential activity against LDPE, including a high-redox potential fungal laccase (*TvL*), a low-redox potential bacterial laccase (*BsL*), and LMCO2, whose redox features had not been previously characterized. By experimentally determining the redox potential of LMCO2, we classified it as a low-potential laccase, consistent with the canonical range of bacterial counterparts. This finding excluded the possibility that LMCO2's ability to act without a mediator is due to an unusually high redox potential and instead highlighted the importance of distinct binding modes in enabling its activity.

Our analyses revealed that PE–laccase interactions are strongly influenced by the hydrophobic residues located around the T1 copper site, as well as by the conformational plasticity of the polymer, which behaves like a wax-like chain capable of adapting to the enzyme's binding pocket. Both TvL and LMCO2 displayed stronger and more extensive contacts with PE than BsL, suggesting that binding efficiency is a decisive factor in modulating catalytic outcomes. In particular, LMCO2, despite being a low-redox potential enzyme, possesses a methionine-rich loop (Met-loop) that acts as an anchoring element, stabilizing PE near the T1 site for prolonged time intervals. Such a stable enzyme polymer complex could compensate for the unfavorable thermodynamics of electron transfer in the absence of mediators, thereby explaining the unique behavior of LMCO2 compared to BsL.

These results indicate that the oxidation of PE cannot be explained solely in terms of redox potential but must also consider the mode and stability of enzyme–substrate binding. Beyond the specific case studies presented here, our work establishes a generalizable computational framework for the investigation of PE-oxidizing enzymes. Detailed structural information on enzyme–polymer interactions remains challenging to obtain experimentally; therefore, computational methods represent a valuable complement, as already demonstrated in studies on lytic polysaccharide monooxygenases (LPMOs) interacting with crystalline cellulose and chitin [74–77].

Importantly, our study pioneers the use of a more realistic PE model to explore enzymatic oxidation while maintaining manageable computational costs. We also demonstrate that static approaches such as molecular docking, even when applied to either simplified linear hydrocarbons or more complex polymer fragments, are insufficient to capture the dynamic and subtle determinants of enzyme–PE interactions. In some cases, purely static models may even lead to misleading

conclusions, as illustrated by the behavior of BsL in our analyses. By integrating molecular dynamics simulations, we were able to employ a sufficiently large PE model that included not only the polymer chain but also a significant portion of the protein environment near the binding site. This approach made it possible to identify the residues that support polymer anchoring in the vicinity of the T1 copper center, while at the same time revealing acidic residues that are likely to participate in proton transfer during the reaction. In addition, it provided the means to evaluate how water molecules can access the T1 pocket, a feature that may play a nucleophilic role and thus significantly influence the oxidation mechanism.

Collectively, these insights provide a valuable framework for guiding future mutagenesis studies aimed at improving laccase activity toward PE. They also contribute to rationalizing the observed variability in enzymatic performance across different laccases. We expect that the computational strategy presented here will inspire experimental validation and new investigations, advance our mechanistic understanding of laccase-mediated polymer oxidation, and promote the design of more efficient biocatalysts for plastic bioremediation.

References

1. Tournier, V.; Duquesne, S.; Guillamot, F.; Cramail, H.; Taton, D.; Marty, A.; André, I. Enzymes' Power for Plastics Degradation. Chem Rev 2023, 123, 5612–5701, doi:10.1021/acs.chemrev.2c00644.
2. Amobonye, A.; Bhagwat, P.; Singh, S.; Pillai, S. Plastic Biodegradation: Frontline Microbes and Their Enzymes. Science of The Total Environment 2021, 759, 143536, doi:10.1016/j.scitotenv.2020.143536.
3. Jin, J.; Arciszewski, J.; Auclair, K.; Jia, Z. Enzymatic Polyethylene Biorecycling: Confronting Challenges and Shaping the Future. J Hazard Mater 2023, 460, 132449, doi:10.1016/j.jhazmat.2023.132449.
4. Rovaletti, A.; De Gioia, L.; Fantucci, P.; Greco, C.; Vertemara, J.; Zampella, G.; Arrigoni, F.; Bertini, L. Recent Theoretical Insights into the Oxidative Degradation of Biopolymers and Plastics by Metalloenzymes. Int J Mol Sci 2023, 24, 6368, doi:10.3390/ijms24076368.
5. Pometto, A.L.; Lee, B.T.; Johnson, K.E. Production of an Extracellular Polyethylene-Degrading Enzyme(s) by Streptomyces Species. Appl Environ Microbiol 1992, 58, 731–733, doi:10.1128/aem.58.2.731-733.1992.
6. Fujisawa, M.; Hirai, H.; Nishida, T. Degradation of Polyethylene and Nylon-66 by the Laccase-Mediator System. J Polym Environ 2001, 9, 103–108, doi:10.1023/A:1020472426516.
7. Sui, B.; Wang, T.; Fang, J.; Hou, Z.; Shu, T.; Lu, Z.; Liu, F.; Zhu, Y. Recent Advances in the Biodegradation of Polyethylene Terephthalate with Cutinase-like Enzymes. Front Microbiol 2023, 14, doi:10.3389/fmicb.2023.1265139.
8. Nguyen, B.-N.T.; Lim, J.Y.C. Emerging Green Approaches for Valorization of Plastics with Saturated Carbon Backbones. Trends Chem 2024, 6, 100–114, doi:10.1016/j.trechm.2024.01.001.
9. Chandra, R.; Chowdhary, P. Properties of Bacterial Laccases and Their Application in Bioremediation of Industrial Wastes. Environ Sci Process Impacts 2015, 17, 326–342, doi:10.1039/C4EM00627E.
10. Gräff, M.; Buchholz, P.C.F.; Le Roes-Hill, M.; Pleiss, J. Multicopper Oxidases: Modular Structure, Sequence Space, and Evolutionary Relationships. Proteins: Structure, Function, and Bioinformatics 2020, 88, 1329–1339, doi:10.1002/prot.25952.
11. Mot, A.C.; Silaghi-Dumitrescu, R. Laccases: Complex Architectures for One-Electron Oxidations. Biochemistry (Moscow) 2012, 77, 1395–1407, doi:10.1134/S0006297912120085.
12. Jones, S.M.; Solomon, E.I. Electron Transfer and Reaction Mechanism of Laccases. Cellular and Molecular Life Sciences 2015, 72, 869–883, doi:10.1007/s00018-014-1826-6.

13. Loi, M.; Glazunova, O.; Fedorova, T.; Logrieco, A.F.; Mulè, G. Fungal Laccases: The Forefront of Enzymes for Sustainability. Journal of Fungi 2021, 7, 1048, doi:10.3390/jof7121048.

14. Sowmya, H. V.; Ramalingappa; Krishnappa, M.; Thippeswamy, B. Degradation of Polyethylene by Trichoderma Harzianum—SEM, FTIR, and NMR Analyses. Environ Monit Assess 2014, 186, 6577–6586, doi:10.1007/s10661-014-3875-6.

15. Sowmya, H. V.; Ramalingappa; Krishnappa, M.; Thippeswamy, B. Degradation of Polyethylene by Penicillium Simplicissimum Isolated from Local Dumpsite of Shivamogga District. Environ Dev Sustain 2015, 17, 731–745, doi:10.1007/s10668-014-9571-4.

16. Gómez-Méndez, L.D.; Moreno-Bayona, D.A.; Poutou-Piñales, R.A.; Salcedo-Reyes, J.C.; Pedroza-Rodríguez, A.M.; Vargas, A.; Bogoya, J.M. Biodeterioration of Plasma Pretreated LDPE Sheets by Pleurotus Ostreatus. PLoS One 2018, 13, e0203786, doi:10.1371/journal.pone.0203786.

17. Kang, B.R.; Kim, S. Bin; Song, H.A.; Lee, T.K. Accelerating the Biodegradation of High-Density Polyethylene (HDPE) Using Bjerkandera Adusta TBB-03 and Lignocellulose Substrates. Microorganisms 2019, 7, 304, doi:10.3390/microorganisms7090304.

18. Di Napoli, M.; Silvestri, B.; Castagliuolo, G.; Carpentieri, A.; Luciani, G.; Di Maro, A.; Sorbo, S.; Pezzella, A.; Zanfardino, A.; Varcamonti, M. High Density Polyethylene (HDPE) Biodegradation by the Fungus Cladosporium Halotolerans. FEMS Microbiol Ecol 2023, 99, doi:10.1093/femsec/fiac148.

19. Ray, A.S.; Rajasekaran, M.; Uddin, M.; Kandasamy, R. Laccase Driven Biocatalytic Oxidation to Reduce Polymeric Surface Hydrophobicity: An Effective Pre-Treatment Strategy to Enhance Biofilm Mediated Degradation of Polyethylene and Polycarbonate Plastics. Science of The Total Environment 2023, 904, 166721, doi:10.1016/j.scitotenv.2023.166721.

20. Ruan, Y.; Hu, F.; Zhao, J.; Li, Y.; Ling, J.; Cao, J.; Zhang, L. Degradation of Polyethylene Particles by Trichoderma Harzianum and Recombinant Laccase Cloned from the Strain. J Appl Polym Sci 2023, 140, doi:10.1002/app.54599.

21. Gong, Z.; Jin, L.; Yu, X.; Wang, B.; Hu, S.; Ruan, H.; Sung, Y.-J.; Lee, H.-G.; Jin, F. Biodegradation of Low Density Polyethylene by the Fungus Cladosporium Sp. Recovered from a Landfill Site. Journal of Fungi 2023, 9, 605, doi:10.3390/jof9060605.

22. Ramamurthy, K.; Thomas, N.P.; Gopi, S.; Sudhakaran, G.; Haridevamuthu, B.; Namasivayam, K.R.; Arockiaraj, J. Is Laccase Derived from Pleurotus Ostreatus Effective in Microplastic Degradation? A Critical Review of Current Progress, Challenges, and Future Prospects. Int J Biol Macromol 2024, 276, 133971, doi:10.1016/j.ijbiomac.2024.133971.

23. Santo, M.; Weitsman, R.; Sivan, A. The Role of the Copper-Binding Enzyme – Laccase – in the Biodegradation of Polyethylene by the Actinomycete Rhodococcus Ruber. Int Biodeterior Biodegradation 2013, 84, 204–210, doi:10.1016/j.ibiod.2012.03.001.

24. Zhang, A.; Hou, Y.; Wang, Q.; Wang, Y. Characteristics and Polyethylene Biodegradation Function of a Novel Cold-Adapted Bacterial Laccase from Antarctic Sea Ice Psychrophile Psychrobacter Sp. NJ228. J Hazard Mater 2022, 439, 129656, doi:10.1016/j.jhazmat.2022.129656.

25. Yao, C.; Xia, W.; Dou, M.; Du, Y.; Wu, J. Oxidative Degradation of UV-Irradiated Polyethylene by Laccase-Mediator System. J Hazard Mater 2022, 440, 129709, doi:10.1016/j.jhazmat.2022.129709.

26. Zadjelovic, V.; Erni-Cassola, G.; Obrador-Viel, T.; Lester, D.; Eley, Y.; Gibson, M.I.; Dorador, C.; Golyshin, P.N.; Black, S.; Wellington, E.M.H.; et al. A Mechanistic Understanding of Polyethylene Biodegradation by the Marine Bacterium Alcanivorax. J Hazard Mater 2022, 436, 129278, doi:10.1016/j.jhazmat.2022.129278.

27. Gollan, M.; Black, G.; Munoz-Munoz, J. A Computational Approach to Optimising Laccase-Mediated Polyethylene Oxidation through Carbohydrate-Binding Module Fusion. BMC Biotechnol 2023, 23, 18, doi:10.1186/s12896-023-00787-5.

28. Gao, R.; Liu, R.; Sun, C. A Marine Fungus Alternaria Alternata FB1 Efficiently Degrades Polyethylene. J Hazard Mater 2022, 431, 128617, doi:10.1016/j.jhazmat.2022.128617.

29. Zampolli, J.; Mangiagalli, M.; Vezzini, D.; Lasagni, M.; Ami, D.; Natalello, A.; Arrigoni, F.; Bertini, L.; Lotti, M.; Di Gennaro, P. Oxidative Degradation of Polyethylene by Two Novel Laccase-like Multicopper Oxidases from Rhodococcus Opacus R7. Environ Technol Innov 2023, 32, 103273, doi:10.1016/j.eti.2023.103273.

30. Shafana Farveen, M.; Madhavan, T.; Narayanan, R. Association of Laccase from Bacillus Cereus O2-B and Pseudomonas Aeruginosa O1-P with the Bio-Degradation of Polymers: An in Vitro to in Silico Approach. Biodegradation 2023, 34, 383–403, doi:10.1007/s10532-023-10028-3.

31. Tao, X.; Ouyang, H.; Zhou, A.; Wang, D.; Matlock, H.; Morgan, J.S.; Ren, A.T.; Mu, D.; Pan, C.; Zhu, X.; et al. Polyethylene Degradation by a Rhodococcous Strain Isolated from Naturally Weathered Plastic Waste Enrichment. Environ Sci Technol 2023, 57, 13901–13911, doi:10.1021/acs.est.3c03778.

32. Zhang, Y.; Plesner, T.J.; Ouyang, Y.; Zheng, Y.-C.; Bouhier, E.; Berentzen, E.I.; Zhang, M.; Zhou, P.; Zimmermann, W.; Andersen, G.R.; et al. Computer-Aided Discovery of a Novel Thermophilic Laccase for Low-Density Polyethylene Degradation. J Hazard Mater 2023, 458, 131986, doi:10.1016/j.jhazmat.2023.131986.

33. Zeng, B.; Fu, Y.; Ye, J.; Yang, P.; Cui, S.; Qiu, W.; Li, Y.; Wu, T.; Zhang, H.; Wang, Y.; et al. Ancestral Sequence Reconstruction of the Prokaryotic Three-Domain Laccases for Efficiently Degrading Polyethylene. J Hazard Mater 2024, 476, 135012, doi:10.1016/j.jhazmat.2024.135012.

34. Yao, Z.; Seong, H.J.; Jang, Y.-S. Degradation of Low Density Polyethylene by Bacillus Species. Appl Biol Chem 2022, 65, 84, doi:10.1186/s13765-022-00753-3.

35. da Rocha, A.B.; de Aquino Saraiva, R.; de Siqueira, V.M.; Yogui, G.T.; de Souza Bezerra, R.; de Assis, C.R.D.; Sousa, M.S.B.; de Souza Buarque, D. Shrimp Laccase Degrades Polycyclic Aromatic Hydrocarbons from an Oil Spill Disaster in Brazil: A Tool for Marine Environmental Bioremediation. Mar Pollut Bull 2023, 194, 115445, doi:10.1016/j.marpolbul.2023.115445.

36. Bourbonnais, R.; Paice, M.G. Oxidation of Non-phenolic Substrates. FEBS Lett 1990, 267, 99–102, doi:10.1016/0014-5793(90)80298-W.

37. Baiocco, P.; Barreca, A.M.; Fabbrini, M.; Galli, C.; Gentili, P. Promoting Laccase Activity towards Non-Phenolic Substrates: A Mechanistic Investigation with Some Laccase–Mediator Systems. Org. Biomol. Chem. 2003, 1, 191–197, doi:10.1039/B208951C.

38. Orlando, C.; Rizzo, I.C.; Arrigoni, F.; Zampolli, J.; Mangiagalli, M.; Di Gennaro, P.; Lotti, M.; De Gioia, L.; Marino, T.; Greco, C.; et al. Mechanism of Non-Phenolic Substrate Oxidation by the Fungal Laccase Type 1 Copper Site from Trametes Versicolor : The Case of Benzo[a]Pyrene and Anthracene. Dalton Transactions 2024, 53, 12152–12161, doi:10.1039/D4DT01377H.

39. Santacruz-Juárez, E.; Buendia-Corona, R.E.; Ramírez, R.E.; Sánchez, C. Fungal Enzymes for the Degradation of Polyethylene: Molecular Docking Simulation and Biodegradation Pathway Proposal. J Hazard Mater 2021, 411, 125118, doi:10.1016/j.jhazmat.2021.125118.

40. Zhu, Y.; Zhang, Y.; Zhan, J.; Lin, Y.; Yang, X. Axial Bonds at the T1 Cu Site of Thermus Thermophilus <scp>SG</Scp> 0.5 <scp>JP</Scp> 17-16 Laccase Influence Enzymatic Properties. FEBS Open Bio 2019, 9, 986–995, doi:10.1002/2211-5463.12633.

41. Durão, P.; Bento, I.; Fernandes, A.T.; Melo, E.P.; Lindley, P.F.; Martins, L.O. Perturbations of the T1 Copper Site in the CotA Laccase from Bacillus Subtilis: Structural, Biochemical, Enzymatic and Stability Studies. JBIC Journal of Biological Inorganic Chemistry 2006, 11, 514–526, doi:10.1007/s00775-006-0102-0.

42. Cui, H.; Zhang, L.; Söder, D.; Tang, X.; Davari, M.D.; Schwaneberg, U. Rapid and Oriented Immobilization of Laccases on Electrodes via a Methionine-Rich Peptide. ACS Catal 2021, 11, 2445–2453, doi:10.1021/acscatal.0c05490.

43. Singh, S.K.; Roberts, S.A.; McDevitt, S.F.; Weichsel, A.; Wildner, G.F.; Grass, G.B.; Rensing, C.; Montfort, W.R. Crystal Structures of Multicopper Oxidase CueO Bound to Copper(I) and Silver(I). Journal of Biological Chemistry 2011, 286, 37849–37857, doi:10.1074/jbc.M111.293589.

44. Wang, H.; Liu, X.; Zhao, J.; Yue, Q.; Yan, Y.; Gao, Z.; Dong, Y.; Zhang, Z.; Fan, Y.; Tian, J.; et al. Crystal Structures of Multicopper Oxidase CueO G304K Mutant: Structural Basis of the Increased Laccase Activity. Sci Rep 2018, 8, 14252, doi:10.1038/s41598-018-32446-7.

45. Borges, P.T.; Brissos, V.; Hernandez, G.; Masgrau, L.; Lucas, M.F.; Monza, E.; Frazão, C.; Cordeiro, T.N.; Martins, L.O. Methionine-Rich Loop of Multicopper Oxidase McoA

Follows Open-to-Close Transitions with a Role in Enzyme Catalysis. ACS Catal 2020, 10, 7162–7176, doi:10.1021/acscatal.0c01623.

46. Brissos, V.; Borges, P.T.; Núñez-Franco, R.; Lucas, M.F.; Frazão, C.; Monza, E.; Masgrau, L.; Cordeiro, T.N.; Martins, L.O. Distal Mutations Shape Substrate-Binding Sites during Evolution of a Metallo-Oxidase into a Laccase. ACS Catal 2022, 12, 5022–5035, doi:10.1021/acscatal.2c00336.

47. Pronk, S.; Páll, S.; Schulz, R.; Larsson, P.; Bjelkmar, P.; Apostolov, R.; Shirts, M.R.; Smith, J.C.; Kasson, P.M.; van der Spoel, D.; et al. GROMACS 4.5: A High-Throughput and Highly Parallel Open Source Molecular Simulation Toolkit. Bioinformatics 2013, 29, 845–854, doi:10.1093/bioinformatics/btt055.

48. Zhang, L.; Cui, H.; Dhoke, G. V.; Zou, Z.; Sauer, D.F.; Davari, M.D.; Schwaneberg, U. Engineering of Laccase CueO for Improved Electron Transfer in Bioelectrocatalysis by Semi-Rational Design. Chemistry – A European Journal 2020, 26, 4974–4979, doi:10.1002/chem.201905598.

49. Arregui, L.; Ayala, M.; Gómez-Gil, X.; Gutiérrez-Soto, G.; Hernández-Luna, C.E.; Herrera de los Santos, M.; Levin, L.; Rojo-Domínguez, A.; Romero-Martínez, D.; Saparrat, M.C.N.; et al. Laccases: Structure, Function, and Potential Application in Water Bioremediation. Microb Cell Fact 2019, 18, 200, doi:10.1186/s12934-019-1248-0.

50. Singh, G.; Bhalla, A.; Kaur, P.; Capalash, N.; Sharma, P. Laccase from Prokaryotes: A New Source for an Old Enzyme. Rev Environ Sci Biotechnol 2011, 10, 309–326, doi:10.1007/s11157-011-9257-4.

51. Hullo, M.-F.; Moszer, I.; Danchin, A.; Martin-Verstraete, I. CotA of Bacillus Subtilis Is a Copper-Dependent Laccase. J Bacteriol 2001, 183, 5426–5430, doi:10.1128/JB.183.18.5426-5430.2001.

52. Martins, L.O.; Durão, P.; Brissos, V.; Lindley, P.F. Laccases of Prokaryotic Origin: Enzymes at the Interface of Protein Science and Protein Technology. Cellular and Molecular Life Sciences 2015, 72, 911–922, doi:10.1007/s00018-014-1822-x.

53. Gentil, S.; Rousselot-Pailley, P.; Sancho, F.; Robert, V.; Mekmouche, Y.; Guallar, V.; Tron, T.; Le Goff, A. Efficiency of Site-Specific Clicked Laccase–Carbon Nanotubes Biocathodes towards O 2 Reduction. Chemistry – A European Journal 2020, 26, 4798–4804, doi:10.1002/chem.201905234.

54. Bianchi, G.; Pessina, A.; Ami, D.; Signorelli, S.; de Divitiis, M.; Natalello, A.; Lotti, M.; Brambilla, L.; Brocca, S.; Mangiagalli, M. Sustainable Production of a Biotechnologically Relevant β-Galactosidase in Escherichia Coli Cells Using Crude Glycerol and Cheese Whey Permeate. Bioresour Technol 2024, 406, 131063, doi:10.1016/j.biortech.2024.131063.

55. Olivé, M.; Engvall, M.; Ravenscroft, G.; Cabrera-Serrano, M.; Jiao, H.; Bortolotti, C.A.; Pignataro, M.; Lambrughi, M.; Jiang, H.; Forrest, A.R.R.; et al. Myoglobinopathy Is an Adult-Onset Autosomal Dominant Myopathy with Characteristic Sarcoplasmic Inclusions. Nat Commun 2019, 10, 1396, doi:10.1038/s41467-019-09111-2.

56. Bellei, M.; Bortolotti, C.A.; Di Rocco, G.; Borsari, M.; Lancellotti, L.; Ranieri, A.; Sola, M.; Battistuzzi, G. The Influence of the Cys46/Cys55 Disulfide Bond on the Redox and Spectroscopic Properties of Human Neuroglobin. J Inorg Biochem 2018, 178, 70–86, doi:10.1016/j.jinorgbio.2017.10.005.

57. Jumper, J.; Hassabis, D. Protein Structure Predictions to Atomic Accuracy with AlphaFold. Nat Methods 2022, 19, 11–12, doi:10.1038/s41592-021-01362-6.

58. Abraham, M.J.; Murtola, T.; Schulz, R.; Páll, S.; Smith, J.C.; Hess, B.; Lindahl, E. GROMACS: High Performance Molecular Simulations through Multi-Level Parallelism from Laptops to Supercomputers. SoftwareX 2015, 1–2, 19–25, doi:10.1016/j.softx.2015.06.001.

59. Maier, J.A.; Martinez, C.; Kasavajhala, K.; Wickstrom, L.; Hauser, K.E.; Simmerling, C. Ff14SB: Improving the Accuracy of Protein Side Chain and Backbone Parameters from Ff99SB. J Chem Theory Comput 2015, 11, 3696–3713, doi:10.1021/acs.jctc.5b00255.

60. Li, Z.; Song, L.F.; Li, P.; Merz, K.M.Jr. Systematic Parametrization of Divalent Metal Ions for the OPC3, OPC, TIP3P-FB, and TIP4P-FB Water Models. J Chem Theory Comput 2020, 16, 4429–4442, doi:10.1021/acs.jctc.0c00194.

61. Li, P.; Merz, K.M.Jr. Taking into Account the Ion-Induced Dipole Interaction in the Nonbonded Model of Ions. J Chem Theory Comput 2014, 10, 289–297, doi:10.1021/ct400751u.

62. Zhang, W.; Larson, R.G. Direct All-Atom Molecular Dynamics Simulations of the Effects of Short Chain Branching on Polyethylene Oligomer Crystal Nucleation. Macromolecules 2018, 51, 4762–4769, doi:10.1021/acs.macromol.8b00958.

63. Zhang, X.; Li, Z.; Lu, Z.; Sun, C. Molecular Dynamics Simulation of the Linear Low-Density Polyethylene Crystallization. Journal of Chemical Physics 2001, 115, 3916–3922, doi:10.1063/1.1389856.

64. Case, D.A.; Aktulga, H.M.; Belfon, K.; Cerutti, D.S.; Cisneros, G.A.; Cruzeiro, V.W.D.; Forouzesh, N.; Giese, T.J.; Götz, A.W.; Gohlke, H.; et al. AmberTools. J Chem Inf Model 2023, 63, 6183–6191, doi:10.1021/acs.jcim.3c01153.

65. Trott, O.; Olson, A.J. AutoDock Vina: Improving the Speed and Accuracy of Docking with a New Scoring Function, Efficient Optimization, and Multithreading. J Comput Chem 2010, 31, 455–461, doi:10.1002/jcc.21334.

66. Kaus, J.W.; Pierce, L.T.; Walker, R.C.; McCammon, J.A. Improving the Efficiency of Free Energy Calculations in the Amber Molecular Dynamics Package. J Chem Theory Comput 2013, 9, 4131–4139, doi:10.1021/ct400340s.

67. Bannwarth, C.; Caldeweyher, E.; Ehlert, S.; Hansen, A.; Pracht, P.; Seibert, J.; Spicher, S.; Grimme, S. Extended <scp>tight-binding</Scp> Quantum Chemistry Methods. WIREs Computational Molecular Science 2021, 11, doi:10.1002/wcms.1493.

68. He, Z.; Chipot, C.; Roux, B. Committor-Consistent Variational String Method. J Phys Chem Lett 2022, 13, 9263–9271, doi:10.1021/acs.jpclett.2c02529.

69. Worrall, J.A.R.; Machczynski, M.C.; Keijser, B.J.F.; di Rocco, G.; Ceola, S.; Ubbink, M.; Vijgenboom, E.; Canters, G.W. Spectroscopic Characterization of a High-Potential Lipo-Cupredoxin Found in Streptomyces Coelicolor. J Am Chem Soc 2006, 128, 14579–14589, doi:10.1021/ja064112n.

70. Liu, J.; Chakraborty, S.; Hosseinzadeh, P.; Yu, Y.; Tian, S.; Petrik, I.; Bhagi, A.; Lu, Y. Metalloproteins Containing Cytochrome, Iron–Sulfur, or Copper Redox Centers. Chem Rev 2014, 114, 4366–4469, doi:10.1021/cr400479b.

71. Zhang, X.; Li, Z.; Lu, Z.; Sun, C. Molecular Dynamics Simulation of the Linear Low-Density Polyethylene Crystallization. J Chem Phys 2001, 115, 3916–3922, doi:10.1063/1.1389856.

72. Harmandaris, V.A.; Mavrantzas, V.G.; Theodorou, D.N. Atomistic Molecular Dynamics Simulation of Polydisperse Linear Polyethylene Melts. Macromolecules 1998, 31, 7934–7943, doi:10.1021/ma980698p.

73. Rungswang, W.; Narkchamnan, K.; Petcharat, N.; Thitisak, B.; Pathaweeisariyakul, T. Primitive Structure and Its Morphology for Describing Highly Branched Structure of Low-Density Polyethylene. Polymer Bulletin 2017, 74, 3229–3242, doi:10.1007/s00289-016-1893-y.

74. Galli, C.; Madzak, C.; Vadalà, R.; Jolivalt, C.; Gentili, P. Concerted Electron/Proton Transfer Mechanism in the Oxidation of Phenols by Laccase. ChemBioChem 2013, 14, 2500–2505, doi:10.1002/cbic.201300531.

75. Mehra, R.; Muschiol, J.; Meyer, A.S.; Kepp, K.P. A Structural-Chemical Explanation of Fungal Laccase Activity. Sci Rep 2018, 8, 17285, doi:10.1038/s41598-018-35633-8.

76. Bissaro, B.; Isaksen, I.; Vaaje-Kolstad, G.; Eijsink, V.G.H.; Røhr, Å.K. How a Lytic Polysaccharide Monooxygenase Binds Crystalline Chitin. Biochemistry 2018, 57, 1893–1906, doi:10.1021/acs.biochem.8b00138.

77. Berhe, M.H.; Song, X.; Yao, L. Improving the Enzymatic Activity and Stability of a Lytic Polysaccharide Monooxygenase. Int J Mol Sci 2023, 24, 8963, doi:10.3390/ijms24108963.

SECTION 2

Computational Studies on Metalloenzymes for Biodegradable Waste Valorization.

The second section of Chapter 3 provided a concise overview of the results obtained from two studies, corresponding to Papers IV and V. This chapter presents a detailed investigation of these works, currently in progress, focusing on two metalloenzymes involved in the degradation and valorization of biodegradable waste. The analyses, based on classical molecular dynamics (MD) simulations, explore the structural dynamics, substrate interactions, and catalytic properties of two key enzymatic systems: the CYP152 family of cytochrome P450 peroxygenases and the bacterial lytic polysaccharide monooxygenase (LPMO) SmAA10.

Chapter 7

Rational Design of CYP450SPα Mutants for Enhanced Lipid Waste Conversion: Dynamic Comparison with OleTJE

Here, the CYP152 enzyme family is examined, with a focus on the design and analysis of mutant variants to develop biohybrid systems with improved catalytic performance.

The CYP152 family, part of the bacterial cytochrome P450 superfamily, includes metal-dependent enzymes such as SPα, BSβ, and OleTJE, which are characterized by their ability to function as self-sufficient peroxygenases. These enzymes directly utilize hydrogen peroxide (H_2O_2) in the catalytic cycle, without requiring external redox partners or proton sources, thereby simplifying the process and increasing efficiency. The CYP152 class is capable of enzymatically converting fatty acids, derived from waste marine biomass, into terminal alkenes through oxidative decarboxylation, as well as producing hydroxylated fatty acids via α- and β-position hydroxylation. These reactions make CYP152 enzymes particularly suitable for the synthesis of sustainable, second-generation biofuels with low environmental impact. The unique properties of these enzymes position them as promising tools in synthetic biology and in the valorization of organic waste, contributing to the transition toward a circular and sustainable economy. However, effective industrial application requires enzyme optimization to withstand non-natural operating conditions. The development of hybrid biosystems, combining different biological scaffolds, can enhance catalytic activity and stability compared to native proteins. In this context, computational methods serve as essential tools to support enzyme engineering.

In this study, three mutant variants of the wild-type CYP152SPα enzyme were designed and analyzed through MD simulations to develop biohybrid systems with enhanced enzymatic performance. The simulations conducted both in the apo form and in the presence of the fatty acid substrate C16:0, enabled exploration of the conformational landscape of the enzymes and their interactions with the molecular

environment and ligand. Detailed analysis of the MD trajectories allowed identification of the most stable conformation for each variant and assessment of the individual mutations' impact, intending to select the system exhibiting the best catalytic and stability properties for biotechnological applications.

7.1 Introduction

The growing need to reduce global greenhouse gas emissions to prevent irreversible climate change has made the development of alternative and sustainable energy sources increasingly urgent [1]. In this context, second-generation biofuels, derived from non-edible biomass and organic waste, represent a promising solution compared to first-generation biofuels [2], whose production competes with food crops, thereby reducing food availability and the net effectiveness in terms of CO_2 reduction [3].

Among the most abundant and underutilized waste materials are fishery by-products, such as fish scales and crustacean shells, which amount to approximately 7 million tons per year and are particularly rich in lipids and fatty acids [4,5]. These components can be converted into high-value-added compounds through low-impact biotechnological processes. In particular, metal-dependent oxidative enzymes, such as bacterial cytochrome P450s (CYPs), have proven to be key tools in the valorization of lipid-rich waste due to their ability to convert fatty acids into alkenes, alkanes, and alcohols [6–8].

Cytochrome P450 enzymes of the CYP152 family, the focus of this study, exhibit specific hydroxylation and decarboxylation activities on fatty acids. Notably, P450SPα (CYP152B1) catalyzes selective hydroxylation at the Cα position [9], P450BSβ (CYP152A1) hydroxylates both the Cα and Cβ positions [10], and P450OleTJE (CYP152L1) predominantly catalyzes the oxidative decarboxylation of fatty acids to produce terminal alkenes, with higher catalytic efficiency compared to other members of the family (see Figure 7.1) [11,12].

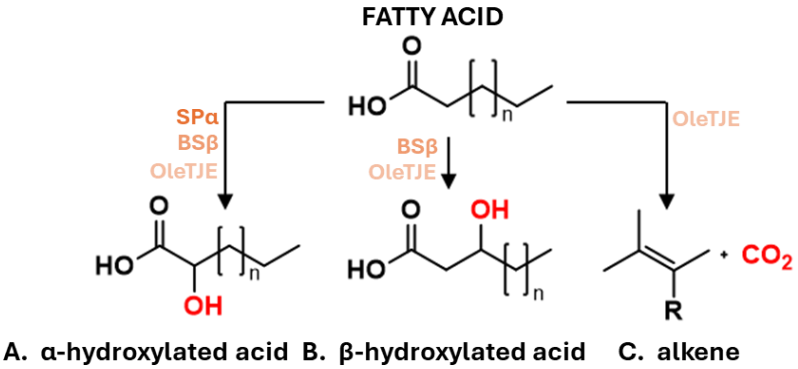

Figure 7.1: Representation of the enzymatic reactions involved in the transformation of fatty acids into functionalized derivatives, such as hydroxylated fatty acids (via hydroxylation reactions) and alkenes (through decarboxylation processes with CO_2 released as a byproduct). Each reaction is catalyzed by specific cytochromes, indicated with the acronyms SPα, BSβ, and OleTJE, shown above the respective arrows.

Cytochromes of the CYP152 class, such as P450SPα, utilize H_2O_2 as a cofactor in the so-called *peroxide shunt*, thereby bypassing the use of molecular oxygen typical of the classical CYP catalytic cycle [13–15]. This enzymatic subclass catalyzes hydroxylation reactions (at the α or β position) and oxidative decarboxylation, yielding terminal alkenes that are suitable for use as biofuels [16,17]. Enzymes like P450OleTJE exhibit higher catalytic efficiency compared to P450SPα, making the latter an ideal model for targeted enzyme engineering [18,19].

Furthermore, the reuse of fatty acids derived from food waste [20–22]. or agro-industrial residues [23], including oily waste and palm oil mill effluent (POME) [24], represents an effective strategy to reduce both solid and liquid waste as well as greenhouse gas (GHG) emissions [25]. Due to their hydrophobic nature, fatty acids can serve as substrates in highly selective enzymatic reactions [26,27], contributing to the production of fuels and chemicals traditionally derived from petrochemical sources [28,29].

In the framework of the circular economy, the ability to convert waste into valuable resources aligns with a sustainable vision of industrial processes, overcoming the still-dominant linear production model [30–32]. For these technologies to achieve industrial relevance, however, oxidative enzymes must be optimized to function under non-natural operational conditions, with enhanced catalytic activity.

Bacterial CYP enzymes offer numerous advantages: they are soluble, catalytically self-sufficient, and amenable to modulation through protein engineering techniques. Additionally, they can be integrated with other biological scaffolds to create more efficient hybrid biosystems [33], expanding the range of compatible substrates and reaction conditions [34,35].

This research project aims to support the rational design of metal-dependent oxidative enzymes capable of transforming recalcitrant substrates found in lipid-rich marine biomass into second-generation biofuels. Specifically, the work will focus on:

- Structural and dynamic analysis of CYP450SPα, in comparison with the more catalytically active P450OleTJE;
- Computational design and simulation of P450SPα mutants to improve catalytic performance;
- Evaluation of the influence of specific mutations on structure and function;
- Application of computational techniques such as MD simulations to investigate structural stability and enzyme–substrate affinity.

MD simulations will enable the exploration of the conformational landscape of the enzymes in explicit solvent, allowing for the identification of representative structures through trajectory clustering. These data will guide the *de novo* design of PAMETs (peptidic artificial metalloenzymes) optimized for biomass valorization [36–38]. This work represents a strategic step toward the development of more efficient hybrid biosystems [39], capable of operating under non-physiological conditions, contributing to the advancement of renewable enzyme-based technologies.

7.2 Computational Details

The initial coordinates for the CYP450SPα protein were obtained from the available crystal structure with PDB ID: 3AWM [40]. Classical MD simulations were performed on apo systems, including: the wild-type protein (WTf); a single mutant at position 173 (G173F, M1f); a single mutant at position 288 (F288A, M2f); and a double mutant at both positions (G173F/F288A, M12f). In these systems, the ligand (C16:0 fatty acid) was manually removed.

For substrate-bound systems, simulations were performed on the same four constructs (WT, M1, M2, and M12), preserving the substrate coordinates (C16:0) from the 3AWM PDB file. All mutations were introduced using UCSF Chimera version 1.16 [41]. The protein systems were solvated in a cubic box with a 10 Å buffer using TIP3P water molecules and neutralized with counterions [42].

Classical MD simulations were carried out for 200 ns per system, in triplicate, yielding a total simulation time of 4,8 μs. Input files were prepared using the GROMACS software package [43]. The CHARMM36 force field [44] (July 2022 update) was employed, with TIP3P water. To preserve the correct coordination of the heme iron, specific “special bonds” [45] were defined between the ferric ion and the deprotonated cysteine residue (CYM).

Both apo and substrate-bound solvated systems were subjected to initial minimization and relaxation using positional harmonic restraints (50 kcal mol^{-1} $Å^{-2}$) on all atoms. The minimization protocol included 5000 steps of steepest descent (SD) followed by 5000 steps of conjugate gradient (CG). Systems were then gradually heated to 303.2 K over 20 ns under NVT conditions using a Langevin thermostat. Equilibration proceeded under isobaric conditions (1 bar) using the NPT ensemble with a Berendsen barostat (τp = 2.0 ps). Production runs were performed for 200 ns with a 2 fs integration timestep, using the SHAKE algorithm to constrain bonds involving hydrogen atoms and the Particle Mesh Ewald (PME) method for long-range electrostatics [46]. A geometric RMSD-based clustering analysis (GROMOS algorithm [47], 3 Å cutoff) was applied to identify the most populated representative conformations for each system.

Additionally, 200 ns MD simulations, also in triplicate, were performed for the OleTJE protein (PDB ID: 4L54 [48]) in both apo and substrate-bound states (using the same C16:0 coordinates as in 3AWM), contributing an additional 0,6 μs of simulation time. This brought the total simulation time to 5,4 μs. All simulation conditions for OleTJE were kept identical to those used for SPα and its variants to ensure dynamic comparability across systems.

7.3 Study of Access Pathways to the Active Site and Implications for Mutagenesis.

The X-ray crystallographic structure of CYP450 SPα (PDB: 3AWM) [40] was used as the starting model for classical molecular dynamics simulations. As with all bacterial cytochromes P450, its structure is characterized by the presence of a porphyrin-type heme ring (Figure 7.2). Thanks to the well-defined position of the active site within specific domains, these enzymes are highly amenable to targeted manipulations. As previously mentioned, this class of bacterial cytochromes P450 is interesting due to its ability to function as peroxygenases (CYP152).

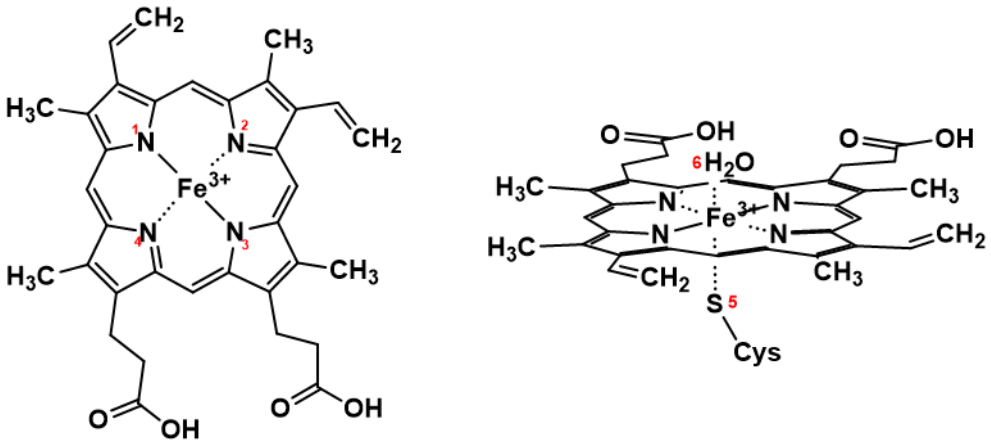

Figure 7.2: Chemical structure of the porphyrin ring of cytochrome P450. Four planar bonds coordinate the iron with the nitrogen atoms of the porphyrin and two axial bonds located above and below the plane of the ring. In this case, the axial ligands are the sulfur atom of a cysteine and a water molecule

This enzymatic subclass is capable of converting fatty acids through oxidative decarboxylation and, via hydroxylation at the α and β positions, produces hydroxylated fatty acids and/or terminal alkenes. The initial crystallographic structure of P450SPα was superimposed onto those of other enzymes, P450BSβ (PDB ID: 1LZO [49]) and P450OleTJE (PDB ID: 4L40 [48]), see Figure 7.3, to highlight key structural differences that enable improved positioning of the fatty acid within the catalytic pocket. Considering OleTJE's ability to catalyze not only hydroxylation reactions at the α or β positions but also fatty acid decarboxylation, many studies have sought to replicate this activity in other CYP152 systems through targeted mutagenesis.
In particular, the introduction of a histidine residue at position 85, considered fundamental in OleTJE for its role as a proton donor in the decarboxylation reaction, has been proposed as a promising strategy. However, the outcomes of these attempts have been limited. For example, in BSβ, the insertion of a histidine at the analogous position did not lead to a significant increase in decarboxylase activity.

Arginine, located at positions 241, 242, and 245 in SPα, BSβ, and OleTJE, respectively, has proven to be a key residue, with its mutation resulting in a complete loss of catalytic activity [50]. Visual analysis identified two possible access channels for fatty acids, located on the enzyme's front side near residue R241, which appears to be primarily responsible for the enzyme's catalytic activity [51].

From structural superposition, other residues such as G173 and F288 were also found to be indirectly involved in this reaction, playing a key role in enhancing the catalytic activity of CYP152SPα.

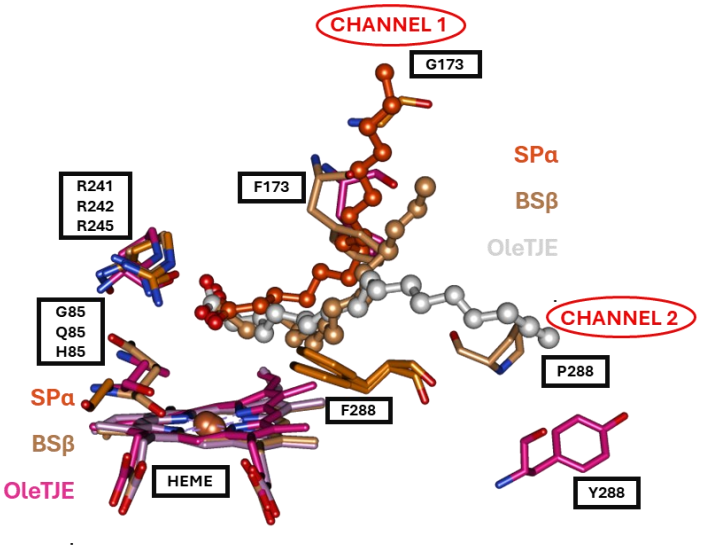

Figure 7.3: Superposition of the 3 crystal structures, SPα (orange), BSβ (beige), and OeTJE (white).

In the SPα system, tunnels and their connected cavities were identified using the software Caver Analyst 3.0 [52]. These data were then compared with those from the BSβ and OleTJE systems to highlight any structural differences. The main objective of this analysis was to identify the preferential pathway of water molecules toward the catalytic site, which is presumed to coincide with the substrate access route to the active site.

Specifically, as shown in Figure 7.4, the highest-priority tunnels are highlighted in blue: in the BSβ and OleTJE systems (channel 2), this represents the preferred pathway followed by the substrate, whereas in SPα, the tunnel corresponding to this route (channel 1) does not appear to be the primary one. Starting from the identified tunnels, the largest connected cavities were then calculated to verify the possible ligand access sites (see Figure 7.4B).

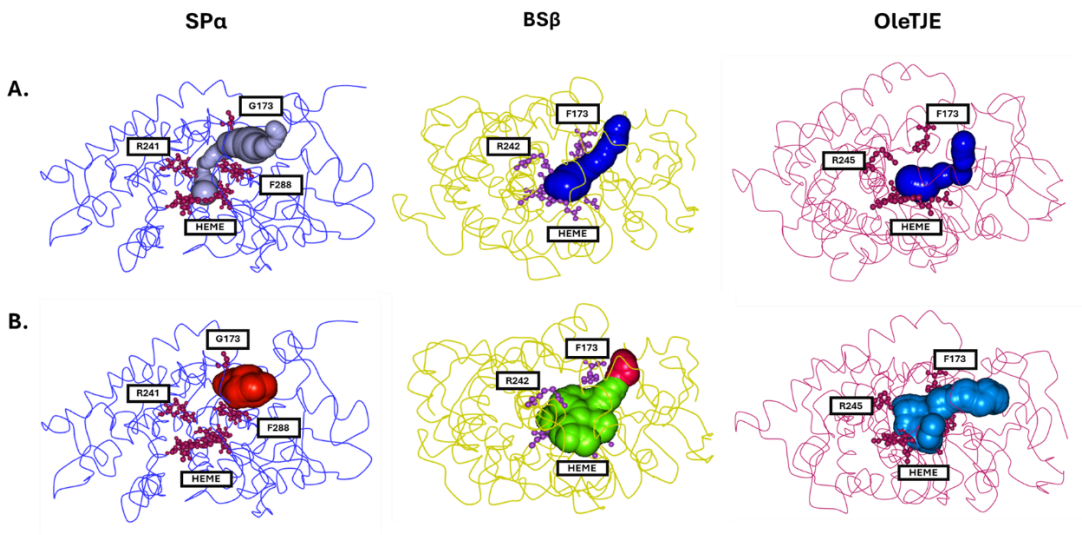

Figure 7.4: A) Graphical representation of the Tunnel, top, and cavity, bottom. B) The probe radius chosen for the cavity calculation is 2.3 Å.

Based on structural data, three mutant systems were designed starting from SPα: the first, named M12, carries two simultaneous mutations compared to the wild type (WT, SPα), namely G173F and F288A; the second, M1, contains a single mutation at position 173 (G173F); the third, M2, a single mutation at position 288 (F288A).

The mutations in the M12 system were hypothesized following the structural superposition of the three CYP152 enzymes (Figure 7.3). In particular, the replacement of glycine with the bulkier phenylalanine at position 173 was intended to create a steric effect that pushes the substrate closer to the heme group, thereby improving alignment with the catalytic center and potentially increasing the reaction efficiency. Conversely, the substitution of phenylalanine with a smaller alanine at position 288 aims to reduce steric hindrance, facilitating substrate access to the active site and allowing a more proper positioning near the catalytic center.

To support these hypotheses, prior to molecular dynamics simulations, a tunnel and cavity analysis was performed for the M12 system, comparing it with the wild type and OleTJE systems (Figure 7.5). In the M12 system, a tunnel similar in both priority and trajectory to that of OleTJE was identified, which is instead very different from the one present in SPα. Moreover, the analysis highlighted the formation of a new cavity near the heme cofactor in the M12 system, absent in the wild-type structure, which could represent a new access site for the ligand.

The M1 and M2 systems were mainly selected to evaluate the individual contribution of each mutation on the structural and functional behavior of the enzyme.

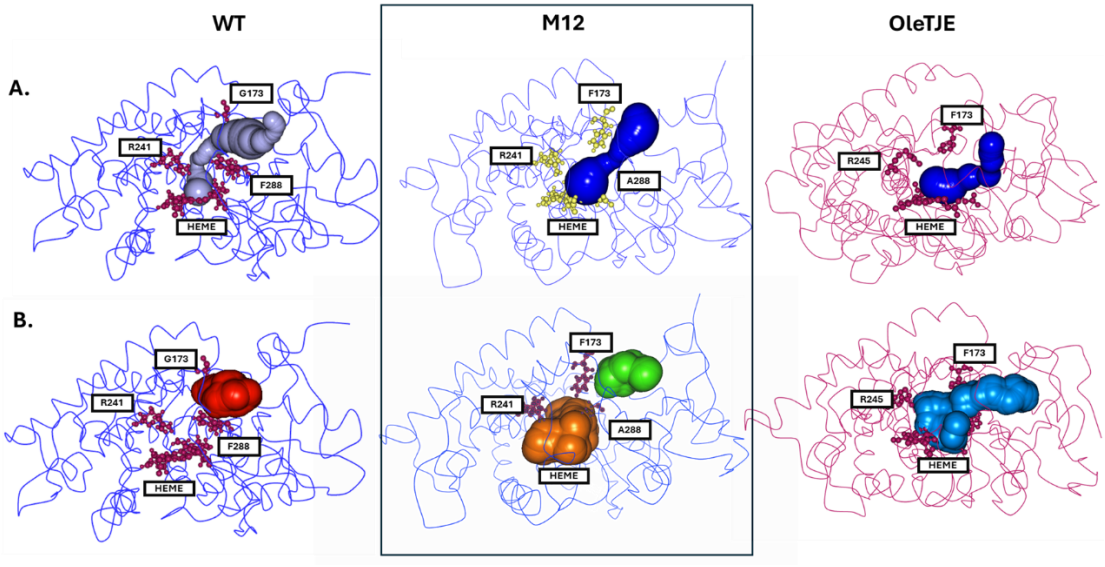

Figure 7.5: Graphical representations of the Tunnels and cavities in M12$_f$. Compared with the wild Type and OleTJ system

7.4 Structural stability analysis of the enzymes in the absence of ligands via molecular dynamics

MD simulations lasting 200 ns were performed for all systems in their free (apo) form. The trajectory analysis revealed excellent protein stability throughout the entire simulation.

In all systems, the porphyrin ring contains a central Fe^{3+} cation. The iron is coordinated to the four nitrogen atoms of the porphyrin's pyrrolic rings, while a thiolate cysteine provides the fifth (proximal) ligand, and a water molecule, positioned about 2.1 Å above the heme iron, acts as the sixth (distal) ligand. This arrangement results in a hexacoordinated heme group in the CYP152 enzymes, as shown in Figure 2. To maintain a consistent coordination sphere and position during the entire simulation, a restraint was applied to residue CYM361 before the minimization phase.

The MD trajectory analysis revealed high structural homogeneity of the protein during the simulation. This finding was also confirmed by the RMSF plot analysis, which shows similar fluctuations for all four free systems, with maximum values around 6 Å located in amino acids of the chain's terminal region. Regarding the mutations, the RMSF profile overlay highlights that the substitution of glycine with phenylalanine at position 173 (G173F) increases the local flexibility of the protein, affecting its molecular motions. This result was expected considering the larger size of phenylalanine compared to glycine. Conversely, the mutation at position 288 does not appear to alter the flexibility of the surrounding residues.

Interestingly, in the M12 system, the fluctuation at position 173 is less pronounced compared to the M1 system, suggesting that the presence of alanine at position 288 confers greater rigidity to the overall system (Figure 7.6).

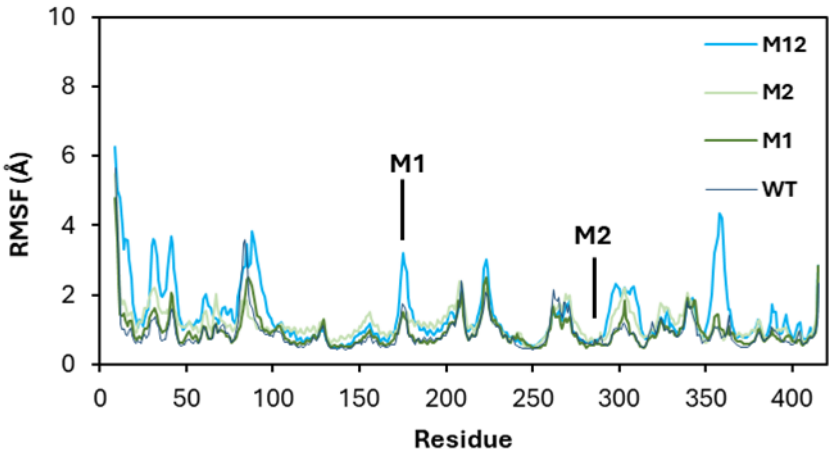

Figure 7.6: Overlay of RMSF plots from MD simulations of the free-form CYP152 and its mutants M1f, M2f, and M12f

7.5 Structural comparison between WT and M12

As previously mentioned, the system is quite stable, and the presence of the ligand is expected to further stabilize it during the simulation. The rigidity of the complex is confirmed in Figure 7.7B, where the protein chain appears almost perfectly superimposed on the initial crystallographic structure. The trajectory was analyzed to investigate the cause of the folding observed in the β-sheet near the hexacoordinated cysteine at position 361 in the WT system; however, no significant movements were detected during the simulation, leading to the conclusion that this is a visualization artifact of the software.

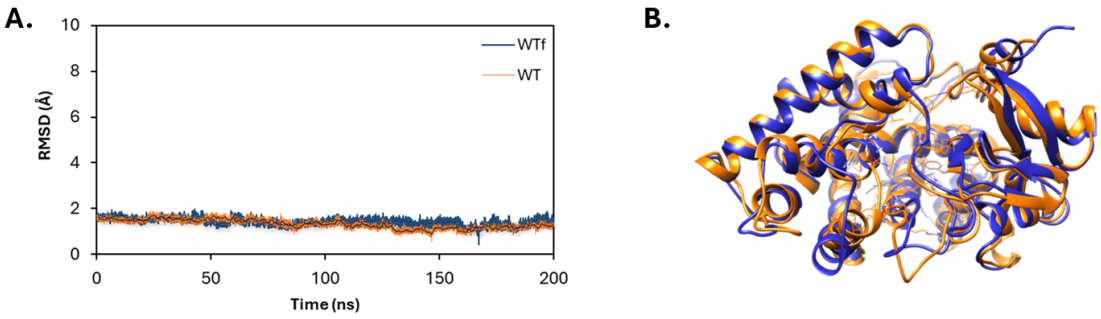

Figure 7.7: A) shows the RMSD overlap between the WT system (orange) and its apo form (blue). B) displays the structural overlap between the WT system's representative MD cluster (orange) and the corresponding X-ray structure (blue).

In the M12 system, the RMSD values, although remaining around 2 Å during the first 100 ns, tend to further stabilize in the second half of the simulation, settling around 1 Å, as shown in Figure 8A. This trend is likely due to the introduced mutations; in particular, the mutation at position 173 closes the channel where the fatty acid was originally positioned, which during the simulation is shifted toward the entrance of another channel, now made accessible by the substitution of phenylalanine at position 288 with alanine (Figure 7.8B). Therefore, greater fluctuations are observed in the first part of the simulation, attributable to the repositioning of the substrate toward the new channel.

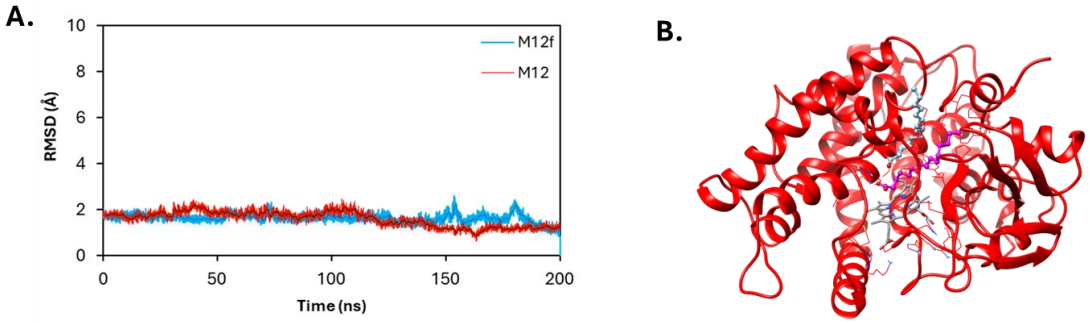

Figure 7.8: A) shows the RMSD comparison between the M12 system (red) and the apo form (cyan). B) presents a front view of the M12 system, with the substrate colored purple after the MD simulation and light blue before the simulation.

In both systems, the substrate establishes specific interactions with the arginine residue at position 241 (R241), which is essential for ligand recognition. In particular, the O2 oxygen atom of the substrate's carboxyl group forms a hydrogen bond with the H-Nε group of the R241 side chain (Figure 7.9A), while the O1 oxygen interacts with the HH21-N hydrogen of the same residue (Figure 7.9A).

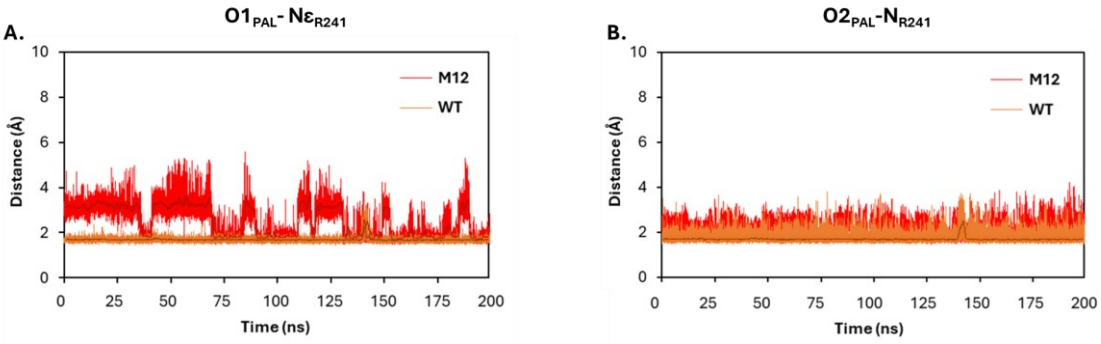

Figure 7.9: A) shows the distances between O1 of the substrate and Nε of Arg241, while B) shows the distances between O2 of the substrate and the nitrogen atom of Arg241.

The most representative conformations of the WT and M12 systems are shown in Figures 7.10A and 7.10B, respectively, clearly highlighting the different substrate behaviors during the molecular dynamics simulations. In Figure 7.10A, it can be

observed that in the WT system, the fatty acid shifts toward an alternative channel whose entrance is blocked by the phenylalanine at position 288. This displacement is caused by polar and sterically bulky residues near glycine 173. Since access to the second channel is hindered, the substrate fails to correctly position itself and tends to fold onto itself (Figure 7.10C). In contrast, in the M12 system, the substitution of phenylalanine with a smaller amino acid, alanine, frees the channel, allowing the substrate to enter the correct catalytic site, as shown in Figure 7.10D. Although the overall position and orientation of the substrate differ between the two systems, in both cases, the carboxyl group is oriented toward the side chain of R241, within the heme binding pocket (Figures 7.10C and D).

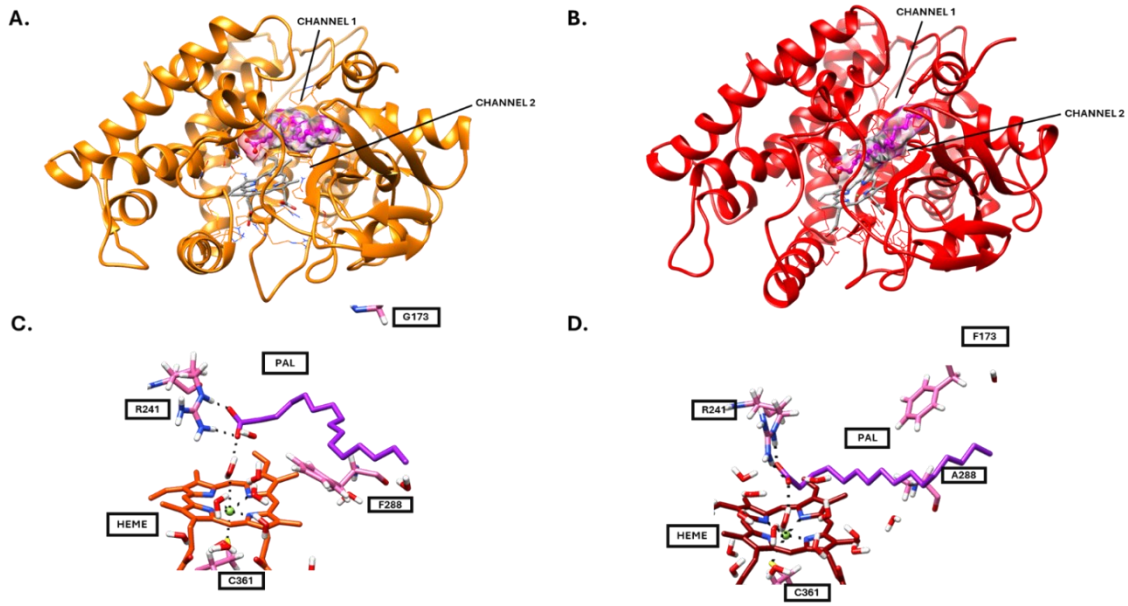

Figure 7.10: A) shows the side view of the WT system, highlighting the two channels of interest. B) shows the side view of the M12 system with the same two channels. C) depicts the orientation of palmitic acid in the WT system, while D) shows its orientation in the M12 system.

The analysis of the radial distribution function (RDF) revealed that the presence of the substrate within the channel differently affects the first and second hydration shells of the heme iron (~2 Å and 5 Å), calculated for Fe_HEME – Ow, in the WT and M12 complexes (Figure 7.11). Specifically, when comparing the two systems, the first peak is less intense in M12, suggesting that water molecules occupy the cavity less often. This phenomenon is attributed to a better positioning of the substrate within the channel, which, by increasing the lipophilicity near the HEME group, pushes water molecules away from the porphyrin iron, thereby facilitating the entry of hydrogen peroxide, responsible for the hydroxylation of the C16:0 fatty acid.

This analysis represents the core of the project, as it demonstrates how the introduced mutations improve the active site environment, optimizing substrate interaction and potentially enhancing the enzyme's catalytic efficiency.

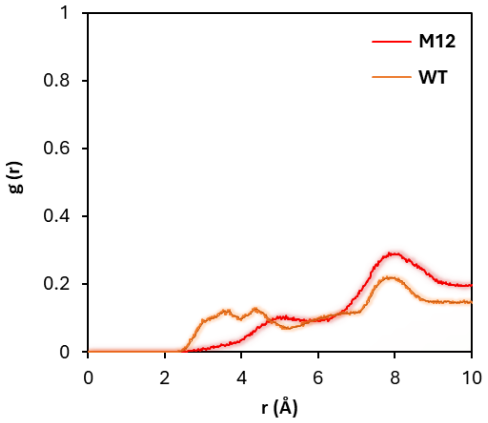

Figure 7.11: RDF overlay for FeHEME–Ow distances in the WT complex (orange) and M12 complex (red).

7.6 Assessment of the Contributions of the M1 and M2 Mutations

To evaluate the individual contributions of the mutations, 200 ns molecular dynamics simulations were performed for both the M1 and M2 complexes. In the case of M1 (Figure 7.12C), it is observed that the fatty acid, compared to its original position, shifts towards an alternative channel, the entrance of which is blocked by phenylalanine at position 288. This displacement is more pronounced than in the wild type, due to the presence of the bulky phenylalanine at position 173, which significantly directs the ligand sterically. However, the fatty acid is unable to access the second channel, becoming trapped between the two phenylalanines at positions 173 and 288, preventing proper substrate positioning for the reaction.

Conversely, in the M2 system, visual inspection of the most representative conformation obtained from the MD simulation reveals that the substitution of phenylalanine with alanine at position 288, while opening the channel the fatty acid attempts to enter, does not allow optimal substrate positioning (Figure 7.12D). This is attributed to the absence of the mutation at position 173, which plays a significant role in promoting substrate displacement.

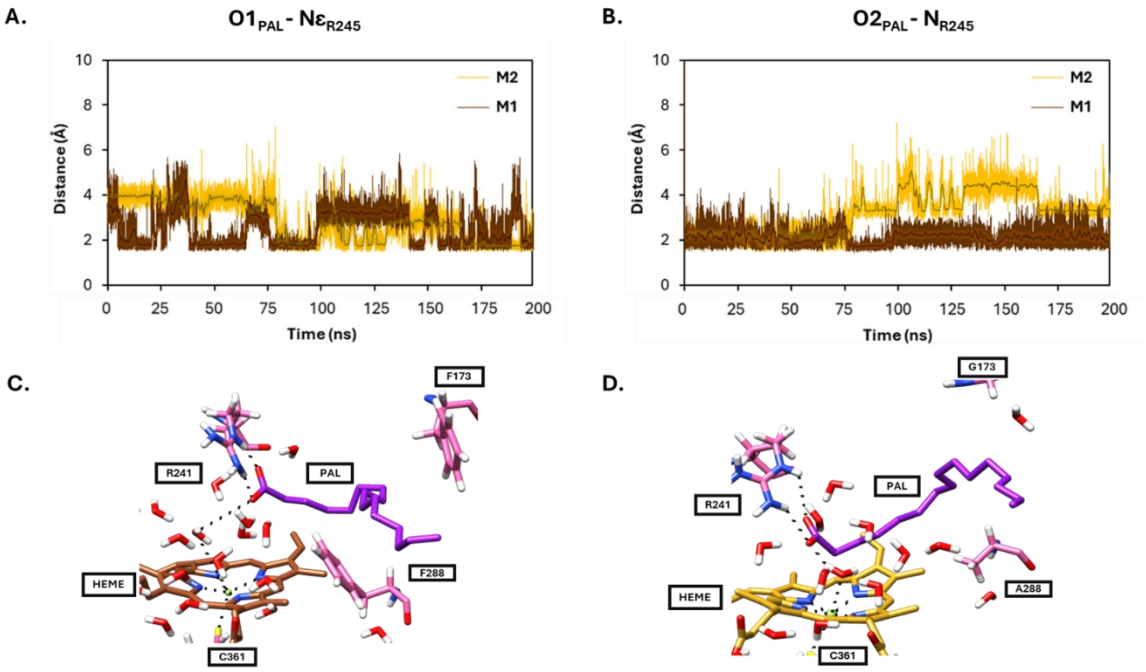

Figure 7.12: A) shows the distances between O1 of palmitic acid (O1PAL) and Nε of Arg241, while B) shows the distances between O2PAL and N of Arg241. C) depicts the orientation of palmitic acid in the M1 system, whereas D) shows its orientation in the M2 system.

Analysis of the distances between the substrate and residue R241 in both systems shows that the behavior in M2 is nonlinear; however, the interaction between the O2 oxygen of the substrate's carboxyl group and the Nε atom of the R241 side chain (Figure 7.12A), as well as between the O1 oxygen of the carboxyl group and the backbone nitrogen of the same residue (Figure 7.12B), can still be confirmed. These data indicate that the single mutations contribute, albeit modestly, to the optimal positioning of the ligand.

The radial distribution function (RDF) analysis further highlighted that the presence of the substrate in the channel differently affects the first and second hydration shells of the porphyrin iron, calculated for FeHEME – Ow, in the M1 and M2 complexes (Figure 7.13). Comparing all four systems, minimal differences are observed for M1 and M2 relative to the wild type; in fact, the most significant peak variations occur only in the third hydration shell (~7 Å).

This result provides additional support for the previously formulated hypothesis. It can therefore be concluded that the single mutations marginally influence substrate positioning, whereas the synergistic effect of the two mutations in the M12 system leads to an optimal substrate positioning with more pronounced effects.

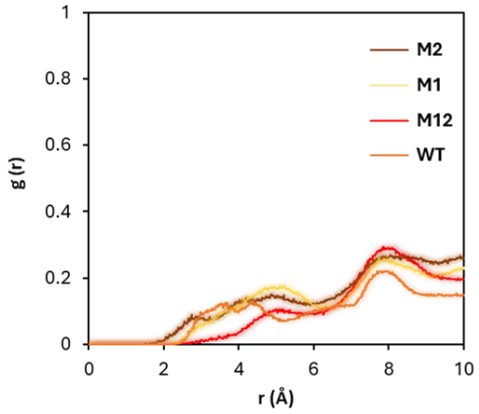

Figure 7.13: shows the overlay of the radial distribution functions (RDF) for all four complexes, highlighting differences in the hydration shells around the heme iron. The comparison reveals subtle variations in water molecule distributions among the complexes.

It is important to highlight that, based on the radial distribution function (RDF) data, a continuous exchange of water molecules occurs throughout the simulation. The graph shows that the iron atom is periodically surrounded by water molecules. Water molecules are also present in the channel of the M12 system, as in all other complexes. However, to observe this phenomenon in the first hydration shell of M12, a longer simulation time would be required.

As discussed earlier, in the M12 system, the substrate properly positions itself within the access channel. In contrast, in the wild type, the substrate cannot efficiently enter the channel (Figures 7.10C and D) because the hydrocarbon chain tries to move toward the active site but is sterically blocked by phenylalanine at position 288. In the M1 system, the bulky phenylalanine at position 173 favors substrate orientation toward channel 2; however, optimal positioning is prevented by the blockage caused by F288 (Figure 7.12C). In the M2 system, where phenylalanine at position 173 is replaced by glycine, a less favorable behavior compared to M12 is observed. Despite the surrounding residues pushing the aliphatic chain toward channel 2, the absence of the steric contribution from phenylalanine limits correct substrate positioning, preventing it from optimally settling as in the M12 system (Figure 7.12D).

Therefore, it remains evident that the mutations exert a synergistic effect, facilitating the correct and stable positioning of the substrate within the active site.

7.7 Evaluation of the Structural Dynamics of OleTJE, SPα, and M12

To further investigate this hypothesis, molecular dynamics simulations were performed on the P450 OleTJE system with two main objectives: (i) to verify whether the overall dynamic behavior of OleTJE resembles that observed in the M12 mutant, which showed the most promising results, as well as in the other two mutants; and (ii) to assess the presence and extent of the movement of the loop comprising residues G82–L86, to determine whether similar structural flexibility is also present in OleTJE. This analysis is particularly relevant because the absence of a proton-donating residue at position 85 in our system represents a potential limitation for the decarboxylation reaction. If loop movement is also confirmed in OleTJE, it would further strengthen the validity of our mutational strategy and suggest that, in a favorable structural context such as that observed in M12, a targeted mutation at position 85 could be a promising direction for the enzyme's functional optimization. The 200 ns simulations were conducted for both the apo form of OleTJE (OleTJEf) and the complex with palmitic acid (OleTJE), to compare OleTJE's dynamic behavior to that observed in our selected mutant M12 and SPα, thus providing additional validation of our results.

The obtained data were compared with those of the M12 system, clearly showing a dynamic behavior fully comparable to that of OleTJE (Figure 7.14). This result supports the conclusion that the mutations introduced at positions G173F and F288A are critical for improving the catalytic efficiency of the CYP450SPα system.

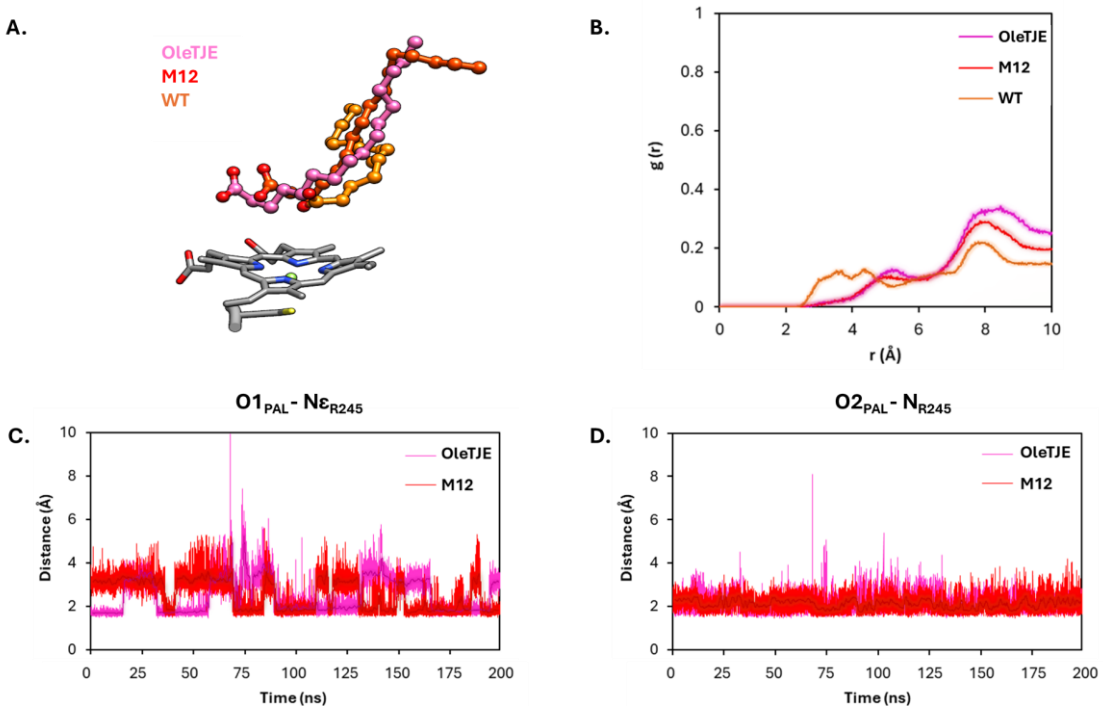

Figure 7.14: A) shows the orientation of palmitic acid in the OleTJE system (purple) superimposed with the WT (orange) and M12 (red) orientations. B) displays the overlay of the RDF profiles for OleTJE, WT, and M12.C) reports the distances between O1 of palmitic acid (O1PAL) and Nε of Arg241. D) shows the distances between O2 of palmitic acid (O2PAL) and N of Arg241.

The overlay of the RMSF profiles (Figure 7.15A) highlights, in the mutated M12 system, a pronounced peak localized at residues G82–L86, corresponding to a loop that, as observed during the simulations, undergoes a significant displacement compared to its position in the WT system. Specifically, in the M12 system, this peak is shifted by approximately 6 Å. Notably, this loop contains a glycine at position 85, whereas in OleTJE and BSβ, the same position is occupied by histidine and glutamine, respectively. This observation is particularly relevant for the engineering of the enzyme's decarboxylation activity. As previously mentioned, in the OleTJE system, the histidine at position 85 acts as a proton donor and is involved in the fatty acid decarboxylation reaction. However, in our models, the loop containing residue 85 is positioned too far from the active site in the WT form, potentially rendering an isolated mutation at this position ineffective.

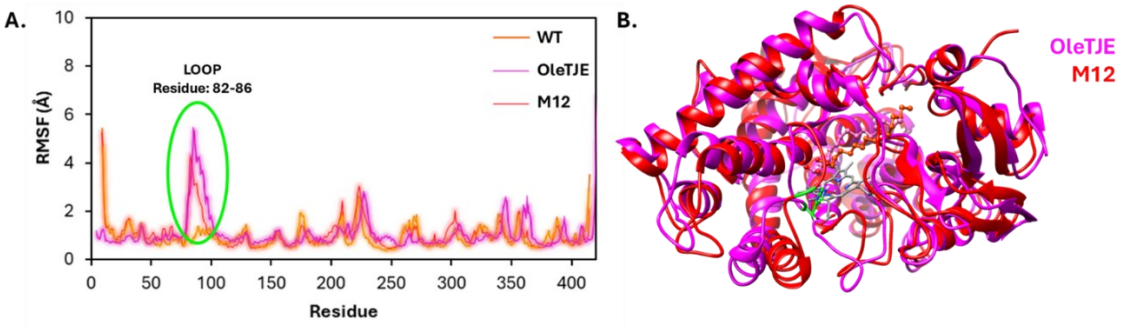

Figure 7.15: A) shows the superimposition of RMSF profiles for WT, M12, and OleTJE. B) presents the overlay of OleTJE and M12 RMSF profiles, highlighting the movement of the loop.

In the M12 mutant, conversely, the loop movement toward the porphyrin ring observed during the simulation suggests that residue 85, if suitably modified, could be positioned near the heme group and assume a functional role in catalysis. Although this mutation has not yet been introduced, these findings open promising perspectives for a future targeted intervention at this site. In conclusion, this latest analysis confirms the substantial overlap in dynamic behavior between M12 and OleTJE.

7.8 Conclusions

The molecular dynamics simulations conducted in this work have provided new and significant insights into the molecular mechanisms governing the activity of the P450SPα enzyme. The comparative analysis of the designed mutants allowed the identification of amino acid modifications capable of improving the catalytic efficiency of the system, with particular emphasis on the double mutant M12 (G173F/F288A), whose dynamic behavior closely overlaps with that of the native OleTJE system.

These results highlight how targeted and synergistic modifications can significantly influence substrate positioning and the microenvironment of the active site, indirectly modulating access to the heme group and the hydration of the catalytic iron. In particular, the importance of correct substrate orientation and the role of the dynamics of specific structural loops, including the one containing residue 85, emerged; the potential involvement of this residue in the decarboxylation reaction represents a future avenue of considerable interest.

The computational methodologies adopted are confirmed as effective tools to guide the rational design of engineered enzymes with optimized characteristics. Looking ahead, the next developments of the project are structured as follows

I. Further investigation of the dynamic behavior of the loop containing residue 85, aimed at evaluating the impact of targeted mutations on catalytic functionality.
II. Extension of the approach to additional enzymes of the CYP450 family to identify recurring structural patterns associated with specific activities.
III. Integration of experimental approaches for validation of computational models and optimization of the most promising variants.

This research line, focused on the fine modulation of CYP450 activity, represents an important step towards the valorization of natural biomass, particularly through the selective transformation of fatty acids into higher-value products such as hydrocarbons and biochemical intermediates useful for industrial and environmental applications, including second-generation biofuels.

References

1. Yan, N.; Chen, X. Sustainability: Don't Waste Seafood Waste. Nature 2015, 524, 155–157, doi:10.1038/524155a.

2. Mohr, A.; Raman, S. Lessons from First Generation Biofuels and Implications for the Sustainability Appraisal of Second Generation Biofuels. Energy Policy 2013, 63, 114–122, doi:10.1016/j.enpol.2013.08.033.

3. Fairley, P. Introduction: Next Generation Biofuels. Nature 2011, 474, S2–S5, doi:10.1038/474S02a.

4. Horn, S.J.; Vaaje-Kolstad, G.; Westereng, B.; Eijsink, V. Novel Enzymes for the Degradation of Cellulose. Biotechnol Biofuels 2012, 5, 45, doi:10.1186/1754-6834-5-45.

5. Maschmeyer, T.; Luque, R.; Selva, M. Upgrading of Marine (Fish and Crustaceans) Biowaste for High Added-Value Molecules and Bio(Nano)-Materials. Chem Soc Rev 2020, 49, 4527–4563, doi:10.1039/C9CS00653B.

6. Reina, R.; Liers, C.; García-Romera, I.; Aranda, E. Enzymatic Mechanisms and Detoxification of Dry Olive-Mill Residue by Cyclocybe Aegerita, Mycetinis Alliaceus and Chondrostereum Purpureum. Int Biodeterior Biodegradation 2017, 117, 89–96, doi:10.1016/j.ibiod.2016.11.029.

7. Wolf, M.E.; Hinchen, D.J.; DuBois, J.L.; McGeehan, J.E.; Eltis, L.D. Cytochromes P450 in the Biocatalytic Valorization of Lignin. Curr Opin Biotechnol 2022, 73, 43–50, doi:10.1016/j.copbio.2021.06.022.

8. Seafood from Catch and Aquaculture for a Sustainable Supply; Poli, B.M., Parisi, G., Eds.; Firenze University Press: Firenze, 2008; Vol. 42; ISBN 978-88-8453-745-4.

9. Matsunaga, I.; Sumimoto, T.; Ueda, A.; Kusunose, E.; Ichihara, K. Fatty Acid-specific, Regiospecific, and Stereospecific Hydroxylation by Cytochrome P450 (CYP152B1) from Sphingomonas Paucimobilis : Substrate Structure Required for A-hydroxylation. Lipids 2000, 35, 365–371, doi:10.1007/s11745-000-533-y.

10. Hammerer, L.; Friess, M.; Cerne, J.; Fuchs, M.; Steinkellner, G.; Gruber, K.; Vanhessche, K.; Plocek, T.; Winkler, C.K.; Kroutil, W. Controlling the Regioselectivity of Fatty Acid Hydroxylation (C 10) at A- and B-Position by CYP152A1 (P450Bsβ) Variants. ChemCatChem 2019, 11, 5642–5649, doi:10.1002/cctc.201901679.

11. Matthews, S.; Belcher, J.D.; Tee, K.L.; Girvan, H.M.; McLean, K.J.; Rigby, S.E.J.; Levy, C.W.; Leys, D.; Parker, D.A.; Blankley, R.T.; et al. Catalytic Determinants of Alkene Production by the Cytochrome P450 Peroxygenase OleTJE. Journal of Biological Chemistry 2017, 292, 5128–5143, doi:10.1074/jbc.M116.762336.

12. Matthews, S.; Tee, K.L.; Rattray, N.J.; McLean, K.J.; Leys, D.; Parker, D.A.; Blankley, R.T.; Munro, A.W. Production of Alkenes and Novel Secondary Products by P450 Ole <scp> T JE </Scp> Using Novel H 2 O 2 -generating Fusion Protein Systems. FEBS Lett 2017, 591, 737–750, doi:10.1002/1873-3468.12581.

13. Munro, A.W.; McLean, K.J.; Grant, J.L.; Makris, T.M. Structure and Function of the Cytochrome P450 Peroxygenase Enzymes. Biochem Soc Trans 2018, 46, 183–196, doi:10.1042/BST20170218.

14. Ebrecht, A.C.; Smit, M.S.; Opperman, D.J. Natural Alternative Heme-Environments Allow Efficient Peroxygenase Activity by Cytochrome P450 Monooxygenases. Catal Sci Technol 2023, 13, 6264–6273, doi:10.1039/D3CY01207G.

15. Matsunaga, I.; Yamada, A.; Lee, D.-S.; Obayashi, E.; Fujiwara, N.; Kobayashi, K.; Ogura, H.; Shiro, Y. Enzymatic Reaction of Hydrogen Peroxide-Dependent Peroxygenase Cytochrome P450s: Kinetic Deuterium Isotope Effects and Analyses by Resonance Raman Spectroscopy. Biochemistry 2002, 41, 1886–1892, doi:10.1021/bi011883p.

16. Yan, J.; Liu, Y.; Wang, C.; Han, B.; Li, S. Assembly of Lipase and P450 Fatty Acid Decarboxylase to Constitute a Novel Biosynthetic Pathway for Production of 1-Alkenes from Renewable Triacylglycerols and Oils. Biotechnol Biofuels 2015, 8, 34, doi:10.1186/s13068-015-0219-x.

17. Monteiro, R.R.C.; da Silva, S.S.O.; Cavalcante, C.L.; de Luna, F.M.T.; Bolivar, J.M.; Vieira, R.S.; Fernandez-Lafuente, R. Biosynthesis of Alkanes/Alkenes from Fatty Acids or Derivatives (Triacylglycerols or Fatty Aldehydes). Biotechnol Adv 2022, 61, 108045, doi:10.1016/j.biotechadv.2022.108045.

18. Onoda, H.; Tanaka, S.; Watanabe, Y.; Shoji, O. Exploring Hitherto Uninvestigated Reactions of the Fatty Acid Peroxygenase CYP152A1: Catalase Reaction and Compound I Formation. Faraday Discuss 2022, 234, 304–314, doi:10.1039/D1FD00065A.

19. Jiang, Y.; Peng, W.; Li, Z.; You, C.; Zhao, Y.; Tang, D.; Wang, B.; Li, S. Unexpected Reactions of α,B-Unsaturated Fatty Acids Provide Insight into the Mechanisms of CYP152 Peroxygenases. Angewandte Chemie International Edition 2021, 60, 24694–24701, doi:10.1002/anie.202111163.

20. Strazzera, G.; Battista, F.; Garcia, N.H.; Frison, N.; Bolzonella, D. Volatile Fatty Acids Production from Food Wastes for Biorefinery Platforms: A Review. J Environ Manage 2018, 226, 278–288, doi:10.1016/j.jenvman.2018.08.039.

21. Lukitawesa; Patinvoh, R.J.; Millati, R.; Sárvári-Horváth, I.; Taherzadeh, M.J. Factors Influencing Volatile Fatty Acids Production from Food Wastes via Anaerobic Digestion. Bioengineered 2020, 11, 39–52, doi:10.1080/21655979.2019.1703544.

22. Fonseca, J.M.; Teleken, J.G.; de Cinque Almeida, V.; da Silva, C. Biodiesel from Waste Frying Oils: Methods of Production and Purification. Energy Convers Manag 2019, 184, 205–218, doi:10.1016/j.enconman.2019.01.061.

23. Leiva-Candia, D.E.; Pinzi, S.; Redel-Macías, M.D.; Koutinas, A.; Webb, C.; Dorado, M.P. The Potential for Agro-Industrial Waste Utilization Using Oleaginous Yeast for the Production of Biodiesel. Fuel 2014, 123, 33–42, doi:10.1016/j.fuel.2014.01.054.

24. Wu, T.Y.; Mohammad, A.W.; Jahim, J.Md.; Anuar, N. A Holistic Approach to Managing Palm Oil Mill Effluent (POME): Biotechnological Advances in the Sustainable Reuse of POME. Biotechnol Adv 2009, 27, 40–52, doi:10.1016/j.biotechadv.2008.08.005.

25. Zhang, C.; Xu, T.; Feng, H.; Chen, S. Greenhouse Gas Emissions from Landfills: A Review and Bibliometric Analysis. Sustainability 2019, 11, 2282, doi:10.3390/su11082282.

26. Lynen, F.; Ochoa, S. Enzymes of Fatty Acid Metabolism. Biochim Biophys Acta 1953, 12, 299–314, doi:10.1016/0006-3002(53)90149-8.

27. Hayes, D.G. Enzyme-Catalyzed Modification of Oilseed Materials to Produce Eco-friendly Products. J Am Oil Chem Soc 2004, 81, 1077–1103, doi:10.1007/s11746-004-1024-2.

28. Jaroensuk, J.; Intasian, P.; Wattanasuepsin, W.; Akeratchatapan, N.; Kesornpun, C.; Kittipanukul, N.; Chaiyen, P. Enzymatic Reactions and Pathway Engineering for the Production of Renewable Hydrocarbons. J Biotechnol 2020, 309, 1–19, doi:10.1016/j.jbiotec.2019.12.010.

29. Lee, S.Y.; Kim, H.U.; Chae, T.U.; Cho, J.S.; Kim, J.W.; Shin, J.H.; Kim, D.I.; Ko, Y.-S.; Jang, W.D.; Jang, Y.-S. A Comprehensive Metabolic Map for Production of Bio-Based Chemicals. Nat Catal 2019, 2, 18–33, doi:10.1038/s41929-018-0212-4.

30. Sariatli, F. Linear Economy Versus Circular Economy: A Comparative and Analyzer Study for Optimization of Economy for Sustainability. Visegrad Journal on Bioeconomy and Sustainable Development 2017, 6, 31–34, doi:10.1515/vjbsd-2017-0005.

31. Lim, M.K.; Lai, M.; Wang, C.; Lee, S.Y. Circular Economy to Ensure Production Operational Sustainability: A Green-Lean Approach. Sustain Prod Consum 2022, 30, 130–144, doi:10.1016/j.spc.2021.12.001.

32. Antonioli, D.; Ghisetti, C.; Mazzanti, M.; Nicolli, F. Sustainable Production: The Economic Returns of Circular Economy Practices. Bus Strategy Environ 2022, 31, 2603–2617, doi:10.1002/bse.3046.

33. Nastri, F.; D'Alonzo, D.; Leone, L.; Zambrano, G.; Pavone, V.; Lombardi, A. Engineering Metalloprotein Functions in Designed and Native Scaffolds. Trends Biochem Sci 2019, 44, 1022–1040, doi:10.1016/j.tibs.2019.06.006.

34. Schwizer, F.; Okamoto, Y.; Heinisch, T.; Gu, Y.; Pellizzoni, M.M.; Lebrun, V.; Reuter, R.; Köhler, V.; Lewis, J.C.; Ward, T.R. Artificial Metalloenzymes: Reaction Scope and Optimization Strategies. Chem Rev 2018, 118, 142–231, doi:10.1021/acs.chemrev.7b00014.

35. Lombardi, A.; Pirro, F.; Maglio, O.; Chino, M.; DeGrado, W.F. De Novo Design of Four-Helix Bundle Metalloproteins: One Scaffold, Diverse Reactivities. Acc Chem Res 2019, 52, 1148–1159, doi:10.1021/acs.accounts.8b00674.

36. Nastri, F.; Chino, M.; Maglio, O.; Bhagi-Damodaran, A.; Lu, Y.; Lombardi, A. Design and Engineering of Artificial Oxygen-Activating Metalloenzymes. Chem Soc Rev 2016, 45, 5020–5054, doi:10.1039/C5CS00923E.

37. Maglio, O.; Chino, M.; D'Alonzo, D.; Leone, L.; Nastri, F.; Lombardi, A. Peptide-Based Artificial Metalloenzymes by Design. In Peptide and Protein Engineering for Biotechnological and Therapeutic Applications; WORLD SCIENTIFIC, 2023; pp. 371–420.

38. Chino, M.; Maglio, O.; Nastri, F.; Pavone, V.; DeGrado, W.F.; Lombardi, A. Artificial Diiron Enzymes with a De Novo Designed Four-Helix Bundle Structure. Eur J Inorg Chem 2015, 2015, 3371–3390, doi:10.1002/ejic.201500470.

39. Torres Castillo, N.E.; Melchor-Martínez, E.M.; Ochoa Sierra, J.S.; Ramírez-Torres, N.M.; Sosa-Hernández, J.E.; Iqbal, H.M.N.; Parra-Saldívar, R. Enzyme Mimics In-Focus: Redefining the Catalytic Attributes of Artificial Enzymes for Renewable Energy Production. Int J Biol Macromol 2021, 179, 80–89, doi:10.1016/j.ijbiomac.2021.03.002.

40. Fujishiro, T.; Shoji, O.; Nagano, S.; Sugimoto, H.; Shiro, Y.; Watanabe, Y. Crystal Structure of H2O2-Dependent Cytochrome P450SPα with Its Bound Fatty Acid Substrate. Journal of Biological Chemistry 2011, 286, 29941–29950, doi:10.1074/jbc.M111.245225.

41. Pettersen, E.F.; Goddard, T.D.; Huang, C.C.; Couch, G.S.; Greenblatt, D.M.; Meng, E.C.; Ferrin, T.E. UCSF Chimera—A Visualization System for Exploratory Research and Analysis. J Comput Chem 2004, 25, 1605–1612, doi:10.1002/jcc.20084.

42. Price, D.J.; Brooks, C.L. A Modified TIP3P Water Potential for Simulation with Ewald Summation. J Chem Phys 2004, 121, 10096–10103, doi:10.1063/1.1808117.

43. Van Der Spoel, D.; Lindahl, E.; Hess, B.; Groenhof, G.; Mark, A.E.; Berendsen, H.J.C. GROMACS: Fast, Flexible, and Free. J Comput Chem 2005, 26, 1701–1718, doi:10.1002/jcc.20291.

44. Huang, J.; MacKerell, A.D. CHARMM36 All-Atom Additive Protein Force Field: Validation Based on Comparison to NMR Data. J Comput Chem 2013, 34, 2135–2145, doi:10.1002/jcc.23354.

45. Lemkul, J.A. Introductory Tutorials for Simulating Protein Dynamics with GROMACS. J Phys Chem B 2024, 128, 9418–9435, doi:10.1021/acs.jpcb.4c04901.

46. Petersen, H.G. Accuracy and Efficiency of the Particle Mesh Ewald Method. J Chem Phys 1995, 103, 3668–3679, doi:10.1063/1.470043.

47. Ezerski, J.C.; Cheung, M.S. CATS: A Tool for Clustering the Ensemble of Intrinsically Disordered Peptides on a Flat Energy Landscape. J Phys Chem B 2018, 122, 11807–11816, doi:10.1021/acs.jpcb.8b08852.

48. Belcher, J.; McLean, K.J.; Matthews, S.; Woodward, L.S.; Fisher, K.; Rigby, S.E.J.; Nelson, D.R.; Potts, D.; Baynham, M.T.; Parker, D.A.; et al. Structure and Biochemical

Properties of the Alkene Producing Cytochrome P450 OleTJE (CYP152L1) from the Jeotgalicoccus Sp. 8456 Bacterium. Journal of Biological Chemistry 2014, 289, 6535–6550, doi:10.1074/jbc.M113.527325.

49. Parthasarathy, S.; Ravindra, G.; Balaram, H.; Balaram, P.; Murthy, M.R.N. Structure of the Plasmodium Falciparum Triosephosphate Isomerase−Phosphoglycolate Complex in Two Crystal Forms: Characterization of Catalytic Loop Open and Closed Conformations in the Ligand-Bound State ,. Biochemistry 2002, 41, 13178–13188, doi:10.1021/bi025783a.

50. Yadav, S.; Shaik, S.; Siddiqui, S.A.; Kalita, S.; Dubey, K.D. Local Electric Fields Dictate Function: The Different Product Selectivities Observed for Fatty Acid Oxidation by Two Deceptively Very Similar P450-Peroxygenases OleT and BSβ. J Chem Inf Model 2022, 62, 1025–1035, doi:10.1021/acs.jcim.1c01453.

51. Pickl, M.; Kurakin, S.; Cantú Reinhard, F.G.; Schmid, P.; Pöcheim, A.; Winkler, C.K.; Kroutil, W.; de Visser, S.P.; Faber, K. Mechanistic Studies of Fatty Acid Activation by CYP152 Peroxygenases Reveal Unexpected Desaturase Activity. ACS Catal 2019, 9, 565–577, doi:10.1021/acscatal.8b03733.

52. Chovancova, E.; Pavelka, A.; Benes, P.; Strnad, O.; Brezovsky, J.; Kozlikova, B.; Gora, A.; Sustr, V.; Klvana, M.; Medek, P.; et al. CAVER 3.0: A Tool for the Analysis of Transport Pathways in Dynamic Protein Structures. PLoS Comput Biol 2012, 8, e1002708, doi:10.1371/journal.pcbi.1002708.

Chapter 8

Molecular Dynamics of the Metallo-enzyme Lytic Polysaccharide Monooxygenase (LPMO) SmAA10 and its interactions with β-chitin

This paragraph introduces the investigation of a bacterial Lytic Polysaccharide Monooxygenase (LPMO), emphasizing its structural dynamics and key molecular interactions during chitin degradation, explored through molecular dynamics simulations.

Global warming and the increasing scarcity of fossil resources are driving both the scientific and industrial communities to develop sustainable solutions for the production of energy and materials. In this context, the valorization of biomass, particularly non-edible organic waste, represents a promising strategy. Among the various available residues, waste from the fishery industry, such as crustacean shells, fish scales, and bones, is of particular interest due to its high chitin content. Chitin is a natural polysaccharide that is abundant but highly crystalline and poorly soluble, which makes its degradation and reuse challenging. In recent years, the use of natural enzymes known as Lytic Polysaccharide Monooxygenases has opened new possibilities for the efficient transformation of chitin into higher-value products such as biofuels, bioalcohols, or platform chemicals for industry. These enzymes, which contain a copper ion at the active site, are capable of cleaving chitin oxidatively, thereby facilitating its degradation even under highly crystalline conditions.

In this work, we employed molecular dynamics (MD) simulations to investigate the behaviour of a bacterial LPMO, SmAA10, in the presence of a β-chitin fragment. The analysis focused on structural fluctuations, non-covalent interactions, and relevant molecular motions. The trajectory analysis confirmed the overall stability of the enzyme–substrate complex, with limited fluctuation and maintenance of copper coordination throughout the simulation. Key interactions, such as hydrogen bonds and π–π stacking, were identified as critical for molecular recognition. These findings enhance our understanding of LPMO function and provide a useful

foundation for protein engineering efforts aimed at improving enzymatic performance for industrial applications in biomass valorization. Indeed, the integration of computational techniques with experimental data represents a strategic approach to accelerating the development of sustainable biocatalysts for biomass transformation and environmental bioremediation.

8.1 Introduction

The growing concern over global warming and greenhouse gas (GHG) emissions has driven the scientific and industrial communities to seek sustainable alternatives to fossil fuels. In this context, the conversion of biomass into fuels and chemicals is gaining increasing relevance [1]. The use of renewable resources of biological origin represents a promising strategy to address the depletion of fossil reserves while offering a carbon-neutral route for energy and chemical production [2,3].

Biomass, defined as renewable organic matter, can originate from a wide variety of sources: wood and wood residues, crops and by-products, animal manure, food industry waste, and sewage sludge [4]. The valorization of these resources can lead to the production of advanced biofuels and high-value-added chemicals. In particular, lignocellulosic waste and non-edible organic residues are considered ideal feedstocks for the production of second-generation biofuels, as they do not compete with the food supply chain [5]. Among the various types of biomass, a still underexplored yet promising sector is represented by waste from the fishery industry, such as crustacean shells, fish bones, and scales. This waste, with an estimated global production of approximately 7 million tons per year [6]. contains up to 40% chitin [7], a highly crystalline nitrogen-containing polysaccharide. Chitin, composed of N-acetyl-D-glucosamine units linked by β-1,4-glycosidic bonds [8], is one of the most abundant polysaccharides on Earth, mainly found in crustacean exoskeletons and fungal cell walls [9,10]. However, its poor solubility and chemical resistance make its degradation and valorization challenging. As a result, despite an estimated production of over 10 million tons per year, most chitin is still disposed of as waste [7].

In recent years, the bioconversion of chitin using specific microorganisms and enzymes has emerged as an eco-friendly strategy to transform this waste into high-value products, such as bioalcohols, chitooligosaccharides, and other derivatives [11–13]. The enzymes involved in this process include chitinases, chitosanases, chitin deacetylases, and, notably, LPMOs [14–17]. LPMOs represent a recently discovered class of oxidative metalloenzymes characterized by a copper-containing active site known as the histidine brace (shown in Figure 8.1), capable of cleaving C–C and C–O bonds oxidatively in crystalline substrates such as cellulose,

hemicellulose, starch, and chitin [18,19]. First identified in 2010 (CBP21 from *Serratia marcescens*) [20], they are now classified in the CAZy database under auxiliary activities (AA) and grouped into several families: AA10 (bacterial) [21], AA15 (insect), active on both cellulose and chitin [22], and AA9, AA11, AA13, AA14, AA16 (fungal), mainly active on cellulose and hemicellulose [23–27], each with varying substrate specificities.

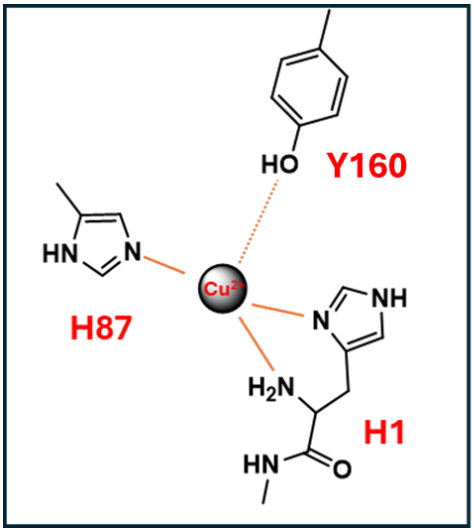

Figure 8.1: Schematic representation of the active site of the LPMO enzyme, known as the histidine brace. The divalent copper ion (Cu^{2+}) is coordinated by two histidine residues: H1, which provides both the terminal amino group and the imidazole ring, and H87, which contributes an imidazole ring. This coordination mode, known as the histidine brace, is highly conserved among LPMOs. Additionally, the residue at position 160, which can be either a tyrosine (Y) or a phenylalanine (F) depending on the enzyme, contributes to stabilizing the active site environment.

This study focused on the characterization of a chitin-active bacterial enzyme belonging to the AA10 subfamily [28,29], the *Serratia marcescens* LPMO (SmAA10, formerly known as CBP21 [20]) Biotechnological interest in LPMOs has rapidly increased due to their ability to enhance the degradation of recalcitrant biopolymers, making them key players in biomass valorization and environmental bioremediation applications [30]. The use of purified enzymes, as opposed to traditional microbial fermentation, offers several advantages, including shorter reaction times, higher yields, and improved process efficiency [31]. In this context, optimizing LPMOs through protein engineering is crucial to tailor their properties for industrial operating conditions.

Computational techniques, particularly MD simulations, are increasingly recognized as essential tools for investigating enzyme-substrate interactions and catalytic mechanisms at the atomic level [32,33]. These approaches enable the

exploration of conformational flexibility, substrate access pathways, and molecular interactions governing catalysis, thereby providing key insights for the rational design of more stable, specific, and efficient biocatalysts. The integration of computational and experimental data thus represents a promising strategy to accelerate the development of next-generation enzymes. In this work, theoretical approaches are employed to investigate the molecular mechanisms of LPMOs, with a particular focus on enzyme-substrate interactions and the still poorly understood aspects of their reactivity. The ultimate goal is to provide a framework for future studies, both computational and experimental, aimed at optimizing these biocatalysts for applications in biofuel production and environmental bioremediation.

8.2 Computational Details

We conducted a Classical Molecular Dynamics simulation lasting 200 ns at 302 K for the LPMO sm10AA system in complex with a polymeric fragment of β-chitin composed of 24 units × 5 chains × 5 layers. The structure was provided by the group of Orio Malys from the Institut des sciences moléculaires de Marseille. The systems were placed in an orthorhombic box with a 10 Å margin from the protein, containing TIP3P water molecules [34] and counterions to neutralize the total charge. For the simulation, we used a combination of force fields ff14SB [35]/GLYCAM 06j [36], the latter being the updated version of the GLYCAM force field, specifically designed for simulating carbohydrates and glycoproteins. The Cu^{2+} metal ion was described using the nonbonded 12-6-4 LJ-Type model [37]. Finally, positional restraints with a force constant of approximately 2 kcal $mol^{-1}Å^2$ were applied to all Cα carbon atoms of the chitin monomers to maintain the desired initial conformation during the simulation.

The smAA10 and β-chitin complex was initially minimized and relaxed by applying positional harmonic restraints on all atoms (50 kcal $mol^{-1}Å^2$) with 5000 steps of steepest descent (SD), followed by 5000 steps of conjugate gradient (CG). In the second phase, the entire system was gradually heated to 300 K over 20 ns, followed by 5 ns at 300 K using a Langevin thermostat in the NVT ensemble. The NPT ensemble was then applied at a constant pressure of 1 bar using the Berendsen barostat with a time constant τp = 0.1 ps. The production phase was carried out for 200 ns of molecular dynamics, selecting an integration time step of 1 fs, with the SHAKE algorithm coupled (in all simulations, including preparatory ones) to the Particle Mesh Ewald (PME) summation method [38]. Electrostatic and long-range interactions were calculated with a cutoff of 12 Å. The GROMACS 2021 package [39] was used to perform the MD simulations.

Molecular Dynamics Analysis: Once the structural stability of the LPMO enzyme was verified through RMSD (Root Mean Square Deviation) and RMSF (Root Mean Square Fluctuation) analyses, confirming that the system was stable with consistent fluctuations well below 2 Å, representative conformations of the system were selected by performing clustering based on the RMSD of the entire trajectory. The GROMOS algorithm [40] was used with a cutoff of 2 Å based on RMSD to identify the most populated representative conformations. It was verified that the coordination of Cu^{2+} was maintained by monitoring the minimum distance between this ion and the polysaccharide fragment. Hydrogen bond (H-bond) analyses, distance analyses, and the Radial Distribution Function (RDF) were performed using the VMD visualization program [41] and the integrated tools in GROMACS 2021 [39] to identify non-covalent interactions between LPMO and β-chitin.

Principal Component Analysis (PCA) was performed using the cpptraj module [42] of AntechamberTools 16 [43] to extract large-scale collective motions occurring in the MD simulation of the complex, providing insights into the main conformational changes along the MD trajectories.

8.3 Molecular Dynamics Simulations Setup

As widely reported in the literature, MD simulations play a crucial role in studying enzyme–substrate recognition processes [44] In particular, for enzymes such as LPMO SmAA10, which are involved in chitin degradation, these simulations allow for a deeper understanding of the interaction mechanisms with the substrate and help elucidate the polysaccharide chain cleavage process [28] thereby supporting and complementing experimental observations [45]. In this study, we carried out 200 ns of classical MD simulation on the complex between SmAA10 and a polymeric fragment of β-chitin composed of 24 repeating units arranged in 5 chains and 5 layers. The initial crystallographic structure was kindly provided by the group of Orio Malys (Institut des Sciences Moléculaires de Marseille). To preserve the initial conformation of the β-chitin fragment during the simulation and prevent non-physiological structural deviations, positional restraints were applied to the Cα carbon atoms of the chitin monomers.

8.4 Conformational Stability of LPMO

Throughout the simulation, the Root Mean Square Deviation (RMSD) and Root Mean Square Fluctuation (RMSF) analyses confirmed the overall structural stability of the system. As shown in Figure 8.2A, RMSD values remained well below 2 Å, indicating high structural stability of the enzyme over the simulation timeframe. The RMSF analysis (Figure 8.2B), computed for each residue of the LPMO, revealed a localized

peak around 1.5 Å at tyrosine residue 27, suggesting a region of increased local flexibility. This behavior may be attributed both to the structural conformation of the protein and to the solvent exposure of the residue, which could facilitate its mobility.

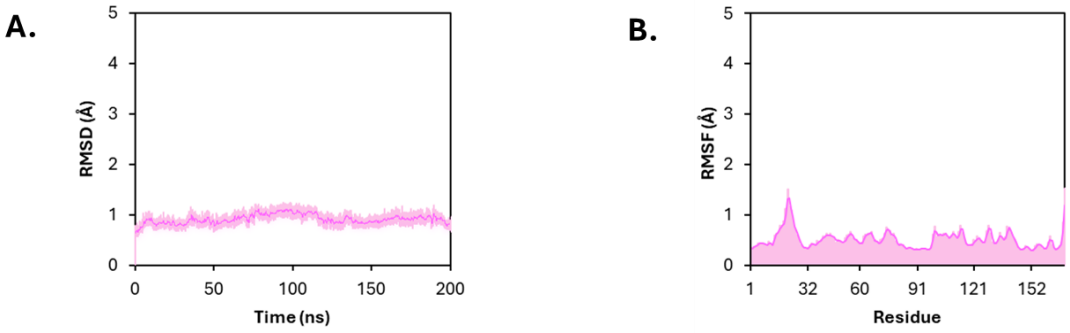

Figure 8.2: A) shows the RMSD trend of the entire LPMO structure over time, relative to the initial conformation, with fluctuations consistently contained around 1 Å. B) illustrates the RMSF, which represents the flexibility of individual residues along the amino acid sequence. Localized peaks are observed, particularly around residue 27, indicating more flexible regions that are potentially involved in interactions with the solvent or the substrate.

Furthermore, the conformational analysis performed through geometric clustering revealed substantial structural homogeneity throughout the entire simulation, confirming the preservation of the enzyme's initial conformation, as shown in Figure 8.3.

A.

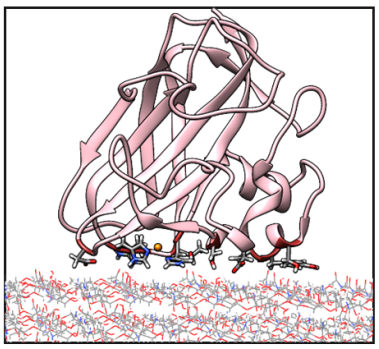

B.

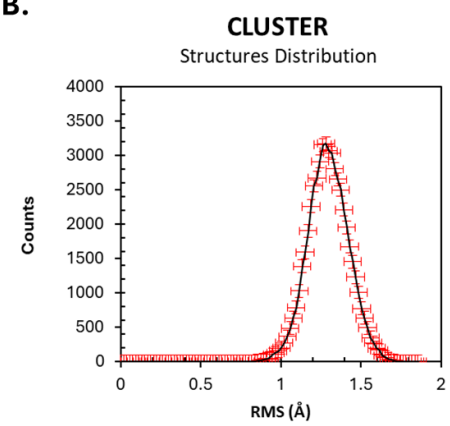

n° CLUSTER	Total frame	Avg d (Å)	CENTROID
1	325	1.30	157000.119

Figure 8.3: Clustering Analysis of LPMO. A) Structural representation of the protein interacting with the substrate surface. B) Distribution of structures obtained through RMSD-based clustering, highlighting a single predominant cluster. The plot shows a distribution centered around 1.3 Å, corresponding to the average distance from the centroid, as summarized in the table below, which reports the main characteristics of the identified cluster

8.5 Active Site Accessibility and the Role of Water

After confirming the maintenance of Cu^{2+} coordination, the minimum distance between the metal ion and the polysaccharide fragment was analyzed, showing stable values around 5–6 Å, as illustrated in Figure 8.4A. This result is consistent with the expected catalytic mechanism, in which the presence of water molecules intercalated between the metal site and the polysaccharide is essential to enable hydrolysis.

Indeed, a critical aspect for catalysis is the accessibility of the copper coordination site when the enzyme is bound to the substrate. If the copper ion were completely shielded from the bulk solvent, it would also be inaccessible to potential reducing agents required for electron transfer.

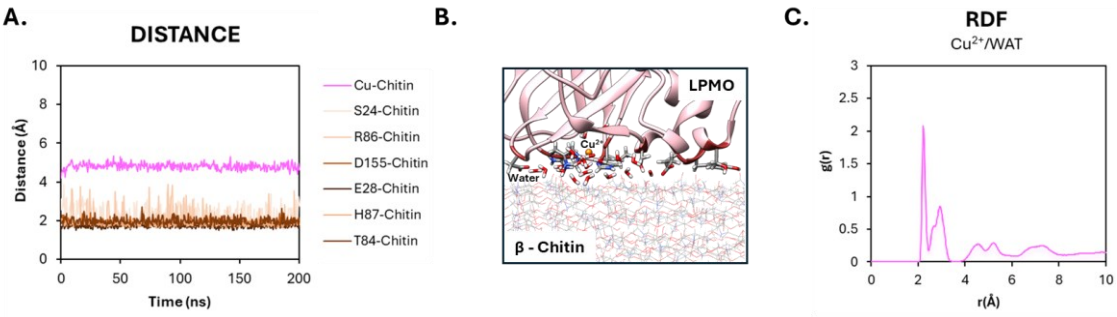

Figure 8.4: A) Time evolution of the minimum distance between the Cu^{2+} ion and the β-chitin fragment (shown in lilac) during the molecular dynamics simulation. The lines in various shades of brown represent the minimum distances between Cu^{2+} and key amino acid residues involved in substrate binding. B) Spatial representation of water molecules intercalated between the metal center and the β-chitin fragment, highlighting the formation of a hydration layer at the active site. C) Radial distribution function (RDF) between Cu^{2+} and water molecules, showing a well-defined peak around 2.1 Å, indicative of the stable presence of solvent molecules within the first hydration shell of the copper ion throughout the simulation.

The obtained model supports the existence of a tightly bound monolayer of water molecules surrounding the copper ion (Figure 8.4C). The presence of these water molecules was further confirmed by calculating the radial distribution function (RDF), which highlights the presence of water in the first two hydration shells around the copper ion (Figure 8.4B).

8.6 Molecular Dynamics Simulations of Enzyme–Substrate Interactions

The geometry of the LPMO active site did not undergo significant changes during the simulation, and the enzyme remained stably bound to the polysaccharide fragment. Based on this observation, we proceeded to identify the polar residues involved in maintaining the interaction with the substrate through hydrogen bonding. The identified residues are listed in Table 8.1. Subsequently, we analyzed the distances between the most representative residues and the chitin monomers, confirming the persistence of these interactions throughout the simulation period (Figure 8.4).

DONOR	ACCEPTOR	OCCUPANCY
T84-Side	**β-Chitin**	**50.19%**
H87-Side	**β-Chitin**	**41.89%**
S31-Side	β-Chitin	0.57%
β-Chitin	**E28-Side**	**68.87%**
K53-Side	β-Chitin	10.75%
K15-Side	β-Chitin	0.19%
Q30-Side	β-Chitin	8.30%
β-Chitin	**D155-Main**	**42.45%**
β-Chitin	Y27-Side	2.45%
R86-Side	**β-Chitin**	**25.28%**
β-Chitin	**E28-Side**	**18.68%**
S24-Side	**β-Chitin**	**19.06%**
S54-Side	β-Chitin	0.38%

Table 8.1: Hydrogen bonds observed in LPMO, highlighting specific donor–acceptor interactions. % Occupancy refers to the frequency with which each hydrogen bond is present throughout the molecular dynamics simulation. A higher percentage indicates a more stable or persistent interaction.

To evaluate the presence of additional significant interactions beyond hydrogen bonding, a radial distribution function (RDF) analysis was performed to investigate potential π interactions. These analyses revealed a particularly relevant π–π interaction between monomer 237 of β-chitin and tyrosine residue 27 of the protein, as shown in Figure 8.5.

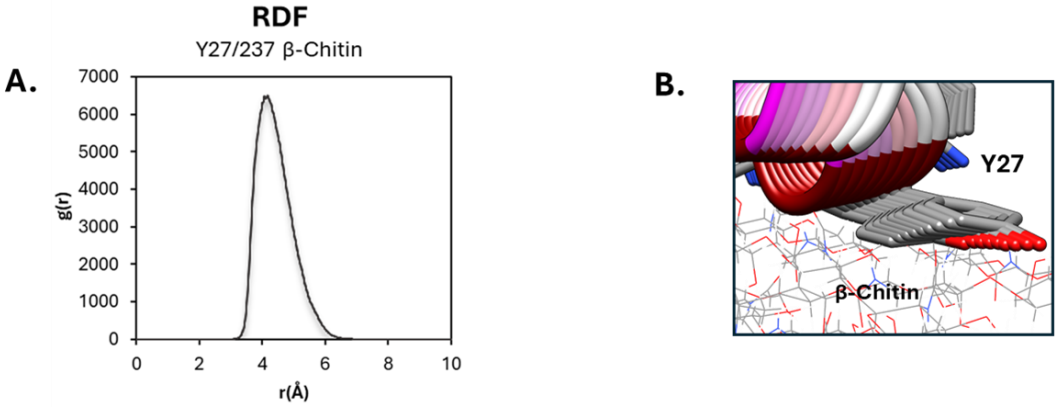

Figure 8.5: A) Radial distribution function (RDF) between Y27 and monomer 237 of β-chitin, showing a sharp peak at 4.5 Å that indicates a preferred interaction distance. B) Three-dimensional molecular representation of β-chitin and residue Y27, highlighting the π–π interaction.

8.7 PCA Analysis – Analysis of the Dynamic Movements of the Complex

Finally, to identify the most significant concerted motions of the LPMO–chitin complex, principal component analysis (PCA) was applied. This allowed visualization of the main residue displacements near the β-chitin fragment, once again highlighting the role of tyrosine residue 27 (Y27), previously identified.

An initial visual inspection of the simulation revealed a rotation of the enzyme around the polymer, a motion attributable to hydrogen bonding interactions between polar residues and the substrate. PCA confirmed that the predominant mode of motion in the complex is a dynamic capping rocking movement (Figure 8.6). This adaptation enables the protein to cover the polysaccharide surface, enhancing binding affinity and interaction stability. Such movement is frequently observed in polysaccharide-binding enzymes, facilitating recognition of surface topology. The capping mechanism can act as a switch, regulating access to the active site similarly to gating mechanisms found in ion channels or regulated enzymes.

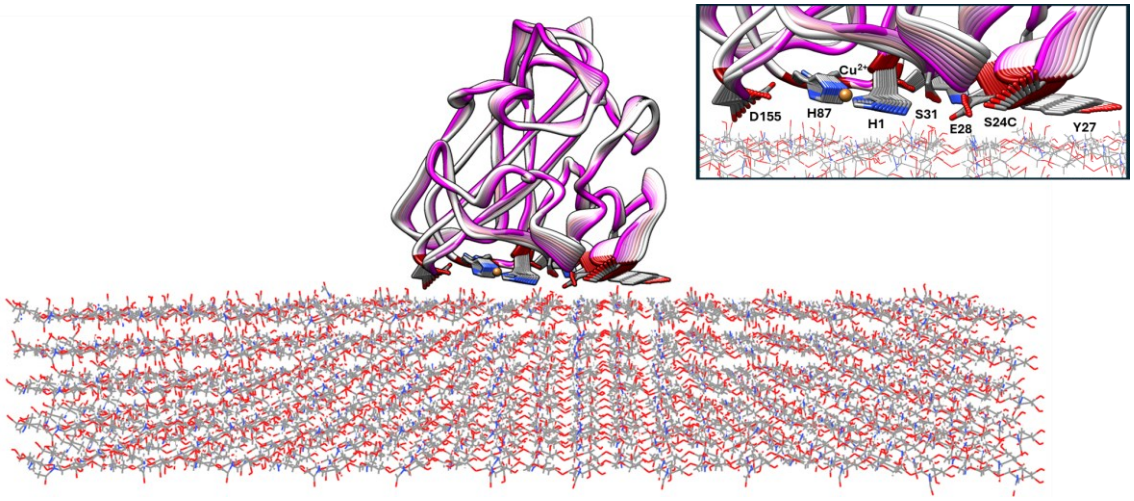

Figure 8.6: Principal Component Analysis (PCA) of the molecular dynamics trajectory of the complex. The plot displays the projection of the sampled conformations onto the first two principal components (PC1 and PC2), which capture the dominant concerted motions of the system. The analysis highlights a prevailing rocking motion of the enzyme over the polysaccharide surface (dynamic capping), accompanied by localized fluctuations, particularly involving residue Y27.

In addition to the rocking movement, the analysis identified a mixed mode of translational and oscillatory motions, which likely reflect the structural adaptation required for specific substrate recognition, catalysis, and the maintenance of stable contact with the polysaccharide surface.

8.8 Conclusions

The increasing need to valorize renewable resources and biological waste has driven attention towards innovative enzymes such as LPMOs, capable of overcoming the recalcitrance of natural polymers like chitin. In this work, through molecular dynamics simulations, we investigated the structural and dynamic mechanisms governing the interaction between the LPMO SmAA10 and a crystalline fragment of β-chitin.

Molecular dynamics simulations performed on the LPMO SmAA10–β–chitin complex revealed remarkable structural stability of the system, with low RMSD deviation and limited local fluctuations, indicative of a well-preserved enzyme-substrate interaction throughout the trajectory. The accessibility of the Cu^{2+} catalytic center was maintained due to the stable presence of structured water molecules within the first hydration shells, an essential condition for catalytic efficiency and availability to redox agents.

Intermolecular interactions, including persistent hydrogen bonds and a π–π interaction between residue Y27 and chitin, were found to be crucial for complex stability. Principal component analysis revealed the existence of concerted dynamic modes, among which a rocking capping movement facilitates the enzyme's conformational adaptation to the polysaccharide surface, likely associated with a dynamic modulation of substrate recognition and binding affinity. Additionally, oscillatory and translational modes suggest a degree of structural plasticity potentially functional for catalytic orientation along the polysaccharide matrix. Overall, the obtained data support a dynamic and adaptive model of enzyme-substrate interaction, where conformational flexibility plays a key role in regulating active site accessibility and catalytic process efficiency.

These structural insights are fundamental to guiding protein engineering strategies and the design of optimized biocatalysts. Looking ahead, frames extracted from the molecular dynamics simulations may serve as input for EPR spectroscopy simulations aimed at experimentally validating the coordination modes and motions observed, thereby providing an even deeper understanding of LPMO function and regulation under physiological and applied conditions.

References

1. Fülöp, L.; János Ecker An Overview of Biomass Conversion: Exploring New Opportunities. PeerJ 2020, 8.
2. Maurya, P.K.; Mondal, S.; Kumar, V.; Singh, S.P. Roadmap to Sustainable Carbon-Neutral Energy and Environment: Can We Cross the Barrier of Biomass Productivity? Environmental Science and Pollution Research 2021, 28, 49327–49342, doi:10.1007/s11356-021-15540-8.
3. Osman, A.I.; Mehta, N.; Elgarahy, A.M.; Al-Hinai, A.; Al-Muhtaseb, A.H.; Rooney, D.W. Conversion of Biomass to Biofuels and Life Cycle Assessment: A Review. Environ Chem Lett 2021, 19, 4075–4118, doi:10.1007/s10311-021-01273-0.
4. Al-Hamamre, Z.; Saidan, M.; Hararah, M.; Rawajfeh, K.; Alkhasawneh, H.E.; Al-Shannag, M. Wastes and Biomass Materials as Sustainable-Renewable Energy Resources for Jordan. Renewable and Sustainable Energy Reviews 2017, 67, 295–314, doi:10.1016/j.rser.2016.09.035.
5. Sweeney, M.D.; Xu, F. Biomass Converting Enzymes as Industrial Biocatalysts for Fuels and Chemicals: Recent Developments. Catalysts 2012, 2, 244–263, doi:10.3390/catal2020244.
6. Yan, N.; Chen, X. Sustainability: Don't Waste Seafood Waste. Nature 2015, 524, 155–157, doi:10.1038/524155a.
7. Maschmeyer, T.; Luque, R.; Selva, M. Upgrading of Marine (Fish and Crustaceans) Biowaste for High Added-Value Molecules and Bio(Nano)-Materials. Chem Soc Rev 2020, 49, 4527–4563, doi:10.1039/C9CS00653B.
8. Jang, M.; Kong, B.; Jeong, Y.; Lee, C.H.; Nah, J. Physicochemical Characterization of A-chitin, B-chitin, and Γ-chitin Separated from Natural Resources. J Polym Sci A Polym Chem 2004, 42, 3423–3432, doi:10.1002/pola.20176.
9. Terkula Iber, B.; Azman Kasan, N.; Torsabo, D.; Wese Omuwa, J. A Review of Various Sources of Chitin and Chitosan in Nature. J Renew Mater 2022, 10, 1097–1123, doi:10.32604/jrm.2022.018142.
10. Bowman, S.M.; Free, S.J. The Structure and Synthesis of the Fungal Cell Wall. BioEssays 2006, 28, 799–808, doi:10.1002/bies.20441.
11. Wang, Y.; Van Le, Q.; Yang, H.; Lam, S.S.; Yang, Y.; Gu, H.; Sonne, C.; Peng, W. Progress in Microbial Biomass Conversion into Green Energy. Chemosphere 2021, 281, 130835, doi:10.1016/j.chemosphere.2021.130835.
12. Kaczmarek, M.B.; Struszczyk-Swita, K.; Li, X.; Szczęsna-Antczak, M.; Daroch, M. Enzymatic Modifications of Chitin, Chitosan, and Chitooligosaccharides. Front Bioeng Biotechnol 2019, 7, doi:10.3389/fbioe.2019.00243.

13. Nastri, F.; D'Alonzo, D.; Leone, L.; Zambrano, G.; Pavone, V.; Lombardi, A. Engineering Metalloprotein Functions in Designed and Native Scaffolds. Trends Biochem Sci 2019, 44, 1022–1040, doi:10.1016/j.tibs.2019.06.006.

14. Hemsworth, G.R.; Johnston, E.M.; Davies, G.J.; Walton, P.H. Lytic Polysaccharide Monooxygenases in Biomass Conversion. Trends Biotechnol 2015, 33, 747–761, doi:10.1016/j.tibtech.2015.09.006.

15. Borisova, A.S.; Isaksen, T.; Dimarogona, M.; Kognole, A.A.; Mathiesen, G.; Várnai, A.; Røhr, Å.K.; Payne, C.M.; Sørlie, M.; Sandgren, M.; et al. Structural and Functional Characterization of a Lytic Polysaccharide Monooxygenase with Broad Substrate Specificity. Journal of Biological Chemistry 2015, 290, 22955–22969, doi:10.1074/jbc.M115.660183.

16. Guo, X.; An, Y.; Liu, F.; Lu, F.; Wang, B. Lytic Polysaccharide Monooxygenase – A New Driving Force for Lignocellulosic Biomass Degradation. Bioresour Technol 2022, 362, 127803, doi:10.1016/j.biortech.2022.127803.

17. Liaqat, F.; Eltem, R. Chitooligosaccharides and Their Biological Activities: A Comprehensive Review. Carbohydr Polym 2018, 184, 243–259, doi:10.1016/j.carbpol.2017.12.067.

18. Quinlan, R.J.; Sweeney, M.D.; Lo Leggio, L.; Otten, H.; Poulsen, J.-C.N.; Johansen, K.S.; Krogh, K.B.R.M.; Jørgensen, C.I.; Tovborg, M.; Anthonsen, A.; et al. Insights into the Oxidative Degradation of Cellulose by a Copper Metalloenzyme That Exploits Biomass Components. Proceedings of the National Academy of Sciences 2011, 108, 15079–15084, doi:10.1073/pnas.1105776108.

19. Vaaje-Kolstad, G.; Houston, D.R.; Riemen, A.H.K.; Eijsink, V.G.H.; van Aalten, D.M.F. Crystal Structure and Binding Properties of the Serratia Marcescens Chitin-Binding Protein CBP21. Journal of Biological Chemistry 2005, 280, 11313–11319, doi:10.1074/jbc.M407175200.

20. Vaaje-Kolstad, G.; Westereng, B.; Horn, S.J.; Liu, Z.; Zhai, H.; Sørlie, M.; Eijsink, V.G.H. An Oxidative Enzyme Boosting the Enzymatic Conversion of Recalcitrant Polysaccharides. Science (1979) 2010, 330, 219–222, doi:10.1126/science.1192231.

21. Book, A.J.; Yennamalli, R.M.; Takasuka, T.E.; Currie, C.R.; Phillips, G.N.; Fox, B.G. Evolution of Substrate Specificity in Bacterial AA10 Lytic Polysaccharide Monooxygenases. Biotechnol Biofuels 2014, 7, 109, doi:10.1186/1754-6834-7-109.

22. Garron, M.-L.; Henrissat, B. The Continuing Expansion of CAZymes and Their Families. Curr Opin Chem Biol 2019, 53, 82–87, doi:10.1016/j.cbpa.2019.08.004.

23. Bennati-Granier, C.; Garajova, S.; Champion, C.; Grisel, S.; Haon, M.; Zhou, S.; Fanuel, M.; Ropartz, D.; Rogniaux, H.; Gimbert, I.; et al. Substrate Specificity and Regioselectivity of Fungal AA9 Lytic Polysaccharide Monooxygenases Secreted by Podospora Anserina. Biotechnol Biofuels 2015, 8, 90, doi:10.1186/s13068-015-0274-3.

24. Hemsworth, G.R.; Henrissat, B.; Davies, G.J.; Walton, P.H. Discovery and Characterization of a New Family of Lytic Polysaccharide Monooxygenases. Nat Chem Biol 2014, 10, 122–126, doi:10.1038/nchembio.1417.

25. Frandsen, K.E.H.; Poulsen, J.-C.N.; Tovborg, M.; Johansen, K.S.; Lo Leggio, L. Learning from Oligosaccharide Soaks of Crystals of an AA13 Lytic Polysaccharide Monooxygenase: Crystal Packing, Ligand Binding and Active-Site Disorder. Acta Crystallogr D Struct Biol 2017, 73, 64–76, doi:10.1107/S2059798316019641.

26. Tuveng, T.R.; Østby, H.; Tamburrini, K.C.; Bissaro, B.; Hegnar, O.A.; Stepnov, A.A.; Várnai, A.; Berrin, J.; Eijsink, V.G.H. Revisiting the AA14 Family of Lytic Polysaccharide Monooxygenases and Their Catalytic Activity. FEBS Lett 2023, 597, 2086–2102, doi:10.1002/1873-3468.14694.

27. Filiatrault-Chastel, C.; Navarro, D.; Haon, M.; Grisel, S.; Herpoël-Gimbert, I.; Chevret, D.; Fanuel, M.; Henrissat, B.; Heiss-Blanquet, S.; Margeot, A.; et al. AA16, a New Lytic Polysaccharide Monooxygenase Family Identified in Fungal Secretomes. Biotechnol Biofuels 2019, 12, 55, doi:10.1186/s13068-019-1394-y.

28. Bissaro, B.; Isaksen, I.; Vaaje-Kolstad, G.; Eijsink, V.G.H.; Røhr, Å.K. How a Lytic Polysaccharide Monooxygenase Binds Crystalline Chitin. Biochemistry 2018, 57, 1893–1906, doi:10.1021/acs.biochem.8b00138.

29. Forsberg, Z.; Røhr, Å.K.; Mekasha, S.; Andersson, K.K.; Eijsink, V.G.H.; Vaaje-Kolstad, G.; Sørlie, M. Comparative Study of Two Chitin-Active and Two Cellulose-Active AA10-Type Lytic Polysaccharide Monooxygenases. Biochemistry 2014, 53, 1647–1656, doi:10.1021/bi5000433.

30. Gao, W.; Yin, H. Insight into the Peroxygenase Activity of Lytic Polysaccharide Monooxygenases (LPMO): Recent Progress and Mechanistic Understanding. Chemical Physics Reviews 2023, 4, doi:10.1063/5.0161517.

31. Marco Túlio Pardini Gontijo; José Guilherme Prado Martin Biovalorization of Agri-Waste for the Production of Polyphenols. In CRC Press; 2023; pp. 97–122.

32. Mushrif, S.H.; Vasudevan, V.; Krishnamurthy, C.B.; Venkatesh, B. Multiscale Molecular Modeling Can Be an Effective Tool to Aid the Development of Biomass Conversion Technology: A Perspective. Chem Eng Sci 2015, 121, 217–235, doi:10.1016/j.ces.2014.08.019.

33. Rovaletti, A.; De Gioia, L.; Fantucci, P.; Greco, C.; Vertemara, J.; Zampella, G.; Arrigoni, F.; Bertini, L. Recent Theoretical Insights into the Oxidative Degradation of Biopolymers and Plastics by Metalloenzymes. Int J Mol Sci 2023, 24, 6368, doi:10.3390/ijms24076368.

34. Mark, P.; Nilsson, L. Structure and Dynamics of the TIP3P, SPC, and SPC/E Water Models at 298 K. J Phys Chem A 2001, 105, 9954–9960, doi:10.1021/jp003020w.

35. Maier, J.A.; Martinez, C.; Kasavajhala, K.; Wickstrom, L.; Hauser, K.E.; Simmerling, C. Ff14SB: Improving the Accuracy of Protein Side Chain and Backbone Parameters from Ff99SB. J Chem Theory Comput 2015, 11, 3696–3713, doi:10.1021/acs.jctc.5b00255.

36. Kirschner, K.N.; Yongye, A.B.; Tschampel, S.M.; González-Outeiriño, J.; Daniels, C.R.; Foley, B.L.; Woods, R.J. GLYCAM06: A Generalizable Biomolecular Force Field. Carbohydrates. J Comput Chem 2008, 29, 622–655, doi:10.1002/jcc.20820.

37. Li, P.; Song, L.F.; Merz, K.M. Parameterization of Highly Charged Metal Ions Using the 12-6-4 LJ-Type Nonbonded Model in Explicit Water. J Phys Chem B 2015, 119, 883–895, doi:10.1021/jp505875v.

38. Petersen, H.G. Accuracy and Efficiency of the Particle Mesh Ewald Method. J Chem Phys 1995, 103, 3668–3679, doi:10.1063/1.470043.

39. Van Der Spoel, D.; Lindahl, E.; Hess, B.; Groenhof, G.; Mark, A.E.; Berendsen, H.J.C. GROMACS: Fast, Flexible, and Free. J Comput Chem 2005, 26, 1701–1718, doi:10.1002/jcc.20291.

40. Ezerski, J.C.; Cheung, M.S. CATS: A Tool for Clustering the Ensemble of Intrinsically Disordered Peptides on a Flat Energy Landscape. J Phys Chem B 2018, 122, 11807–11816, doi:10.1021/acs.jpcb.8b08852.

41. Humphrey, W.; Dalke, A.; Schulten, K. VMD: Visual Molecular Dynamics. J Mol Graph 1996, 14, 33–38, doi:10.1016/0263-7855(96)00018-5.

42. Roe, D.R.; Cheatham, T.E. PTRAJ and CPPTRAJ: Software for Processing and Analysis of Molecular Dynamics Trajectory Data. J Chem Theory Comput 2013, 9, 3084–3095, doi:10.1021/ct400341p.

43. Junmei Wang; Wei Wang; JPeter A. Kollman; David A. Case Antechamber, An Accessory Software Package For Molecular Mechanical Calculations . J Am Chem Soc 2001.

44. Laurent, C.V.F.P.; Breslmayr, E.; Tunega, D.; Ludwig, R.; Oostenbrink, C. Interaction between Cellobiose Dehydrogenase and Lytic Polysaccharide Monooxygenase. Biochemistry 2019, 58, 1226–1235, doi:10.1021/acs.biochem.8b01178.

45. Su, H.; Guo, C.; Zhao, H.; Dong, H.; Sun, J.; Mao, X. Functional Characterization of a Lytic Polysaccharide Monooxygenase EbLPMO10A That Contributes to β-Chitin Degradation by Chitinase. Food Chem 2025, 474, 143225, doi:10.1016/j.foodchem.2025.143225.

Conclusions

This doctoral thesis has deepened the study of substrate–enzyme interactions through a multiscale computational approach, integrating methodologies from force field–based theories to quantum chemistry, including molecular docking, classical molecular dynamics, and quantum mechanical calculations based on density functional theory (DFT). The main objective was to develop theoretical protocols capable of supporting the rational design of efficient biocatalysts, with potential applications in bioremediation and the valorization of renewable resources.

Understanding enzymatic catalysis requires molecular detail that a single computational technique cannot provide. The multiscale protocol applied here modeled different stages of the catalytic process: docking predicted ligand–enzyme recognition modes and provided realistic starting structures, MD simulations characterized structural flexibility, active-site dynamics, substrate access pathways, and interaction stability, while DFT calculations on cluster models of catalytic sites probed the electronic structure, forming a theoretical basis for optimizing enzymatic reactivity. Residue-level interaction analyses and MM-PBSA binding affinity estimates offered further guidance for identifying mutagenic sites.

Overall, the findings provide mechanistic insights and practical guidance for enzyme engineering. The strategies developed can be applied broadly to predict and enhance biocatalyst performance in industrially relevant processes such as plastic recycling, pollutant degradation, and biomass conversion.

The research is organized in two main sections. The first part focused on degradative enzymes involved in the depolymerization of non-biodegradable plastics, such as PET and PE, including the effects of specific mutations. It also explored new enzymatic targets of environmental interest, such as laccases, assessing their dynamic behavior and ability to degrade unconventional hydrocarbon substrates.

The first study focused on FAST-PETase interactions with a tetrameric PET substrate (4PET), providing new insights into polyethylene terephthalate depolymerization and the role of enzyme flexibility. Molecular dynamics simulations revealed that at 50 °C the enzyme adopts a more plastic conformation in the active-site region (Figure 4.6C), facilitating productive substrate alignment. Key residues W185,

W159, and Y87 stabilize PET's aromatic units through hydrophobic and π-stacking interactions (Figures 4.6E–4.6F), promoting the characteristic "W-shaped" conformation of 4PET. DFT calculations indicated that this high-energy, enzyme-induced conformation facilitates ester bond cleavage, explaining the enhanced hydrolytic activity of FAST-PETase (Figure 4.7). These results provide a rational basis for engineering PET-recycling biocatalysts under mild conditions.

The second study investigated PAH oxidation, revealing mechanisms of anthracene (ANT) and benzo[a]pyrene (BaP) oxidation by the T1 copper site of Trametes versicolor laccase. Combining docking (Figure 5.3), molecular dynamics (Figure 5.7), and DFT, water was identified as a key nucleophile, and the energy profiles for both substrates were outlined (Figure 5.8). High activation barriers (Figure 5.9) in the absence of mediators highlight the need for further studies on mediator-assisted oxidation.

The third study compared laccases with different redox potentials, providing insights into polyethylene (PE) oxidation. In bacterial laccases such as LMCO2, low redox potential does not limit activity; efficiency depends mainly on substrate binding stability at the active site (Figure 6.2). Hydrophobic residues around T1 copper and PE conformability facilitate prolonged interactions, while a methionine-rich loop anchors the polymer near the catalytic center (Figure 6.7). QM/MM analyses suggested that direct C–H activation is kinetically unfeasible, indicating LMCO2 likely acts on pre-oxidized groups. These findings show that laccase efficiency relies more on stable enzyme–substrate complexes than on redox potential, informing enzyme engineering and plastic bioremediation strategies.

Collectively, these studies demonstrate that enzyme activity is governed by substrate binding and conformational dynamics, providing a rational basis for enzyme engineering and strategies for plastic bioremediation.

The second part of the thesis focused on metalloprotein mutants aimed at improving the conversion of fatty acids and aromatic compounds into high-value intermediates through rational design guided by docking and molecular dynamics. The fourth study analyzed the P450SPα enzyme, where targeted modifications, particularly in the double mutant M12 (G173F/F288A), enhanced catalytic efficiency (Figure 7.10B). Correct substrate positioning was critical for heme access and hydration of the catalytic iron (Figure 7.13).

The final study examined interactions between LPMO SmAA10 and a crystalline β-chitin fragment. Molecular dynamics revealed a stable complex, maintained by persistent hydrogen bonds, a key π–π interaction involving Y27, and water molecules that ensure access to the Cu^{2+} catalytic center (Figure 8.4). Conformational flexibility facilitated substrate adaptation and regulated catalytic

efficiency, with concerted rocking and capping movements of flexible active sites providing detailed mechanistic insights into enzyme–substrate recognition (Figure 8.6).

Collectively, these studies demonstrate that computationally guided enzyme design can accelerate the development of sustainable biocatalysts. By integrating theoretical predictions with experimental validation, this work provides a framework for iterative optimization, supporting environmentally friendly chemical transformations and improving biocatalyst performance.

In conclusion, this work demonstrates that the integration of multiscale computational methodologies with experimental validation provides a powerful and versatile framework for investigating complex enzymatic systems and guiding the rational design of efficient biocatalysts. The approaches developed here offer mechanistic insights across multiple scales and hold broad potential for sustainable chemical transformations, bioremediation, and industrial biotechnology. By establishing a virtuous cycle of model refinement and empirical validation, this thesis highlights the ability of computationally guided strategies to drive the development of innovative catalytic solutions with reduced environmental impact.

List of Publications

- Orlando, C., Prejanò, M., Russo, N., & Marino, T. **(2023).** On the Role of Temperature in the Depolymerization of PET by FAST-PETase: An Atomistic Point of View on Possible Active Site Pre-Organization and Substrate-Destabilization Effects. *ChemBioChem*, *24*(20), e202300412.

- Orlando, C., Rizzo, I. C., Arrigoni, F., Zampolli, J., Mangiagalli, M., Di Gennaro, P., Lotti, M.,De Gioia,L., Marino, T., Greco, C., & Bertini, L. **(2024).** Mechanism of non-phenolic substrate oxidation by the fungal laccase Type 1 copper site from Trametes versicolor: the case of benzo [a] pyrene and anthracene. *Dalton Transactions*, *53*(29), 12152-12161.

- Orlando, C., Bellei, M., Zampolli, J., Mangiagalli, M., Di Gennaro, P., Lotti, De Gioia, L., , Marino, T., Di Rocco, G., Greco, C., Arrigoni, F., & Bertini, L. **(2025).** Comparative Analysis of Polyethylene-Oxidizing Laccases: Redox Properties and Enzyme-Polyethylene Interaction Mechanism. *ChemSusChem*, e202402253.

- Orlando, C., Giurato, D., Correddu, D., Prejanò, M., Gilardi, G., Marino, T, Lombardi, A., Greco, C., Arrigoni, F., & Bertini, L. Rational Design of CYP450SPα Mutants for Enhanced Lipid Waste Conversion: Dynamic Comparison with OleTJE (Work in progress)

- Orlando, C., Arrigoni, F., Callea, L., Greco, C., Orio, M., & Bertini, L. Molecular Dynamics of the Metallo-enzyme Lytic Polysaccharide Monooxygenase (LPMO) SmAA10 and its interactions with β-chitin (Work in progress)

Other Publications

- Ciardullo, G., Orlando, C., Russo, N., Marchese, E., Galano, A., Marino, T., & Prejanò, M. **(2024).** On the dual role of (+)-catechin as primary antioxidant and inhibitor of viral proteases. *Computers in Biology and Medicine*, *180*, 108953.

- Di Costanzo, L. F., Sgueglia, G., Orlando, C., Polentarutti, M., Leone, L., La Gatta, S., ... & Chino, M. **(2025)**. Structural insights into temperature-dependent dynamics of METPsc1, a miniaturized electron-transfer protein. *Journal of Inorganic Biochemistry*, *264*, 112810.